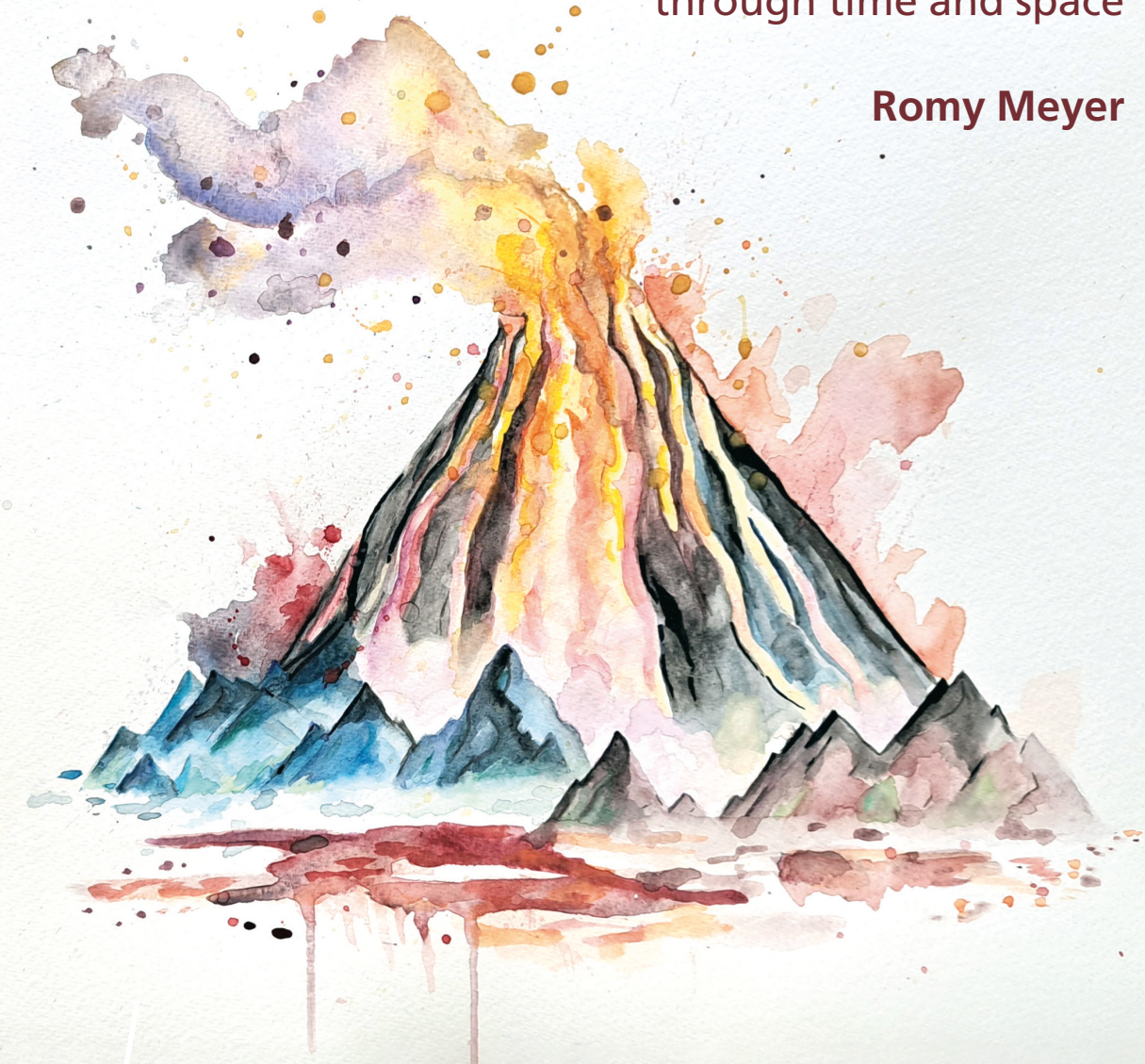
Unravelling Geomagnetic Anomalies

Tracing the South Atlantic Anomaly through time and space

Romy Meyer



368 UTRECHT STUDIES IN EARTH SCIENCES

Unravelling Geomagnetic Anomalies

Tracing the South Atlantic Anomaly through time and space

Geomagnetische anomalieën ontrafeld

De Zuid-Atlantische Anomalie door tijd en ruimte gevolgd

Romy Meyer

Utrecht Studies in Earth Sciences
No. 368

ISBN: 978-90-6266-675-1
DOI: 10.33540/2171
Cover illustration: R. Meyer
Cover design: M. Stoete

Copyright © 2026 by R. Meyer, Utrecht University
All Rights Reserved

Unravelling Geomagnetic Anomalies

Tracing the South Atlantic Anomaly through time and space

Geomagnetische anomalieën ontrafeld

De Zuid-Atlantische Anomalie door tijd en ruimte gevolgd

(met een samenvatting in het Nederlands)

Proefschrift

ter verkrijging van de graad van doctor aan de Universiteit Utrecht op
gezag van de rector magnificus prof. dr. ir. W. Hazeleger, ingevolge
het besluit van het College voor Promoties in het openbaar te verdedigen
op dinsdag 23 juni 2026 des middags te 2.15 uur

door

Romy Meyer

geboren op 18 maart 1996
te Gouda

Promotor:
Prof. dr. W. Krijgsman

Copromotor:
Dr. L.V. de Groot

Beoordelingscommissie:
Dr. A. Di Chiara
Prof. dr. D.J.J. van Hinsbergen
Prof. dr. K.F. Kuiper
Dr. A.R. Niemeijer
Prof. dr. M.L. Osete

The research in this thesis is financed by the Netherlands Organisation for Scientific Research (NWO) under the VIDI grant: VI.Vidi.192.047.

Questions of science - Do not speak as loud as my heart
– The Scientist, Coldplay



Contents

Prologue & Summary **1**

Proloog & Samenvatting **11**

1 Local magnetic anomalies explain bias in paleomagnetic data: consequences for sampling **21**
1.1 Introduction . . . 22
1.2 Paleomagnetic data . . . 24
1.3 Mapping magnetic anomalies . . . 29
1.4 Discussion . . . 33
1.5 Conclusion . . . 38
1.6 Supplementary Information . . . 40

2 Effect of storage conditions on paleointensity results from very young volcanics, the 2021 Tajogaite eruption, La Palma **69**
2.1 Introduction . . . 70
2.2 Geological setting and sampling strategy . . . 72
2.3 Rock Magnetic Characteristics . . . 74
2.4 Paleomagnetic directions . . . 76
2.5 Field intensity . . . 78
2.6 Discussion . . . 83
2.7 Conclusion . . . 88
2.8 Supplementary Information . . . 89

3 A reconnaissance of Quaternary paleomagnetic directions and paleointensities in the East Pacific Ocean (Isla Socorro and Isla San Benedicto, Revillagigedo Archipelago, Mexico) **97**
3.1 Introduction . . . 98
3.2 Geological setting and sampling strategy . . . 99
3.3 Methods . . . 103
3.4 Results . . . 105
3.5 Discussion . . . 111
3.6 Conclusion . . . 116
3.7 Acknowledgments . . . 117
3.8 Supplementary Information . . . 118

4 Paleomagnetic data from recent volcanics of Piton de La Fournaise, La Réunion: constraints on the evolution of the South Atlantic Anomaly **129**
4.1 Introduction . . . 130
4.2 Geological setting and sampling . . . 132
4.3 Rock magnetic characteristics . . . 134
4.4 Paleomagnetic directions . . . 138

4.5 Paleointensity . . . 140
4.6 Discussion . . . 145
4.7 Conclusion . . . 151
4.8 Supplementary Information . . . 153

5 Recent geomagnetic field behaviour in Indonesia: paleodirections and paleointensities from the past 5,000 years from Bali 155
5.1 Introduction . . . 156
5.2 Geological setting and sampling . . . 157
5.3 Rock Magnetic Characteristics . . . 159
5.4 Paleomagnetic directions . . . 163
5.5 Paleointensities . . . 165
5.6 Discussion . . . 170
5.7 Conclusion . . . 176
5.8 Supplementary Information . . . 177

6 Epilogue 181

Curriculum Vitæ 199

Acknowledgements 203

Prologue & Summary

Our planet is surrounded by a magnetic field, acting like a huge shield against harmful solar and cosmic radiation that, if it would not be deflected by the Earth's magnetic field, may damage the atmosphere and disrupt communication systems (Boteler et al., 1998; Courtillot et al., 2007). The Earth's magnetic field can be described with a direction and a strength, and both are constantly changing through time. The research field studying the past variations in the Earth's magnetic field is known as paleomagnetism. By using archaeological materials, volcanic rocks or sediments one can determine the past field value at that location at a specific moment in time. Currently, the Earth's magnetic field is characterised by a region of weak field strength above South America, named the South Atlantic Anomaly (SAA) (Fig. 1). This low intensity anomaly is one of the most intriguing features of today's geomagnetic field. Its present-day behaviour is studied using satellite data but much about the past behaviour of the anomaly is unknown (Campuzano et al., 2019; Engbers et al., 2022; Nilsson et al., 2022). In this thesis, I first focus on studying the reliability of volcanic rocks as paleomagnetic recorders using data from Mt. Etna and La Palma, and then I study the behaviour of the SAA by obtaining paleomagnetic data from three different locations on Earth: the Revillagigedo Archipelago, La Réunion and the island of Bali in Indonesia (Fig. 1).

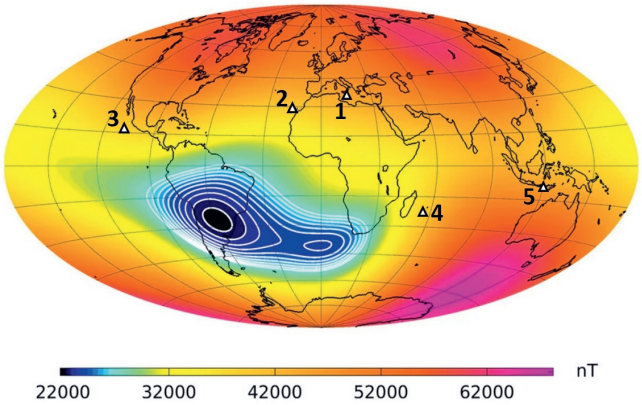


Figure 1: Field intensity at the surface of the Earth in 2020 CE showing the outline of the South Atlantic Anomaly, image from (Finlay et al., 2020). White contour lines are in steps of 500 nT from 22,500 to 27,000 nT. Triangles show the location of the study areas in this thesis, labelled per chapter those are 1) Mt. Etna, Italy, 2) La Palma, Spain, 3) Revillagigedo Archipelago, Mexico, 4) La Réunion and 5) Bali, Indonesia.

Recent variations in the Earth's magnetic field

When averaged over a sufficient amount of time the Earth's magnetic field can be approximated as a geocentric axial dipole (GAD), yet it is continuously changing through time and space. These variations, known as paleosecular variation (PSV), operate on timescales ranging from seconds to millions of years. On the longer timescale, the most prominent expression of field variability is the alternation between periods of stable polarity (chrons or superchrons) and geomagnetic reversals. For example, during the Cretaceous the field maintained a normal polarity for 37 million years before switching polarity in a geomagnetic reversal. Even during such long intervals of stable polarity, the field still exhibits secular variation in direction and intensity. During a geomagnetic reversal the magnetic north and south pole of the Earth switch. Magnetic reversals have occurred very irregularly in the past but on average around every 200,000 years (Ogg, 2020). The last reversal, the Matuyama-Brunhes reversal, took place about 780,000 years ago. The time for a complete reversal to take place may be in the range of hundred or thousands of years (Mahgoub et al., 2023; Sagnotti et al., 2014, 2016; van Grinsven et al., 2025). In contrast to full reversals, Earth's magnetic field also shows excursions, which are mostly only a temporary collapse of the field with directions deviating >45° degrees from the geographic poles. They did occur frequently since the last reversal, an example is the Laschamps excursion around 41,000 years ago when Earth's magnetic field weakened and the poles briefly switched (Guillou et al., 2004). On even shorter timescales geomagnetic jerks occur: sudden, brief changes of the field lasting hundreds of years, or even less. On top of this there is the everlasting secular variation: constant variations in declination, inclination and intensity that make the poles wander around the geographic poles. Secular variation also leads to the variations in declination, which is the angle between the magnetic north and the geographic north, that requires corrections to compass readings depending on where on Earth you are. Secular variation of directions and intensity is measured by magnetic observatories worldwide and by satellites in space. These direct measurements reveal a very interesting feature of today's Earth magnetic field: the South Atlantic Anomaly (SAA).

The SAA is a region of anomalously low field strength located above South-America and the South-Atlantic, and is typically defined as the area where the surface magnetic intensity is below 32 μT (Pavón-Carrasco & De Santis, 2016). In this region, the Van Allen radiation belts are located at a lower altitude than usual (Domingos et al., 2017). The belts contain trapped charged particles from the solar wind, which can pose risks to spacecrafts passing through the area (Heirtzler et al., 2002). The SAA is currently observed to be expanding and seems to split into two minima, one over South America and the other over southern Africa (Fig. 1), while the entire low intensity region is drifting westwards (Domingos et al., 2017). This westward movement is thought to result from the convection of liquid iron in the Earth's outer core. Estimates of the average westward drift rate of the centre of the anomaly vary approximately between ~0.18° to ~0.3° per year (Fürst et al., 2009; Ye et al., 2017). Concurrent with the growing area of the SAA is an overall decrease of the Earth's dipole moment, showing a decrease of 9% between 1840-2015 CE (Finlay et al., 2016; Olson & Amit, 2006). As reversals are expected to happen when the Earth's

magnetic field is weak, there is a scientific debate about whether a continuation of this decrease in dipole moment will lead to a geomagnetic reversal. Moreover, it remains a pressing question whether the SAA represents a precursor to an upcoming reversal.

The present-day variations in the Earth's magnetic field are closely monitored with satellites. However, understanding the changes in the Earth's magnetic field and the evolution of geomagnetic anomalies prior to the direct measurements is equally important. For this, we rely on a different type of data, which is paleomagnetic data.

Paleomagnetism

The first uses of magnetism go back to the sixth century BCE, when Thales of Miletus described the properties of magnetic lodestone, and to the fourth century BCE, when the first compasses were invented in China. Direct recordings of magnetic declination in Europe go back to the 16th century CE. During sea voyages, declination measurements from around the world were recorded in ship logs, used for navigational purposes. Inclinations were only measured occasionally, systematic records of inclination became more common from the 18th century onwards. The very first measurements of the Earth's magnetic field intensity began later. In 1798 CE, Alexander von Humboldt started with systematic observations of relative magnetic intensity. True measurements of the absolute magnetic intensity started around 1832 CE, when Carl Friedrich Gauss developed a magnetometer which was capable to measure the direct field strength. This marked the beginning of absolute systematic intensity measurements. The research field of rock magnetism went through innovations in the early 20th century. Bernhard Brunhes discovered that the natural remanent magnetisation in a rock was oriented in a direction antiparallel to the ambient field in 1906 CE. Additionally, in 1926 CE Motonori Matuyama showed from a stack of lava flows that the younger lavas were normally magnetised, and the older lavas were reversed. Both of them discovered the process of a geomagnetic reversal: the magnetic signals in the rocks had a reversed magnetic polarity which indicated that the Earth's magnetic poles had flipped in the past. The last reversal, Matuyama-Brunhes reversal, was named after them. Laboratory studies on the remanent magnetisation in volcanic rocks were further developed by Johannes Koeningsberger (1930s), Emile and Odette Thellier (1940s) and Takesi Nagata (1940s). They also laid the foundation for paleointensity experiments.

The basic principle of how a rock acquires a magnetisation is relatively easy. When a rock is heated above its Curie temperature, all magnetisations of the mineral particles, such as magnetite, are removed. Upon cooling below the Curie temperature, the magnetisation of the magnetic particles align themselves with the surrounding magnetic field. Thereby they acquire a natural remanent magnetisation (NRM), which reflects the direction and strength of the Earth's magnetic field at that specific moment in time. Sediments may also acquire a magnetisation: the magnetic particles in a water suspension of sediments can rotate freely, and they turn into the direction of the field to acquire a depositional remanent magnetisation when they are deposited. However, this magnetisation is generally much weaker than the magnetisation acquired by igneous bodies. Paleodirections can be obtained from

igneous rocks, archaeological material and sediments. The declination and inclination of a sample is determined by taking oriented samples in the field, and later demagnetising them in the laboratory. This can be done by subsequently heating the samples in steps, or by using alternating fields. After each demagnetisation step the remaining magnetisation in the sample is measured, the results are plotted in an orthogonal vector diagram named the Zijderveld diagram (Zijderveld, 1967). Absolute intensity measurements are not possible for sediments, only for rocks or archaeological material that acquired their magnetisation upon cooling. Furthermore, whereas measuring paleodirections is relatively straightforward, obtaining paleointensity data is much more difficult.

Paleointensity

The most common method to obtain a paleointensity from a rock is to subject it to a series of heating experiments (Thellier, 1959). In the IZZI-Thellier method (Tauxe & Staudigel, 2004), the strength of the ancient geomagnetic field in a rock is estimated by comparing the natural remanent magnetisation (NRM) to a thermal remanent magnetisation (TRM) acquired in a known lab field. Samples are heated in a series of temperature increments, alternating between zero-field, in-field (ZI) steps (Coe, 1967) and in-field, zero-field (IZ) steps (Aitken et al., 1988). The NRM remaining is measured during the zero-field steps, and the TRM gained is measured in the in-field steps. The NRM remaining vs TRM gained is plotted in an Arai diagram (Nagata et al., 1963) (Fig. 2), and the slope of the linear segment of this diagram times the laboratory field is the paleointensity. Unfortunately, not all samples behave ideally for paleointensity experiments. Often the specimens suffer from thermal alteration in the higher temperature steps. To check for this a pTRM check is usually included in the measurement protocol: after each four ZI and IZ steps a previous in-field step is repeated to check whether the pTRM of the lower temperature step can be reproduced (Coe, 1967). Another form of non-ideal behaviour is related to the grain size of the magnetic carrier in the sample. The Thellier type methods are based on three laws; Additivity, Reciprocity and Independence of partial thermoremanent magnetisation. In 1949, Néel (1949) showed that these laws were valid for single domain (SD) grains. However, a bulk volcanic sample is often not purely SD-sized, but is a mixture of SD, pseudo-single domain (PSD) and multi-domain (MD) grain sizes. SD grains are very small, so all spins are aligned into one direction and therefore their remanence is very stable. On the other hand, MD grains are large in size, and the grain is split into several domains with a more unstable remanence. PSD and MD grains may cause the three laws underpinning thermal paleointensity experiments to fail and result in non-linear Arai plots.

To detect such adverse magnetic behaviour, several selection criteria have been proposed to check the quality of paleointensity results. MD behaviour can be detected using the curvature criteria k' and there is a maximum difference a pTRM check may give. Specimens that do not pass the selection criteria are routinely rejected and not included in further interpretations. Applying these criteria, the IZZI-Thellier protocol often results in success rates of only <20%. Therefore, to increase the success rate, various other methods have been proposed. For example the microwave method (Hill & Shaw, 2000; Walton et al., 1993), the multispecimen

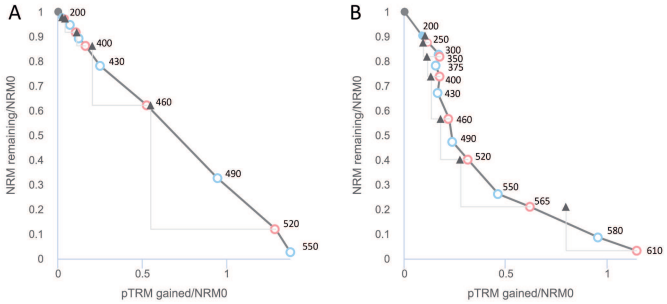


Figure 2: Examples of Arai diagrams with temperature steps given. Blue circles are the ZI-steps, red circles the IZ-steps, and triangles indicate pTRM-checks. Numbers indicate the temperature steps in °C. In A is an example of an ideal paleointensity recorder, the slope of the NRM remaining vs TRM gained is linear. A laboratory field of 50 μT was applied, therefore this specimen yields a paleointensity of 36.4 μT. B shows a specimen that experiences non-ideal behaviour such as sagging and a failing pTRM-check back to temperature step 565°C.

technique (Dekkers & Böhnel, 2006), the pseudo-Thellier technique (De Groot et al., 2013; Tauxe et al., 1995; Yu et al., 2003), and recent advances in end-member modelling (van Grinsven et al., 2023). Nonetheless, the IZZI-Thellier technique remains the most widely applied method for paleointensity determinations and is used in four chapters of this thesis. In contrast to previous studies obtaining low success rates, we achieved success rates well above 20%.

Reliability of volcanic rocks as paleomagnetic recorders

Despite volcanic rocks typically being reliable recorders of the Earth's magnetic field, there are often biases reported in paleomagnetic datasets. Even the samples with linear Arai plots that all pass selection criteria may yield biased paleointensity results (L. V. de Groot et al., 2013). A bias in the paleomagnetic data can be detected when the data is from recent historical flows, emplaced after 1850 CE. Their declination, inclination and intensity result can be compared with the expected field values according to the International Geomagnetic Reference Field (IGRF, (Alken et al., 2021)), or for flows prior to 1900 CE the gufm1 model (Jackson et al., 2000). One location for which the paleomagnetic dataset often does not match with the expected field is Mt. Etna, a volcano on Sicily, Italy. Mt. Etna is a very active volcano with many recent lava flows, and has been extensively studied. In **Chapter 1** we investigated a possible reason for the consistent underestimation reported in paleomagnetic intensity and inclination data for historical flows from Mt. Etna. First, we compiled an overview of all available paleomagnetic data from Mt. Etna, and include new paleomagnetic directional data from seven different historical flows. The paleomagnetic dataset shows no bias in declination, but it does give consistently lower than expected inclinations and intensities. Second, the ambient geomagnetic field was measured at five sites above the surface of the lava flow with a three-axial fluxgate magnetometer. This device measures the magnetic field that a hypothetically new lava flow would record. The field was measured at each site along the lengths of three paths perpendicular to the presumed flow direction at two different

heights above the surface of the lava flow. The paths had different topography, and consisted of at least one ridge and one gully. This allowed for detailed mapping of changes of the ambient geomagnetic field above an irregular topography. The measurements show that inclination and intensity values are lower above gullies, and higher above ridges. Furthermore, deviations were larger for measurements closer to the surface. Therefore, variations in the ambient magnetic field on Mt. Etna seem to be caused by the magnetised terrain below: the irregular topography influences the surrounding magnetic field, creating local magnetic anomalies. Lastly, we simulated what the effect would be on paleomagnetic statistics when a hypothetical new flow would cover the surface. We randomly sampled both the complete fluxgate measurement dataset and only the measurements from the gullies. These tests showed that a high k-value, a precision parameter for the clustering of directional data, does not necessarily predict accurate results. To the contrary, a high k-value might actually indicate that local magnetic anomalies were not averaged out. We highlight the importance of taking samples spread out over a large area, especially in a rugged volcanic terrain, to minimise the effect of local magnetic anomalies. Lastly, we advise future studies to always report sampling strategies in detail.

Taking samples spread out over a larger area was done in **Chapter 2**, where we sampled the very young 2021 lava flow on La Palma at three different locations. By visiting the island in October 2021 while the eruption was still ongoing, the sampled rocks were only 3.5 weeks old when they were measured in the laboratory. We tested whether the intensity of the magnetic field at the time of cooling was reliably recorded by the new flow, how successful the IZZI-Thellier technique was on these extremely young samples, and whether there are changes in the intensity over time. The declination, inclination and intensity were measured from the samples of the 2021 flow immediately upon returning from the field. The results varied per site, however, the average result is close to the expected field value. This confirms the sampling strategy recommended in **Chapter 1**, and implies that this basaltic flow is a good recorder of the Earth's magnetic field. Then, we stored two batches of intensity samples in the Earth's magnetic field, and two batches in a shielded room with a residual field <300 nT. For each storage condition, one batch was measured two years after sampling and the others were measured three years after sampling. Across all batches the average paleointensity result remains approximately similar and in agreement with the known paleofield, although it seems to slightly decrease after three years of storage time. However, the success rate of the paleointensity experiments is lower for some sites after two or three years of storage, so fewer samples pass the quality criteria. Nevertheless, all batches had exceptionally high success rates with the IZZI-Thellier method (>48%). Lastly, there appears to be a small tendency for samples stored out-field to have higher success rates than those stored in-field. During a second fieldwork in 2025, new samples were obtained from the same 2021 lava flow, these samples were thus 'stored' in the natural field for more than three years. Also, Calvo-Rathert et al. (2024) obtained samples from the flow in 2022. Interestingly, both our new samples and those from Calvo-Rathert et al. (2024) were largely unsuccessful with the IZZI-Thellier technique. The decline in success rate for samples stored in a magnetic field may be due to a combination of the 'fragile curvature' process (Tauxe et al., 2021) and the acquisition of viscous

remanent magnetisation (L. V. de Groot et al., 2014a), although differences between sampling the inside or outside of the flow could also play a role.

Geomagnetic anomalies in the Southern Hemisphere
Current geomagnetic field models that capture the evolution of the SAA have contrasting hypothesis about its emergence. The anomaly may be related to a reverse flux patch at the edge of the Large Low-Shear Velocity Province (LLSVP) below Southern Africa (Tarduno et al., 2015), or migrated westwards from the Indian Ocean (Campuzano et al., 2019; Di Chiara & Pavón-Carrasco, 2022; Nilsson et al., 2022). Also the timing of initiation is unknown, possibly as early as 860 CE (Trindade et al., 2018), since 950 CE (Campuzano et al., 2019), at 1250 CE (Tarduno et al., 2015) or as late as 1800 CE (Gubbins et al., 2006). A recurrence of the SAA has also been proposed (Engbers et al., 2022; Nilsson et al., 2022; Shah et al., 2016; Trindade et al., 2018). The main problem with current geomagnetic models is that there is an unequal data coverage: paleomagnetic data from the Northern Hemisphere is overrepresented in the data kernel of the models, while data from the Southern Hemisphere remains scarce. To describe the recent behaviour of the Earth's magnetic field and the development of the SAA, paleomagnetic data from understudied regions, particularly in the Southern Hemisphere is needed. At the same time, even in the Northern Hemisphere there are remote regions without Holocene paleomagnetic records, and filling such gaps is also valuable. We therefore present paleomagnetic data from a remote Northern Hemisphere location in Chapter 3, followed by two Southern Hemisphere locations in Chapters 4 and 5.

In **Chapter 3** we present paleomagnetic data from the remote Revillagigedo Archipelago, Mexico. These islands lie around 400-700 km south-east of the tip of the coast of Baja California. We visited two islands, the uninhabited island of San Benedicto, and the slightly larger island of Socorro. Little research has been done on the islands: no paleomagnetic data is available from San Benedicto and only one paleomagnetic study has been done on Socorro (Sbarbori et al., 2009). For San Benedicto, we present paleomagnetic data from the 1953 CE lava flow. The three sampling sites of the 1953 CE lava flow show different results in paleodirections, but combining the results of the sites comes very close to the expected reference value. This again supports the sampling strategy recommended in **Chapter 1**. The paleointensities of the sites, however, underestimate the expected field value. This might be due to multi-domain effects or arise from local magnetic anomalies as proposed in Chapter 1. From the sampling sites on Socorro, one site was dated using radiocarbon and was assigned an age between 4052-2846 BCE and 4950-2846 BCE (Farmer et al., 1993). This site yielded an interestingly low inclination of 4.2°, whereas 35° is expected at this latitude according to a geocentric axial dipole. This might suggest a previously unknown inclination anomaly in this period, as it is not predicted by geomagnetic models. All other sampling sites on the island of Socorro are older, likely of Pleistocene age. Successfully obtained paleodirections and intensities from these latter lava flows are consistent with expected GAD-values at this latitude, and therefore recorded no anomalous fields directions or intensities.

One hypothesis on the evolution of the SAA is that the feature migrated from the

Indian Ocean westwards. To investigate this hypothesis, we visit the island of La Réunion for **Chapter 4**. La Réunion is an island east of Madagascar in the Indian Ocean, and therefore ideally located to study whether the SAA has influenced this region in the past. Paleomagnetic data was obtained from 18 sampling sites around the frequently erupting Piton de La Fournaise. Most sites yielded successful paleodirections: 10 sites gave reliable paleointensity results. We combined our paleomagnetic data with the results from two previous studies (Béguin, 2020; Tanguy & Le Goff, 2004) to construct a full-vector PSV curve. The dataset of La Réunion consists of a variety of dating techniques, including radiocarbon dated lava flows, locations dated using pioneer trees, and historically documented lava flows. Additionally, there are periods when paleomagnetic data coverage is low due to periods of low volcanic activity. To deal with these two challenges, we used a novel Bayesian method to create PSV curves which we developed in Schanner et al. (2026). This method takes all kinds of age distributions into account, and gives the possibility to use only a simple prior or a global field model as prior for the Bayesian modelling. Using a global field model as prior is especially useful in regions or time periods with low paleomagnetic data coverage. The PSV curves from La Réunion captures rapid directional changes around 1600-1750 CE, and reveal an intensity high around 1400 CE, after which the intensity drops to ~29 μT at 1550 CE. This low intensity might be due to the presence of the SAA. Combined with paleomagnetic data from southern Africa, the data from La Réunion allow for two possible scenarios. The first is that the SAA originated below southern Africa and affected the field at La Réunion before moving westwards. The second option is that it migrated from the Indian Ocean underneath La Réunion prior to 1300 CE, before shifting slightly eastward again to influence the field at La Réunion at 1550 CE.

La Réunion is on the western side of the Indian Ocean, on the eastern side is another underrepresented region in the paleomagnetic dataset: Indonesia. Indonesia lies east of the proposed emergence area of the SAA and within a region where another geomagnetic anomaly has been reported between 1620 CE to 1820 CE, known as the West Pacific Anomaly (WPA) (He et al., 2021; Yue et al., 2024). As there is no paleomagnetic data from volcanic rocks available, and therefore absolute paleointensity data also lack, Indonesia is a key location to investigate both of these anomalies and thereby improve global field models. In **Chapter 5**, we present the first paleodirectional and paleointensity data from the volcanoes of Gunung Batur and Gunung Agung on Bali, Indonesia. The sampled lava flows on Gunung Batur were of historical age, and were suitable for paleodirectional and paleointensity experiments. By comparing the results from these historical lava flows we find that, contrary to the results from **Chapter 1**, inclinations and intensities are higher than expected. Models of inclination anomalies in gullies indicated the effect might be reversed in the Southern Hemisphere (Baag et al., 1995), which could be the reason for this reversed effect. The ages of the sampled volcanics on Gunung Agung were older, approximately from 5000 BCE until the recent lava flow of 1963 CE. We construct a PSV curve based on a simple and a global model prior, which reveal rapid directional variations with, depending on the prior, lower intensities of 32 - 36 μT at ~1000 CE or ~1300 CE. In **Chapter 4**, we observed similar field behaviour at La Réunion, only a few hundred years later. The data from Bali might reveal the initial

phase of the South Atlantic Anomaly, or otherwise might be related to the West Pacific Anomaly. We stress that to distinguish between these two scenarios improved age constraints are needed on the lava flows of Gunung Agung, as well as a more comprehensive global field model. Nonetheless, the results from Agung and Batur demonstrate that these rocks are highly suitable for paleomagnetic methods. A future PSV curve may also assist in dating volcanic deposits in Indonesia and thereby map the eruption history, which is particularly important in regions with hazardous volcanic activity such as Indonesia.

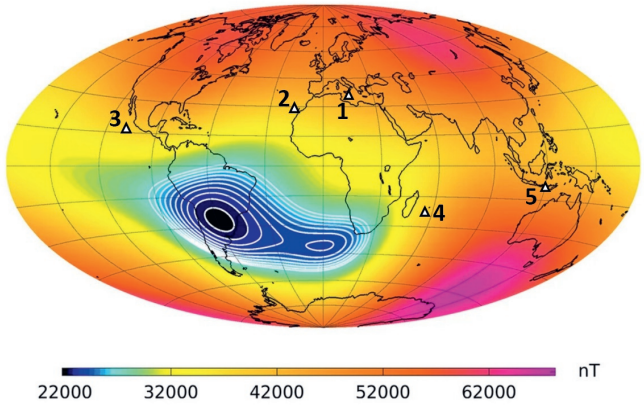


Proloog & Samenvatting

Onze planeet wordt omgeven door een magnetisch veld dat fungeert als een enorm schild tegen schadelijke zonne- en kosmische straling. Als deze straling niet door het aardmagnetisch veld zou worden afgebogen kan het de atmosfeer beschadigen en communicatiesystemen verstoren (Boteler e.a., 1998; Courtillot e.a., 2007). Het aardmagnetisch veld kan worden beschreven aan de hand van een richting en een sterkte, en beide veranderen voortdurend door de tijd heen. Het onderzoeksgebied dat zich bezighoudt met de variaties van het aardmagnetisch veld in het verleden staat bekend als paleomagnetisme. Door gebruik te maken van archeologische materialen, vulkanische gesteenten of sedimenten kunnen we de vroegere veldwaarde op een specifieke locatie en op een bepaald moment in de tijd achterhalen. Op dit moment wordt het aardmagnetisch veld gekenmerkt door een gebied met een zwakke veldsterkte boven Zuid-Amerika, de zogenoemde Zuid Atlantische Anomalie (ZAA) (Fig. 1). Deze anomalie van lage intensiteit is een van de meest intrigerende kenmerken van het huidige geomagnetische veld. Het huidige gedrag ervan wordt bestudeerd met behulp van satellietdata, maar over het gedrag in het verleden is nog veel onbekend (Campuzano e.a., 2019; Engbers e.a., 2022; Nilsson e.a., 2022). In dit proefschrift richt ik mij eerst op het bestuderen van de betrouwbaarheid van vulkanische gesteenten als paleomagnetische archieven, met behulp van data van de Etna en La Palma. Vervolgens onderzoek ik het gedrag van de ZAA door paleomagnetische data te verzamelen van drie verschillende locaties op aarde: de Revillagigedo-archipel, La Réunion en het eiland Bali in Indonesië (Fig. 1).

Recente variaties in het aardmagnetisch veld

Gemiddeld genomen over een voldoende lange tijdsperiode kan het aardmagnetisch veld worden benaderd als een geocentrische axiale dipool (GAD), maar het verandert voortdurend in tijd en ruimte. Deze variaties staan bekend als paleoseculaire variatie (PSV) en vinden plaats op tijdschalen variërend van seconden tot miljoenen jaren. Op langere tijdschalen uit veldvariabiliteit zich vooral in de afwisseling tussen perioden met stabiele polariteit (chrons of superchrons) en geomagnetische omkeringen. Tijdens het Krijt behield het veld bijvoorbeeld voor maar liefst 37 miljoen jaar een normale polariteit voordat de polen wisselden in een geomagnetische omkering. Zelfs tijdens zulke lange intervallen met stabiele polariteit vertoont het veld nog steeds seculaire variatie in richting en intensiteit. Tijdens een geomagnetische omkering wisselen de magnetische noord- en zuidpool van de aarde van plaats. Magnetische omkeringen hebben in het verleden zeer onregelmatig plaatsgevonden, maar gemiddeld ongeveer eens per 200.000 jaar (Ogg, 2020). De laatste omkering, de Matuyama-Brunhes-omkering, vond ongeveer 780.000 jaar geleden plaats. De duur van een volledige omkering ligt waarschijnlijk in de orde van duizenden jaren (Mahgoub e.a., 2023; van Grinsven e.a., 2025). In tegenstelling tot volledige omkeringen vertoont het aardmagnetisch veld ook excursies: dat zijn meestal tijdelijke instortingen van het veld waarbij richtingen meer dan 45° afwij-



Figuur 1: Veldintensiteit aan het aardoppervlak in 2020 CE, met de omtrek van de Zuid Atlantische Anomalie, afbeelding uit (Finlay e.a., 2020). Witte contourlijnen zijn weergegeven in stappen van 500 nT van 22,500 tot 27,000 nT. Driehoeken tonen de locaties van de studiegebieden in dit proefschrift, gelabeld per hoofdstuk: 1) Etna, Italië, 2) La Palma, Spanje, 3) Revillagigedo-archipel, Mexico, 4) La Réunion en 5) Bali, Indonesië.

ken van de geografische polen. Deze excursies kwamen sinds de laatste omkering regelmatig voor, een voorbeeld is de Laschamps-excursie van ongeveer 41.000 jaar geleden. Toen verzwakte het aardmagnetisch veld keerden de polen voor korte tijd om (Guillou e.a., 2004). Op nog kortere tijdschalen treden geomagnetische 'jerks' op: plotselinge, snelle veranderingen in het veld die honderden jaren of nog minder duren. Daarbovenop is er de voortdurende seculaire variatie: constante veranderingen in declinatie, inclinatie en intensiteit waardoor de magnetische polen rond de geografische polen bewegen. Seculaire variatie leidt ook tot veranderingen in declinatie, dat is de hoek tussen het magnetische noorden en geografische noorden, waarvoor kompasmetingen afhankelijk van locatie moeten worden gecorrigeerd. Seculaire variatie in richting en intensiteit wordt gemeten door magnetische observatoria wereldwijd en door satellieten in de ruimte. Deze directe metingen laten een zeer interessant kenmerk zien van het huidige aardmagnetisch veld: de Zuid Atlantische Anomalie (ZAA).

De ZAA is een gebied met zeer lage veldsterkte boven Zuid-Amerika en de Zuid-Atlantische Oceaan en wordt doorgaans gedefinieerd als het gebied waar de magnetische intensiteit aan het oppervlak lager is dan 32 μT (Pavón-Carrasco & De Santis, 2016). In deze regio bevinden de Van Allen-stralingsgordels zich op lagere hoogte dan gebruikelijk (Domingos e.a., 2017). Deze gordels bevatten gevangen geladen deeltjes uit de zonnewind, dat risico's kan opleveren voor ruimtevaartuigen die het gebied passeren (Heirtzler e.a., 2002). Momenteel zien we dat de ZAA zich uitbreidt en lijkt te splitsen in twee minima, één boven Zuid-Amerika en één boven zuidelijk Afrika (Fig. 1), terwijl het gehele lage-intensiteitsgebied westwaarts drijft (Domingos e.a., 2017). Deze westwaartse beweging wordt toegeschreven aan de convectie van vloeibaar ijzer in de buitenkern van de aarde. Schattingen van de

gemiddelde westwaartse driftsnelheid van het centrum van de anomalie variëren tussen ongeveer ~0.18° en ~0.3° per jaar (Fürst e.a., 2009; Ye e.a., 2017). Terwijl het oppervlak van de ZAA groeit neemt ook het dipoolmoment van de aarde af: tussen 1840 en 2015 daalde dat met 9% (Finlay e.a., 2016; Olson & Amit, 2006). Omdat omkeringen worden verwacht wanneer het magnetisch veld zwak is, bestaat er wetenschappelijke discussie over de vraag of deze afname kan leiden tot een geomagnetische omkering. Daarmee is het dus de vraag of de ZAA een voorbode is van een toekomstige omkering.

De huidige variaties in het aardmagnetisch veld worden nauwlettend gevolgd met satellieten. Het begrijpen van veranderingen vóór het tijdperk van directe metingen is echter even belangrijk. Hiervoor vertrouwen we op paleomagnetische data.

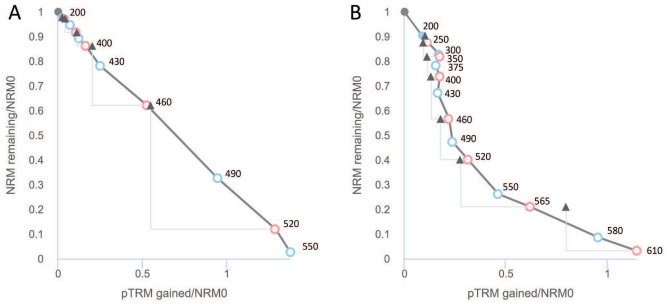
Paleomagnetisme
De eerste toepassingen van magnetisme gaan terug tot de zesde eeuw BCE, toen Thales van Milete de eigenschappen van magnetiet beschreef, en tot de vierde eeuw BCE, toen in China de eerste kompassen werden uitgevonden. Directe registraties van magnetische declinatie in Europa dateren uit de 16e eeuw CE. Tijdens zeevaartreizen werden declinatiemetingen wereldwijd vastgelegd in scheepslogboeken voor navigatiedoeleinden. Systematische metingen van inclinatie kwamen pas vanaf de 18e eeuw vaker voor. De eerste metingen van de absolute magnetische veldsterkte begonnen nog later. In 1798 CE startte Alexander von Humboldt systematische waarnemingen van relatieve magnetische intensiteit. Rond 1832 CE ontwikkelde Carl Friedrich Gauss een magnetometer waarmee de absolute veldsterkte kon worden gemeten. In de vroege 20e eeuw maakte het vakgebied van gesteentemagnetisme belangrijke ontwikkelingen door. Bernhard Brunhes ontdekte in 1906 CE dat de natuurlijke remanente magnetisatie van gesteente tegengesteld kon zijn aan het omgevingsveld. In 1926 CE liet Motonori Matuyama zien dat jongere lavastromen normaal gemagnetiseerd waren en oudere omgekeerd. Hiermee werd het verschijnsel van een geomagnetische omkering ontdekt. De laatste omkering, de Matuyama-Brunhes-omkering, is naar hen vernoemd. Laboratoriumonderzoek naar remanente magnetisatie in vulkanische gesteenten werd verder ontwikkeld door Johannes Koenigsberger (jaren 1930), Emile en Odette Thellier (jaren 1940) en Takesi Nagata (jaren 1940). Zij legden ook de basis voor paleointensiteitsexperimenten.

Het basisprincipe waarmee een gesteente een magnetisatie verkrijgt is relatief eenvoudig. Wanneer een gesteente boven zijn Curietemperatuur wordt verhit, verdwijnen alle magnetisaties van de mineraaldeeltjes, zoals magnetiet. Bij afkoeling onder de Curietemperatuur nemen de magnetische deeltjes de richting aan van het omringende magnetisch veld en verkrijgen ze zo een natuurlijke remanente magnetisatie (NRM). Deze NRM weerspiegelt de richting en sterkte van het aardmagnetisch veld op dat moment. Sedimenten kunnen ook gemagnetiseerd worden: magnetische deeltjes in suspensie kunnen vrij roteren en richten zich bij afzetting uit volgens het veld, wat leidt tot een depositional remanent magnetisation. Deze is normaal gesproken zwakker dan die van stollingsgesteenten. Paleorichtingen worden bepaald met behulp van georiënteerde monsters die in het veld worden ge-

nomen en later in het laboratorium worden gedemagnetiseerd, door middel van verhitting in stappen of met wisselvelden. De resultaten hiervan worden weergegeven in een orthogonaal vectordiagram, het Zijderveld-diagram (Zijderveld, 1967). Absolute intensiteitsmetingen zijn niet mogelijk voor sedimenten, alleen voor gesteenten of voor archeologisch materiaal dat bij afkoeling een magnetisatie kreeg. Het bepalen van paleointensiteit is moeilijker dan het verkrijgen van richtingen.

Paleointensiteit
De meest gebruikte methode om paleointensiteit te bepalen is een reeks verhittingsexperimenten (Thellier, 1959). In de IZZI-Thellier-methode (Tauxe & Staudigel, 2004) wordt de sterkte van het oude geomagnetische veld geschat door de natuurlijke remanente magnetisatie (NRM) te vergelijken met een thermoremanente magnetisatie (TRM) die in een bekend laboratoriumveld is verkregen. Monsters worden stapsgewijs verhit, afwisselend in nulveld- en inveldstappen (ZI) (Coe, 1967) en inveld- en nulveldstappen (IZ) (Aitken e.a., 1988). De resterende NRM wordt gemeten in nulveldstappen, de verkregen TRM na inveldstappen. De resultaten van al deze stappen worden getoond in een Arai-diagram (Nagata e.a., 1963) (Fig. 2); de helling van het lineaire segment vermenigvuldigd met het laboratoriumveld geeft de paleointensiteit. Helaas gedragen niet alle monsters zich ideaal. Thermische alteratie bij hogere temperaturen komt vaak voor. Daarom wordt meestal een pTRM-check uitgevoerd: na elke vier ZI- en IZ-stappen wordt een eerdere veldstap herhaald om te controleren of de pTRM reproduceerbaar is (Coe, 1967). Niet-ideaal gedrag kan naast alteratie ook voortkomen uit de korrelgrootte van het magnetische mineraal. Thellier-methoden zijn gebaseerd op drie wetten: additiviteit, reciprociteit en onafhankelijkheid van partiële thermoremanente magnetisatie. Néel (1949) toonde aan dat deze wetten gelden voor single-domain (SD) korrels. Vulkanische monsters bevatten echter vaak een mengsel van SD-, pseudo-single-domain (PSD)- en multi-domain (MD)-korrels. PSD- en MD-korrels kunnen leiden tot niet-lineaire Arai-diagrammen.

Om minder betrouwbaar magnetisch gedrag te herkennen zijn verschillende selectiecriteria voorgesteld om de kwaliteit van paleointensiteitsresultaten te beoordelen. Multi-domain gedrag kan worden opgespoord met behulp van het krommingscriterium k', en er is een maximale toegestane afwijking voor een pTRM-check. Monsters die niet aan deze selectiecriteria voldoen, worden niet meegenomen in verdere interpretaties. Wanneer deze selectiecriteria worden toegepast, ligt het succespercentage van de IZZI-Thellier-methode vaak onder de 20%. Om dit te verhogen zijn verschillende alternatieve methoden ontwikkeld, zoals de microgolfmethode (Hill & Shaw, 2000; Walton e.a., 1993), de multispecimen-techniek (Dekkers & Böhnel, 2006), de pseudo-Thellier-techniek (De Groot e.a., 2013; Tauxe e.a., 1995; Yu e.a., 2003), en recente ontwikkelingen in end-membermodellering (van Grinsven e.a., 2023). Desondanks blijft de IZZI-Thellier-techniek de meest toegepaste methode in paleointensiteits studies en wordt deze ook in vier hoofdstukken van dit proefschrift toegepast. In tegenstelling tot eerdere studies met lage succespercentages behaalden we succespercentages van ruim boven de 20%.



Figuur 2: Voorbeelden van Arai-diagrammen met de gebruikte temperatuurstappen. Blauwe cirkels zijn de ZI-stappen, rode cirkels de IZ-stappen en driehoeken geven pTRM-checks aan. Cijfers zijn de temperatuursstappen in °C. In A is een voorbeeld van een ideale paleointensiteitsrecorder; de helling van de overbleven NRM versus de TRM verkregen is lineair. Er werd een laboratoriumveld van 50 μT toegepast; dit monster levert daarom een paleointensiteit van 36.4 μT op. B toont een monster dat niet-ideaal gedrag vertoont, zoals 'sagging' en een falende pTRM-check terug naar temperatuurstap 565°C.

Betrouwbaarheid van vulkanische gesteenten als paleomagnetisch archief

Vulkanische gesteenten worden doorgaans beschouwd als betrouwbare registraties van het aardmagnetisch veld. Toch blijken paleomagnetische datasets regelmatig af te wijken van de verwachte veldwaarden. Zelfs monsters met lineaire Araidiagrammen die aan alle selectiecriteria voldoen, kunnen vertekende paleointensiteitsresultaten opleveren (L. V. de Groot e.a., 2013). Een dergelijke bias kan worden vastgesteld wanneer data afkomstig zijn van recente historische lavastromen (na 1850 CE). De gemeten declinatie, inclinatie en intensiteit kunnen dan worden vergeleken met verwachte veldwaarden volgens het International Geomagnetic Reference Field (IGRF, (Alken e.a., 2021)) of, voor lavastromen van vóór 1900 CE, het gufm1-model (Jackson e.a., 2000). Een locatie waar paleomagnetische datasets vaak niet overeenkomen met het verwachte veld is de Etna op Sicilië, Italië. De Etna is een zeer actieve vulkaan met vele recente lavastromen en is uitgebreid bestudeerd. In **Hoofdstuk 1** onderzochten we waarom de gesteenten van historische lavastromen op de Etna vaak te lage inclinaties en intensiteiten geven. Als eerste stelden we een overzicht samen van alle beschikbare paleomagnetische data van de Etna en voegden nieuwe paleomagnetische richtingen toe van zeven historische lavastromen. De dataset vertoont geen bias in declinatie, maar wel consequent lager dan verwachte inclinaties en intensiteiten. Vervolgens werd het huidige magnetisch veld gemeten op vijf locaties boven het oppervlak van een lavastroom met een drie-assige fluxgate-magnetometer. Dit instrument meet het magnetisch veld dat een hypothetisch nieuwe lavastroom zou registreren. Het veld werd gemeten langs drie paden loodrecht op de vermoedelijke stroomrichting, op twee verschillende hoogtes boven het oppervlak. De trajecten hadden variërende topografie, met ten minste één rug en één geul. De metingen tonen aan dat inclinatie- en intensiteitswaarden lager zijn boven geulen en hoger boven ruggen. Afwijkingen zijn bovendien groter dichter bij het oppervlak. Variaties in het omgevingsveld op de Etna lijken dus veroorzaakt te worden door het gemagnetiseerde terrein: de onre-

gelmatige topografie beïnvloedt het lokale magnetisch veld en creëert lokale magnetische anomalieën. Simulaties lieten zien dat een hoge k-waarde (een maat voor hoe goed richtingen clusteren) niet automatisch betekent dat de resultaten correct zijn. Integendeel, een hoge k-waarde kan erop wijzen dat lokale magnetische anomalieën niet zijn uitgemiddeld. We benadrukken daarom het belang van ruimtelijk verspreide bemonstering, vooral in ruig vulkanisch terrein, en adviseren toekomstige studies om bemonsteringsstrategieën altijd gedetailleerd te rapporteren.

Het nemen van monsters verspreid over een groter gebied, werd toegepast in **Hoofdstuk 2**, waar we de hele jonge lavastroom van 2021 op La Palma op drie verschillende locaties hebben bemonsterd. We bezochten het eiland in oktober 2021, terwijl de uitbarsting nog aan de gang was, dus het gesteente was slechts 3.5 week oud toen de monsters in het laboratorium werden gemeten. We hebben getest of de intensiteit van het magnetisch veld op het moment van afkoeling betrouwbaar werd vastgelegd door de nieuwe stroom, hoe succesvol de IZZI-Thellier-techniek was op deze extreem jonge monsters, en of er veranderingen in de intensiteit optreden in de loop van de tijd. De declinatie, inclinatie en intensiteit werden direct na terugkeer van het veldwerk gemeten op de monsters van de lavastroom van 2021. De resultaten verschilden per locatie, maar het gemiddelde komt dicht in de buurt van de verwachte waarde van het magnetisch veld. Dit bevestigt de bemonsteringsstrategie die we aanbevelen in **Hoofdstuk 1** en laat zien dat deze basaltische lava het aardmagnetisch veld goed kan vastleggen. Daarna hebben we twee groepen intensiteitsmonsters opgeslagen in het aardmagnetisch veld en twee groepen in een afgeschermde ruimte met een restveld van <300 nT. Van elke opslagconditie werd één groep twee jaar na bemonstering gemeten en de andere groep drie jaar na bemonstering. Gemiddeld blijven de paleointensiteitsresultaten van alle groepen ongeveer gelijk en komen ze overeen met het bekende magnetisch veld uit die tijd, al lijkt de intensiteit na drie jaar opslag iets lager te worden. Wel zien we dat het slagingspercentage van de paleointensiteitsexperimenten voor sommige locaties lager is na twee of drie jaar opslag, waardoor minder monsters aan de kwaliteitscriteria voldoen. Desondanks hadden alle sets uitzonderlijk hoge slagingspercentages met de IZZI-Thellier-methode (>48%). Ten slotte lijkt er een kleine tendens te zijn dat monsters die buiten een magnetisch veld zijn opgeslagen hogere slagingspercentages hebben dan monsters die in het veld zijn opgeslagen. Tijdens een tweede veldwerk in 2025 verzamelden we nieuwe monsters van dezelfde lavastroom van 2021; deze monsters waren dus meer dan drie jaar 'opgeslagen' in het natuurlijke veld. Ook Calvo-Rathert e.a. (2024) nam in 2022 monsters van deze stroom. Opmerkelijk is dat zowel onze nieuwe monsters als die van Calvo-Rathert e.a. (2024) grotendeels onsuccesvol waren bij toepassing van de IZZI-Thellier-techniek. De afname in slagingspercentage voor monsters die in een magnetisch veld zijn opgeslagen kan het gevolg zijn van een combinatie van het 'fragile curvature'-proces (Tauxe e.a., 2021) en het ontstaan van viskeuze remanente magnetisatie (L. V. de Groot e.a., 2014a), hoewel verschillen tussen het monsteren van de binnen- of buitenzijde van de lavastroom ook een rol kunnen spelen.

Geomagnetische anomalieën op het zuidelijk halfrond

De huidige modellen van het geomagnetisch veld die de ontwikkeling van de ZAA

beschrijven, bevatten uiteenlopende hypothesen over het ontstaan van deze anomalie. De anomalie kan samenhangen met een omgekeerde fluxplek aan de rand van de Large Low-Shear Velocity Province (LLSVP) onder zuidelijk Afrika (Tarduno e.a., 2015). Een andere mogelijkheid is dat de anomalie vanuit de Indische Oceaan naar het westen is verplaatst (Campuzano e.a., 2019; Nilsson e.a., 2022). Ook het tijdstip waarop de anomalie is begonnen, is onbekend: mogelijk al rond 860 CE (Trindade e.a., 2018), sinds 950 CE (Campuzano e.a., 2019), rond 1250 CE (Tarduno e.a., 2015) of pas zo laat als 1800 CE. (Gubbins e.a., 2006). Daarnaast is ook voorgesteld dat de ZAA al meerdere keren in het verleden aanwezig was (Engbers e.a., 2022; Nilsson e.a., 2022; Shah e.a., 2016; Trindade e.a., 2018). Een belangrijk probleem van de huidige geomagnetische modellen is dat de verdeling van de data ongelijk is: er zijn veel meer paleomagnetische data van het noordelijk halfrond in de dataset waarop de modellen zijn gebaseerd, dan van het zuidelijk halfrond. Om het recente gedrag van het aardmagnetisch veld en de ontwikkeling van de ZAA goed te kunnen beschrijven, zijn juist meer paleomagnetische data nodig uit minder onderzochte gebieden, vooral op het zuidelijk halfrond. Tegelijkertijd zijn er zelfs op het noordelijk halfrond afgelegen gebieden waar nog geen paleomagnetische data uit het Holoceen beschikbaar zijn. Ook het opvullen van die hiaten is belangrijk. Daarom presenteren wij in **Hoofdstuk 3** paleomagnetische data van een afgelegen locatie op het noordelijk halfrond, gevolgd door twee locaties op het zuidelijk halfrond in **Hoofdstukken 4 en 5**.

In **Hoofdstuk 3** presenteren we paleomagnetische data van de afgelegen Revillagigedo archipel in Mexico. Deze eilanden liggen ongeveer 400–700 km ten zuidoosten van de zuidpunt van Baja California. We bezochten twee eilanden: het onbewoonde eiland San Benedicto en het iets grotere eiland Socorro. Er is weinig bekend over deze eilanden: van San Benedicto waren nog geen paleomagnetische data beschikbaar en van Socorro bestond slechts één paleomagnetische studie (Sbarbori e.a., 2009). Voor San Benedicto presenteren we paleomagnetische data van de lavastroom uit 1953 CE. De drie bemonsteringslocaties van deze lavastroom laten verschillende paleorichtingen zien, maar wanneer de resultaten van de locaties worden gecombineerd, komen ze erg dicht in de buurt van de verwachte referentiewaarde. Dit ondersteunt opnieuw de bemonsteringsstrategie die wordt aanbevolen in **Hoofdstuk 1**. De paleointensiteiten van de afzonderlijke locaties onderschatten echter de verwachte veldwaarde. Dit kan het gevolg zijn van multi-domain effecten of een gevolg zijn van lokale magnetische anomalieën, zoals voorgesteld in **Hoofdstuk 1**. Van de bemonsteringslocaties op Socorro was één locatie gedateerd met behulp van radiokoolstof met een ouderdom tussen 4052–2846 BCE en 4950–2846 BCE. (Farmer e.a., 1993). Deze locatie liet een opvallende lage inclinatie van 4.2° zien, terwijl op deze breedtegraad volgens een geocentrische axiale dipool een inclinatie van 35° wordt verwacht. Dit kan wijzen op een tot nu toe onbekende inclinatie-anomalie in deze periode, omdat bestaande geomagnetische modellen dit niet voorspellen. Alle andere bemonsteringslocaties op het eiland Socorro zijn ouder, waarschijnlijk uit het Pleistoceen. De succesvol verkregen paleorichtingen en intensiteiten van deze oudere lavastromen komen overeen met de verwachte GAD-waarden op deze breedtegraad en tonen dus geen afwijkende veldrichtingen of -intensiteiten.

Een hypothese over de evolutie van de Zuid Atlantische Anomalie (ZAA) is dat dit verschijnsel vanuit de Indische Oceaan westwaarts is gemigreerd. Om deze hypothese te onderzoeken, bezochten we voor **Hoofdstuk 4** het eiland La Réunion. Dit eiland ligt ten oosten van Madagascar in de Indische Oceaan en is daardoor ideaal gelegen om te bestuderen of de ZAA deze regio in het verleden heeft beïnvloed. Paleomagnetische data werden verkregen van 18 bemonsteringslocaties rondom de zeer actieve vulkaan Piton de La Fournaise. De meeste locaties leverden succesvolle paleorichtingen op; tien locaties gaven betrouwbare paleointensiteitsresultaten. We combineerden onze data met de resultaten uit twee eerdere studies om een volledige vector-PSV-curve te construeren. De dataset van La Réunion bevat verschillende dateringsmethoden, waaronder radiokoolstofdateringen van lavastromenn, dateringen op basis van pionierbomen en historisch gedocumenteerde uitbarstingen. Daarnaast zijn er perioden waarin weinig paleomagnetische data beschikbaar zijn, omdat de vulkanische activiteit toen laag was. Om met deze twee uitdagingen om te gaan, gebruikten we een nieuwe Bayesiaanse methode om PSV-curven te construeren, die we hebben ontwikkeld in Schanner e.a. (2026). Deze methode houdt rekening met verschillende ouderdomsverdelingen en biedt de mogelijkheid om gebruik te maken van een eenvoudige prior of van een globaal geomagnetisch veldmodel als prior. Het gebruik van een globaal veldmodel als prior is vooral nuttig in regio's met weinig data of bij perioden met weinig data. De PSV-curven van La Réunion laten snelle richtingsveranderingen zien rond 1600–1750 CE en tonen een hoge veldsterkte rond 1400 CE, waarna de intensiteit daalt tot ongeveer 29 μT rond 1550 CE. Deze lage intensiteit kan samenhangen met de aanwezigheid van de ZAA. In combinatie met paleomagnetische data uit zuidelijk Afrika maken de data van La Réunion twee mogelijke scenario's mogelijk. Het eerste scenario is dat de ZAA onder zuidelijk Afrika is ontstaan en het veld op La Réunion beïnvloedde voordat zij westwaarts bewoog. Het tweede scenario is dat de anomalie vóór 1300 CE vanuit de Indische Oceaan onder La Réunion migreerde en daarna weer iets oostwaarts verschoof, om rond 1550 CE het veld op La Réunion te beïnvloeden.

La Réunion bevindt zich aan de westzijde van de Indische Oceaan. Aan de oostzijde ligt een andere regio die ondervertegenwoordigd is in de paleomagnetische dataset: Indonesië. Indonesië ligt ten oosten van het voorgestelde ontstaansgebied van de ZAA en ligt binnen een regio waar tussen 1620 en 1820 CE een andere geomagnetische anomalie is gerapporteerd, de West Pacifische Anomalie (WPA). Omdat er nog geen paleomagnetische data van vulkanische gesteenten beschikbaar zijn van Indonesië, en dus ook geen absolute paleointensiteiten, is Indonesië een belangrijke locatie om beide anomalieën te onderzoeken en daarmee mondiale veldmodellen te verbeteren. In **Hoofdstuk 5** presenteren we de eerste paleorichtings- en paleointensiteitsdata van de vulkanen Gunung Batur en Gunung Agung op Bali, Indonesië. De bemonsterde lavastromen op Gunung Batur waren van historische leeftijd en geschikt voor zowel paleorichtings- en paleointensiteitsexperimenten. Door de resultaten van deze historische lavastromen te vergelijken zien we, in tegenstelling tot de bevindingen in **Hoofdstuk 1**, dat inclinaties en intensiteiten hoger zijn dan verwacht. Modellen van inclinatie-anomalieën in geulen suggereren dat dit effect op het zuidelijk halfrond omgekeerd kan zijn (Baag e.a., 1995), wat

deze afwijking mogelijk verklaart. De bemonsterde vulkanische gesteenten op Gunung Agung waren ouder, variërend van circa 5000 BCE tot de recente lavastroom van 1963 CE. We construeerden een PSV-curve op basis van zowel een eenvoudige prior als een globale model prior. Deze curven laten snelle richtingsvariaties zien en, afhankelijk van de gekozen prior, lagere intensiteiten van 32–36 μT rond ongeveer 1000 CE of ongeveer 1300 CE. In **Hoofdstuk 4** zagen we vergelijkbaar veldgedrag op La Réunion, maar dan enkele honderden jaren later. De data van Bali kunnen dus de beginfase van de Zuid Atlantische Anomalie laten zien, of mogelijk verband houden met de West Pacifische Anomalie. We benadrukken dat betere ouderdomsbepalingen van de lavastromen van Gunung Agung nodig zijn om tussen deze twee scenario's te kunnen onderscheiden, evenals een uitgebreider globaal veldmodel. Toch tonen de resultaten van Agung en Batur aan dat deze gesteenten zeer geschikt zijn voor paleomagnetisch onderzoek. Een toekomstige PSV-curve kan bovendien helpen met het dateren van vulkanische afzettingen in Indonesië en zo de uitbarstingsgeschiedenis beter in kaart brengen. Dit is vooral belangrijk in gebieden met gevaarlijke vulkanische activiteit, zoals Indonesië.



1

Local magnetic anomalies explain bias in paleomagnetic data: consequences for sampling

Romy Meyer and Lennart de Groot

Published in Geochemistry, Geophysics, Geosystems, Volume 25, Issue 5
doi: https://doi.org/10.1029/2023GC011319

Abstract *Volcanic rocks are considered reliable recorders of past changes in the Earth's magnetic field. Recent flows, however, sometimes fail to produce the known magnetic field at the time of cooling. Previous research on Mt. Etna suggests paleomagnetic data might not be accurately recorded. Here we test the accuracy of paleomagnetic data obtained from Mt. Etna lavas by comparing paleomagnetic data from historical flows to direct measurements of the magnetic field above the current topography. The inclinations and intensities in both data sets are biased towards lower values, while there is no such trend for the declination. Inclinations are on average 2.9° lower than expected; intensities are on average 8.8 μT lower. The deviations from the expected values depend on the height above the flow. Moreover, the inclinations and intensities vary as a function of topography. Both are higher above ridges and lower in gullies; the variations within a site are up to 14.1° in inclination and 12.9 μT for intensity. To suppress this paleomagnetic data bias it is important to take samples several meters apart and from different parts of the flow whenever possible. While this leads to a higher degree of scatter in paleodirections, the results better represent the Earth's magnetic field at the time of cooling. This emphasizes the importance of reporting paleomagnetic sampling strategies in detail.*

1.1. Introduction

For decades magnetic signals from volcanic rocks have been used as a source to study the ancient behavior of the Earth's magnetic field. Volcanic rocks obtain a natural remanent magnetization which reflects the direction and intensity of the ambient geomagnetic field present during cooling. Paleomagnetic data from well-dated flows (e.g. historical observations, radiocarbon dating) are used to create regional paleosecular variation (PSV) curves, and models that describe the global behavior of the Earth's magnetic field through time. With PSV curves, lava flows from unknown ages may be dated to improve the knowledge of eruption frequency, which is vital for volcanic hazard assessment. An important prerequisite of the reliability of these models is the accuracy of the input data; volcanic rocks are often considered to be excellent recorders of the Earth's magnetic field. Of paleomagnetic data obtained from recent volcanic rocks, however, the inclination and intensity regularly fail to produce their known field values (see overview of 1960 Kilauea flow in Cromwell et al. (2015a), Pavón-Carrasco et al. (2014), and Urrutia-Fucugauchi et al. (2004)) or their reference value from the International Geomagnetic Reference Field (IGRF, Alken et al., 2021).

Recent lavas from Mt Etna, Italy, have been extensively studied in terms of paleodirections and paleointensities. As a result there is a large paleomagnetic dataset, which is regularly inconsistent with the reference values. Moreover, the scatter in paleodirections from a single lava flow is often inexplicably large (Speranza et al., 2006), with inclinations around 2° too shallow (Calvo et al., 2002; Incoronato et al., 2002; Lanza et al., 2005; Rolph, 1997; Rolph & Shaw, 1986; Tanguy et al., 1985, 1999, 2003). Likewise, paleointensities are found to be generally too low (Biggin et al., 2007; L. V. de Groot et al., 2012, 2013; Rolph & Shaw, 1986; Sherwood, 1991). These deviations in both directions and intensities of Mt. Etna data have been attributed to arise from various explanations. Rolph and Shaw (1986) and Rolph

et al. (1987) mention 'magnetic refraction', i.e. the deflection of directions are explained due to some parts of the material being already magnetized while the rest of the material is still cooling (Schurr et al., 1985; Tanguy, 1990; Tarling et al., 1986). This effect is commonly only described and extensively studied in archeomagnetic studies (Schurr et al., 1985). Hill and Shaw (1999) and Biggin et al. (2007) consider 'multi-domain behavior' as possible cause of the observed inaccuracy in paleointensity results: 'sagging' in Arai diagrams of Thellier-type experiments is explained by the presence of multi-domain (MD) grains, leading to inaccurate interpretations of these diagrams. Calvo et al. (2002) and L. V. de Groot et al. (2013) suggest 'transdomain processes' to occur in paleointensity experiments, which means that during heating there is a reorganization of the magnetic domain structure in PSD grains which results in a loss of NRM. Lastly, Hill and Shaw (1999), Biggin et al. (2007) and L. V. de Groot et al. (2013) point to differences between the natural and the laboratory cooling rates for lower than expected paleointensities. In contrast to these rock-magnetic concepts pertaining to the behavior of the magnetic particles during remanence acquisition, the bias in paleomagnetic data might be explained by the presence of local magnetic anomalies, i.e. a local disturbance of the magnetic field induced by the magnetic field from underlying lava flows.

Mt. Etna is characterized by irregular topography; virtually all lava flows are classified as a'a type and the terrain is rough with rubble up to boulder size on the surface (Calvari & Pinkerton, 1998; Kilburn & Lopes, 1988). The lava flow morphology is characterized by channels bounded by levees, which are topographically higher ridges (Hulme, 1974; Tarquini et al., 2012). Mt. Etna lavas are also strongly magnetized. The remanent magnetization of specimens at Mt. Etna sometimes exceeds 20A/m and there is a large deviation between sun and magnetic compass readings (Speranza et al., 2006). The earliest volcanic products of Mt. Etna are dated around 500 ka ago (Branca et al., 2011), therefore all lava flows must be of normal polarity. Previously, measurements of the ambient geomagnetic field above the surface of lava flows were performed with a fluxgate magnetometer on Hawaii (Baag et al., 1995), La Palma and Tenerife (Valet & Soler, 1999) and on Mt. Etna (Tanguy & Le Goff, 2004). Baag et al. (1995) found a maximum declination deflection from the IGRF of -10.7° and -21.1° for inclination, Valet and Soler (1999) report deflections of up to 15° for directions and 20% for intensity. Both attribute these variations in the magnetic field to local magnetic anomalies arising from the highly magnetized underlying terrain. Baag et al. (1995) also developed two-dimensional models of theinclination above various topographic features. These predict different inclination deflections depending on the latitude of the site and the orientation and dip of the slope with respect to the ambient geomagnetic field. The models predict negative inclination anomalies in topographic lows in the Northern Hemisphere but positive anomalies in gullies in the Southern Hemisphere. According to their theory, declination variations only depend on the location of the site with respect to the volcano: negative deviations are expected on the Eastern side of the volcano, and positive ones on the Western side. In contrast, variations in inclination also depend on the latitude and the exact shape of the gully or channel causing the local magnetic anomaly (Baag et al., 1995). They did not predict the influence of magnetic anomalies on the intensity signal. Valet and Soler (1999) suggest that

sampling over a large distance would average out the anomalies, Baag et al. (1995) also suggest this to remove a possible declination bias but according to their models this will not always work for the inclination bias. On Mt. Etna, Tanguy and Le Goff (2004) followed an almost similar procedure and measured the geomagnetic field around 10 times above 12 different sites, while avoiding obvious terrain features. The average of their 124 measurements was close to the expected geomagnetic field. However, when comparing the results on site level there are differences and the averages for their sites show small deviations from the expected geomagnetic field (±3% in intensity and ±1.5° in direction). Tanguy and Le Goff (2004) conclude that there may be some local distortion of the geomagnetic field influencing archeomagnetic results, perhaps caused by dyke swarms in the South Rift Zone of Mt. Etna, but by sampling broadly (i.e. over several widely distributed lava flows of the same eruption) this effect may be minimized. However, it is often not possible to sample similarly aged lava flows on different flanks of a volcano. Furthermore, during measuring they avoided local terrain features, which a future lava flow will not, and this may have improved their results with respect to the studies of Baag et al. (1995) and Valet and Soler (1999), and ours.

Here, we test whether the strongly magnetized terrain of Mt. Etna influences the ambient magnetic field directly above it. First, we compile an overview of paleomagnetic literature data to characterize a potential bias in the data, while also paying attention to which sampling strategy was used. Second, we add new paleomagnetic directional data from 12 sites sampled from 7 different historical flows. Third, we measure the magnetic field above 4 recent lava flows of Mt. Etna, 3 of which were also sampled for paleomagnetic measurements. Instead of several measurements spread out over a lava flow, the measurements are taken in high detail along the length of several paths with varying topography to observe the magnetic field a possible future overlying flow would record. Combining these datasets allows us to characterize the expression of local magnetic anomalies in paleomagnetic measurements, quantify the impact on paleomagnetic statistics, and provide recommendations for paleomagnetic sampling strategies in rough volcanic terrain.

1.2. Paleomagnetic data

1.2.1. Data from previous studies

To characterize a possible bias in paleomagnetic data from Mt. Etna, we compiled an overview of all paleomagnetic results reported by previous studies of lava flows younger than 1850 CE. Older flows were not taken into account because the results will be compared with the expected values according to geomagnetic models; prior to 1850 CE direct full vector measurements of the Earth's magnetic field are not available. The directional dataset (Supp. Table 1.1) consists of the declination, inclination and corresponding precision parameter (k) and α_{95} of 14 flows, which were deposited between 1853 and 1983. The other dataset (Supp. Table 1.2) consists of the paleointensities of 20 flows between 1853 and 2002, including their standard deviation and paleointensity method used.

How samples are generally obtained in the field, i.e. the sampling strategy, dif-

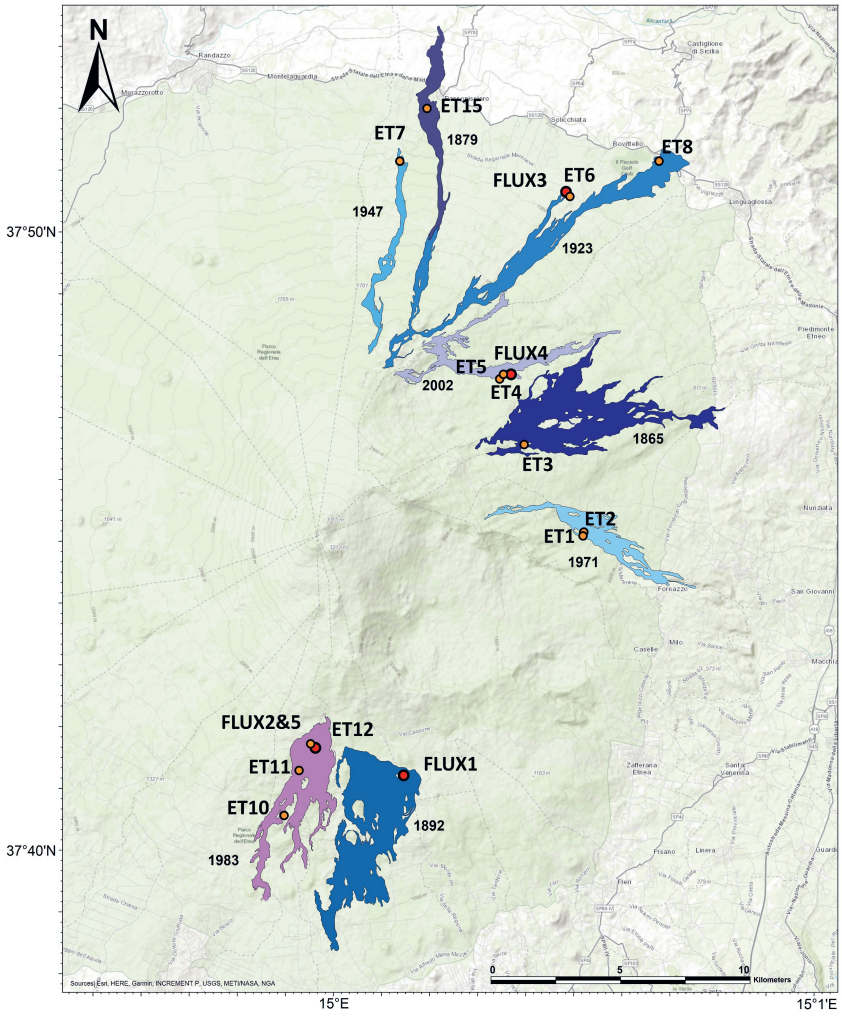


Figure 1.1: Sampling locations on Mt. Etna, Sicily, Italy. ET sites are where paleomagnetic samples were taken and FLUX are AnomalyMapper measurement sites. Outlines of lava flows from Branca et al. (2011).

fers between studies. Studies aiming to produce paleodirections often take samples spread out over a flow, and measurements are deemed reliable when there is a low scatter, a small α_{95}, and/or a high k (Fisher, 1953). For paleointensity studies samples are sometimes taken closer together to ensure homogeneity between the samples (L. V. de Groot et al., 2012, 2013), and results are found reliable when the standard deviation of the paleointensity results is low. These sampling strategies are, however, not universally defined and not all studies report their sampling strategy in detail. Previous studies on Mt. Etna that do report their sampling strategies or describe the sampled flow are: Tanguy et al. (1985, 1999, 2003), who use the 'big sample method', taking samples spread out over a larger area. In contrast, Rolph (1997), Calvo et al. (2002) and Biggin et al. (2007) take their samples from top to bottom at one location of one single flow. The 1971 flow of Rolph (1997) was 2m thick, flow thickness varied for Calvo et al. (2002) between 50cm for the 1910 flow and up to 6m for the 1928 flow. The samples of Biggin et al. (2007) were taken between 10 to 235cm from the base of the flow. For intensity Calvo et al. (2002) sampled the 1928 flow at three different sites. Lastly, L. V. de Groot et al. (2012, 2013) used closely spaced drill cores, 8-12 samples taken less than 1m of each other to ensure sampling homogeneity. L. V. de Groot et al. (2013) also sampled at different vertical levels within a lava flow, if known Supp. Table 1.2 includes the distance to the top and base of the sampled lava flow. Samples of L. V. de Groot et al. (2012)were obtained 0.5-1.5m below the top of the flow.

1.2.2. Directional data from recent flows

To complement the existing paleomagnetic data set, we sampled twelve new sites (Fig. 1.1, named ET) from seven historical flows with ages between 1865 and 2002 during a fieldwork in April 2016. Flow 1923, 1971 and 2002 were sampled twice at different locations and flow 1983 was sampled at three different locations. Some sites were sampled at the same location as in L. V. de Groot et al. (2013) and most samples were taken along road cuts. For each site, standard paleomagnetic cores (2.5cm in diameter, up to 10cm in length) were taken using a petrol powered drill. Cores were drilled several meters apart, at different heights in the flow, and differed in borehole orientations. To orientate the cores the use of a sun compass is preferred to avoid the influence from the surrounding magnetized rock. Unfortunately, the weather did not permit the use of a sun compass during the fieldwork. Instead the samples were oriented using a magnetic compass and readings were corrected for the current declination of the IGRF.

Between four to ten cores per site, depending on the amount of cores available, were selected for paleodirection experiments. Four samples per site were thermally demagnetized in 11 temperature steps: 100, 150, 200, 250, 300, 350, 400, 450, 500, 550, 600°C and measured on a 2G cryogenic magnetometer. Some samples were magnetically so strong that they exceeded the measurement range of the magnetometer, and could not be interpreted. A further four to nine samples were subjected to alternating field demagnetization experiments. Because the samples were strongly magnetized they were sliced in half (A and B specimens), their NRM approximately at alternating field step 0 was in between 0.8 and 13.5 A/m and on average 4.1 A/m (Supp. Table 1.9). The A and B specimens should have the exact

Table 1.1: Sampling sites and directional results this study. For each site the age of the flow, location and elevation (Elv) of sampling is given. The obtained directions per site are given by the parameters: (c/n/N) number of different cores / number of samples accepted / total amount of samples per site, the declination (Dec), inclination (Inc), precision parameter (k), 95 percent confidence interval α_{95}. Furthermore, the age means of four flows (1923,1971,1983 and 2002) are given. For the fluxgate measurement sites only the age of the flow above which was measured, the coordinates and elevation are given here.

Site	Year(CE)	Lat(N)	Long(E)	Elv(m)	c/n/N	Dec(°)	Inc(°)	k	α_{95}(°)
ET1	1971	37.752	15.087	1185	8/14/14	6.46	49.96	156.37	3.19
ET2	1971	37.753	15.087	1200	5/8/11	-4.16	48.26	212.62	3.81
ET3	1865	37.777	15.066	1606	10/18/20	-9.04	53.46	94.51	3.57
ET4	2002	37.796	15.062	1544	6/11/11	0.59	49.63	83.82	5.02
ET5	2002	37.795	15.057	1606	8/20/20	-2.54	48.07	23.69	6.85
ET6	1923	37.845	15.081	866	4/9/9	-17.52	51.54	55.58	6.97
ET7	1947	37.854	15.023	928	7/10/14	-3.45	48.11	101.59	4.82
ET8	1923	37.854	15.113	641	4/9/9	-8.79	43.27	51.22	7.26
ET10	1983	37.676	14.982	1423	8/20/20	0.64	53.49	86.84	3.52
ET11	1983	37.688	14.987	1671	7/12/12	-1.30	44.30	130.48	3.81
ET12	1983	37.695	14.991	1833	6/14/14	-7.15	47.11	118.88	3.66
ET15	1879	37.868	15.032	778	7/12/12	-10.28	47.59	115.65	4.05
1923_{mean}	1923				8/18/18	-12.81	47.49	46.01	5.15
1971_{mean}	1971				13/22/25	2.51	49.45	135.03	2.68
1983_{mean}	1983				21/46/46	-2.39	49.19	81.27	2.35
2002_{mean}	2002				14/31/31	-1.43	48.65	32.31	4.62
FLUX1	1892	37.687	15.019	1620					
FLUX2	1983	37.695	14.992	1833					
FLUX3	1923	37.845	15.081	865					
FLUX4	2002	37.796	15.062	1539					
FLUX5	1983	37.694	14.993	1826					

same paleomagnetic result, differences between them can be attributed to measurement or sample orientation errors in the machine. The samples were demagnetized in a robotized 2G DC-SQUID magnetometer (Mullender et al., 2016) with stepwise increasing alternating fields of 2.5, 5, 7.5, 10, 15, 20, 25, 30, 40, 50, 60, 70, 80, 100, 150, 225 and 270mT. All demagnetization results were analyzed in paleomagnetism.org (Koymans et al., 2016). Afterwards, site mean directions were calculated using Fisher statistics (Fisher, 1953) and the outliers are identified in the VGP distribution with the fixed 45° cut-off (Koymans et al., 2016). All other samples were retained for calculating site means (Fig. 1.2; Table 1.1). The precision parameter k ranges from 23.3 to 207.8, resulting in α_{95} values between 3.2° and 7.3°. Our k-values are on average lower than those from previous studies, in existing data k-values as high as 1070 have been reported (e.g., Tanguy et al., 2003).

Some flows (1923, 1971, 1983 and 2002) were sampled at multiple sites. The directions of these sites were grouped together to calculate 'age means' (Table 1.1). The k-values for these age means are lower than the k-values for individual sites. As the number of samples increases for the age means, the α95-values are also lower than the α_{95}-values of the individual sites. The age means averages out the effect of sites with large deviations from the expected reference values. Therefore these age means might be considered better estimates of the paleomagnetic vector, although the data from some individual sites are closer to the expected field value.

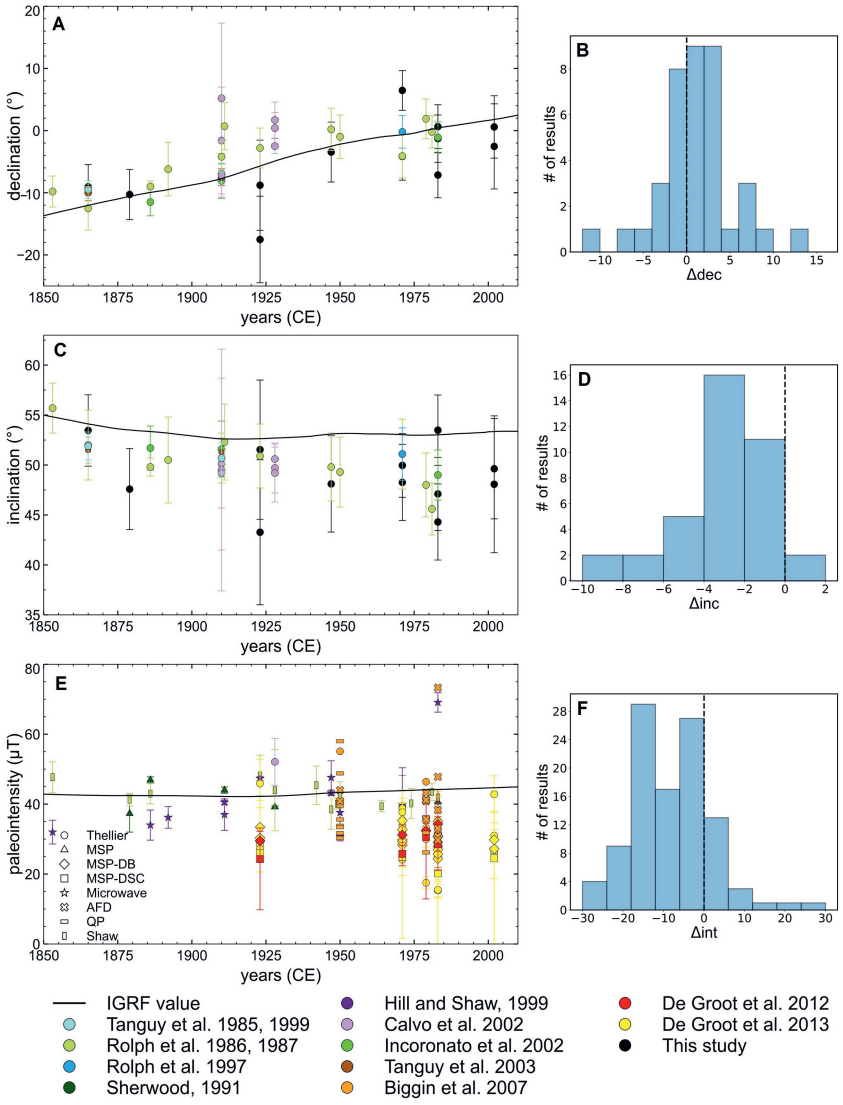


Figure 1.2: The (a) declination, (c) inclination and (e) intensity measurements of recent (>1850 CE) lava flows of Mt. Etna. In (a) and (b) the error bars are the corresponding α_{95} values and in (c) the error bars are the standard deviations. The histograms on the right-hand-side (b,d,f) show the paleomagnetic result - IGRF value. This is the difference (Δ) of the data points with respect to their expected field value.

1.2.3. Bias in paleomagnetic data

All above results are compared with their expected values according to the IGRF-13 model (Alken et al., 2021), or for flows prior to 1900 CE with the gufm1 model (Jackson et al., 2000). The reference geomagnetic field is obtained for every lava flow at the corresponding sampling location and elevation. In older papers the GPS coordinates are not always given. In this case, the reference value was determined using a location from the same flow from another research paper, or the geological map of Branca et al. (2011). Rolph and Shaw (1986) do not provide the exact GPS coordinates but a map with sampling locations, from this map the approximate GPS coordinates and elevations were utilized. In Fig. 1.2 the reference values are compared with the paleomagnetic data set of Mt. Etna, there is a systematic bias in the paleomagnetic data obtained. The declinations are generally in good agreement with the expected values according to the IGRF model: the median difference between the declination of a site and the expected value ($\widetilde{\Delta}$dec) is just 0.8° too high (Fig. 1.2b , declination - IGRF value), and the Δdec is approximately Gaussian distributed around this value. In contrast to the declination, the inclination values are skewed towards lower than expected values. Only two data points yield (slightly) higher than expected values, while the median difference ($\widetilde{\Delta}$inc) is -2.9° (Fig. 1.2d, inclination - IGRF value). Of the flows sampled at multiple sites in this study (1923, 1971, 1983 and 2002) some results are closer to the reference value than others and there are large in between site discrepancies. For the 1923 flow, for example, there is almost a 9° declination difference between the two sites, and an 8° difference in inclination. The majority of the intensity data is also lower than the reference value: the median difference ($\widetilde{\Delta}$int) is -8.8 μT (Fig. 1.2f, intensity - IGRF value).

There is no general correlation between the difference with respect to the reference value and the paleointensity method used. There also seems to be no relation between the observed bias and the orientation of the flank of Mt. Etna where the sampling sites were located. Furthermore, because not all studies reported their sampling strategies it is hard to compare between studies with different sampling strategies. Some that sampled from top to bottom see a slightly larger deviation at the bottom, such as the 1971 flow of Rolph (1997) and the 1983 flow of L. V. de Groot et al. (2013), the latter attributes the deviation to cooling rate differences.

1.3. Mapping magnetic anomalies

The ambient geomagnetic field, i.e. the magnetic field that would be recorded by a new lava flow, was measured at five sites above four lava flows in April 2018 (Fig. 1.1, Supp. Table 1.3). Measurements were made with the AnomalyMapper, the same device as described in B. M. de Groot and de Groot (2019). The AnomalyMapper is equipped with a three-axial fluxgate magnetometer, the Bartington Mag-03 (B. M. de Groot & de Groot, 2019) with a measuring range between 0-100 μT. According to specifications the orthogonality error between the three axes is <0.5°. The temperature offset coefficient of this type is 0.6 nT per degree Celsius, leading to a negligible bias of only a few nT compared to the ambient magnetic fields of 48,000nT measured on Mt. Etna. The AnomalyMapper was used previously in B. M. de Groot and de Groot (2019) to test the variations in declination, inclination and

intensity in a grid of 10x11 points in an area of 20x22m, at different heights above the ground. They found visible variations depending on which height above the surface the measurements were done.

We extend the dataset in B. M. de Groot and de Groot (2019) to five more sites on Mt. Etna. At each site, three 'paths' were measured perpendicular to ridges and gullies to obtain the largest topographic differences possible, with measurement locations being ~1m apart; the three paths were 20 to 80m apart up/down the slope of the lava flow (Supp. Fig. 1). At FLUX1 to FLUX4 the paths were measured twice, with the magnetometer positioned at 100 and 180cm above the ground. The paths of FLUX5 were measured four times at 25, 75, 125 and 175cm above the ground (Supp. Fig. 3–16). In total, we measured the ambient geomagnetic field above the lava flows of Mt. Etna 1,334 times. The exact topography was obtained from the GPS sensor mounted on the magnetometer.

The AnomalyMapper uses a scope to point the magnetometer towards a reference point with a known (GPS) location (B. M. de Groot & de Groot, 2019). Due to the irregular terrain it was not always possible to see the reference point, most often in topographic lows, therefore the declination record is discontinuous for some paths. This did not affect the inclination data, as this is only dependent on the leveling of the magnetometer which is done using a tilt sensor, or the intensity data, that is the length of the total vector measured irrespective of its orientation.

1.3.1. Local magnetic anomalies

For all paths we observe major variations in declination, inclination and intensity above the lava flows. The reference field according to the IGRF-model in April 2018 was calculated for each site at the corresponding GPS coordinates and average elevation (Table 1.1). Here we use the results of path 2 of site FLUX3 at 100cm height and path 1 of site FLUX5 at 125cm height as examples (Fig. 1.3). Of FLUX3, the variation in declination is -6.5 to 5.4°; with a median difference of -3.2° with respect to the expected IGRF-value for measurements done at 100cm above ground. The inclination is on average closer to the IGRF-value, with a median difference of -1.5°, and varies between 46.8 and 58.7°. The intensity varies between 42.1 and 47.9 μT, with a median offset of -0.9 μT. FLUX5 was measured with most detail, and has for the measurements done at 125cm above the ground similar large fluctuations as FLUX3 has at 100cm. Declination varies between -4.2 and 8.7°, with a median difference of -0.9°. Inclination measurements range from 49.7 to 54.2° and the median difference is -1.3°. Finally, the intensity varies between 40.9 and 47.2 μT with a median offset from the IGRF-value of -1.5 μT. The data for all paths and sites generally show similar behavior (Supp. Fig. 3–16; Supp. Table 1.4–1.7). The median deviations with respect to the expected IGRF values for all paths at 100cm (or in the case of FLUX5 at 125cm) above ground in the dataset ranges from -5.9 to -0.9° for $\tilde{\Delta}$dec; -2.2 to 1.1° for $\tilde{\Delta}$inc; and -2.2 to 0.1 μT for $\tilde{\Delta}$int.

1.3.2. Variations with height above surface

The deviations from the expected IGRF-values are largest close to the surface and become less pronounced higher above the flow (Supp. Fig. 2). This is most promi-

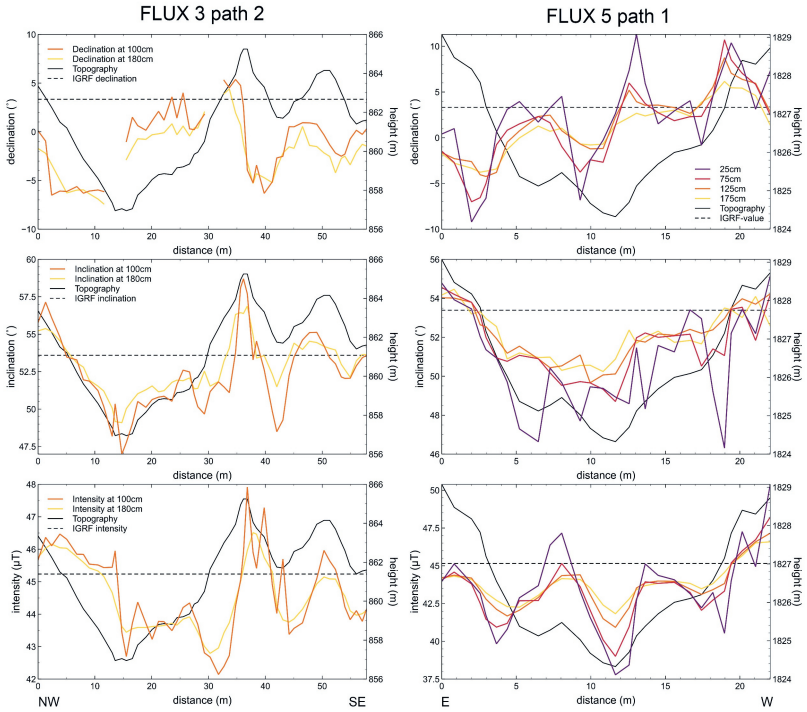


Figure 1.3: Fluxgate measurements of site FLUX3, path 2 (left) and FLUX5, path 1 (right). The variation in declination (top) does not show a clear correlation with topography (black line). The variations in inclination (middle) and intensity (bottom) correlate with the topography variations. Measurements closest to the ground surface (100cm for FLUX3 and 25cm for FLUX5) have the largest variation.

nent in the inclination and intensity data, and less in the declination data. For all three paths of FLUX3 the standard deviation decreases when measurement height above the flow increases (Supp. Fig. 2). This is also reflected in the $\widetilde{\Delta}$ range of values. For path 2 of site FLUX3 the range of declination values is -9.8 to 2° at 100cm above ground and -10.7 to 1° at 180cm, inclination values are -6.6 to 5.1° at 100cm above ground and -4.5 to 3.3° at 180cm, and for the intensity the variation is -3.1 to 2.7 μT at 100cm and only -2.4 to 1.3 at 180cm (Fig. 1.3). Site FLUX5 was measured at four different heights above the surface, with the lowest being at 25cm above ground and the highest at 175cm. The largest spikes in the measurement data are at 25cm height, the level closest to the lava flow (Fig. 1.3). For path 1 of FLUX5, the $\widetilde{\Delta}$dec range decreases from -12.5 to 8.0° at 25cm to -7.1 to 2.8° at 175cm. For the inclination the range at 25cm above the flow is -7.1 to 1.8° and only -3.1 to 1.1° at 175cm. The intensities vary from -7.4 to 5.2 at 25cm, and from 3.3 to 1.4 μT at 175cm above the flow. As the intensity of the magnetic field decays with the power of three as function of distance to its source, the observed gradients as function of height above the flow imply that the source of the local magnetic anomalies must be close to the surface. This means that the magnetic signal of the flow(s) closest to the surface have the most impact on the ambient magnetic field above the flow.

1.3.3. Correlation with topography

Beyond the influence of the height above the flow, both the inclination and intensity variations seem to correlate with changes in topography. All paths are characterized by an irregular topography with at least one distinct gully (Supp. Fig. 3–16). Path 2 of site FLUX3 is a good example of such a distinct gully which is approximately 35m wide and 8m deep (Fig. 1.3). The gully in FLUX5 path 1 is around 20m wide and 4m deep. Both the inclination and intensity are higher above ridges and lower in gullies. For path 2 of FLUX3 the differences compared to the IGRF are +4.1° in inclination and +2.7 μT in intensity with respect to the IGRF-value at 100cm above the highest peak in the profile. At 100cm above the lowest point, i.e. in the gully, the inclination is -5.6° and the intensity -2.4 μT with respect to the IGRF-value. For FLUX5 path 2 most measurements are done in the gully, there is not a clear ridge in the profile but the peaks are located at the edges. At 125cm height above the highest peak the difference with the IGRF-value is +0.6° in inclination and -0.9 μT for intensity. Above the lowest peak they are -3.3° and -4.2 μT, respectively. To statistically assess the correlation between the fluxgate measurements and the topography, the Pearson's correlation coefficient and its corresponding p-value were calculated for each path and at each height. A Pearson's coefficient of +1 is a positive correlation, 0 is no correlation and with -1 there is a negative correlation. In terms of our fluxgate measurements, for a positive correlation the measurement value increases with increasing topography. Supp. Table 1.8 includes all Pearson correlation coefficients for each site and path. In Fig. 1.4 the correlation coefficients are grouped for FLUX1-4 (Fig. 1.4A) based on measurement height above the surface of the lava flows (100 and 180cm). Because FLUX5 was measured at four different levels we consider that site independently in Fig. 1.4B. The median correlation coefficient of declination is around 0 for FLUX1-4, which statistically suggests there is no trend between the declination and the topography. Inclination and intensity have a medium to strong positive correlation, these appear to have a

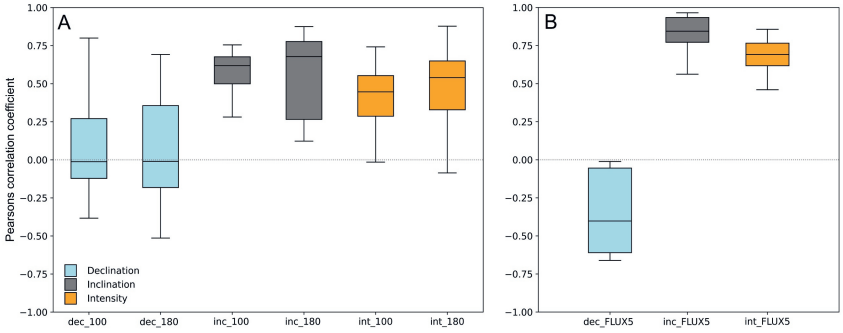


Figure 1.4: Box-plots for Pearson's correlation coefficient of A) FLUX1 to 4 and B) FLUX5. For each path a Pearson's correlation coefficient was calculated between the topography and the declination, inclination or intensity. For FLUX1-4 the coefficients are grouped for inclination, declination and intensity at 100 or 180cm height. For FLUX5 all four different measurement levels (25, 75, 125 and 175cm) are together. See Supp. Table 1.8 for the individual correlation coefficients.

positive trend with topography. Finally, for some paths the intensity signal seems to be slightly offset with respect to the topography, as illustrated at distance 30 to 35m in path 2 of site FLUX3 (Fig. 1.3). This offset, however, is small, not always present and does not correlate with the orientation of the gully or with the orientation with respect to the summit of Mt. Etna.

1.4. Discussion

1.4.1. Systematic bias due to local magnetic anomalies

Paleomagnetic data produced by this and previous studies were compared with the reference value predicted by the IGRF-13 or gufm1 model, both are estimations of the Earth's magnetic field at that time and might not be fully accurate. We, however, expect minor errors in the prediction of these models. Measured values at three different Italian magnetic observatories show a good correlation with the IGRF-model during the period of 1960-2020 (Di Mauro et al., 2021). This confirms that we can reliably compare our paleomagnetic measurements from historical lava flows with the predicted reference values, at least the flows younger than 1960. The gufm1 model is based on full-vector measurements of the Earth's magnetic field between 1850-1899. Especially in Europe the data coverage is good (Jackson et al., 2000), therefore we assume that the errors prior to 1960 might slightly increase but overall to be negligible. The paleomagnetic data set of Mt. Etna shows a systematic bias in both the inclination and intensity, but not for the declination.

The paleomagnetic directions and intensities vary for sites sampled at different locations from a single flow, and sometimes by different studies. The inclinations reported for the 1983 flow, for example, differ 9.1°, and declination for the 1923 flow differs by 8.7° between sites (Fig. 1.2). The sites from a single flow may be hundreds of meters to a few kilometers apart. Our fluxgate measurements cannot explain these between-sites differences, because our fluxgate measurements were taken over short distances. They therefore reveal changes in the ambient field on a

scale of tens of meters. The differences between sites from a single flow may reflect a bias in the ambient magnetic field with a longer wavelength. Another explanation may be that the influence of local topography differs between sites: e.g. if a larger portion of a flow is deposited in a gully, a more prominent bias in the resulting paleomagnetic direction could be expected. It is interesting to note that a large deviation from the IGRF value in inclination does not correlate to a large deviation in declination, and vice versa.

No bias in declination

The declinations of the paleomagnetic data show variation around the expected IGRF-values (Fig. 1.2a,b), but there is no systematic offset. The median declinations in our direct measurements, however, are up to 6.5° lower than the expected IGRF-values. Due to the design of the AnomalyMapper, the declination is prone to errors and potentially a bias (B. M. de Groot & de Groot, 2019). It relies on aiming the AnomalyMapper to a fixed reference point using a scope, while the inclination is determined using a tilt-sensor, and the intensity is independent of the orientation of the device. If the scope is slightly offset in its mount this would lead to a systematic bias in the declinations and limit their interpretation to describing relative variations. The requirement of having a line of sight to a reference point also sometimes prevents determining a declination. Especially in deeper gullies the reference point is sometimes not visible. If the bias in declinations would be strongly positive deep in the gullies, a lack of declination measurements there may also explain the bias towards negative values for the median declinations. For the sites that do have continuous declination data in the gullies, such a trend may be suggested (e.g. site FLUX5 paths 2 and 3 which have Pearson correlation coefficients at 125cm of -0.4 and -0.6, respectively), but it is not present for all sites, and it is certainly not strong enough to explain the deviations in median declinations fully. Lastly, Baag et al. (1995) predicts positive declination deflections on the western side of a volcano, and negative ones on the eastern side. The fluxgate sites and most paleomagnetic sampling sites in this study are only on the northern and southern slopes. Except ET1 and ET2 which were on the eastern flank, but the largest positive declination deflection is of ET1 so this does not correlate.

Bias in inclination

The median difference in inclination (-2.9°) is very close to the inclination shallowing of 3° that Pavón-Carrasco et al. (2014) reported for paleomagnetic data from volcanic products on the Northern Hemisphere for the past 400 years. Our AnomalyMapper measurements indicate that the inclination varies as a function of topography and is lower in the gullies. The correlation between the variations in inclination and topography are strong: the Pearson's correlation coefficient is positive for all sites, and the median coefficient is well above 0.5 for all heights above the surface (Fig. 1.4). We expect the largest volume of a new flow to be deposited in the gullies, where it would record inclinations that are biased to lower values. Therefore our direct field observations with the AnomalyMapper may explain the overall bias in the paleomagnetic inclination data (Fig. 1.2D).

Our observed inclination anomalies agree with the theoretical models of Baag et al.

(1995). Their models predict that on the Northern Hemisphere negative inclination anomalies occur in gullies, or channels. Especially their V-shaped valley models closely resemble some of our inclination anomalies in the gullies, for example as in site FLUX2 path 2. In the models of Baag et al. (1995) these channels are E-W oriented; in our AnomalyMapper measurements the orientation of channels does not seem to correlate with the amount of inclination shallowing. Baag et al. (1995) predicts the inclination anomalies to be negative in gullies on the Northern Hemisphere and positive in the gullies in the Southern Hemisphere, and therefore to be latitudinally dependent. This would imply that our inclination bias on Mt. Etna is specific to this latitude.

Bias in intensity

For the intensities we observe a bias similar as the one for the inclinations: the intensities are biased to somewhat lower values in the gullies. This correlation is supported by the Pearson's coefficients, although somewhat less strong compared to the correlations for the inclinations (Fig. 1.4). The big caveat here is that we only find deviations up to a few (2 to 3 μT) in our AnomalyMapper observations, while the paleomagnetic data generally shows much larger deviations from the expected IGRF field, sometimes up to 20 μT (Fig. 1.2E, F). Our direct field observations therefore only explain a (small) part of the bias observed in our paleomagnetic data.

It is important to emphasize that obtaining a paleointensity is difficult, and that all paleointensity methods have low success rates. The low paleointensities for Mt. Etna have been attributed to 'magnetic refraction' by Rolph and Shaw (1986) and Rolph et al. (1987); 'multi-domain behavior' by Hill and Shaw (1999) and Biggin et al. (2007); 'transdomain processes' by Calvo et al. (2002) and L. V. de Groot et al. (2013); and differences between natural and laboratory cooling rates by Hill and Shaw (1999), Biggin et al. (2007) and L. V. de Groot et al. (2013). The common ground for these rock-magnetic processes is that they violate the central assumptions underpinning paleointensity experiments, e.g. the laws of additivity and reciprocity (Tauxe, 2010), and therefore hamper a reliable reconstruction of the paleointensity. The study of obtaining a reliable paleointensity is an entire research field on its own. Why these aforementioned rock-magnetic processes seem to systematically lead to even lower paleointensities than predicted by our direct field observations is therefore beyond the scope of this study.

1.4.2. The impact on paleomagnetic statistics

If a hypothetical new flow on Mt. Etna would record the ambient magnetic field that we measured directly with the AnomalyMapper, we can simulate what the effect of local magnetic anomalies would be on a paleomagnetic study. More than 20% of the data points in sites FLUX1 and FLUX4 lack declinations, we therefore exclude these sites from this simulation. For the other sites, we randomly drew 10 AnomalyMapper measurements for each site and calculated what the resulting declination, inclination, intensity, k and intensity error (σ) would be. This was repeated a 1000 times and we report the median values for each site in Table 1.2. We expect the largest volume of a new flow to be deposited in the gullies of the underlying flow, we therefore repeated this analysis by selecting only AnomalyMapper

Table 1.2: Random sampling of fluxgate measurements. Simulated paleomagnetic data based on AnomalyMapper measurements. N is the amount of measurements available to take random samples from, $\tilde{\Delta}$dec,inc,int is the difference of the median with the IGRF-value, k med is the median of the precision parameter and σ is the standard deviation of the intensity measurements.

	All measurements						Gully +3m					
Site	N	$\tilde{\Delta}$dec	$\tilde{\Delta}$inc	$\tilde{\Delta}$int	k med	σ	N	$\tilde{\Delta}$dec	$\tilde{\Delta}$inc	$\tilde{\Delta}$int	k med	σ
FLUX2	187	-2.76	-0.81	-0.82	1226	1.26	134	-2.67	-0.96	-1.20	1522	1.12
FLUX3	257	-4.87	-0.38	-0.79	953	1.12	96	-5.12	-1.78	-1.25	1372	1.05
FLUX5	344	-2.27	-0.94	-1.49	461	2.24	188	-0.84	-2.23	-2.69	667	1.89
Average	788	-3.30	-0.71	-1.03	880	1.54	418	-2.88	-1.66	-1.72	1187	1.35
	Gully +2m						Gully +1m					
Site	N	$\tilde{\Delta}$dec	$\tilde{\Delta}$inc	$\tilde{\Delta}$int	k med	σ	N	$\tilde{\Delta}$dec	$\tilde{\Delta}$inc	$\tilde{\Delta}$int	k med	σ
FLUX2	71	-3.03	-1.16	-1.33	1504	1.19	53	-2.82	-1.41	-1.61	1457	1.21
FLUX3	60	-4.89	-2.18	-1.16	1857	1.02	28	-5.15	-2.50	-1.25	2026	1.16
FLUX5	148	-0.55	-2.64	-2.94	908	1.85	88	0.04	-2.94	-3.41	980	1.87
Average	279	-2.82	-1.99	-1.81	1423	1.35	169	-2.64	-2.28	-2.09	1488	1.41

measurements from the gullies. We defined a gully as the lowest point in the topography, the local minimum, and selected the measurements around it up to +1, +2m or +3m height.

The k-value is an expression of how well measurements from individual samples agree. The median k-values are 1226 for FLUX2, 953 for FLUX3, and 461 for FLUX5, when all measurements per site are considered. If a new flow would be deposited deep in the gullies (+1m from the lowest point), the k-values increase to 1457, 2026, and 980, respectively. This illustrates that high k-values in rough volcanic terrain may indicate that a local magnetic anomaly is not averaged out sufficiently. Moreover, it should be emphasized that the AnomalyMapper measurements do not suffer from orientation errors that occur during paleomagnetic sampling and measurements that would certainly lower our simulated k's. k's associated with real paleomagnetic data are therefore expected to be lower than these theoretical upper limits for these flows from our simulation. The standard deviation of paleointensity measurements, σ, is a measure of how well paleointensity results from different samples agree. For this parameter we see for some sites the same trend as for the k-value, but the σ's reported here are negligible compared to the uncertainties arising from paleointensity experiments (e.g., Biggin et al., 2007; L. V. de Groot et al., 2012, 2013).

It is important to emphasize that these theoretical 'maximum' k-values from our simulations only pertain to these specific flows and cannot be generalized to other flows and/or locations. Local circumstances such as the morphology of the underlying terrain and the magnetization of the flows will impact the actual bias at each new location. Our observations do suggest that very high k-values do not necessarily imply that the paleodirection reproduces the expected geomagnetic field at that location within error; while low k-values do not necessarily mean that the paleodirection is unreliable.

1.4.3. Optimal sampling strategies

Our observations have consequences for paleomagnetic sampling strategies. To suppress the influence of local magnetic anomalies arising from the underlying terrain, it is important to take samples for both paleodirectional and paleointensity studies far apart on the outcrop, in an area of several tens of meters wide. If possible, take samples not far from the top of a flow or throughout a flow. If there are substantial differences between samples taken from the top and bottom this could indicate that the bottom of the flow was influenced by the magnetized terrain below.

The question of how many samples (N) are enough for a reliable paleomagnetic result has been addressed previously, although this differs for paleodirectional and paleointensity data. For paleodirections, it was previously shown that the α_{95} uncertainty interval decreases with each additional sample up to N=10 (Tauxe, 2010). Beyond ten samples, the effect of adding more samples on α_{95} is small. Even though we show that a small α_{95} does not imply that the resulting direction is close to the true paleomagnetic direction, an average based on N=10 seems a good target. By bootstrapping a published dataset, Cromwell, Johnson, et al. (2018) showed that the resulting paleomagnetic direction already came close to the published value for only four samples. They therefore suggest a minimum of four samples and a precision parameter k≥50. Here we show that a higher k-value does not necessarily correspond to a more accurate measurement of the expected paleomagnetic direction. A sampling strategy based on only four samples therefore seems less ideal for volcanic terrains with a topography like Mt Etna's. For paleointensities, the variations between samples from a single site can be quite large and the optimum number of samples may be as large as 24 (Paterson et al., 2010), although such a high number is likely not achievable because of the time consuming paleointensity techniques. The CCRIT paleointensity selection criteria demands a minimum of three specimens per site (Cromwell et al., 2015a). This is, however, the absolute minimum, as Paterson et al. (2010) considers studies with N<10 less reliable. Given the low success rates of paleointensity studies, it is advisable to measure at least 10 samples per site, and only accept a result for a site if it is based on a minimum of three samples.

A sun compass is preferable for sample orientation to avoid the influence of local magnetic anomalies on drill core orientations. Other techniques to suppress this influence are backsighting using distinct landmarks (Tauxe, 2010) or a differential GPS technique (Lawrence et al., 2009), originally developed for high-latitude sampling sites but also useful when due to weather conditions a sun compass cannot be used. Sometimes, however, non of these orientation methods are available, and one has to revert to using a magnetic compass for orienting the samples. This was also the case for the paleomagnetic data in this study, as weather conditions only allowed using a magnetic compass. This is not the ideal scenario because Speranza et al. (2006) already demonstrated that there might be significant differences between Sun and magnetic compass declination readings on Mt. Etna. The use of a magnetic compass, however, would only influence the declination of the sample orientation. When determining a magnetic direction for a site/flow the results of

several samples are averaged. We do not find a systematic trend between the magnetic declination and topography (Fig. 1.4); and the declination of paleomagnetic data from Mt. Etna does not show a systematic deviation from their expected values (Fig. 1.2B). This implies that the error made by using a magnetic compass can be reduced when samples are taken well spread out over the flow, with different bore hole orientations, and on different sides of an outcrop.

If a paleomagnetic protocol prescribes the use of sister specimens it is necessary to take multiple groups of samples to average out local magnetic anomalies. Then, it is important to avoid using samples from the same group to determine the paleodirection or paleointensity of the entire cooling unit. Finally, if a certain cooling unit is accessible at different locations, e.g. on both sides of a lava flow, higher or lower on a mountain, or even at different flanks of the volcano, taking multiple sites from a cooling unit several hundreds of meters apart and calculating 'age means' greatly increases the chance of being closer to the 'true' paleomagnetic vector at the time of cooling. In practice it is often difficult to find multiple lava flows of the same eruption on different flanks of the mountain, in this case sampling as widely as possible on one site is the only option. As shown in Table 1.2, it is possible that when the samples are taken spread out over an outcrop and the area is affected by magnetic anomalies, a low k-value is obtained - but this does not necessarily indicate a poor paleomagnetic result. It is worth noting that taking samples well spread out over the flow and from different parts also averages out possible variations in the properties of the magnetic minerals present in the sample (e.g., L. V. de Groot et al., 2014a; Thellier, 1977).

To follow all optimal sampling strategy recommendations is of course often difficult during paleomagnetic fieldwork because of limitations in availability and/or accessibility of outcrops. This emphasizes the need to report the sampling strategy in high detail in forthcoming publications and as metadata in data repositories.

1.5. Conclusion

Paleomagnetic data from recent flows of Mt. Etna often yield lower inclinations and intensities than expected from the IGRF. Inclinations are on average 2.9° lower than expected, the intensities are on average 8.8 μT lower. The declination of paleomagnetic data does not show a systematic bias from the expected IGRF fields. The bias in inclination can be explained by local magnetic anomalies due to the underlying irregular terrain of Mt. Etna. Our direct measurements of the current geomagnetic field made with a three-axial fluxgate magnetometer above the strongly magnetized lava flows show that inclination varies as function of topography: the inclination is biased to lower values in the gullies and higher values above ridges. The site level variations in inclinations are up to 14.1°. The largest deviations are found closest to the surface, which emphasizes the influence of the underlying terrain on the ambient magnetic field. For the intensities we find similar behavior as for the inclinations: a systematic bias that correlates with topography, with a maximum within site variation of 12.9 μT. The bias found, however, only explains a small portion of the bias in intensities reported in paleomagnetic data for Mt. Etna.

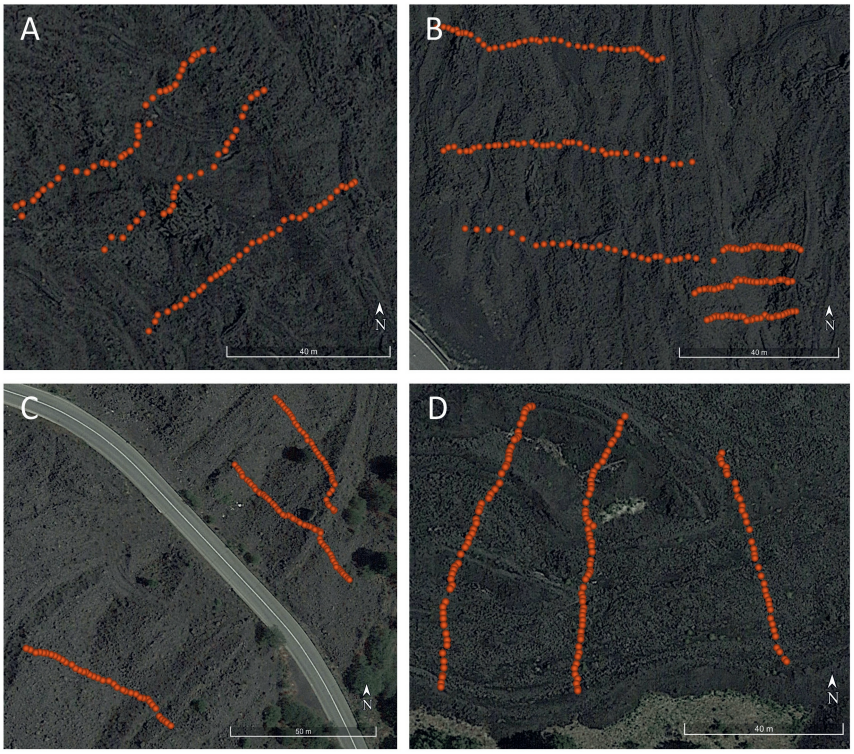
Our observations have implications for optimal paleomagnetic sampling strategies. The variation of the geomagnetic field on Mt. Etna with topography emphasizes the need to take samples spread out over a larger area. This may lower the k-value but averages out local magnetic anomalies best. Because local morphology of the volcanic terrain and magnetic properties of the rocks will influence local magnetic anomalies elsewhere, it is difficult to generalize our findings for Mt. Etna any further. Nevertheless, our findings illustrate that the sampling strategy should always be reported alongside paleomagnetic data and preferably also in metadata of paleomagnetic data in repositories.

Acknowledgments
Esmee Waardenburg, Meeke van Ede, Maartje van de Biggelaar, Lynn Vogel, and Wout Krijgsman are kindly acknowledged for their help in the field and with (the processing of) the measurements. Bertwin de Groot developed the AnomalyMapper. This project has received funding from the Dutch Research Council (NWO) under its Talent program (VENI grant 863.15.003 and VIDI grant VI.Vidi.192.047 to LVdG).

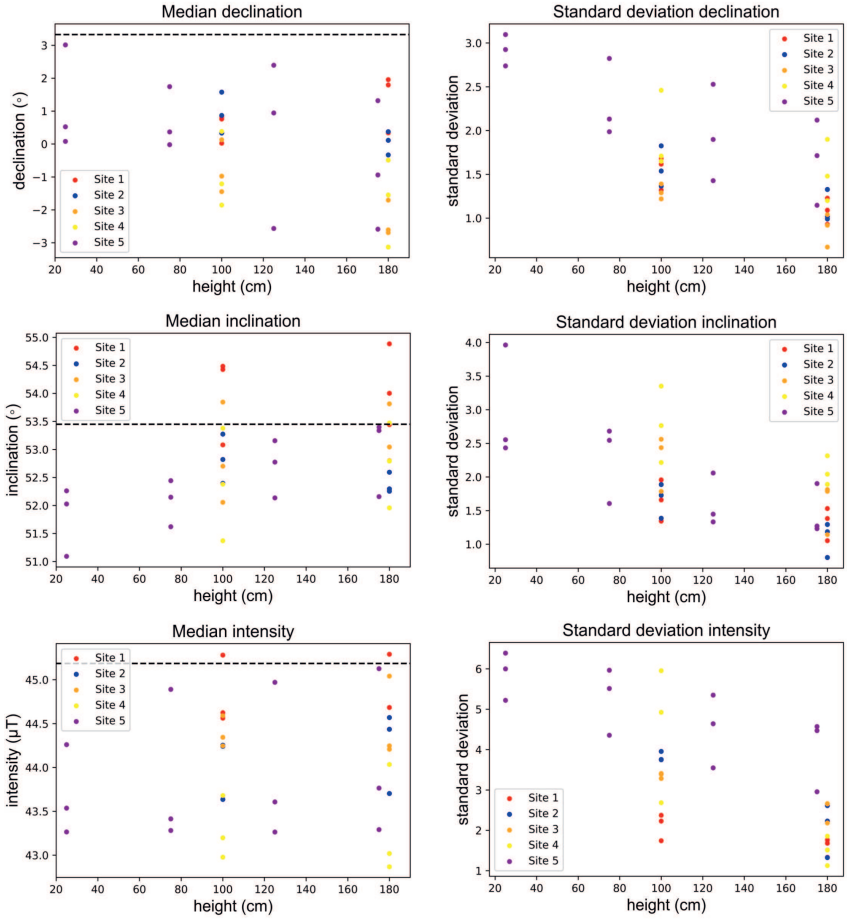
Open Research
All paleomagnetic data measured in this study can be found in MagIC (DOI: 10.7288/V4/MAGIC/20068) (Meyer & de Groot, 2024b). The AnomalyMapper data is available at Yoda (DOI: 10.24416/UU01-NQXN82) (Meyer & de Groot, 2024a).

1

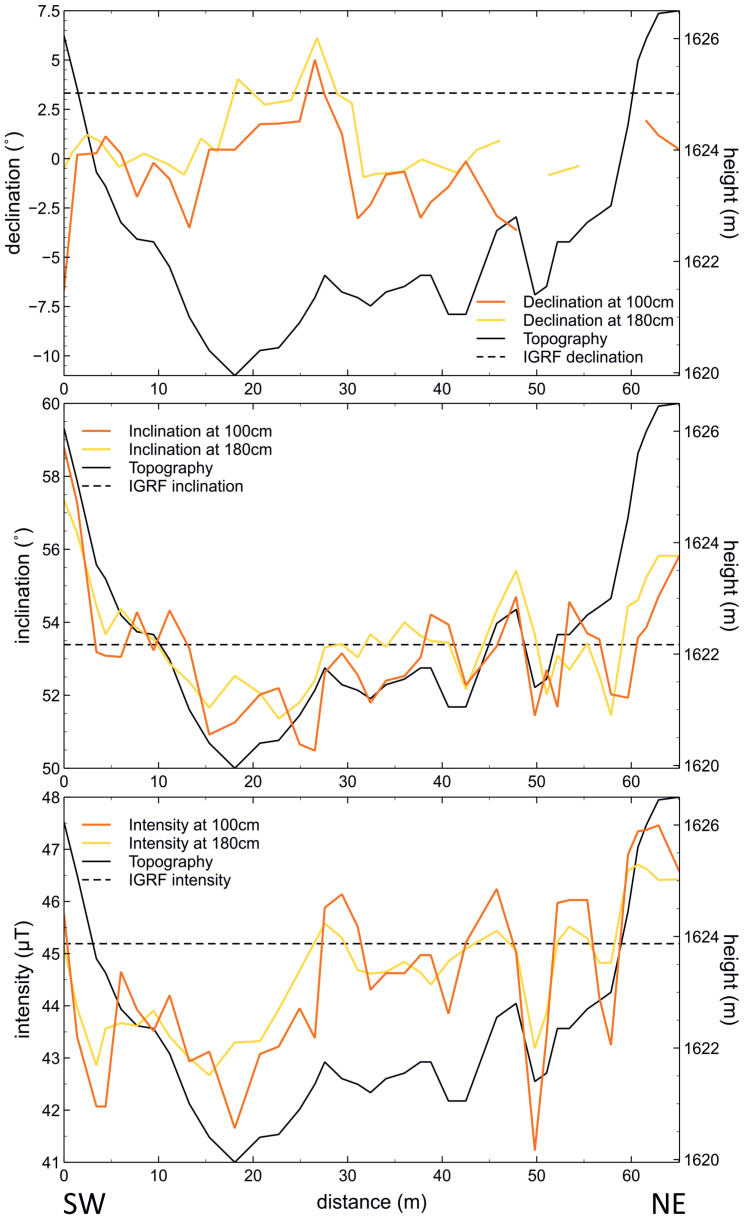
1.6. Supplementary Information



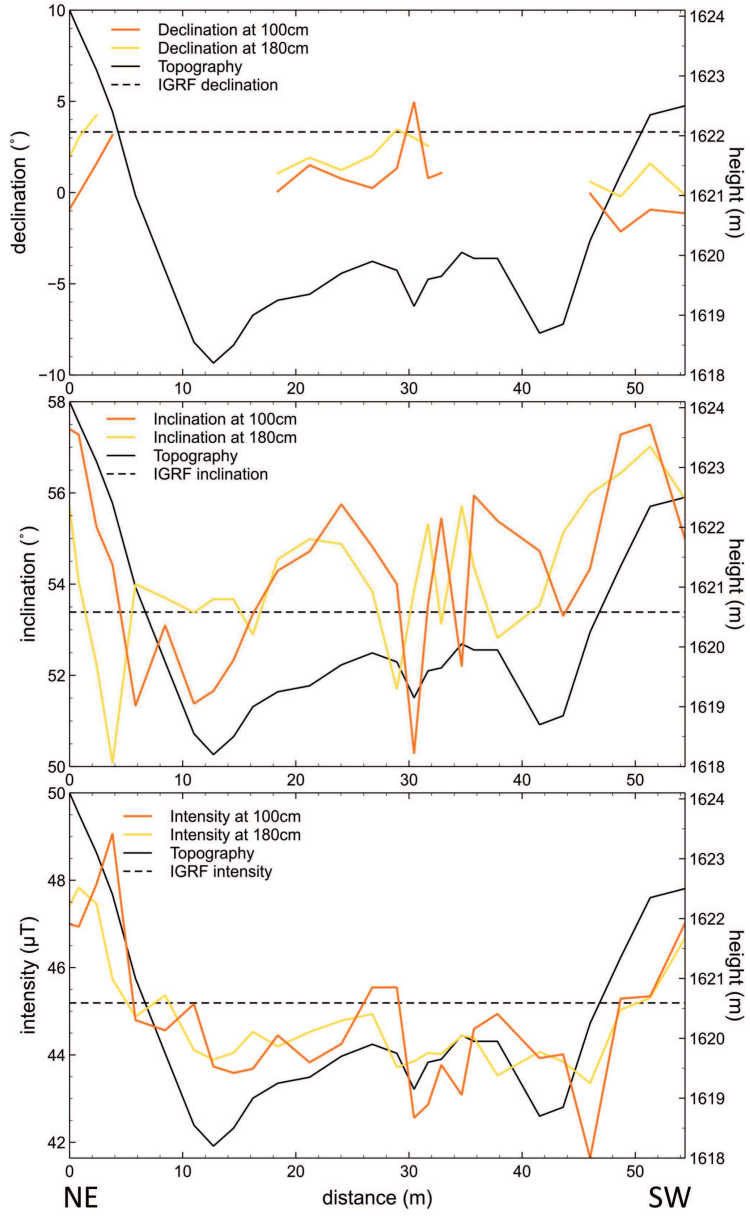
Supplementary Figure 1.1: Locations of the AnomalyMapper measurements for the three different paths. A) site FLUX1, B) site FLUX2 and FLUX5 (right corner), C) site FLUX3, and D) site FLUX4



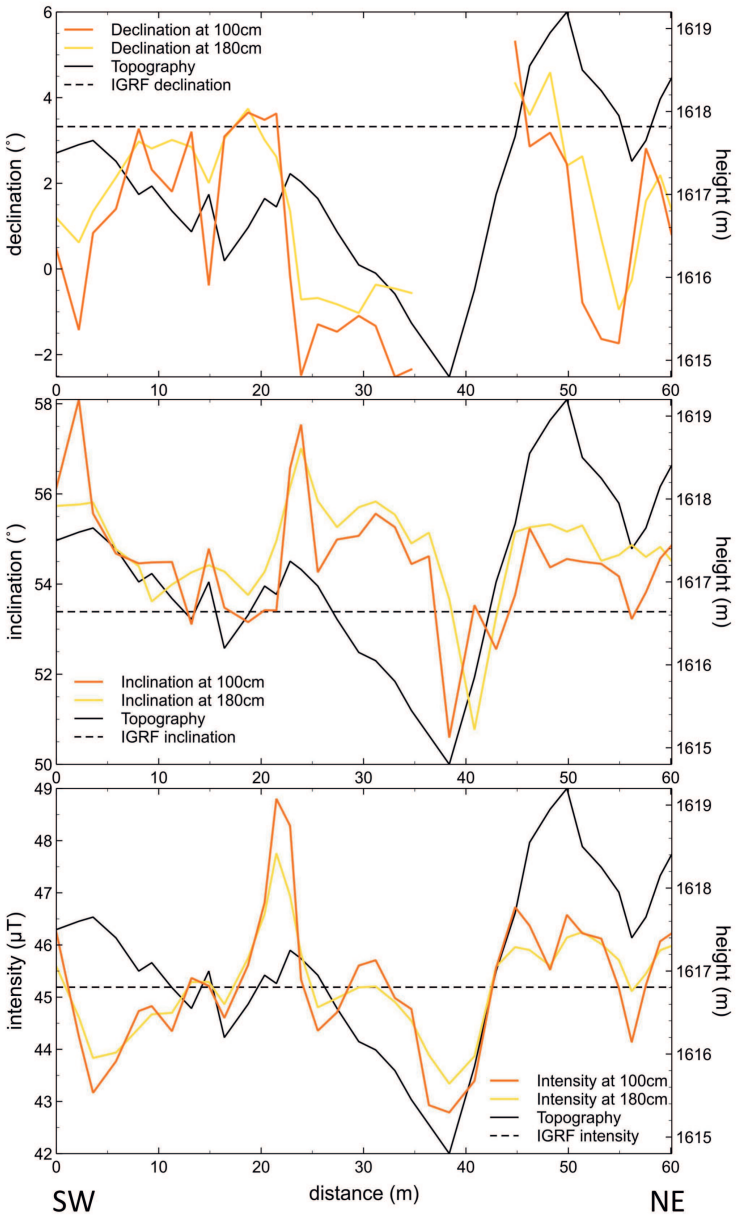
Supplementary Figure 1.2: Median declination, inclination and intensity and their standard deviations for each site and path against the measuring height above the lava flow. Dotted line is the expected IGRF value



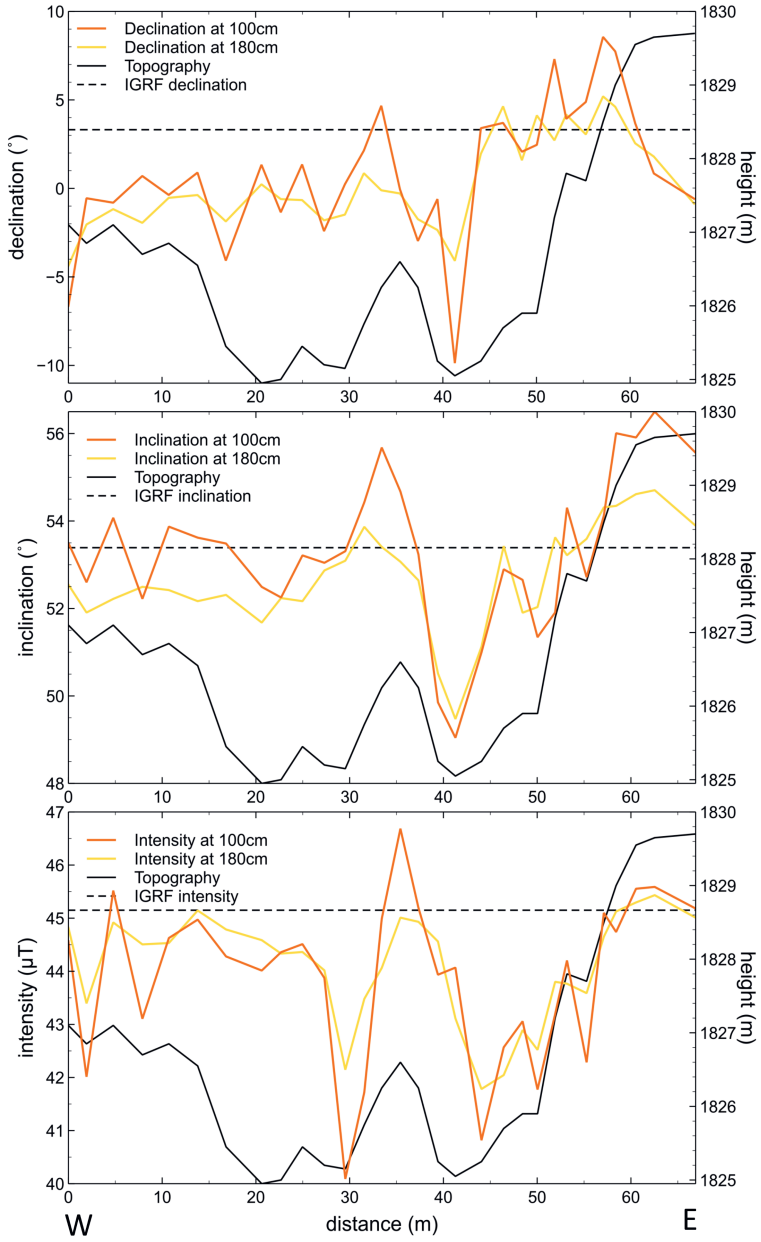
Supplementary Figure 1.3: FLUX1 path 1



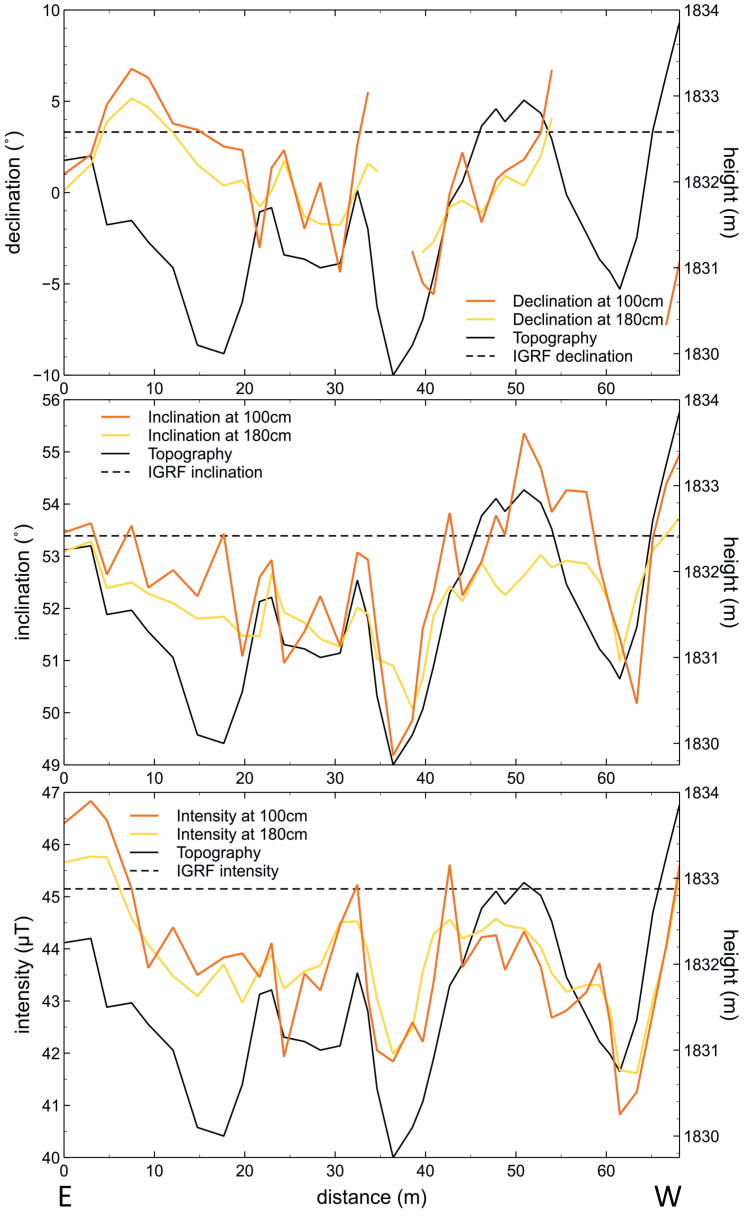
Supplementary Figure 1.4: FLUX1 path 2



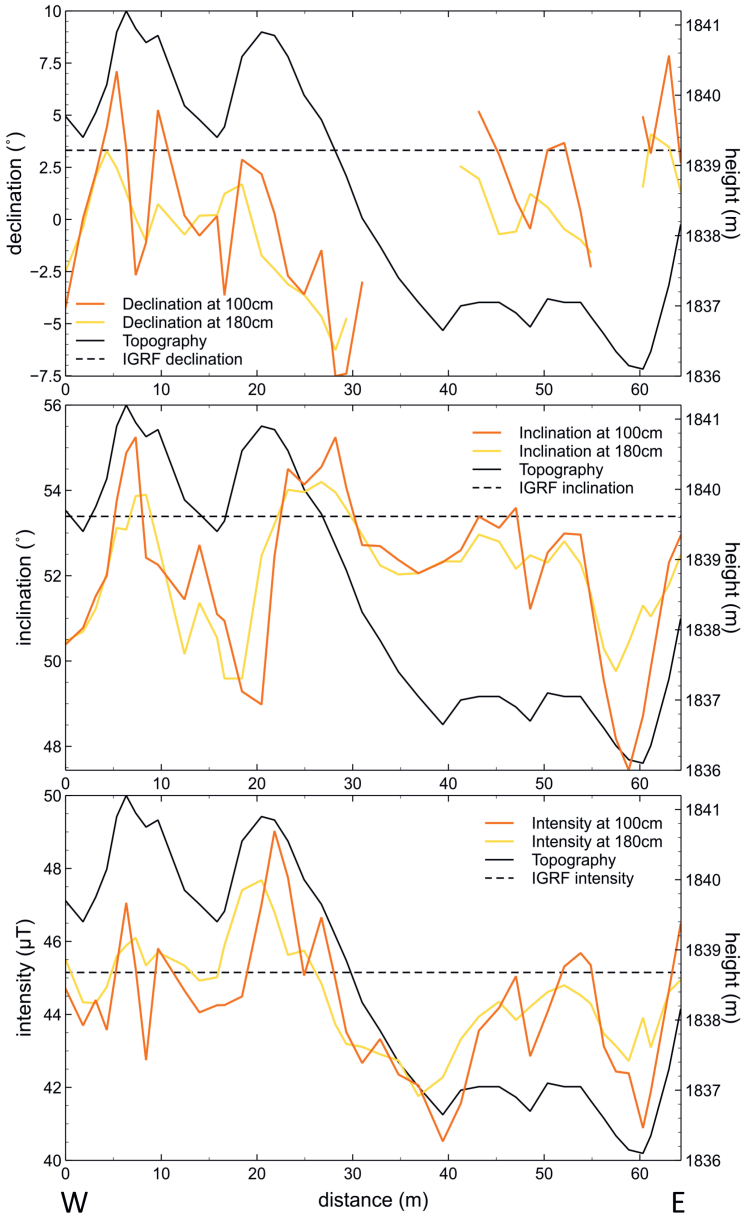
Supplementary Figure 1.5: FLUX1 path 3



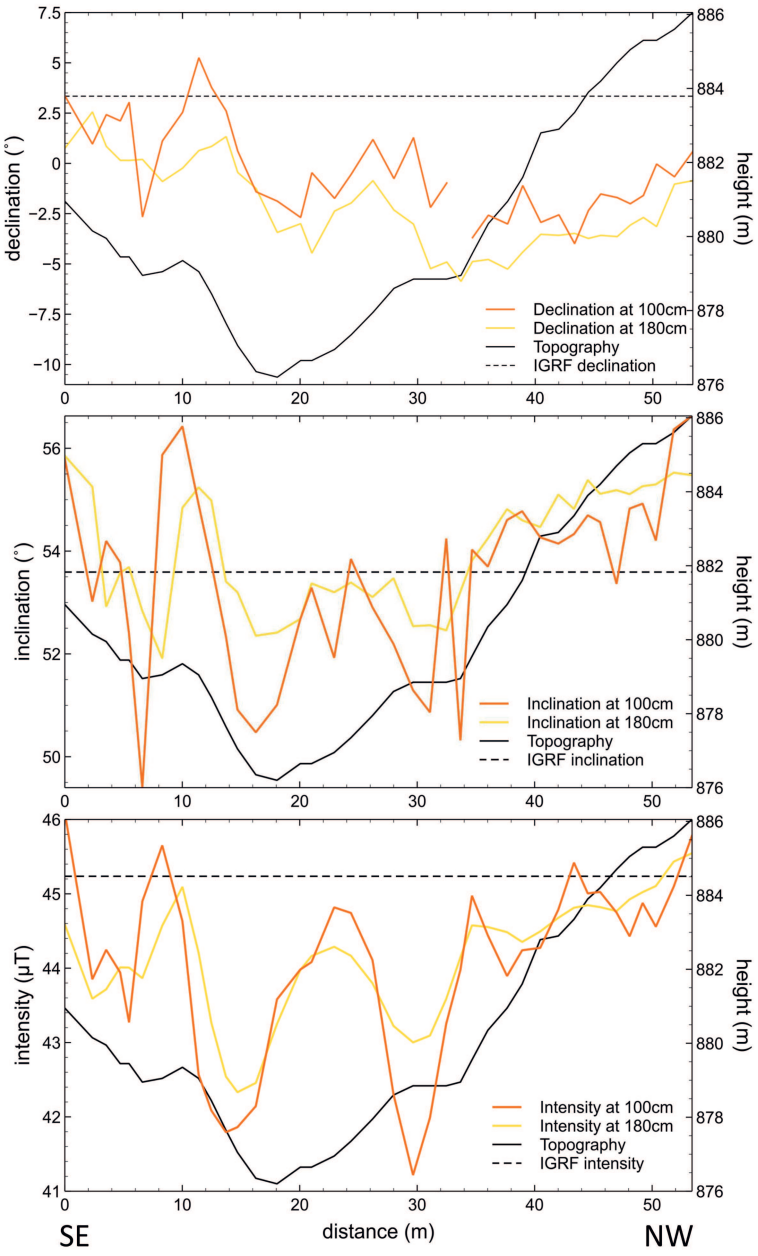
Supplementary Figure 1.6: FLUX2 path 1



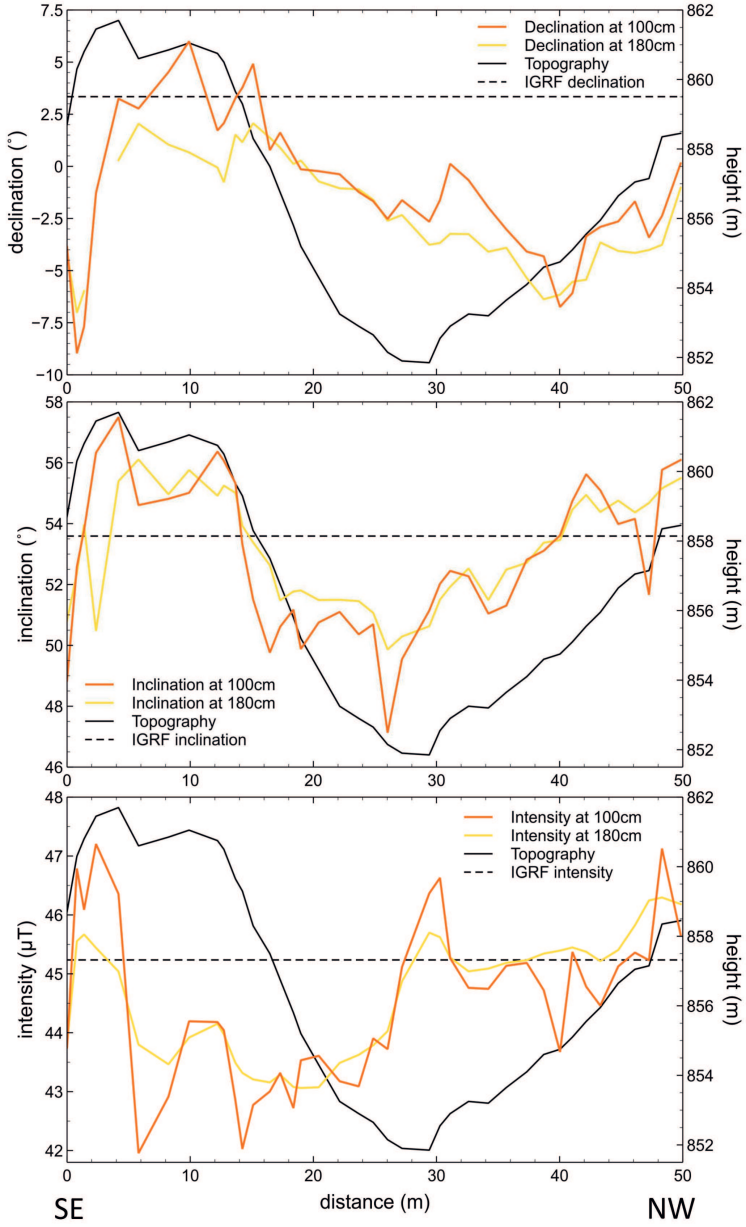
Supplementary Figure 1.7: FLUX2 path 2



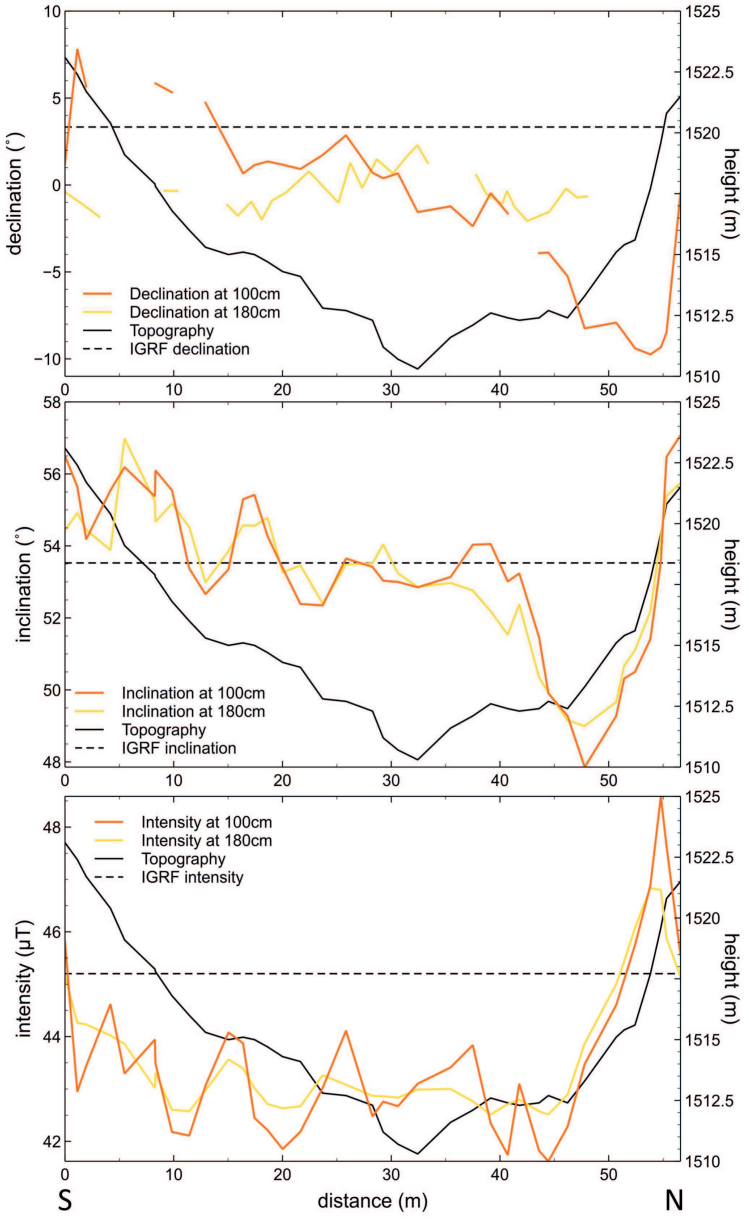
Supplementary Figure 1.8: FLUX2 path 3



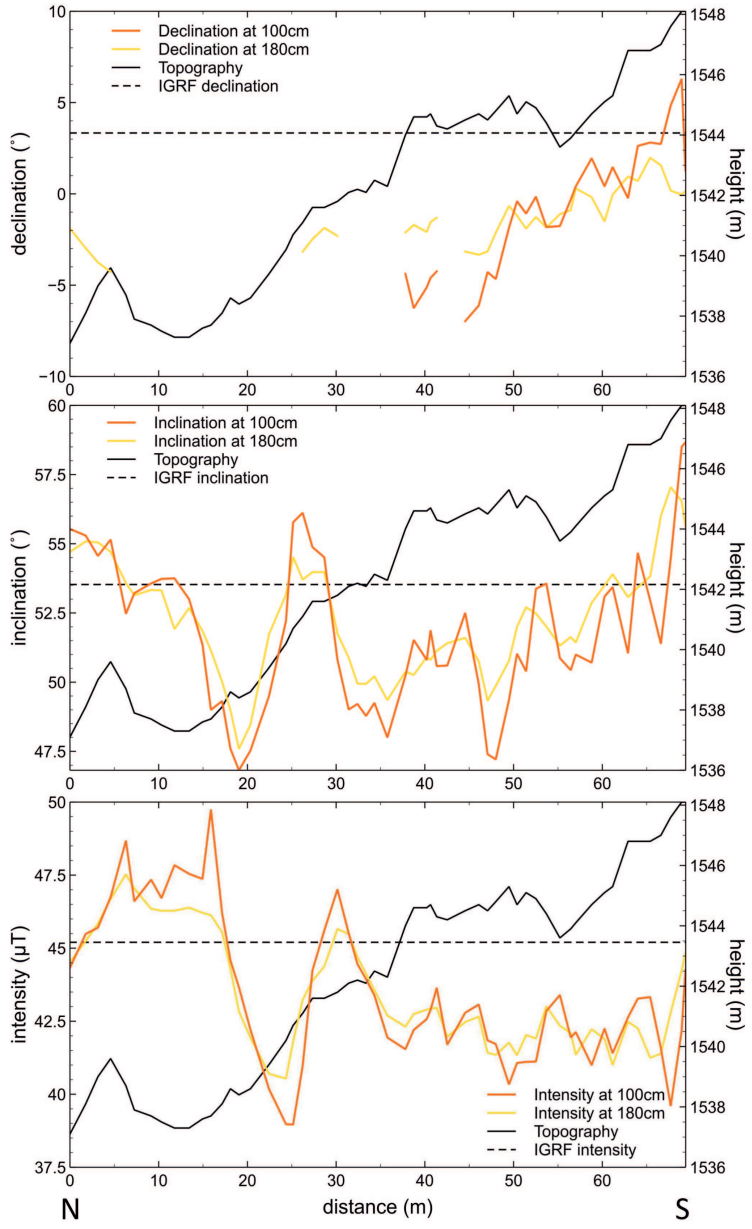
Supplementary Figure 1.9: FLUX3 path 1



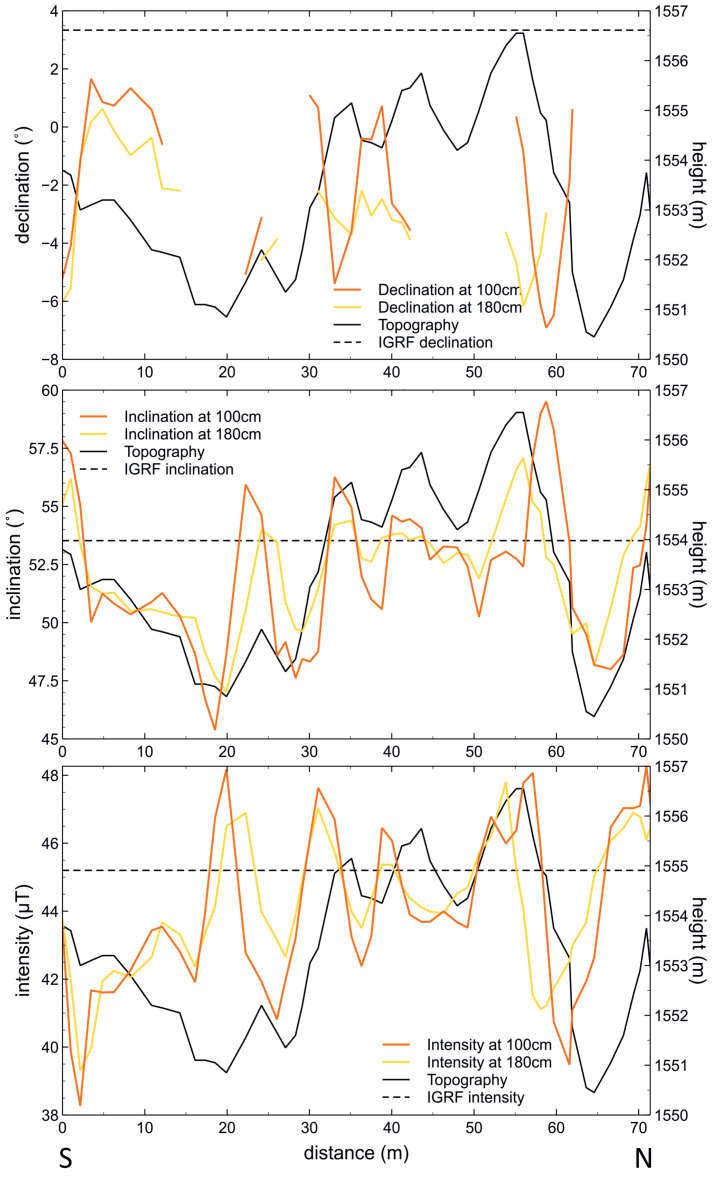
Supplementary Figure 1.10: FLUX3 path 3



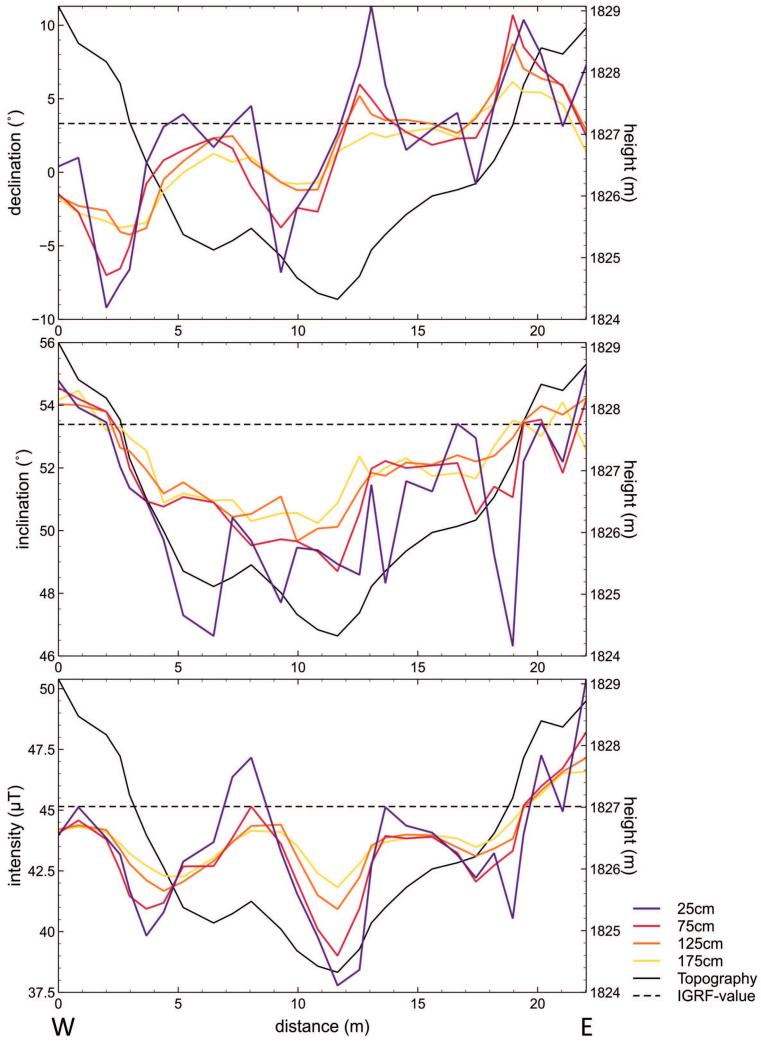
Supplementary Figure 1.11: FLUX4 path 1



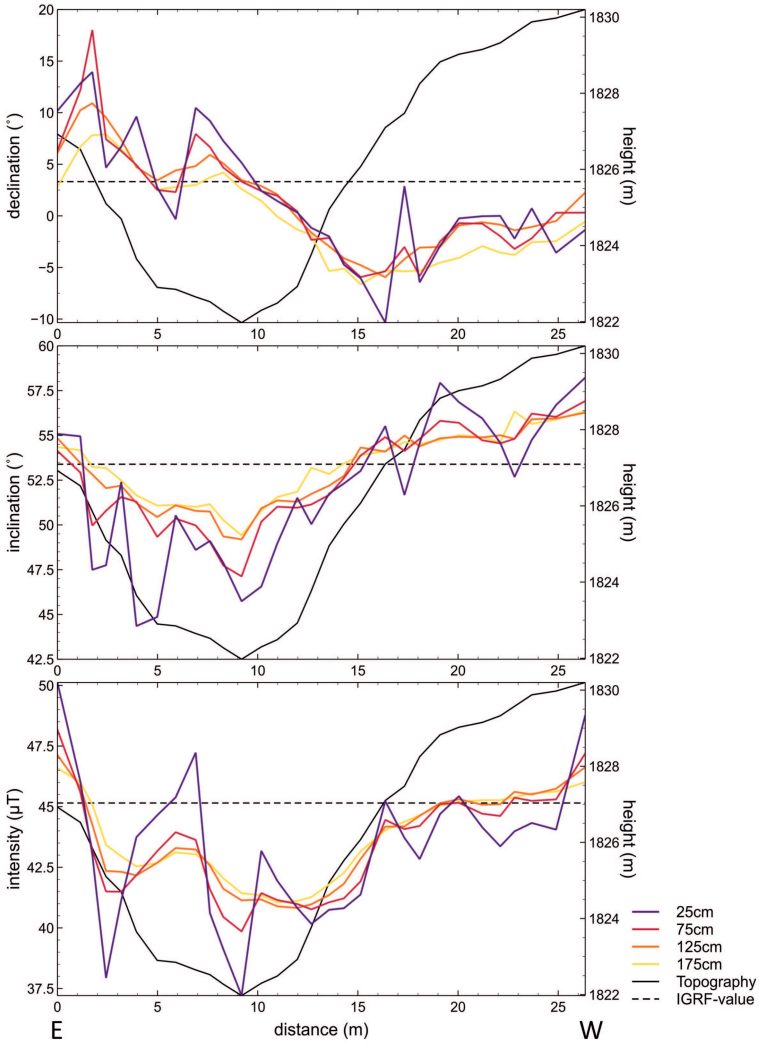
Supplementary Figure 1.12: FLUX4 path 2



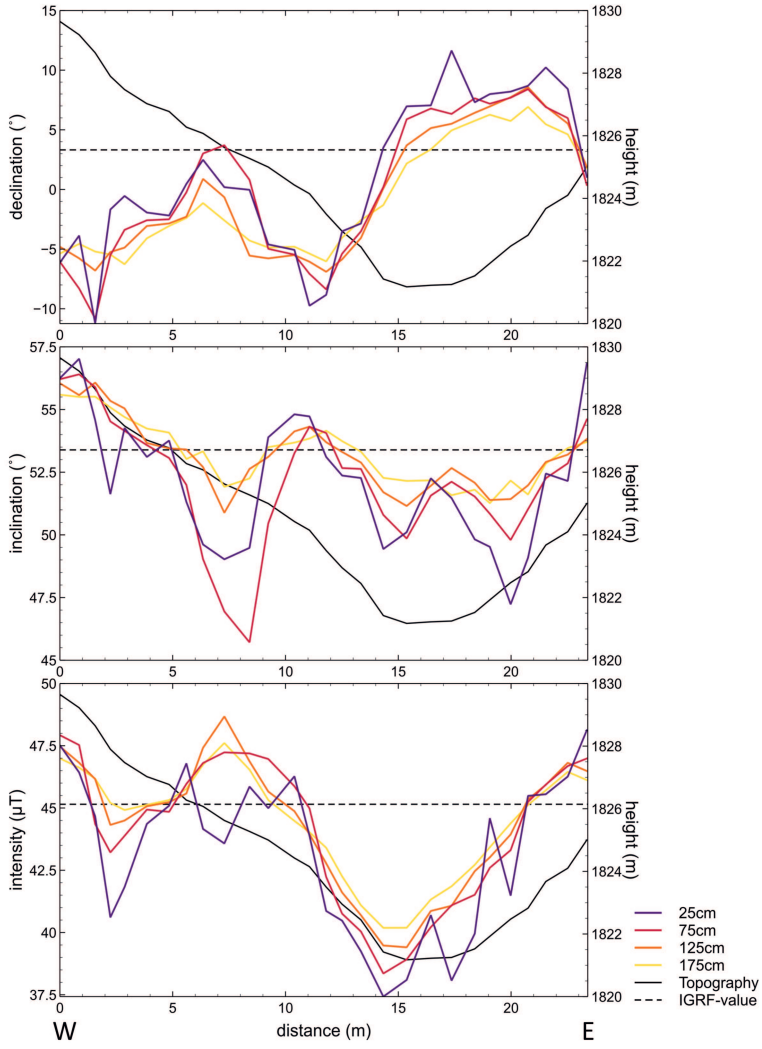
Supplementary Figure 1.13: FLUX4 path 3



Supplementary Figure 1.14: FLUX5 path 1



Supplementary Figure 1.15: FLUX5 path 2



Supplementary Figure 1.16: FLUX5 path 3

Supplementary Table 1.1: Declination and inclination results of previous studies. For each site, the age of the flow is given and if known the GPS location, elevation (Elv) number of samples (N), declination (°), inclination (°), precision parameter (k), 95 percent confidence interval $\alpha 95$, method used (thermal or alternating field demagnetization, Th/AF). All used a sun compass for orientation in the field.

Paper	Age	Lat (N)	Long (E)	Elv (m)	N	Dec (°)	Inc (°)	k	a95	Th/Af
Tanguy et al. 1985, 1999	1910				11	-6.9	50.7	760	1.5	AF
Tanguy et al. 1985, 1999	1865				18	-9.5	51.9	583	1.4	AF
Rolph et al. 1986, 1987	1853				5	-9.8	55.7		2.5	AF
Rolph et al. 1986, 1987	1865				5	-12.5	52		3.5	AF
Rolph et al. 1986, 1987	1886				5	-9	49.8		0.9	AF
Rolph et al. 1986, 1987	1892				5	-6.2	50.5		4.3	AF
Rolph et al. 1986, 1987	1910				5	-4.2	50.7		2.5	AF
Rolph et al. 1986, 1987	1911				5	0.7	52.3		3.8	AF
Rolph et al. 1986, 1987	1923				5	-2.8	50.9		3.2	AF
Rolph et al. 1986, 1987	1947				5	0.2	49.8		3.4	AF
Rolph et al. 1986, 1987	1950				5	-1	49.3		3.5	AF
Rolph et al. 1986, 1987	1971				5	-4.1	51.1		3.5	AF
Rolph et al. 1986, 1987	1979				5	1.9	48		3.2	AF
Rolph et al. 1986, 1987	1981				5	-0.2	45.6		2.6	AF
Rolph et al. 1997	1971	37.747	15.099	1015	19	-0.2	51.1	163.7	2.6	AF
Calvo et al. 2002	1910	37.648	14.992	1034	9	-1.6	50.1	36.7	8.6	AF
Calvo et al. 2002	1910	37.648	14.992	1034	9	5.2	49.5	19	12.1	AF
Calvo et al. 2002	1910	37.648	14.992	1034	22	-7.2	49.2	80.1	3.5	AF
Calvo et al. 2002	1928	37.763	15.124	852	22	0.4	49.7	157.1	2.5	AF
Calvo et al. 2002	1928	37.763	15.124	852	51	1.7	49.2	49.9	2.9	AF
Calvo et al. 2002	1928	37.762	15.164	852	35	-2.5	50.6	436	1.2	AF
Incoronato et al. 2002	1886	37.62	15.01	906	10	-11.5	51.7	467.9	2.2	Th
Incoronato et al. 2002	1910	37.63	15.00	890	7	-8.1	51.6	481.6	2.8	Th
Incoronato et al. 2002	1983	37.67	14.99	1296	10	-1.1	49	594.6	2.5	Th
Tanguy et al. 2003	1910				10	-7.5	51.3	1070	1.35	AF
Tanguy et al. 2003	1865				14	-10	51.5	824	1.3	AF

Supplementary Table 1.2: Intensity results of previous studies. If known the following parameters are given: the site, age of the flow, GPS location, elevation (Elv) distance to the top (Top) and bottom (Base) of the flow, number of samples (N), paleointensity measured (PI), standard deviation (s.d.), method used. CONV: conventional Coe-modified Thellier protocol, AFD: identical as CONV but with a single AF demagnetisation treatment to a peak field of 5mT, QP: quasi-perpendicular single-heating approach.

Paper	Site	Age	Lat (N)	Long (E)	Elv (m)	Top	Base	N	PI (μT)	s.d.	Method
Rolph et al. 1986, 1987		1853						5	47.7	4.4	Shaw
Rolph et al. 1986, 1987		1879						5	41.3	1.8	Shaw
Rolph et al. 1986, 1987		1886						5	43	2.9	Shaw
Rolph et al. 1986, 1987		1923						5	48.2	5.8	Shaw
Rolph et al. 1986, 1987		1928						5	44.0	11.6	Shaw
Rolph et al. 1986, 1987		1942						5	45.4	5.5	Shaw
Rolph et al. 1986, 1987		1947						5	38.5	5.7	Shaw
Rolph et al. 1986, 1987		1949						5	40.1	1.5	Shaw
Rolph et al. 1986, 1987		1950						5	42.6	3.8	Shaw
Rolph et al. 1986, 1987		1964						5	39.4	1.6	Shaw
Rolph et al. 1986, 1987		1974						5	40.2	4.3	Shaw
Rolph et al. 1986, 1987		1981						5	43.5	2.5	Shaw
Rolph et al. 1986, 1987		1983						5	41.9	2.4	Shaw
Rolph et al. 1997		1971	37.747	15.099	1015			19	39.2	9	Shaw
Sherwood, 1991		1879						10	37.3	5.3	MSP
Sherwood, 1991		1886						10	46.9	0.9	MSP
Sherwood, 1991		1911						10	44.0	0.9	MSP
Sherwood, 1991		1928						10	39.2	0.3	MSP
Sherwood, 1991		1983						10	40.6	1.6	MSP
Hill and Shaw, 1999	1853-1	1853						3	32.0	3.4	Microwave
Hill and Shaw, 1999	1886-5	1886						2	34.0	4.3	Microwave
Hill and Shaw, 1999	1892-5	1892						3	36.2	3.1	Microwave
Hill and Shaw, 1999	1911-3	1911						2	37	4.5	Microwave
Hill and Shaw, 1999	1911-7	1911						3	40.5	0.6	Microwave
Hill and Shaw, 1999	1923-4	1923						2	28.7	4.4	Microwave
Hill and Shaw, 1999	1923-8	1923						3	47.3	0.6	Microwave
Hill and Shaw, 1999	1947-1	1947						3	43.2	0.7	Microwave
Hill and Shaw, 1999	1947-3	1947						2	47.6	4.8	Microwave
Hill and Shaw, 1999	1950-11	1950						2	30.7	1.2	Microwave
Hill and Shaw, 1999	1950-12	1950						3	37.6	3.5	Microwave
Hill and Shaw, 1999	1971-9	1971						2	39.8	10.6	Microwave
Hill and Shaw, 1999	1983-10	1983						3	69.1	2.8	Microwave
Hill and Shaw, 1999	1983-2	1983						2	31.2	9.3	Microwave

Paper	Site	Age	Lat (N)	Long (E)	Elv (m)	Top	Base	N	PI (μT)	s.d.	Method
Calvo et al. 2002		1928	37.763	15.124	852			6	52.1	6.7	Thellier
Biggin et al. 2007		1979						2	40.9	5.5	CONV
Biggin et al. 2007		1950						1	55.1	-	CONV
Biggin et al. 2007		1983						7	40.8	14.46	AFD
Biggin et al. 2007		1979						5	40.5	2.53	AFD
Biggin et al. 2007		1950						2	42.5	1.55	AFD
Biggin et al. 2007		1983						22	40.4	7.19	QP
Biggin et al. 2007		1979						19	37.2	4.41	QP
Biggin et al. 2007		1950						9	39.1	8.56	QP
De Groot et al. 2012	23-2	1923	37.854	15.114	640			5	29.5	25.2-33.2	MSP-DB
De Groot et al. 2012	23-2	1923	37.854	15.114	640			5	24.3	9.8-32.2	MSP-DSC
De Groot et al. 2012	71-3C	1971	37.753	15.087	1193			15	31.2	28.2-34.1	MSP-DB
De Groot et al. 2012	71-3C	1971	37.753	15.087	1193			15	25.8	22.4-29.0	MSP-DSC
De Groot et al. 2012	79-1	1979	37.741	15.099	970			18	32.4	30.3-34.5	MSP-DB
De Groot et al. 2012	79-1	1979	37.741	15.099	970			5	30.6	12.9-40.5	MSP-DSC
De Groot et al. 2012	83-4A	1983	37.695	14.991	1832			16	34.3	26.5-44.2	MSP-DB
De Groot et al. 2012	83-4A	1983	37.695	14.991	1832			16	28.5	21.0-36.4	MSP-DSC
De Groot et al. 2013	23-1A	1923	37.845	15.018	1115	0.25	1.35	7	28.3	2.4	Thellier
De Groot et al. 2013	23-1B	1923	37.845	15.018	1115	0.93	0.68	15	30.3	26.3-33.7	MSP-DB
De Groot et al. 2013	23-1B	1923	37.845	15.018	1115	0.93	0.68	5	26.0	20.6-30.3	MSP-DSC
De Groot et al. 2013	23-1C	1923	37.845	15.018	1115	1.5	0.2	6	27.2	3	Thellier
De Groot et al. 2013	23-1C	1923	37.845	15.018	1115	1.5	0.2	11	33.4	24.8-41	MSP-DB(air)
De Groot et al. 2013	23-1C	1923	37.845	15.018	1115	1.5	0.2	11	36.9	29.7-44.6	MSP-DB(argon)
De Groot et al. 2013	23-2	1923	37.854	15.114	640	0.95	0.65	8	45.9	6.9	Thellier
De Groot et al. 2013	71-1	1971	37.752	15.087	1186	0.5	1.2	8	32.3	4.3	Thellier
De Groot et al. 2013	71-1	1971	37.752	15.087	1186	0.5	1.2	23	32.7	30-35.1	MSP-DB
De Groot et al. 2013	71-1	1971	37.752	15.087	1186	0.5	1.2	18	28.3	23.9-31.9	MSP-DB 160°C
De Groot et al. 2013	71-1	1971	37.752	15.087	1186	0.5	1.2	5	28.8	1.5-40.5	MSP-DSC
De Groot et al. 2013	71-2A	1971	37.748	15.099	1015	0.33	1.22	8	38.8	5.2	Thellier
De Groot et al. 2013	71-2A	1971	37.748	15.099	1015	0.33	1.22	18	29.8	26.7-32.6	MSP-DB
De Groot et al. 2013	71-2A	1971	37.748	15.099	1015	0.33	1.22	5	24.9	19.6-28.9	MSP-DSC

Paper	Site	Age	Lat (N)	Long (E)	Elv (m)	Top	Base	N	PI (μT)	s.d.	Method
De Groot et al. 2013	71-2B	1971	37.748	15.099	1015	0.8	0.72	8	37.7	3.9	Thellier
De Groot et al. 2013	71-2B	1971	37.748	15.099	1015	0.8	0.72	10	35.3	30.8-40.2	MSP-DB
De Groot et al. 2013	71-2B	1971	37.748	15.099	1015	0.8	0.72	12	38.0	31.2-45	MSP-DB(argon)
De Groot et al. 2013	71-2C	1971	37.748	15.099	1015	1.25	0.09	9	35.4	3	Thellier
De Groot et al. 2013	71-3A	1971	37.753	15.087	1193	0.95	0.1	9	29.2	3	Thellier
De Groot et al. 2013	71-3B	1971	37.753	15.087	1193	0.5	0.55	8	34.0	3.5	Thellier
De Groot et al. 2013	71-3C	1971	37.753	15.087	1193	0.15	0.55	9	24.1	2.1	Thellier
De Groot et al. 2013	71-3C	1971	37.753	15.087	1193	0.15	0.55	20	29.2	27.2-31.2	MSP-DB
De Groot et al. 2013	79-1A	1979	37.741	15.099	970	0.15	1.4	6	17.5	1.7	Thellier
De Groot et al. 2013	79-1B	1979	37.741	15.099	970	0.75	0.75	8	30.0	2.4	Thellier
De Groot et al. 2013	79-1C	1979	37.741	15.099	970	1.4	0.1	9	33.2	2.8	Thellier
De Groot et al. 2013	83-1B	1983	37.676	14.982	1472	0.45	1.35	15	27	24.2-31.5	MSP-fast
De Groot et al. 2013	83-1B	1983	37.676	14.982	1472	0.45	1.35	7	25.4	15.9-31.8	MSP-slow
De Groot et al. 2013	83-1C	1983	37.676	14.982	1472	0.9	0.9	9	29.1	27.1-31.5	MSP-fast
De Groot et al. 2013	83-1C	1983	37.676	14.982	1472	0.9	0.9	7	25.4	15.9-31.8	MSP-slow
De Groot et al. 2013	83-1D	1983	37.676	14.982	1472	1.33	0.47	15	29.1	26.4-32	MSP-fast
De Groot et al. 2013	83-1D	1983	37.676	14.982	1472	1.33	0.47	9	25.6	13.5-32.6	MSP-slow
De Groot et al. 2013	83-1E	1983	37.676	14.982	1472	1.68	0.12	15	24.4	22-26.8	MSP-fast
De Groot et al. 2013	83-1E	1983	37.676	14.982	1472	1.68	0.12	7	18.5	0.9-27.4	MSP-slow
De Groot et al, 2013	83-2	1983	37.676	14.982	1472			9	28.3	4.7	Thellier
De Groot et al, 2013	83-3	1983	37.845	15.081	864			7	35.3	8.3	Thellier
De Groot et al, 2013	83-3	1983	37.845	15.081	864			23	35.0	30.6-37.4	MSP-DB
De Groot et al, 2013	83-3	1983	37.845	15.081	864			18	27.9	24.4-31	MSP-DB
De Groot et al, 2013	83-3	1983	37.845	15.081	864			5	25.2	0-42.2	MSP-DSC

Paper	Site	Age	Lat (N)	Long (E)	Elv (m)	Top	Base	N	PI (μT)	s.d.	Method
De Groot et al, 2013	83-4A	1983	37.695	14.991	1832	1.6	0.15	7	25.6	5.3	Thellier
De Groot et al, 2013	83-4A	1983	37.695	14.991	1832	1.6	0.15	20	25.7	18.4-32.5	MSP-DB
De Groot et al, 2013	83-4B	1983	37.695	14.991	1832	1.1	0.95	7	27.0	7.7	Thellier
De Groot et al, 2013	83-4B	1983	37.695	14.991	1832	1.1	0.95	12	30.8	26.3-35	MSP-DB
De Groot et al, 2013	83-4C	1983	37.695	14.991	1832	0.28	1.2	6	15.3	1.8	Thellier
De Groot et al, 2013	83-5	1983	37.695	14.991	1832	0.26	0.25	6	15.5	2.4	Thellier
De Groot et al, 2013	83-6	1983	37.688	14.987	1667	0.9	-	6	15.5	2.4	Thellier
De Groot et al, 2013	83-6	1983	37.688	14.987	1667	0.9	-	15	30.6	26.3-34.3	MSP-DB
De Groot et al, 2013	83-6	1983	37.688	14.987	1667	0.9		5	20.2	0-36	MSP-DSC
De Groot et al, 2013	02-1C	2002	37.796	15.062	1541	1.8	0.2	7	42.8	5.3	Thellier
De Groot et al, 2013	02-1C	2002	37.796	15.062	1541	1.8	0.2	5	27.2	0-43.9	MSP-DB
De Groot et al, 2013	02-1C	2002	37.796	15.062	1541	1.8	0.2	5	24.5	0-37.9	MSP-DSC
De Groot et al, 2013	02-2	2002	37.795	15.057	1603	1.3	-	8	31.0	3.7	Thellier
De Groot et al, 2013	02-2	2002	37.795	15.057	1603	1.3	-	10	29.8	23.8-34.7	MSP-DB
De Groot et al, 2013	02-2	2002	37.795	15.057	1603	1.3	-	5	26.8	18.7-32.7	MSP-DSC

Supplementary Table 1.3: Details of AnomalyMapper measurements. For each FLUX-site (Site), the age of the flow (Age) and the corresponding paleomagnetic sampling site (Pmag site) and paths (Path) are given. For each path its length (Length), the lowest and highest point in the path (Topography), the heights above the ground at which measurements were made (Heights), and the total number of measurements (N measurements) are specified.

Site	Age	Pmag site	Path	Length (m)	Topography (m)	Heights (cm)	N measurements
FLUX1	1892	-	1	65	1620-1627	100 & 180	78
			2	54	1618-1624	100 & 180	54
			3	60	1615-1619	100 & 180	72
FLUX2	1983	ET12	1	69	1825-1830	100 & 180	60
			2	68	1830-1834	100 & 180	78
			3	64	1836-1841	100 & 180	84
FLUX3	1923	ET6	1	53	876-886	100 & 180	78
			2	58	857-865	100 & 180	110
			3	49	852-862	100 & 180	80
FLUX4	2002	ET4	1	56	1510-1523	100 & 180	76
			2	69	1537-1548	100 & 180	112
			3	71	1550-1556	100 & 180	108
FLUX5	1983	ET12	1	22	1824-1829	25, 75, 125 & 175	112
			2	26	1822-1830	25, 75, 125 & 175	120
			3	23	1821-1830	25, 75, 125 & 175	112

Supplementary Table 1.4: AnomalyMapper measurements. Median declination (°), inclination (°) and intensity (μT) with the standard deviation per site at 100 and 180cm above the surface.

Site	Path	dec 100	dec 180	inc 100	inc 180	int 100	int 180
FLUX1	Path 1	0.03 ± 2.37	0.34 ± 1.76	53.08 ± 1.66	53.44 ± 1.38	44.62 ± 1.62	44.68 ± 1.09
	Path 2	0.76 ± 1.74	1.95 ± 1.33	54.43 ± 1.96	54.00 ± 1.53	44.56 ± 1.68	44.44 ± 1.23
	Path 3	0.83 ± 2.23	1.80 ± 1.68	54.49 ± 1.34	54.88 ± 1.05	45.28 ± 1.32	45.29 ± 0.93
FLUX2	Path 1	0.87 ± 3.96	-0.33 ± 2.61	53.27 ± 1.73	52.59 ± 1.19	44.24 ± 1.54	44.43 ± 1.02
	Path 2	1.58 ± 3.75	0.37 ± 2.23	52.82 ± 1.39	52.25 ± 0.80	43.64 ± 1.37	43.70 ± 0.99
	Path 3	0.33 ± 3.76	0.11 ± 2.46	52.39 ± 1.89	52.30 ± 1.29	44.25 ± 1.83	44.57 ± 1.33
FLUX3	Path 1	-0.87 ± 2.30	-2.69 ± 2.18	53.84 ± 1.79	53.82 ± 1.14	44.25 ± 1.22	44.21 ± 0.80
	Path 2	0.13 ± 3.41	-1.70 ± 2.66	52.06 ± 2.56	52.80 ± 1.81	44.34 ± 1.28	44.25 ± 0.99
	Path 3	-1.45 ± 3.39	-2.61 ± 2.66	52.70 ± 2.44	53.04 ± 1.79	44.59 ± 1.39	45.04 ± 1.04
FLUX4	Path 1	0.39 ± 4.92	-0.49 ± 1.13	53.38 ± 2.22	53.47 ± 1.91	43.20 ± 1.66	43.02 ± 1.25
	Path 2	-1.85 ± 5.96	-1.55 ± 1.51	51.37 ± 2.76	51.96 ± 2.07	42.98 ± 2.51	42.87 ± 1.89
	Path 3	-1.21 ± 2.69	-3.13 ± 1.85	52.38 ± 3.35	52.79 ± 2.39	43.68 ± 2.46	44.03 ± 1.90

Supplementary Table 1.5: AnomalyMapper measurements of FLUX5. Median declination (°), inclination (°) and intensity (μT) with the standard deviation per path at 25, 75, 125 and 175cm above the surface.

Path		Dec 25	Dec 75	Dec 125	Dec 175	Inc 25	Inc 75	Inc 125	Inc 175	Int 25	Int 75	Int 125	Int 175
Path 1	Median	3.01	1.75	2.39	1.32	51.09	51.62	52.14	52.16	43.26	43.28	43.61	43.77
	S.d.	5.22	4.36	3.55	2.96	2.43	1.61	1.33	1.23	2.74	1.99	1.43	1.15
Path 2	Median	0.52	0.37	0.94	-0.94	52.03	52.15	52.77	53.34	43.54	43.41	43.26	43.29
	S.d.	6.00	5.51	4.64	4.47	3.96	2.68	2.06	1.90	2.93	2.13	1.90	1.71
Path 3	Median	0.08	-0.02	-2.57	-2.59	52.26	52.44	53.16	53.40	44.26	44.89	44.97	45.13
	S.d.	6.39	5.97	5.35	4.57	2.55	2.55	1.45	1.27	3.10	2.82	2.53	2.12

Supplementary Table 1.6: Difference of the median with the IGRF-value for AnomalyMapper measurement sites FLUX1-4 and their different paths. $\tilde{\Delta}$ declination (°), inclination (°) and intensity (μT) at 100 and 180cm above the surface.

Site	Path	$\tilde{\Delta}$dec 100	$\tilde{\Delta}$dec 180	$\tilde{\Delta}$inc 100	$\tilde{\Delta}$inc 180	$\tilde{\Delta}$int 100	$\tilde{\Delta}$int 180
FLUX1	Path 1	-3.30	-2.98	-0.30	0.06	-0.53	-0.47
	Path 2	-2.56	-1.37	1.04	0.62	-0.59	-0.72
	Path 3	-2.49	-1.52	1.10	1.50	0.13	0.14
FLUX2	Path 1	-2.45	-3.65	-0.12	-0.80	-0.91	-0.72
	Path 2	-1.74	-2.94	-0.57	-1.14	-1.51	-1.45
	Path 3	-2.98	-3.20	-1.00	-1.09	-0.90	-0.58
FLUX3	Path 1	-4.21	-6.03	0.25	0.22	-0.99	-1.03
	Path 2	-3.21	-5.05	-1.54	-0.79	-0.89	-0.99
	Path 3	-4.79	-5.95	-0.89	-0.55	-0.65	-0.20
FLUX4	Path 1	-2.95	-3.83	-0.15	-0.05	-2.00	-2.18
	Path 2	-5.19	-4.88	-2.15	-1.57	-2.22	-2.33
	Path 3	-4.54	-6.46	-1.15	-0.73	-1.52	-1.17

Supplementary Table 1.7: Difference of the median with the IGRF-value for AnomalyMapper measurement site FLUX5. Given are the Δ declination, inclination and intensity for each path (dec1 is the declination difference for path 1) at four heights above the surface.

Height	$\tilde{\Delta}$dec 1	$\tilde{\Delta}$dec 2	$\tilde{\Delta}$dec 3	$\tilde{\Delta}$inc 1	$\tilde{\Delta}$inc 2	$\tilde{\Delta}$inc 3	$\tilde{\Delta}$int 1	$\tilde{\Delta}$int 2	$\tilde{\Delta}$int 3
25cm	-0.30	-2.79	-3.24	-2.30	-1.36	-1.13	-1.88	-1.61	-0.89
75cm	-1.57	-2.95	-3.33	-1.77	-1.24	-0.95	-1.87	-1.74	-0.26
125cm	-0.92	-2.37	-5.88	-1.25	-0.61	-0.23	-1.54	-1.89	-0.18
175cm	-2.00	-4.25	-5.90	-1.23	-0.05	0.01	-1.38	-1.86	-0.02

Supplementary Table 1.8: Pearson's correlation coefficient for the fluxgate measurements. Given are the inclination, declination and intensity (Inc, Dec, Int) at 100 and 180cm height above the surface for FLUX1-4 and at 25, 75, 125 and 175cm above the surface for FLUX5.

FLUX 1	Dec100	Inc100	Int100	Dec180	Inc180	Int180
Path1	-0.1023	0.6705	0.5546	-0.1301	0.8062	0.5825
Path2	-0.3833	0.6333	0.7416	0.0223	0.1229	0.8780
Path3	0.2472	0.2807	0.4483	0.3709	0.2484	0.5161
FLUX 2	Dec100	Inc100	Int100	Dec180	Inc180	Int180
Path1	0.3859	0.6942	0.4446	0.3986	0.7188	0.5166
Path2	-0.0601	0.7551	0.4406	-0.0416	0.8108	0.5625
Path3	-0.1797	0.3319	0.6179	-0.2443	0.2713	0.7660
FLUX 3	Dec100	Inc100	Int100	Dec180	Inc180	Int180
Path1	-0.1015	0.6052	0.5387	-0.1609	0.7671	0.7582
Path2	0.0362	0.7405	0.2956	0.0552	0.8747	0.4281
Path3	0.3422	0.6424	-0.0150	0.3512	0.6373	-0.0860
FLUX 4	Dec100	Inc100	Int100	Dec180	Inc180	Int180
Path1	0.1069	0.5553	0.5530	-0.4833	0.5412	0.6129
Path2	0.8004	0.0810	-0.6172	0.6925	0.1697	-0.6295
Path3	-0.2765	0.5733	0.2586	-0.5143	0.7197	0.0316
FLUX 5	Dec25	Inc25	Int25	Dec75	Inc75	Int75
Path1	-0.0567	0.7111	0.4885	-0.0108	0.8559	0.6259
Path2	-0.4028	0.8333	0.4604	-0.3791	0.9335	0.7663
Path3	-0.6067	0.5623	0.5939	-0.6385	0.4592	0.6857
FLUX 5	Dec125	Inc125	Int125	Dec175	Inc175	Int175
Path1	-0.0324	0.9356	0.6673	-0.0477	0.8601	0.6980
Path2	-0.4008	0.9646	0.8423	-0.5063	0.9633	0.8572
Path3	-0.6193	0.7923	0.7276	-0.6606	0.8252	0.7672

Supplementary Table 1.9: NRM of the samples interpreted in this study. A and B samples are from the same paleomagnetic core and measured with alternating field demagnetization experiments. Samples noted with X- are demagnetized thermally.

Sample	NRM(μA/m)	Sample	NRM(μA/m)	Sample	NRM(μA/m)	Sample	NRM(μA/m)
ET1-1A	3092908	ET4-2B	3257553	ET8-2A	8462077	ET15-1A	3509292
ET1-1B	2930121	ET4-3A	3443849	ET8-2B	7299002	ET15-1B	3199333
ET1-2A	13511401	ET4-3B	3702208	ET8-3A	7608797	ET15-2A	9535772
ET1-3A	6828289	ET4-4A	4120059	ET8-3B	6624950	ET15-2B	7462288
ET1-3B	5894238	ET4-4B	4772933	ET8-4A	5041369	ET15-3A	8014720
ET1-4A	3409072	ET5-1A	5244755	ET8-4B	4963602	ET15-3B	5679607
ET1-4B	8243283	ET5-1B	5631377	ET10-1A	2873601	ET15-4A	2925096
ET1-5A	5435003	ET5-2A	3886582	ET10-1B	2457480	ET15-4B	2770129
ET1-5B	7029630	ET5-2B	3871541	ET10-2A	5285084	ET15-5A	4523973
ET1-6A	5156109	ET5-3A	4910945	ET10-2B	4662239	ET15-5B	4907541
ET1-6B	4845787	ET5-3B	4490898	ET10-3A	3239964	ET1-X7	4827813
ET2-1A	2708659	ET5-4A	3794956	ET10-3B	4424104	ET1-X8	6970862
ET2-1B	1713699	ET5-4B	4440607	ET10-4A	2875667	ET1-X10	5203466
ET2-2A	2026065	ET5-5A	4526611	ET10-4B	2574870	ET2-X4	5692232
ET2-2B	1053086	ET5-5B	4683804	ET10-5A	3255704	ET3-X6	3479066
ET2-3A	2892208	ET5-6A	1761023	ET10-5B	3310312	ET3-X12	5323614
ET2-3B	2695999	ET5-6B	2672738	ET10-6A	4416003	ET4-X1	3763388
ET2-4A	1225170	ET5-7A	5189950	ET10-6B	4734828	ET4-X2	3535889
ET2-4B	1294795	ET5-7B	4769996	ET10-7A	3551614	ET4-X7	5939519
ET2-5A	2872171	ET5-8A	2420816	ET10-7B	3593348	ET5-X1	5293338
ET2-5B	3113476	ET5-8B	1957681	ET10-8A	5404135	ET5-X2	3647215
ET3-1A	1281908	ET6-1A	3551925	ET10-8B	4954208	ET5-X6	3645919
ET3-1B	1184509	ET6-1B	3149407	ET11-1A	4475224	ET5-X7	4392351
ET3-2A	1684043	ET6-2A	2695712	ET11-1B	4895059	ET6-X6	5456887
ET3-2B	1532256	ET6-2B	3036555	ET11-1C	5170786	ET7-X1	2622103
ET3-3A	1984353	ET6-3A	6018155	ET11-2A	3757785	ET7-X7	4162528
ET3-3B	1789187	ET6-3B	5240134	ET11-2B	4255364	ET7-X8	2588562
ET3-4A	2162886	ET6-4A	3165071	ET11-3A	4362736	ET8-X2	3611097
ET3-4B	2106486	ET6-4B	3095686	ET11-3B	3927018	ET10-X1	4054887
ET3-5A	1474009	ET7-1A	5012518	ET11-3C	3694101	ET10-X2	3920099
ET3-5B	1538818	ET7-1B	4160444	ET12-1A	3617137	ET10-X7	4423374
ET3-6A	948775	ET7-2A	6804917	ET12-1B	3168212	ET10-X8	4626168
ET3-6B	1029318	ET7-2B	5880862	ET12-2A	9687689	ET11-X1	3383326
ET3-7A	1099807	ET7-3A	5840308	ET12-2B	10577655	ET11-X9	5257113
ET3-7B	1420304	ET7-3B	3303745	ET12-3A	4731036	ET11-X7	4314440
ET3-8A	761847	ET7-4A	5809016	ET12-3B	4129426	ET11-X8	6798544
ET3-8B	758202	ET7-4B	5031405	ET12-4A	7348584	ET12-X7	4221618
ET3-9A	1316996	ET7-5	5229006	ET12-4B	7084175	ET12-X8	4323160
ET3-9B	1336292	ET7-6A	3712982	ET12-5A	8376841	ET15-X5	5067583
ET4-1A	2518621	ET7-6B	3897407	ET12-5B	7605274	ET15-X6	2358392
ET4-1B	2571713	ET8-1A	2928274	ET12-6A	3667464		
ET4-2A	2909900	ET8-1B	5154923	ET12-6B	3431768		


HOZELOCK

2

Effect of storage conditions on paleointensity results from very young volcanics, the 2021 Tajogaite eruption, La Palma

Romy Meyer, Rosa. A. de Boer and Lennart V. de Groot

Abstract *Our knowledge of Earth's past magnetic field strength relies primarily on paleointensity experiments. These experiments are, despite recent methodological advances, notorious for their high failure rates. In this study, we assess whether the very young lava flow from the 2021 Tajogaite eruption accurately records the Earth's magnetic field and whether its magnetic signal changes over time. At the time of sampling, the samples were at most 3.5 weeks old. Five batches of samples for intensity measurements were prepared, the first was measured immediately in 2021, the four others were stored either randomly oriented in the Earth's magnetic field or in a zero-field environment. Additionally, samples were obtained from the inside and outside of the flow. The stored batches were measured in 2024 and 2025, and their results were compared with newly collected samples from a field campaign in 2025. There are small differences in paleointensity results and success rates between batches, suggesting subtle viscous changes in remanence over time. Overall, there seems to be a tendency for samples stored out-field to perform better, and exterior flow samples yield more reliable results than interior ones.*

2.1. Introduction

Understanding variations in the Earth's magnetic field strength over time has long been a central topic in paleomagnetism. The methods for recovering absolute paleointensities from archaeological materials, and later volcanic rocks, were developed since the 1930s (Thellier, 1938, 1959). However, these paleointensity experiments such as the Thellier-Thellier method are time consuming and notorious for their high failure rates (e.g. L. V. de Groot et al. (2013) and Kosterov and Prévot (1998)). During a Thellier experiment the initial remanence (NRM) is replaced in several heating steps with a partial thermal remanence (pTRM) in a known laboratory field. The method relies on the assumption that a magnetization blocked at a certain temperature can be unblocked by reheating to the same temperature in a zero magnetic field. The Thellier method is based on three fundamental laws, Additivity, Reciprocity and Independence of partial thermoremanent magnetization (see Tauxe (2010)). Additivity states that the total TRM is the sum of pTRMs acquired over smaller temperature intervals; Reciprocity is that the blocking temperature equals the unblocking temperature; and Independence that a pTRM gained in one temperature interval is independent by those acquired in other intervals. These laws were proven by Néel to be valid for single domain (SD) grains (Néel, 1949).

There are several reasons why these laws are often violated, and Thellier-method often fails. The first is that the material often does not contain purely SD sized grains, but is a combination of multiple grain sizes. Especially the presence of the larger multi domain (MD) grains can cause Thellier's laws to fail, by introducing differences between blocking and unblocking temperatures. Whereas SD grains normally produce linear Arai plots, MD grains often yield curved, sagging, or zigzagged Arai plots (Dunlop et al., 2005). Another issue with the heating experiments is thermally induced alteration at increasingly higher temperature steps, leading to irreversible changes in a sample's capacity to acquire a remanence (Coe, 1967). Third, for low ancient fields there may be a non-linear relationship of the TRM to the field

in which the remanence was acquired (Selkin et al., 2007). Another factor which was proposed to influence the experiments was differences between laboratory and natural cooling rates (Biggin et al., 2007; Yu, 2011). Finally, paleointensity methods are based on the assumption that when a rock obtained a magnetization in an ancient field, this magnetization is stable and will not change over time. However, this assumption has been challenged (Koenigsberger, 1938), as the original magnetization may be altered by residing in a magnetic field for long periods of time, a process known as viscous (re)magnetization (Dunlop & Özdemir, 1997; Tauxe, 2010). A low temperature viscous remanent magnetization (VRM) in magnetites is usually easily removed (Dunlop & Özdemir, 1997). But in case the VRM is larger than the NRM, it may affect the original record of the geomagnetic field in the material (Yu & Tauxe, 2006).

Time dependent magnetization changes in volcanic rocks have been recently studied by L. V. de Groot et al. (2014a) and Tauxe et al. (2021) and Fabian (2024). L. V. de Groot et al. (2014a) and Fabian (2024) introduced a special form of a viscous remanent magnetization. They observed metastable domain states which evolved into more stable lower energy configurations. This process was described as a trapdoor viscous remanent magnetization (tdVRM), leading to unstable TRM behaviour and therefore violation of the Thellier method laws. Tauxe et al. (2021) focused on the curvature of Arai plots. They performed aging experiments on samples, and observed that initially straight Arai plots developed an increased curvature after being stored in a laboratory field for two years, an effect named fragile curvature (Santos & Tauxe, 2019; Sbarbori et al., 2009; Shaar & Tauxe, 2015; Tauxe et al., 2021). This could be related to the relaxation from a local energy minimum to a stable state with higher unblocking temperatures, violating Thellier's law of Reciprocity (Tauxe et al., 2021).

In this study, we test how well the intensity signal is initially recorded by volcanic rocks and whether it changes after being stored for several years, both in an ambient magnetic field and under zero-field conditions. These aging experiments are performed on very young lava rocks collected specifically for this purpose during the 2021 volcanic eruption on La Palma, Spain. A study by Calvo-Rathert et al. (2024) obtained samples from the same 2021 La Palma lava flow in September 2022 (Calvo-Rathert et al., 2024). Unexpectedly, many of these samples showed a strong viscous overprint. While the mean paleomagnetic directions were close to the expected field value, their paleointensity experiments yielded a low success rate, although the accepted measurements agreed with the expected value according to the International Geomagnetic Reference Field (IGRF, (Alken et al., 2021)). The samples of the 2021 La Palma lava flow used in our study were no more than 3.5 weeks old at the time of sampling. Therefore, they are ideal for testing whether the intensity signal is initially well-stored but alters over time, potentially leading to unsuccessful Thellier-style measurements, such as observed by Calvo-Rathert et al. (2024). From the samples obtained in 2021, five intensity batches were made. The first one was measured immediately upon returning from the field. The other batches were stored at paleomagnetic laboratory Fort Hoofddijk, Utrecht. Two of them were stored in random orientations in the Earth's magnetic field, and two

were stored in a field-free environment. From each of them, one batch was measured in 2024 and the other in 2025. The results from these batches are compared with samples obtained during a new fieldwork in 2025 and thus were aligned with the ambient magnetic field for more than three years.

2.2. Geological setting and sampling strategy

La Palma (28.7°N, 17.8°W) is one of the Canary Islands, a volcanic archipelago consisting of seven islands off the coast of North West Africa. The classic model of formation of the archipelago is that of a mantle plume (Negredo et al., 2022) which started around 68 Ma ago (Troll & Carracedo, 2016). As the African plate moves to the east this leaves a chain of volcanoes where the age of the volcanoes decreases from east to west. La Palma is one of the the youngest islands of the archipelago (2 Ma), together with El Hierro (1.1 Ma) (Carracedo et al., 1999). The northern part of the island consists of the older Caldera de Taburiente and the southern part is formed by a volcanic ridge named the Cumbre Vieja. The ridge formed from around 125 ka ago (Carracedo et al., 1999) and most recent volcanic activity is centred here. Before the eruption of 2021, there were six historic eruptions of which the most recent lava flow is from 1971 CE. The eruption of 2021, named the Tajogaite eruption, started on 19th September 2021 and finished on the 13th of December that year. Its 85 days makes it the longest eruption in the recorded history of the island (Dayton et al., 2023).

2.2.1. Sampling strategy

This study consists of two different sampling campaigns to the 2021 lava flow. The first sampling campaign was during the eruption, from 28 to 30 October 2021, when three sites were sampled (LP1, LP2 and LP3). The second sampling campaign was done in February 2025. During this fieldwork, LP1 and LP2 were resampled (LP1-2025, LP2-2025). The location of LP3 was no longer accessible because new lava covered the outcrop in the last phase of the eruption. Instead, an additional three sites (LP4, LP5 and LP6) were sampled at different locations (Fig. 2.1, Table 2.1). The lava at LP1 and LP3 formed between 11-17 October 2021, the lava at LP2 between 4-10 October, at LP4 between 18-24 October, at LP5 between 22-28 November and lastly LP6 between 1-7 November 2021 (map Emergency Response Coordination Centre ERCC). During the first field campaign, the sampled rocks were a maximum of 3.5 weeks old and because the eruption was still ongoing, only the top of the edges of the flow were accessible. During the second field campaign in 2025, access to the top of the flow was restricted and samples were obtained from road cuts.

At each sampling site, between 10 to 20 paleomagnetic samples (up to 25mm in diameter and 10cm in length) were taken with a water-cooled petrol-powered drill. Samples were collected spread out over the outcrop and from different blocks for sites LP1, LP1-2025, LP2 and LP3. For the other sites sampled in 2025 the samples were taken closer together. During the 2021 campaign, samples from sites LP1 and LP3 were taken along two ridges, together with volcanic glass at these locations. Sampling at the location of LP2 was more difficult in 2021, due to the persistent southwestern wind most ash had accumulated in this region and the flow was very

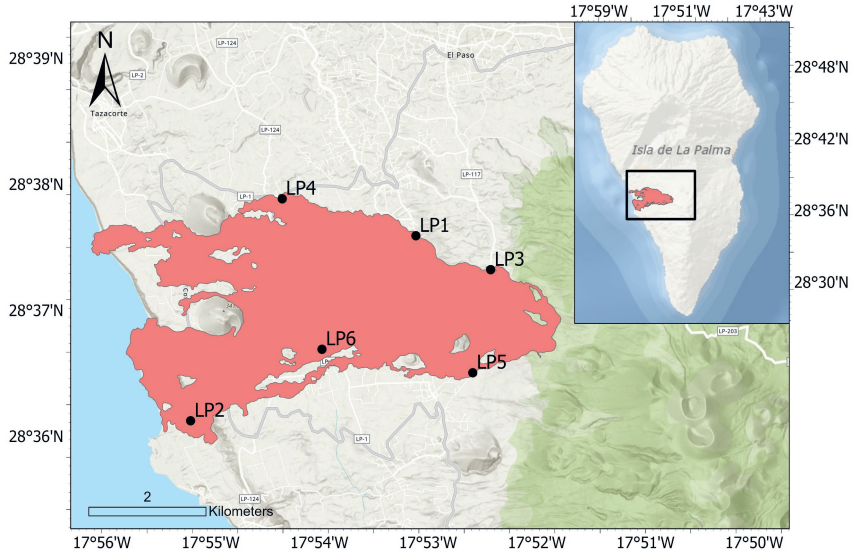


Figure 2.1: Sampling locations on the island of La Palma, Spain. Sampling sites are from the field campaign in 2021 (LP1, LP2 and LP3) and the field campaign in 2025 (LP1, LP2, LP4, LP5 and LP6). Red area is the outline of the 2021 lava flow

aa' like with large blocks. We sampled the three largest blocks at site LP2 that we could find to minimize the risk of post-cooling rotations. In 2025, access to the lava flow area was restricted, and as a result sampling was limited to blocks exposed in road cuts. Samples were always oriented with a magnetic compass and where possible with a sun compass. Due to the ash cloud this was not possible for most samples from LP1 and some of LP3. For each site the reference value according to the IGRF is calculated at that specific location, elevation and date of lava formation. At LP1, LP2 and LP3 the intensity of the Earth's magnetic field was also measured multiple times with a fluxgate magnetometer around 1m above the surface of the lavaflow (Table 2.1). The field was measured 17 times, and was on average 39.1 μT. This is slightly higher than the 38.7 μT indicated by the IGRF. In 2021 we took mu-metal containers with us in the field, and the samples were stored in those until they arrived at Fort Hoofddijk paleomagnetic laboratory where they were immediately transferred to and kept in the magnetically shielded room. Due to the larger numbers of samples taken, this was not possible during the 2025 sampling campaign, when the samples were stored and transported in the Earth's magnetic field before they were stored in the shielded room in the laboratory upon arrival.

2.2.2. Sample processing

The samples obtained in 2021 were taken to see how accurate the magnetic field is stored in volcanic samples, and whether the original magnetization may be altered by residing in an ambient magnetic field for certain periods of time. To study such a potential viscous effect, the samples were processed in two specific ways.

Table 2.1: Sampling sites and rock magnetic characteristics. Given are the sites, latitude and longitude, the year in which samples were taken (YS), elevation (Elv), IGRF-values for declination (D_{ref}), inclination (I_{ref}) and intensity (Int_{ref}). Int_{flux} is the average intensity signal above the lava flow directly measured by a fluxgate magnetometer.

Site	Lat(N)	Long(E)	YS	Elv(m)	D_{ref}	Inc_{ref}	Int_{ref}	Int_{flux}
LP1	28.6262	-17.8852	2021	521	-4.866	37.134	38.692	39.644
LP1	28.6261	-17.8850	2025	520	-4.866	37.134	38.692	
LP2	28.6021	-17.9197	2021	30	-4.883	37.094	38.688	39.689
LP2	28.6043	-17.9203	2025	35	-4.883	37.098	38.689	
LP3	28.6220	-17.8738	2021	736	-4.869	37.105	38.686	38.063
LP4	28.6313	-17.9057	2025	319	-4.871	37.144	38.697	
LP5	28.6084	-17.8765	2025	651	-4.847	37.095	38.681	
LP6	28.6115	-17.8995	2025	380	-4.864	37.106	38.687	

First, samples were taken from the end of the core (typically 4–10 cm from the flow surface; labelled A), and second, from the cores' exterior, representing the exposed outcrop surface (labelled B). In paleointensity studies, specimens are routinely taken from the deeper end of the core as the outside may be more susceptible to surface weathering. This weathering probably did not yet occur during the 3.5 weeks that these young rocks were exposed. Therefore, we test whether there is a substantial difference between inside or outside samples of very fresh rock surfaces.

The second sample processing technique is related to the long-time storage of samples. From the samples obtained in 2021, five measurement batches were made. Of the first batch, the directions and intensities were measured directly after the fieldwork. An additional four batches of samples were prepared for paleointensity measurements only and stored at Fort Hoofddijk. Two batches were stored in a random orientation in the Earth's magnetic field (in-field), while the other two were stored out of the Earth's magnetic field in a shielded room (out-field). Of each storage batch, one batch was measured in February 2024 and the other in June 2025.

Lastly, the samples obtained during the fieldwork in February 2025 have been in the Earth's magnetic field on La Palma for three more years after the eruption, and were therefore 'aligned' with their imparting field direction for a prolonged period of time. These samples were used to test how accurately they reproduce the expected field intensity when stored along that vector. Because these samples were obtained from road-cuts, which is already the inside of a core, we did not distinguish between A- or B-samples.

2.3. Rock Magnetic Characteristics

Rock magnetic analyses were performed to identify the remanence magnetization carriers and test the suitability of the samples for paleomagnetic measurements. From the 2021 samples the Curie Temperature (T_C) was measured on a horizontal translation Curie Balance (Mullender et al., 1993). Of site LP1, from nine cores an inside (A) and outside (B) sample was measured as well as one volcanic glass

sample. Of site LP2, from ten cores an A- and B-sample was measured and of site LP3 eight A- and B-samples were measured and one volcanic glass sample. For the 2025 samples two samples per site were measured. Most of the 2021 samples were heated from room temperature up to 600°C and lowered again to room temperature. The samples from 2025, and a few samples per site for the 2021 samples, were heated in steps of 75, 225, 300, 375, 450, 525 and 600°C. After each step the temperature was lowered by 75°C to check the reversibility of the signal, the temperature at which the signal is not reversible any more is determined as the alteration temperature (T_{alt}). Usually, measuring one sample per site is sufficient to determine the Curie and alteration temperature. The sampled sites from 2021 were measured in more detail, and the Curie temperature and amount of alteration varies between the samples. Examples are in Fig. 2.2A-C, and all Curie plots are in Supp. Fig. 2.2-2.6. For site LP1, some samples show a fully reversible curve (LP1-glass, Fig. 2.2, LP1-2B, Supp. Fig. 2.2), whereas others have an alteration temperature of 300-375°C (LP1-1A, Supp. Fig. 2.2, LP2-5 2025, Supp. Fig. 2.6). LP3 shows similar behaviour, only the glass sample has a reversible thermomagnetic curve (Supp. Fig. 2.5). LP2 behaves more ideally, only LP2-7A has an alteration temperature around 450°C and all others are fully reversible (Supp. Fig. 2.3, 2.4). The Curie temperature varies between the samples. Most samples without alteration show one single Curie temperature around 460°C (LP1-glass or LP2-12B, Supp. Fig. 2.3, 2.4). Others yield two distinct Curie temperatures, one lower around 180-230°C, indicative of a larger amount of Ti-rich titanomagnetite, and a higher one around 460-540°C, consistent with low-Ti titanomagnetite approaching the Curie temperature of magnetite. Generally, the A-samples exhibit more alteration at a lower temperature and therefore indicate less suitable behaviour for paleointensity experiments compared to the B-samples. Samples obtained in 2025 show the same variability in Curie temperature, and except for LP4, an alteration temperature of 300°C.

To assess the magnetic domain state of the samples hysteresis experiments were performed. Three to five A-samples and three to five B-samples were measured for the 2021 sites, as well as one volcanic glass sample for site LP1 and LP3. For the 2025 samples only one sample per site was measured. For each sample, a hysteresis loop and back-field curve was measured on an PMC 3900 Alternating Gradient Magnetometer, with a maximum field set at 500 mT and an averaging time of 150 ms. The contribution of paramagnetic minerals to the signal was removed by a slope correction of 70%. The saturation magnetization (M_s), remanent saturation magnetization (M_{rs}) and coercive force (B_c) were derived from the hysteresis loop. The remanent coercive force (B_{cr}) was obtained from the DCD curve. The ratio of remanence (M_{rs}/M_s) and coercivity (B_{cr}/B_c) of the samples are plotted in the Day-diagram (Day et al., 1977). Depending on the ratio of M_{rs}/M_s and B_{cr}/B_c the bulk magnetic state is labelled as single-domain (SD), pseudo single-domain (PSD) or multi-domain (MD). Almost all samples from the 2021 flow of La Palma end up in the PSD domain (Fig. 2.2F), which is an expected result for a volcanic rock (Tauxe et al., 2002). Only sample LP3-4A (Fig. 2.2D) falls in the MD range. Despite that all samples come from the same flow, they show a wide scatter within the PSD domain, but many plot closer to the SD range of the SD-MD mixing curves (Dunlop, 2002). For LP3, some B-samples seem to be more SD than the A-samples, but this is

not seen as clearly in the other sites. For the 2025 sampling sites, LP1 and LP5 plot closest to the SD-range.

In addition to the hysteresis measurements, First Order Reversal Curves (FORCs) (C. R. Pike et al., 1999; Roberts et al., 2000) were measured for two A-samples and two B-samples per site. For each sample a suite of 200 FORCs was measured using the same Alternating Gradient Magnetometer, the saturating field was set at 200 mT, the averaging time at 200 ms and Hu ranged from -40 mT to 40 mT. The FORC data were processed using FORCinel 3.08 (Harrison & Feinberg, 2008) and the VARIFORC algorithm (Egli, 2013). The results for samples LP2-13A and 13B and LP3-15A and 15B are shown in Fig. 2.2G-J. Site LP1 and LP3 show similar behaviour. The FORCs exhibit a small vertical spread at Bc = 20 mT, accompanied by an extending central ridge. For LP3-15B, there is a wider distribution of the signal around the central ridge (Fig. 2.2J). LP2-13A and LP2-13B have a wider distribution at Bc = 0, and a characteristic boomerang shape in the region of Bu <0, which points to single vortex state behavior (Fig. 2.2H). Overall, the FORC diagrams indicate vortex type behaviour and the influence of MD grains, in agreement with the samples plotting in the PSD field in the Day diagram.

2.4. Paleomagnetic directions

Paleomagnetic directions were only determined for the samples obtained in 2021. For each site, four samples were thermally demagnetized in steps of 50°C up until 600°C. After each thermal demagnetization step the remaining magnetization was measured on a 2G cryogenic magnetometer. In addition to thermal demagnetization experiments, eight (LP1 and LP2) or seven (LP3) specimens were measured using alternating field (AF) demagnetization experiments on a robotized 2G DC-SQUID cryogenic magnetometer (Mullender et al., 2016). The specimens were demagnetized in AF steps of 0, 2.5, 5, 7.5, 10, 15, 20, 25, 30, 40, 50, 60, 70, 80, 100, 150, 200, 225, and 270mT. During all measurements the samples were kept in a magnetically shielded environment. The demagnetization results were analysed in paleomagnetism.org (Koymans et al., 2016, 2020) in which the Characteristic Remanent Magnetization (ChRM) was identified in the orthogonal vector diagrams. Site mean directions were calculated with Fisher statistics (Fisher, 1953) and some outliers were identified in the VGP distribution using the 45° cut-off. The samples of site LP2 showed clear evidence of movement during cooling in both the thermal and AF demagnetizations (Fig. 2.2K). Therefore, only the lower temperature interval of 0-300°C was interpreted for three thermally demagnetized samples of LP2, and for the five AF demagnetized samples only the first range of AF steps were used. The other four samples are excluded from interpretation as they were complete outliers due to the post solidification movement. In contrast to site LP2, the ChRM-direction of the samples from LP1 and LP3 was mostly a straight line to the origin (Fig. 2.2J, L). Declinations were determined using the magnetic and sun compass readings, Table 2.2 shows the results of both, but the k-values and α_{95} are reported based on the sun compass readings. There are minor variations between the results based on the magnetic and sun compass readings: the magnetic compass declination is around 1-2° different from the sun compass declination. Since the sun compass is

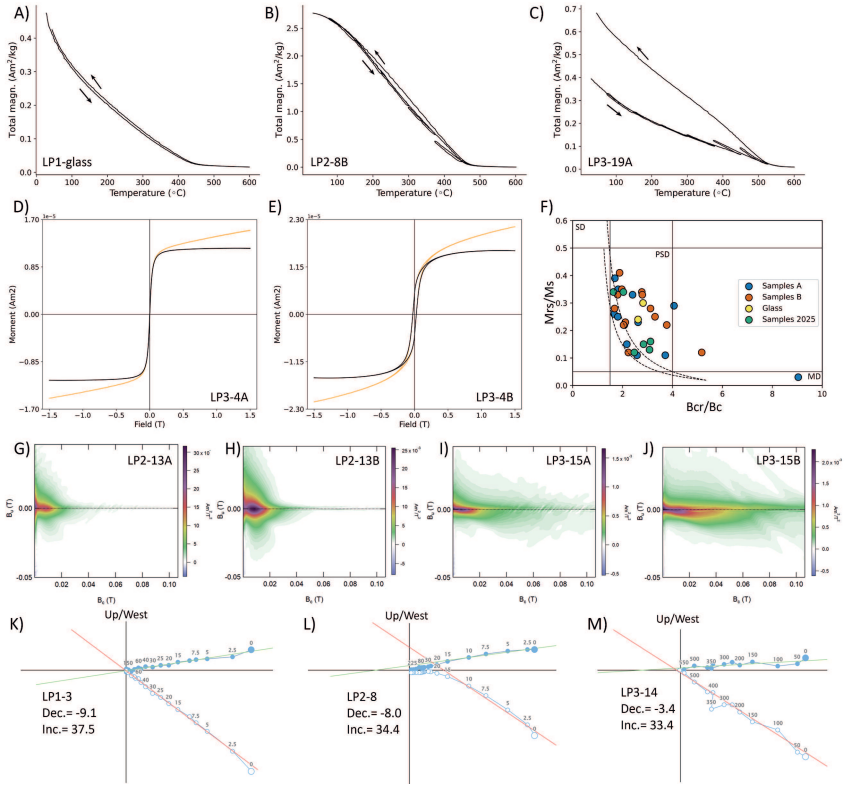


Figure 2.2: Rock magnetic and directional results. Representative examples of magnetization vs temperature plots of A) LP1-glass, B) LP2-8B and C) LP3-19A. Heating curve is indicated with a downward pointed arrow, cooling curve is pointing upward. Hysteresis loops are shown for D) LP3-4A and E) LP3-4B, in orange is the raw data and the black curve has a 70% paramagnetic contribution correction. The M_{rs}/M_s and B_{cr}/B_c for the hysteresis measurements are plotted in the Day-Diagram (F). The measurements are divided into the A- or B-samples, two volcanic glass measurements and samples from 2025. The dashed lines are the theoretical mixing curves for uniaxial shape anisotropy and negative cubic shape anisotropy from Dunlop (2002). In G-J are FORC diagrams of LP2 and LP3. Zijderveld diagrams with declination and inclination results are given for K) LP1-3, L) LP2-8 and M) LP3-14. The closed circles are the declination and open circles are the inclination demagnetization steps. Straight line through the steps indicate the interpreted ChRM direction, step 350°C at LP3-14 is not used for interpretation.

the preferred method of orientation, the results below are discussed based on this orientation method.

2.4.1. Results

Interestingly, the directional results of sites LP1, LP2 and LP3 show large between-site variations. The declination between the sites varies with as much as 6.7°, and the inclination with 9.5°. The smallest α_{95} and highest k-value is from site LP3. We compare the directional results of the sites with the IGRF value given in Table 2.1. LP2 gives the least accurate results, even though the k-value of this site is 160, the declination is 5.9° higher than expected and the inclination is 5.3° lower with a total angular deviation of 7.2°. It seems that even though we were careful in selecting the most reliable ChRM-direction steps, the results for this site might still be influenced by the block rotation. Site LP1 and LP3 are more accurate: the difference in declination of LP1 compared to the reference value is 2.2°, and especially the declination of LP3 is close to the expected value with only a 0.8° difference. The inclination deviates more: LP1 has an inclination that is 4.1° higher and LP3's inclination is 4.9° lower than expected. The total angular deviation of LP1 is lowest with 4.8°, which is remarkable given the low k-value of this site.

When the sites are grouped (Table 2.2) into a single average for the entire flow, the k-value decreases, but both the α_{95} and the difference with the IGRF reference value are lower as well. Because the direction of LP2 might be affected by block rotation, the grouped results using only LP1 and LP3 are also provided. Because the inclination of LP1 is higher than expected and the inclination of LP3 lower, the average result of LP1 and LP3 is very close to the IGRF-value. The declination is only 0.6° higher and inclination is 0.6° lower. The angular difference of LP1 and LP3 combined is just 0.8°.

Table 2.2: The obtained directions per site are given by the parameters: (n/N) number of samples accepted / total amount of samples per site, the declination (D), declination from sun compass readings (D_{sun}), inclination (I), 95 percent confidence interval (α_{95}), precision parameter (k), and the separate errors for declination (ΔD_x) and inclination (ΔI_x). ΔD, ΔD_{sun} and ΔI are the difference with the IGRF values given in Table 2.1 and ΔAng is the angular difference between the vectors. The grouped directions of LP1+2+3 and LP1+3 are also given.

Site	n/N	D(°)	D_{sun} (°)	I(°)	α95(°)	k	ΔD_x	ΔI_x	ΔD	ΔD_{sun}	ΔI	ΔAng
LP1	10/12	-1.3	-2.6	41.2	5.5	77.7	6.2	7.6	3.5	2.2	4.1	4.8
LP2	8/12	-0.2	1.0	31.8	4.4	160.5	4.3	6.4	4.7	5.9	-5.3	7.2
LP3	11/11	-6.7	-5.6	32.2	3.4	182.0	3.4	5.2	-1.8	-0.8	-4.9	4.9
LP1+2+3	29/35	-3.9	-2.8	35.2	2.8	89.5	2.9	4.0	1.0	2.1	-1.9	2.5
LP1+3	21/23	-5.9	-4.3	36.5	3.5	85.9	3.8	5.3	-1.0	0.6	-0.6	0.8

2.5. Field intensity

Compared to the directional measurements, the intensity signal in the samples is measured more thoroughly, as the samples obtained in 2021 were divided into five measurement batches. The samples obtained on La Palma in 2025 were measured directly after returning from the field. The results from all batches will be compared to check if there have been any changes in the capacity of the samples to store a

TRM during this time period.

For each batch 10-11 specimens from the same sampling cores were selected and subjected to the IZZI-Thellier paleointensity measurement method (Tauxe & Staudigel, 2004). Of the 2021 samples, for each sample an inner (A) and outer (B) specimen was measured, which resulted in 20 to 22 specimens per site. For LP1 and LP3 a further 5 glass specimens were measured. From the 2025 sampling sites, between 10 to 25 specimens were subjected to the method. All specimens were glued into glass vials with quartz wool and kaliumsilicate. During the IZZI-Thellier experiment, the specimens were heated in several steps whereby the natural remanent magnetization (NRM) was progressively replaced by a partial thermal remanent magnetization (pTRM) under a laboratory field of 50 μT. Because the thermal demagnetization behaviour of the specimens differed at site-level, all specimens were measured in extreme detail. The specimens were all subjected to the same temperature steps with increments of only 30°C up to 590°C, or until they lost their magnetization. After each cycle of zero-field, in-field (Coe, 1967) and in-field, zero-field (Aitken et al., 1988) steps a pTRM-check was included to check whether the specimen's ability to carry a remanent magnetization has changed, resulting in a 'ZIIZP'-protocol. The specimens were measured on a 2G cryogenic magnetometer and during measuring kept in a magnetically shielded room.

The intensity results were interpreted using paleointensity.org (Béguin et al., 2020). To assess the quality of the results, six different sets of selection criteria were applied. These are: TTA and TTB (Leonhardt et al., 2004), SELCRIT2 (Selkin & Tauxe, 2000), PICRIT03 (Kissel & Laj, 2004), CLASS-A (L. V. de Groot et al., 2014b) and CCRIT (Cromwell et al., 2015b). The first four are modified as proposed by (Paterson et al., 2014). CCRIT is the strictest criterion and has a curvature criteria of k'<0.164, the others have the curvature criteria set at k'<0.35. From all interpretations that passed a set of selection criteria the average paleointensity and standard deviation were calculated. This means that interpretations that passed more than one set of selection criteria were included more often, and therefore these more reliable interpretations receive more weight. In addition to the site-level results, average intensities and uncertainties were analysed separately for the A- and B-samples.

2.5.1. Results 2021 samples

Analysing the samples obtained in 2021, we find that paleointensities and success rates, e.g. the accepted specimens divided by the number of samples, vary among the different sites and batches measured. The paleointensity results for each site and batch are given in Table 2.3 and shown in Fig. 2.4. In addition to the average paleointensity, the standard deviation, success rate of the batch and the average curvature of the Arai plot of the samples was also determined. The paleointensity results and success rates are also split for the inside (A) and outside (B) samples as shown in Fig. 2.5. We will describe the results of each site separately below, starting with the variations in success rate before discussing intensity variations.

LP1-2021

The specimens of site LP1 from the 2021 batch yielded a high success rate of 76% (Table 2.3). Interestingly, the success rate for the 2024 in-field stored samples drops to 48%, while it is notably higher for the out-field stored samples from the same batch, at 80%. A similar pattern is observed in the specimens measured in 2025, where out-field samples are clearly more successful than the in-field stored samples (Fig. 2.4). This difference is also reflected in the absolute curvature of the Arai plots, k'abs is higher for the in-field samples than the out-field samples, suggesting more non-ideal behaviour. Comparing the inside (A) and the outside (B) samples, the success rate of the B-samples is higher across all batches except for the 2025 out-field batch (Fig. 2.5).

The average paleointensity of site LP1 exceeds the expected 38.711 μT for all batches (Fig. 2.4). Values are above 41 μT for the 2021 and 2024 out-field batches, and lowest for the 2025 out-field batch at 39.916 μT. Standard deviations range from 2.65 to 3.35 μT, with the smallest variation observed in the 2025 batches. Comparing A- and B-samples, the 2021 batch shows similar paleointensity values for both groups (Fig. 2.5), whereas larger differences appear in later batches. In 2024, B-samples are closer to the reference value, while in the 2025 in-field batch, A-samples yield higher intensities (41.992 μT) than B-samples (37.967 μT). The 2025 out-field batch shows the opposite trend, with A-samples giving lower paleointensities.

LP2-2021

Similar to site LP1, site LP2 also yields high success rates across the different batches, ranging from 59.1% to 95.5%. For the batch measured in 2024, the out-field samples again yield higher success rates than the in-field samples. However, this trend is reversed in the 2025 batches. Here, the in-field samples hold the highest success rate of the LP2 batches. Again, the success rate seems to follow the pattern of k'abs. Comparing the k'abs from batches of the same year, a higher k'abs results in lower success rates. Across all batches the B-samples have higher success rates than the A-samples (Fig. 2.5).

The average paleointensity of site LP2 is the least accurate among all sites. The paleointensity is between 4.877 and 8.569 μT lower than the expected IGRF-value. The σ is also relatively large, between 5.52 and 7.3 (Table 2.3). As also seen in LP1, the average paleointensity for the 2024 in-field stored samples is lower, at 30.138 μT lower, while the out-field samples show a higher value of 33.650 μT. This pattern is reversed for the 2025 batch. The paleointensity results, when divided into A- or B-samples, show no consistent pattern (Fig. 2.5), except that LP2 is the only site where a clear difference between the groups is already present in the 2021 batch.

LP3-2021

LP3 is the most successful site as almost all specimens across the different batches pass at least one of the sets of selection criteria. An example of the Arai plots obtained from LP3 from the different batches is shown in Fig. 2.3. Similar to the results seen in the 2024 batches from LP1 and LP2, the 2024 in-field samples are again slightly less successful than the out-field samples (Fig. 2.4). In 2025, both in-

and out-field batches have a 100% success rate, together with the lowest k'abs of all batches. With the exception of the 2021 batch, all B-samples passed the selection criteria. A-samples from the 2021 and 2024 batches were less successful, but in 2025 they also achieved a 100% success rate (Fig. 2.5).

Not only the success rate of LP3 is high, the average paleointensity is also closest to the reference value. The ΔInt ranges from 0.102 to -1.053 μT, with a standard deviation between 3.42 to 5.99. Compared to the results obtained in 2021, the paleointensity has decreased by 1.458 μT in 2025. The paleointensity result of the A and B samples is similar in 2021. In 2024 and 2025, the in-field B-samples result in a higher paleointensity, whereas the out-field stored B-samples yield a lower intensity.

All sites sampled in 2021

To provide a complete overview we combine the results from all three sites that were sampled during the eruption in 2021 (Table 2.3, Supp. Fig. 2.1). Both the paleodirectional and the paleointensity results from LP2 clearly deviate from the expected IGRF value. We find that these large deviations are most likely caused by the rotation of some of the blocks sampled at site LP2. While a few segments of temperature steps passed selection criteria, the rotation most likely influenced the entire intensity signal. Because this site experienced block rotation, we also give the results of only combining LP1 and LP3 in Table 2.3 and Supp. Fig. 2.1.

The samples measured immediately in 2021 yield success rates around 80%. After storing the samples in a magnetic field for two years, the success rate drops. The samples stored in a field free environment remain at a similar success rate. However, after storing the samples for three years, the success rate of the in-field samples is around 80% again, the sample value that it was in 2021. Interestingly, after storing the samples out of the Earth's magnetic field for three years, the success rate has even increased to above 90%.

Comparing the average paleointensities, we observe that the average paleointensity of LP1+2+3 is around or slightly below the expected field value. However, due to the LP2 rotation the results of only combining LP1 and LP3 are more reliable than those based on all three sites. The paleointensity values of LP1+LP3 are higher compared to the full dataset. There is no clear trend visible since there are only minor paleointensity variations between the batches. We do note that the values obtained in 2025 are slightly lower than those from 2021.

2.5.2. Results 2025 samples

In contrast to all batches of the samples obtained in 2021, the samples obtained and measured in 2025 have markedly lower success rates and less accurate paleointensity results (Fig. 2.4). For site LP1-2025, the success rate dropped to 52% with a very large σ and a difference with the reference value of 13.6 μT. LP2-2025 was unsuccessful, as there is only one interpretation that passes a set of selection criteria. The newly sampled sites, LP4, LP5 and LP6 have success rates varying between 40 to

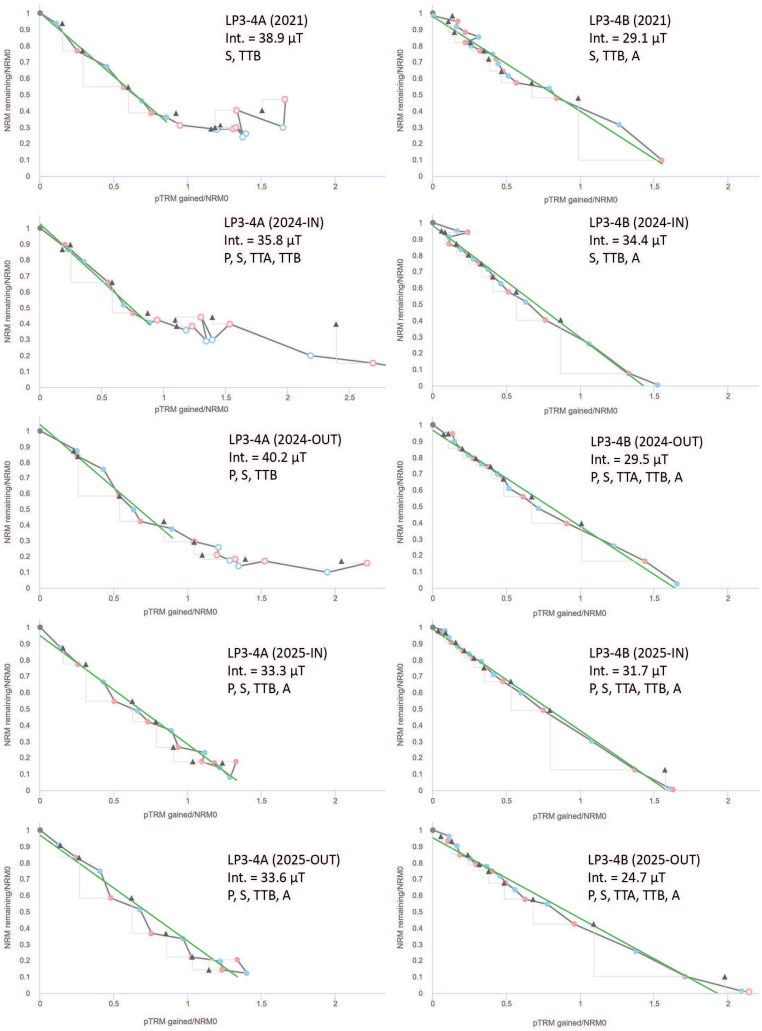


Figure 2.3: Arai plots of LP3-4A and LP3-4B across the different batches. The given intensity is according to the green line which represents the greatest segment accepted by paleointensity selection criteria. Blue circles are the ZI-steps, red circles are the IZ-steps, and triangles indicate pTRM-checks. Selection criteria are PICRIT (P), SELCRIT (S), TTA, TTB, CLASSA (A) and CCRIT (C).

71.4%. These lower success rates are reflected in higher k' values, which range from 0.68 to 1.02. Amongst the 2025 sampling sites, LP5 is most successful and accurate. The paleointensity difference with the reference value is -3.58 μT. Sites LP4 and LP6 have differences of 15.6 μT and -9.12 μT, respectively. Because these results are notably different from the results of the 2021 batches, and all have relatively high σ/PI values, we did not combine the results from these sites with any of the 2021 sites.

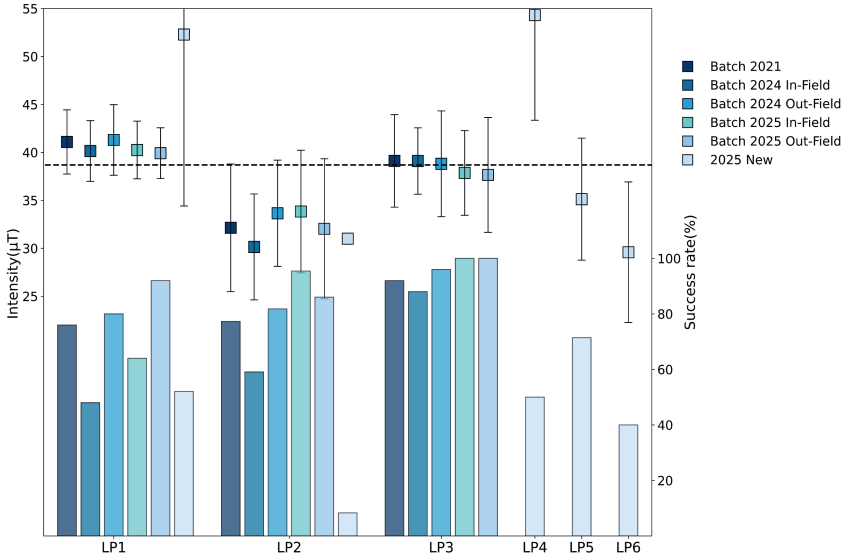


Figure 2.4: Paleointensity results of LP1, LP2 and LP3, from the samples obtained in 2021, and for LP1 and LP2 also the new samples from 2025. LP4, LP5 and LP6 are samples obtained in 2025. Shown are the intensity results at the top (squares), with the standard deviation, for each sampling site and in- or out-field batch measured in 2024 or 2025. The striped line is the expected paleointensity value. The bar plots at the bottom indicate the success rate of the sites.

2.6. Discussion

We first discuss the paleodirectional and paleointensity results from the samples collected and measured in 2021, including recommendations on sampling and measuring techniques. Then we discuss the differences between samples from the inside and outside part of a flow, and end with the effect of storage conditions on paleointensity results.

2.6.1. Paleomagnetic directions

The directions obtained in 2021 show variability between sites, with declination and inclination variations up to 6.5° and 9.4°, respectively. The orthogonal vector diagrams of LP2 indicate evidence of block rotations. Therefore, the directions of LP1 and LP3 are deemed most reliable. Combining the results from LP1 and LP3 resulted in a lower k-value but a remarkably accurate direction of only a 0.6° difference in both declination and in inclination. Previously, it was suggested that tak-

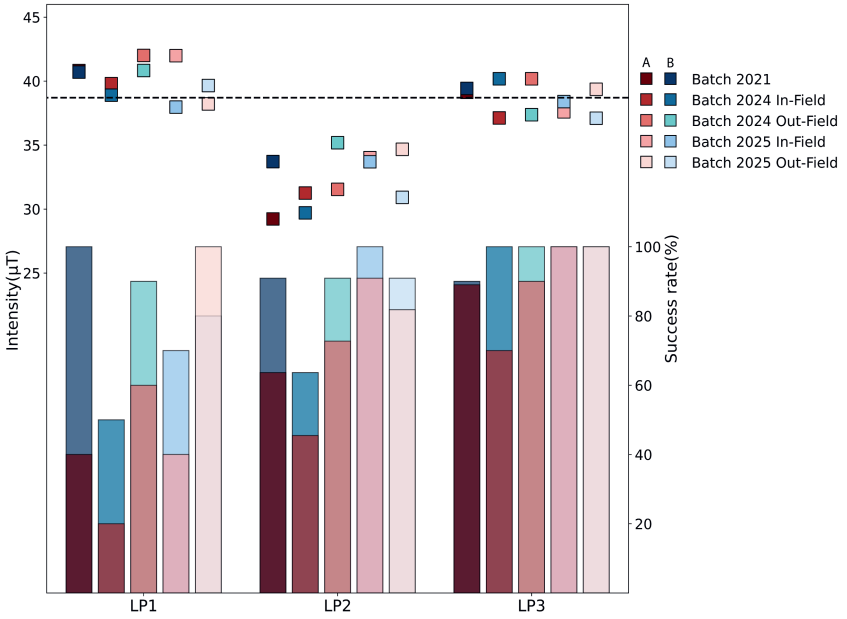


Figure 2.5: Similar paleointensity results as Figure 2, but divided into inside (A, red) and outside (B, blue) samples. Shown are the intensity results at the top (squares) for each sampling site and in- or out-field batch measured in 2024 or 2025, with again the striped line as the expected paleointensity value. The bar plots at the bottom indicate the success rate.

Table 2.3: Paleointensity results. The obtained paleointensities per site are given by the following parameters: the year in which the samples were obtained (YS=Year Measured), the year in which the batch was measured (YM=Year Measured), if they were stored in a magnetically free environment (OUT) or in the Earth's magnetic field (IN), number of samples accepted/total number of samples (n/N), number of interpretations (n_int), resulting paleointensity (PI), standard deviation (σ), standard deviation divided by the paleointensity (σ/PI), the curvature of the Arai plot (k'), the success rate (SR) and difference with the with the IGRF values given in Table 2.1 (ΔInt).

YS	YM	Stored	n/N	n_int	PI (μT)	σ	σ/PI	k'	SR (%)	ΔInt
Results site LP1										
2021	2021	-	19/25	1978	41.086	3.35	8.14	0.52	76	2.375
2021	2024	IN	12/25	494	40.141	3.17	7.90	0.65	48	1.430
2021	2024	OUT	19/25	1492	41.297	3.68	8.92	0.38	80	2.586
2021	2025	IN	16/25	1648	40.250	3.01	7.48	0.58	64	1.539
2021	2025	OUT	23/25	1582	39.916	2.65	6.63	0.51	92	1.205
2025	2025	-	13/25	186	52.292	17.88	34.2	0.8	52	13.6
Results site LP2										
2021	2021	-	17/22	1135	32.133	6.65	20.70	0.29	77.3	-6.574
2021	2024	IN	13/22	540	30.138	5.52	18.32	0.43	59.1	-8.569
2021	2024	OUT	18/22	825	33.650	5.54	16.46	0.23	81.8	-5.057
2021	2025	IN	21/22	962	33.830	6.39	18.88	0.31	95.5	-4.877
2021	2025	OUT	19/22	1472	32.031	7.3	22.8	0.41	86.3	-6.676
2025	2025	-	1/12	1	31	-	-	1.04	8.3	-7.7
Results site LP3										
2021	2021	-	23/25	2214	39.110	4.82	12.33	0.4	92	0.405
2021	2024	IN	23/25	2179	39.074	3.42	8.75	0.29	88	0.369
2021	2024	OUT	24/25	1721	38.807	5.52	14.22	0.32	96	0.102
2021	2025	IN	25/25	2971	37.859	4.42	11.68	0.20	100	-0.846
2021	2025	OUT	25/25	2765	37.652	5.99	15.92	0.20	100	-1.053
Results site LP4, LP5, LP6										
2025	LP4	-	5/10	94	54.317	10.97	20.20	0.75	50	15.6
2025	LP5	-	15/21	416	35.120	6.36	18.12	0.68	71.4	-3.58
2025	LP6	-	4/10	35	29.583	7.33	24.79	1.02	40	-9.12
Combined results LP1, LP2 and LP3										
2021	2021	-	58/72	5585	38.483	5.81	15.10	0.38	80.6	-0.224
2021	2024	IN	48/72	3213	37.736	5.14	13.62	0.46	66.3	-0.972
2021	2024	OUT	61/72	4038	38.673	5.65	14.62	0.31	83.1	-0.034
2021	2025	IN	62/72	5581	37.870	4.96	13.09	0.37	86.1	-0.838
2021	2025	OUT	67/72	5819	36.846	6.42	17.42	0.37	93.1	-1.862
Combined results LP1 and LP3										
2021	2021	-	42/50	4450	40.103	4.26	10.6	0.39	82	1.395
2021	2024	IN	35/50	2673	39.271	3.40	8.66	0.46	68	0.563
2021	2024	OUT	43/50	2605	39.963	4.92	12.3	0.25	82	1.255
2021	2025	IN	41/50	4774	38.673	4.11	10.62	0.39	82	-0.035
2021	2025	OUT	48/50	4393	38.480	5.14	13.36	0.35	96	-0.228

ing samples spread out is the best strategy for paleomagnetic studies (Meyer & de Groot, 2024). While k-values may decrease by doing so, any influence from the underlying magnetized terrain would be averaged and this leads to more accurate paleodirections. Since site LP1 and LP3 were sampled 1.2km apart and their averaged directions are very accurate, the sampling strategy of taking samples distributed over a larger area may indeed lead to more accurate results. While sampling over such large distances is often not feasible, taking samples across the widest possible area remains a valuable approach.

2.6.2. Paleointensity

In addition to the high accuracy of the directional data, the intensity results from the samples obtained in 2021 were also very successful. Compared to the outside (B) samples, the inside (A) samples often yielded somewhat lower success rates. The thermomagnetic curves of the inside samples generally showed less ideal behaviour than the outside samples, which might partly explain the lower success rates. Nevertheless, many thermomagnetic curves indicated non-ideal behaviour, yet most samples still passed at least one of the sets of selection criteria. This may be due to the use of the very small temperature steps of only 30°C during the IZZI-Thellier measurement. An example is the thermomagnetic curve of LP3-4A (Supp. Fig. 2.4): thermal alteration is visible from 375°C onwards. Because of the small temperature steps the lower and intermediate steps can be interpreted and do give correct interpretations (Fig. 2.3). For such samples, excluding the high temperature steps did not significantly affect the overall success rate of the batches. While using such small temperature increments is not always feasible, it highlights the need for careful selection of optimal temperature steps. It also shows that samples with thermal alteration in the higher temperature steps do not necessarily need to be discarded.

The paleointensity result of LP2 is lower than expected across all batches. As mentioned before, this is most likely caused by the block rotation during cooling. In contrast, the IZZI-Thellier results of site LP1 consistently yielded higher paleointensities than expected. During the fieldwork we also took fluxgate magnetometer intensity measurements above the surfaces of the lava flows at LP1, LP2, and LP3. At LP1 and LP2 these measurements indicated a slightly higher intensity then expected, whereas at LP3 the values were somewhat lower. It is possible that, instead of recording the 38.692 μT expected from the IGRF, the lava flow at LP1 recorded the higher intensity of 39.644 μT influenced by the underlying terrain. Again, such effects are most likely averaged out when sampling over large areas (Meyer & de Groot, 2024).

2.6.3. Inside or outside samples

In 2021, we took samples from both the inside and the outside of standard paleomagnetic cores. For LP1, LP2, and LP3, the outside of the cores corresponds to the natural surface of the lava flow, which cooled most rapidly. In most cases, samples from the inside yielded lower success rates than the outer samples. In paleomagnetic studies, specimens are typically taken from the core interior to minimize the effects of alteration due to surface weathering. However, in the very young sam-

ples of this study some signs of alteration were already visible in the thermomagnetic curves. Moreover, the alteration was more pronounced in the inside samples, and therefore seem to not be caused by the exposure to the environment. We explain this different behaviour between inside and outside samples by a difference in cooling rate. The outside of a sample cools more rapidly, and faster cooling is often associated with single-domain sized particles and therefore a higher success rates in paleointensity experiments (Cromwell et al., 2015b; Cromwell, Trusdell, et al., 2018). This is supported by the rapidly cooled volcanic glass samples from LP1 and LP3, which showed both ideal Arai plots, a high success rate, and accurate paleointensity results. Additionally, the 2025 specimens of this study and Calvo-Rathert et al. (2024) were often from road-cuts and therefore the interior of the flow. In contrast to the samples collected in 2021, the samples obtained in 2025 yielded low success rates and large differences with the expected intensity values. In the Day-diagram, four of the 2025 sampling sites plot closer towards the MD side of the SD-MD mixing curves. Site LP1 and LP5 plot closest to the SD range (Fig. 2.2F), and compared to the other 2025 sampling sites yielded the most successful interpretations. The non-ideal behaviour observed in the paleointensity experiments may be explained by the 2025 samples having been taken from the flow interior, where slower cooling likely produced a higher proportion of multidomain (MD) grains. However, this is not very clearly seen in the FORC diagrams of LP2 and LP3 (Fig. 2.2G-J). Nonetheless, it seems that the interior of a flow is not necessarily better, at least for paleointensity experiments.

2.6.4. Effect of storage conditions

The paleointensity samples were stored in the ambient geomagnetic field, out of the Earth's magnetic field and on La Palma itself aligned with the natural magnetic field. The success rate of the sites seems to be slightly dependent on storage conditions. Samples stored out of the field generally yield a higher success rate than in-field stored samples. This is especially visible in the results of LP1. Unexpectedly, specimens stored for three years out of the Earth's magnetic field get even higher success rates than the original specimens. Samples that aged for three years on La Palma, yield the lowest success rates and least accurate paleointensities across all sampling sites. Even samples obtained one year after the eruption had low success rates (Calvo-Rathert et al., 2024). Therefore, it seems that storing samples out of a magnetic field is preferred over in-field storage. The reason for the changes in success rate over the years can be partially explained.

We observe that after storing the samples for two years in an ambient geomagnetic field, the success rates drop and generally the k' curvature value increases. This is in line with fragile curvature (Tauxe et al., 2021): Arai diagrams tend to become more curved when the samples are aged in a magnetic field. Additionally, Tauxe et al. (2021) observed that the paleointensity lowers for the specimens which show fragile curvature. This might explain the lower intensities for the 2025 batch of LP3, although it does not explain the large success rates of this site.

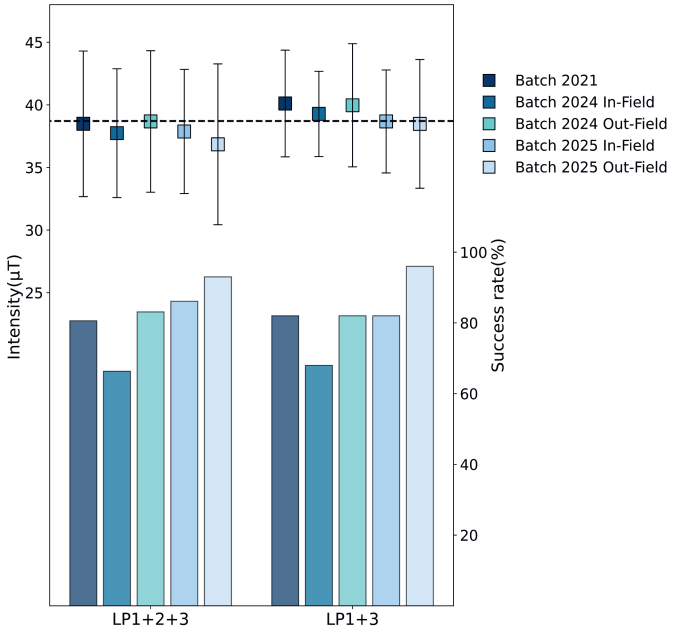
Storing paleointensity samples in a zero-field environment has not been tested extensively. We observe that samples that were stored out-field tend to perform

better in paleointensity experiments than those stored in-field. In L. V. de Groot et al. (2014a), magnetic force microscopy samples were stored for one year in a zero field environment, and they observed unstable pTRM domains that seemed to evolved back into a domain state that more closely resembles the original NRM configuration over time. This suggests that, in the absence of an external field, the magnetic domains in the samples relax into the energetically most favourable state, whereas when they are exposed to an ambient field there is a driving force that causes the magnetic domain states to evolve into alternative local energy minima. Such metastable domain configurations with a shift from a high energy state towards a low energy state, was described as the trapdoor VRM process (Fabian, 2024), in which high-energy states are irreversibly depleted over time. Such viscous local energy minima reconfigurations may explain why some in-field batches yield lower paleointensity success rates compared to sister samples that were stored out-field, where no external driving force is present. The higher success rate observed again in the 2024 batch, however, remains unresolved. For future studies, it would be interesting to test whether success rates improve for older samples if they are first stored in a zero-field environment before the paleointensity is measured.

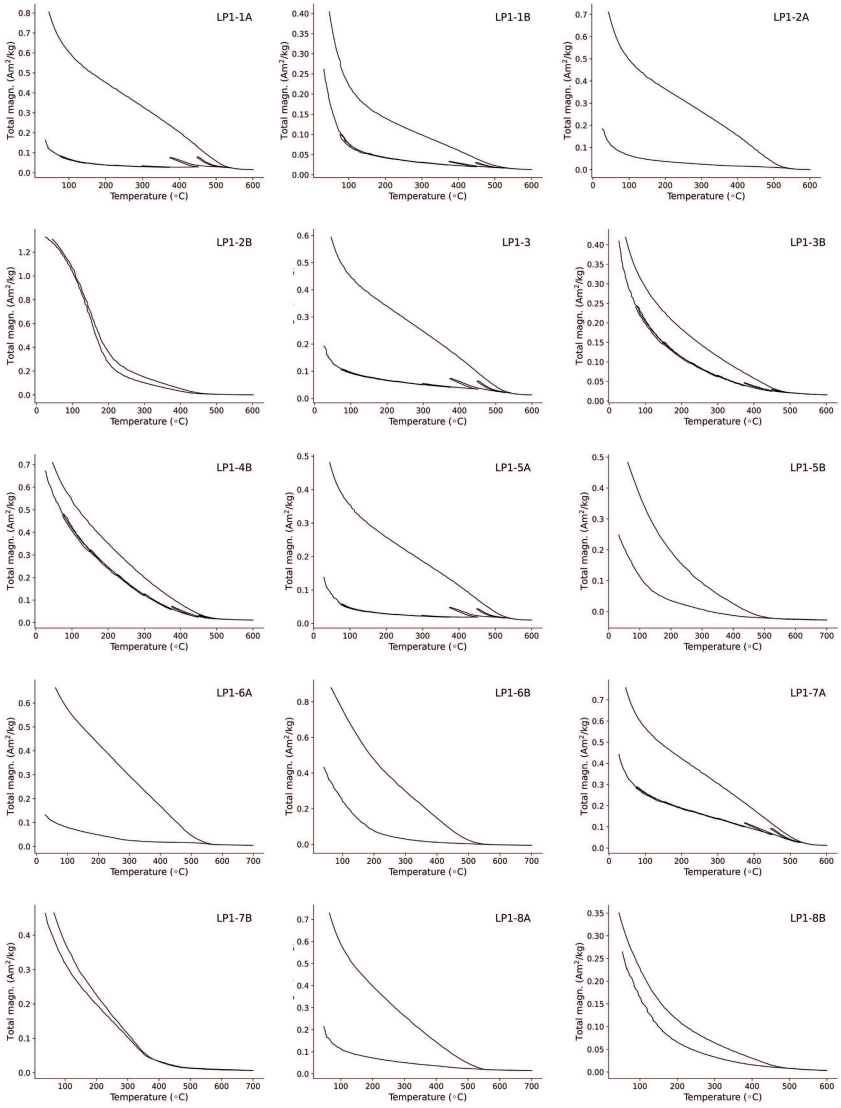
2.7. Conclusion

The very detailed paleointensity measurements in this study carried out on the very young lava from the 2021 Tajogaite eruption provided unique insights in changes in the intensity signal over time. First, samples obtained from the outside, or surface of the flow generally performed better in paleointensity experiments. They yield higher success rates, which may be related to faster cooling and the presence of single domain sized particles. Second, storage conditions seemed to influence the success rate of the experiments. Samples stored out of the Earth's magnetic field often yielded higher success rates than those stored in-field. The same flow was re-sampled in 2025, when only the interior of the flow could be sampled. These samples yielded much lower success rates. The variations in success rates and paleointensity results may reflect a combination of the process of fragile curvature and the reconfiguration of viscous local energy minima. It remains to be tested whether the behaviour of samples affected by viscous processes in paleointensity experiments can be improved by storing them for extended periods in a magnetically shielded environment.

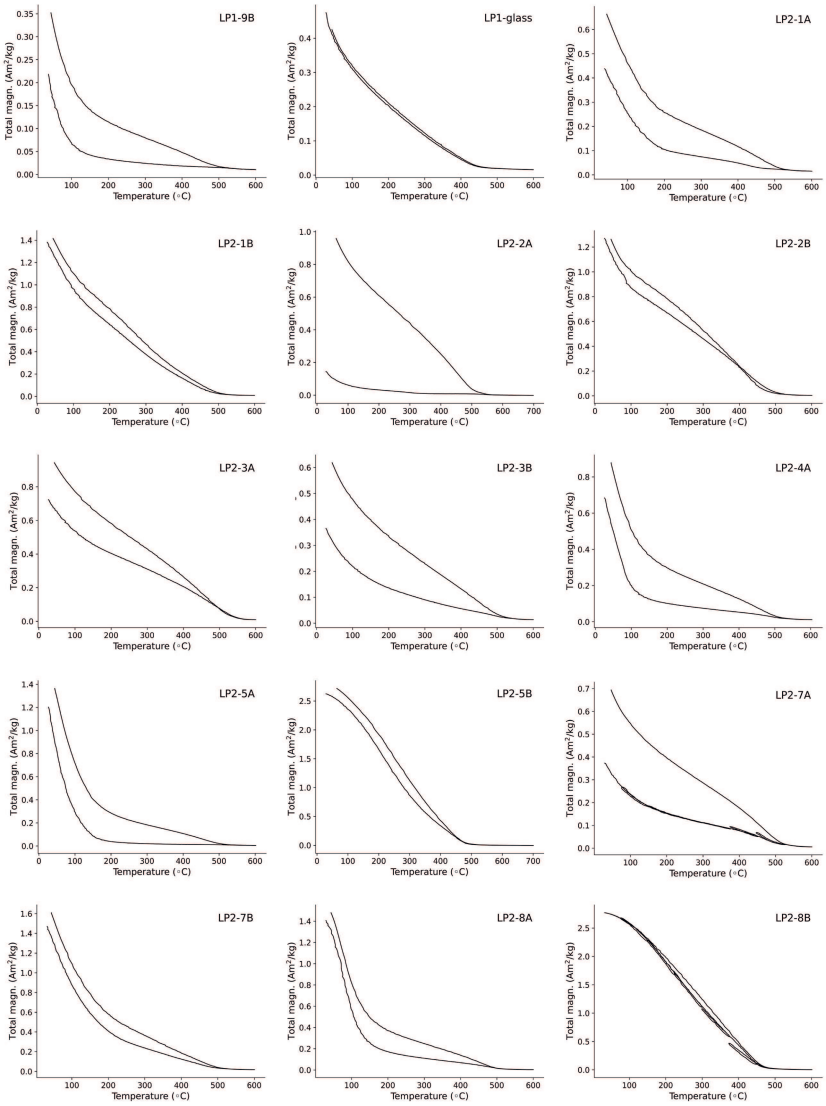
2.8. Supplementary Information



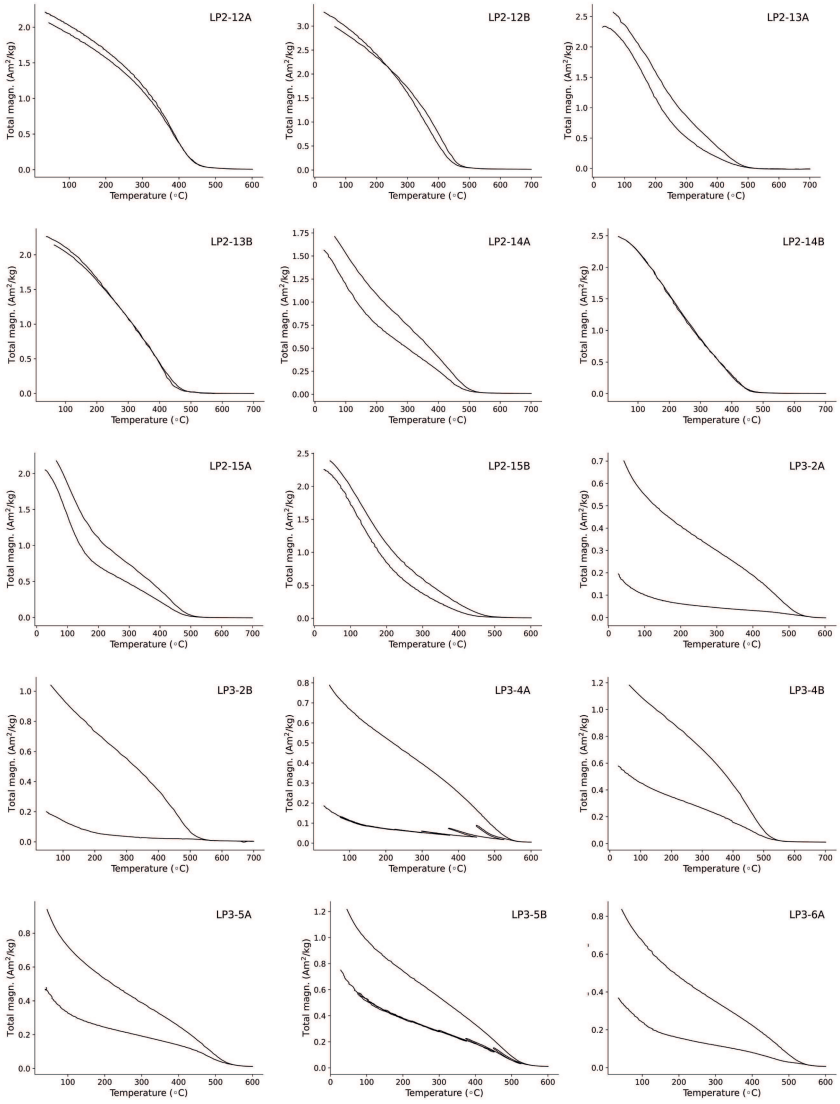
Supplementary Figure 2.1: Paleointensity results of all sites combined and of LP1 and LP3 combined. Shown are the intensity results at the top (squares) the in- or out-field batch measured in 2024 or 2025. Striped line is the expected paleointensity value. The bar plots at the bottom indicate the success rate.



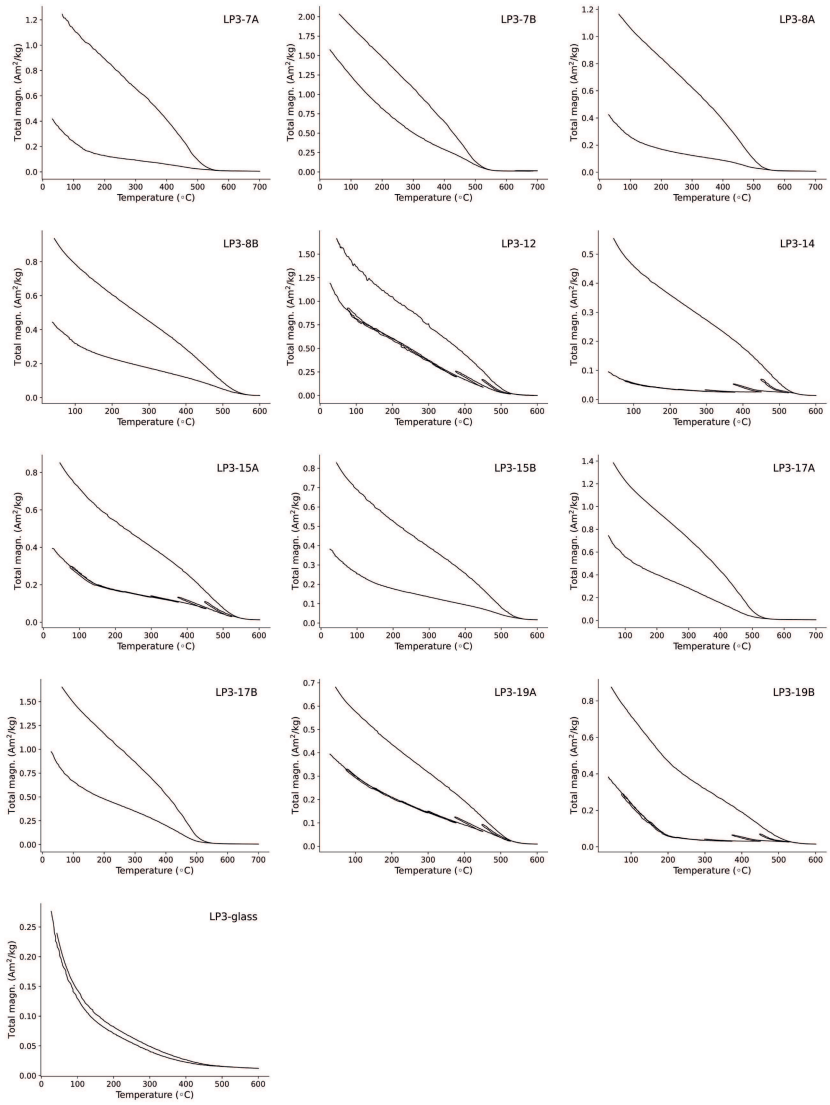
Supplementary Figure 2.2: Thermomagnetic curves of site LP1



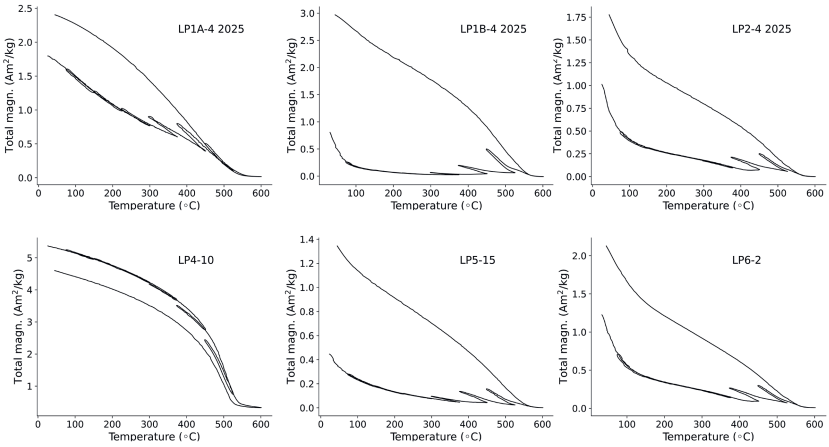
Supplementary Figure 2.3: Thermomagnetic curves of site LP1 and LP2



Supplementary Figure 2.4: Thermomagnetic curves of site LP2 and LP3



Supplementary Figure 2.5: Thermomagnetic curves of site LP3



Supplementary Figure 2.6: Thermomagnetic curves of the sites sampled in 2025.



3

A reconnaissance of Quaternary paleomagnetic directions and paleointensities in the East Pacific Ocean (Isla Socorro and Isla San Benedicto, Revillagigedo Archipelago, Mexico)

Romy Meyer, Douwe J.J. van Hinsbergen, Pablo Dávila-Harris, Peter C. Lippert, Mélody Philippon, Lennart V. de Groot

Submitted to Physics of the Earth and Planetary Interiors

Abstract *The Earth's magnetic field is continuously changing both temporally and spatially. Recent geomagnetic field variations on decadal to centennial timescales are well documented over the past ~400 years; such secular variation in the past, however, is less well described. Determining such changes requires a rock record, that in the realm of the Pacific Ocean is only available from often uninhabited volcanic Islands. Here, we present paleomagnetic data from Isla Socorro and Isla San Benedicto, two islands in the Mexican Revillagigedo Archipelago in the eastern Pacific Ocean. On Isla San Benedicto, we sampled a lava delta from the 1952 CE eruption. The average direction from three locations is very close to the expected value. The intensity outcome, however, varies from 27.4 μT to 41.9 μT, whereas an intensity of 42.8 μT is expected according to the IGRF. We attribute this variation to a combination of rock magnetic and local magnetic anomaly disturbances induced by the underlying magnetic terrain. On Isla Socorro, we sampled the most recently deposited lavas in the island's southeast. Only one of these sites is associated with an absolute age constraint, with calibrated radiocarbon ages of 4052-2846 BCE and 4950-2846 BCE. Interestingly, this site yielded a very shallow inclination of 4.2°, whereas a Geocentric Axial Dipole predicts an inclination of 35° at this latitude. This might indicate a local distortion in the Earth's magnetic field at Revillagigedo during that period, possibly related to recurrent South Atlantic Anomaly–like behaviour. The paleointensities for the Socorro sites are in the range of 30-47 μT, which is consistent with the expected range of secular variation in this region.*

3.1. Introduction

The Earth is protected from solar storms and cosmic radiation by its magnetic field. The Earth's magnetic field is dominantly dipolar, but non-dipolar contributions cause high variability in direction and intensity in both time and space (Tauxe & Kent, 2004). At each location on Earth, the magnetic field can be described by a vector consisting of a declination, inclination, and intensity. Since the 17th century variations in declination and inclination have been measured directly, and since the 19th century scientists recorded the intensity of the geomagnetic field as well. To understand the variations in the Earth's magnetic field prior to that we rely on paleomagnetic data. Such data can be obtained from both sedimentary and volcanic rocks, or from archaeological artefacts. For the absolute intensity of the past Earth's magnetic field one can only rely on archaeological material and volcanic rocks, and particularly for oceans like the Pacific, which covers one third of the area of our planet, obtaining such records is a challenge. As a result, the paleomagnetic dataset is not equally distributed over the globe, as archaeological or volcanic samples are not available everywhere and are often located in difficult to reach regions, such as isolated volcanic islands or regions in the Southern Hemisphere (GEOMAGIA50, Brown et al. (2015)). Therefore, obtaining paleomagnetic data from additional locations to improve the global distribution of paleomagnetic data is important. The aim of this study is to obtain paleomagnetic data from the youngest lava flows at two volcanoes of the remote Mexican archipelago of Revillagigedo during a multidisciplinary investigation of the islands in 2022. This extends the paleomagnetic database with data from a remote and few accessible area and may contribute to improving our understanding of the behaviour of the Earth's magnetic field over

the last ~5000 years.

On San Benedicto island, a volcanic eruption created a large lava delta in the south-east in 1952 CE. We collected samples from three sampling locations on this 1952 CE lava delta. Therefore, we can compare the paleomagnetic data obtained on San Benedicto with the reference value according to the International Geomagnetic Reference Field (IGRF, Alken et al. (2021)), to check how well this lava records the Earth's magnetic field. We also visited Isla Socorro, the largest island of the Revillagigedo Archipelago. Previously, the study of Sbarbori et al. (2009) obtained full-vector paleomagnetic data from Isla Socorro. They found a mean direction of -2.8° in declination and 40.2° in inclination, which aligns approximately to the expected Geocentric Axial Dipole (GAD) direction of 35° for this location. The average paleointensity of their sites was 30±7.1 μT, which corresponds to an average virtual axial dipole moment (VADM) of 67.6±16 ZAm^2. This is lower than the current field strength of about 38.5 μT or 87 ZAm^2 in the Revillagigedo Archipelago. The Sbarbori et al. (2009) sampling locations were mainly from the oldest, pre- and syn-caldera deposits (540-370 ka). The post-caldera formations are the youngest according to Bohrson et al. (1996) (<180 ka) but only four of the Sbarbori et al. (2009) sampling sites are from the two post-caldera formations. These post-caldera formations are located in the south-eastern quadrant of the island. Therefore, this part of Socorro was the focus of our paleomagnetic field campaign. We present paleomagnetic data from nine sampling locations on Isla Socorro that are most likely of Pleistocene age. One of the sampling locations was dated to uncalibrated 4690±270 BP and 5040±460 BP using ^{14}C (Farmer et al., 1993).

3.2. Geological setting and sampling strategy

The Revillagigedo Archipelago comprises four volcanic islands: Socorro, San Benedicto, Clarión, and Roca Partida (Fig. 1A). These remote islands are situated in the Pacific Ocean between 400-700 km southeast of the tip of the coast of Baja California, Mexico. In March 2022 we visited Isla Socorro and Isla San Benedicto as part of a multidisciplinary field expedition, where we collected samples for this paleomagnetic reconnaissance survey. The two islands are approximately 50 km apart and both located at the northern part of the Mathematician ridge near the Clarion Fracture Zone (Bryan, 1966). The Mathematician ridge is an abandoned mid-ocean ridge spreading center, the northern boundary of which went extinct ~3.15 Ma ago after which spreading shifted to the East Pacific Rise (Mammerickx et al., 1988). The spreading center became inactive before the oldest known eruptions of Socorro, which may be the youngest part of a hotspot track (Fleitout & Moriceau, 1992). Currently, there are active fumaroles near the summit of the Evermann volcano on Socorro and the most recent significant reported activity was in 1993 CE when floating scoriaeous blocks from a submarine vent on Socorro rose to the surface (Siebe et al., 1995). Earlier small eruptions are summarized in Bryan (1966) and probably occurred on Socorro in 1951, 1896, and 1848 CE. Von Humboldt (1811) mentioned the observation of floating pumice during an expedition in 1803 CE. Although none of these activity reports mention the formation of lava flows, they indicate that Isla Socorro shows signs of volcanic activity and therefore young volcanic deposits might

be present. On San Benedicto we know young volcanic deposits are accessible: a series of eruptions in 1952-1953 created a completely new volcano: Volcán Bárcena (Richards, 1959) (Fig. 1B,D).

3.2.1. Isla San Benedicto

Isla San Benedicto is the second largest island of the Revillagigedo archipelago, although it is just 4 km long by 2 km wide (Fig. 1B) and uninhabited. The most recent episode of volcanic activity started in August 1952 and created the Bárcena volcano. Few geological studies were done on the island; the most extensive research is by (Richards, 1959, 1965, 1966), carried out in 1952-1957 in the aftermath of the volcanic eruption. The eruption created the Bárcena tephra cone, located south of the older crater Herrera. Volcanism of the older crater probably occurred during the Pleistocene (Richards, 1959) but none of the deposits are dated. The young Bárcena cone is predominantly composed of trachydacite tuffaceous material, tephra, and fine ash layers. Adjacent to the southeastern part of the cone, a lava delta formed in December 1952 to February 1953 when blocky aa lava flowed out of a basal fissure into the ocean (Richards, 1966) (Fig. 3.1D). Most volcanics are trachybasalt and trachyandesites; samples from the lava delta are chemically classed as sodic trachytes (Richards, 1966). We collected samples at three locations (SB1-3) on the northern part of the lava delta (Fig. 1.1B, Table 3.1).

3.2.2. Isla Socorro

Isla Socorro is the largest of the four Revillagigedo islands, approximately 17 km long and 16 km wide (Fig. 3.1C). The highest point of 1130 m belongs to the top of the basaltic shield volcano the Cerro Evermann. Isla Socorro is uninhabited, except for a navy base in the south. This part of the island is also the least vegetated area and there are some roads; therefore most previous research was done here. The island's exposed units are generally grouped in two phases of volcanic activity: the pre- and syn-caldera phase (540-370 ka) and the post-caldera phase (<180 ka) (Bohrson et al., 1996; Bryan, 1959; Bryan, 1966). The post-caldera phase is further divided into the Cerro Evermann Formation and the Lomas Coloradas Formation. Both formed simultaneously in the 180-12 ka period, the oldest 40Ar/39Ar age of 179±2 ka and the youngest $^{40}Ar/^{39}Ar$ age of 12±2 ka are both from the Cerro Evermann Formation. There is one very recent dated deposit, with uncalibrated radiocarbon ages of 4690±270 BP and 5040±460 BP from lacustrine deposits (Farmer et al., 1993) located within the Lomas Coloradas Formation in the saddle area between two scoria cones. When calibrated in MatCal (Lougheed & Obrochta, 2016) with the ^{14}C calibration curve IntCal20 (Reimer et al., 2020), these age ranges fall between 4052-2846 BCE and 4950-2846 BCE, respectively. The lacustrine deposits are overlain by a basaltic lava that must be younger. According to Bohrson et al. (1996), the Lomas Coloradas Formation erupted between 150 to 70 ka. However, these recent radiocarbon ages indicate volcanic activity did not completely cease after 70 ka. Therefore, sampling this formation and the nearby region of the young basaltic flow were the main aims for the paleomagnetic fieldwork.

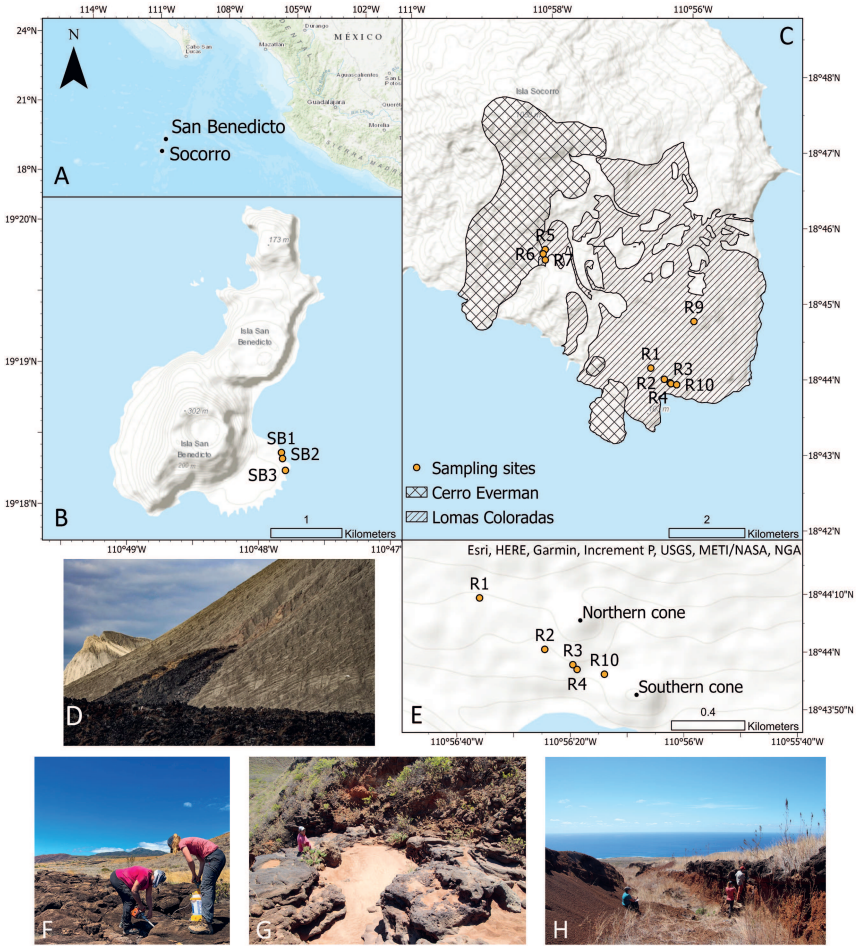


Figure 3.1: Sampling locations in the Revillagigedo Archipelago, Mexico (A) were on the islands of San Benedicto (B) and Isla Socorro (C). The outcrop area of the Cerro Evermann and Lomas Coloradas Formations on Isla Socorro are after Bohrson et al. (1996). In (E) are the sampling sites around the scoria cones, the northern cone is unit 7 and the southern cone is unit 8. Pictures from the field expedition are from (D) the fissure on the southeastern side of Volcano Bárcena on San Benedicto with the 1952 CE lava delta in the front, (F) sampling location R3 on Socorro, (G) the river gully of sampling location R7 and (H) sampling location R9

3.2.3. Sampling Strategy

Previous paleomagnetic work of the Lomas Coloradas and Cerro Evermann Formations was done by Sbarbori et al. (2009). Those authors obtained samples from four lavas within these formations. One site was in the Lomas Coloradas Formation, which showed non-ideal behaviour during paleointensity experiments and could not be interpreted. The other three sites were within the Cerro Evermann Formation, of which one was discarded because of magnetic biasing from lightning strikes. We collected samples from a total of nine locations from the Lomas Coloradas Formation on the south-east of the island, referred to as R-sites (Fig. 3.1C), the youngest and stratigraphically highest of the local stratigraphy. Because the objective was to sample recent lavas, only the radiometric dating technique with radiocarbon (^{14}C) could be useful. We were not able to collect additional material for ^{14}C dating of the sites, and we therefore explore whether anomalous directions or paleointensities are apparent that may warrant additional research. Site R10 was sampled closest to the dated deposit with ^{14}C ages of 4690±270 BP and 5040±460 BP. Since detailed GPS coordinates were not published for the flow above the dated rocks, we used the geological map, pictures, and descriptions provided to assure that the lava we sampled corresponds to the black vesicular basalt described in Farmer et al. (1993).

Since specific age constraints were not available, Bohrson et al. (1996) assigned relative age relations to units within the Lomas Coloradas Formation, labelled younger or older than the adjacent unit in their geological map. We sampled volcanic deposits from four of these units (Table 3.1). For some units we have multiple sampling locations, so we can test whether their paleomagnetic directions and intensities are similar and therefore whether these deposits might be of similar age. Sampling site R1 corresponds most likely to a small strip of the larger flow unit 15; site R9 is sampled in a river gully in this unit as well (Fig. 3.1F). Sampling sites R2, R3, R4, and R10 were taken around two scoria cones (Fig. 3.1E). Flow unit 7 is the northern cone; in this unit we sampled our sites R2, R3, and R4. Site R10 was taken from the saddle area between the two scoria cones of which the northern cone is unit 7 and the southern cone is unit 8. According to Farmer et al. (1993), the basaltic flow is from the northern cone. Site R10 was indeed sampled on a flow directed downward from the northern cone to the southeast, but because the location is within flow unit 8 we will assign both unit numbers to site R10. Finally, sampling sites R5, R6, and R7 were from flow unit 17. R5 and R6 are sampled on top of a massive appearing lava flow; R7 is sampled in a river gully (Fig. 3.1G) at a lower elevation, and this lava flow could be older than the one sampled at R5 and R6. One unoriented block was collected at site R8, and therefore this site was not further used in this study. According to Bohrson et al. (1996), units 7 and 8 are the youngest of the units we sampled on Isla Socorro, preceded by unit 17, and unit 15 is the oldest.

For each site, between 10 to 20 paleomagnetic samples up to 15 cm in length and 25 mm in diameter were collected with a standard gas-powered paleomagnetic drill. Samples were taken over several 10s of meters of the exposure and taken from different blocks, which were checked to have cooled in-situ. For most locations, samples were obtained from the top of the flow unit. Except for site R9, where only the

side of the lava was accessible, and sites R1 and R3 from which samples were taken from both the side and top of the flow. Orienting paleomagnetic cores is preferably done with a solar compass to avoid any influence of possibly strongly magnetized neighbouring rocks on the measured declination. This was done except where the exposure was in the shade or during overcast weather conditions. Hence samples from sites SB1, SB2, SB3, and R1 were only oriented with a magnetic compass.

3.3. Methods

3.3.1. Rock Magnetic Characteristics

The remanence magnetization carriers and suitability of the samples for paleomagnetic measurements were tested with rock magnetic analyses. The Curie temperature (T_C) was measured to identify the best temperature steps for paleointensity experiments. T_C was measured on a horizontal translation Curie Balance (Mullender et al., 1993). For each site, one small sample (20-30 mg) was heated from room temperature to subsequently higher temperatures of 75, 225, 300, 375, 450, 525 and 600 °C. After each step the temperature was lowered by 75 °C to check the reversibility of the signal. The highest temperature at which the magnetic signal is still reversible is referred to as the alteration temperature (T_{alt}). The Curie temperature was determined using the two-tangent method.

The magnetic domain state of the samples was assessed with hysteresis measurements. One sample (5-15 mg) per site was measured on an Alternating Gradient Magnetometer, and for each sample a hysteresis loop and back-field/DCD curve was measured. The maximum field was set to 500 mT with an averaging time of 150 ms. The slope correction of the hysteresis loop was set to 70% to remove the paramagnetic contribution to the magnetic signal. The saturation magnetization (M_s), remanent saturation magnetization (M_{rs}), and coercive force (B_c) were calculated from the hysteresis loop. The remanent coercive force (B_{cr}) was obtained from the DCD curve. The ratio of remanence (M_{rs}/M_s) and coercivity (B_{cr}/B_c) can inform whether the sample is in the single domain (SD), pseudo-single domain (PSD), or multi-domain (MD) range in the Day diagram (Day et al., 1977), although this interpreted space has limitations with mixed coercivity and mineralogy (Roberts et al., 2018). Most of the (titano)magnetite-carrying igneous rocks in paleomagnetic studies are expected to be within the pseudo-single domain range. To provide more information about the domain state of the samples, in addition to the classic hysteresis measurements First Order Reversal Curves (FORCs) (C. R. Pike et al., 1999) were measured. The FORCs were measured using the same alternating gradient magnetometer, the saturating field was set at 200 mT, the averaging time at 200ms and Hu ranged from -40mT to 40 mT. From one sample per site a total of 240 FORCs were measured and the FORC data were processed using FORCinel 3.08 (Harrison & Feinberg, 2008) with the VARIFORC algorithm (Egli, 2013). All smoothing parameters are in Supp. Table 3.2.

3.3.2. Paleodirections

To determine the paleomagnetic direction of the sites, samples were subjected to both thermal and alternating field (AF) demagnetization experiments. Four sam-

ples per site were thermally demagnetized in steps of 50 °C up to 600 °C. For the SB-sites this was limited to two samples per site, as these three sampling locations are expected to give the same result and therefore all specimens can be grouped afterwards. After each thermal demagnetization step the remaining magnetization was measured on a 2G cryogenic magnetometer. Some samples from sites R3, R4, R5, and R6 were magnetically very strong and therefore measured on a JR-6 spinner magnetometer. AF demagnetization experiments were performed using a robotized 2G DC-SQUID cryogenic magnetometer (Mullender et al., 2016). For the SB-sites, six samples were subjected to AF demagnetization and for the R-sites eight samples were used. These samples were demagnetized in 18 AF steps ranging from 0 to 270 mT. During all measurements, the samples were kept in a magnetically shielded environment. The demagnetization results were analysed using paleomagnetism.org online data reduction software (Koymans et al., 2016, 2020) and plotted in Zijderveld diagrams (Zijderveld, 1967). The Characteristic Remanent Magnetization (ChRM) was identified as a straight line to the origin. Samples with a Maximum Angular Deviation (MAD)>10° were removed from further interpretation. Site mean directions were calculated with Fisher statistics (Fisher, 1953) and the outliers were identified in the Virtual Geomagnetic Pole (VGP) distribution using a 45° cutoff. For sites that were sampled close together, i.e., in the same flow or unit, or that show similar directional results, we checked whether they share a Common True Mean Direction (CTMD). When the CTMD test is positive the directions are statistically indistinguishable (Tauxe, 2010) and the sampled rocks may represent the same spot reading of the paleomagnetic field. This can be interpreted as such sites recording a coeval remanence.

3.3.3. Paleointensities

The absolute paleointensity of the sites was determined using Thellier-Thellier type (Thellier, 1959) paleointensity measurements. Between six (SB-sites) to eight (R-sites) specimens were subjected to the IZZI-Thellier technique (Tauxe & Staudigel, 2004), which combines the zero-field, in-field (ZI) method (Coe, 1967) and the in-field, zero-field, (IZ) method (Aitken et al., 1988). After each group of four steps (ZIIZ) we included a partial thermal remanent magnetization (pTRM) check (Coe et al., 1978) to check for changes to the capacity of the samples to acquire a TRM. The samples were glued with quartz-wool and a potassium silicate solution into small glass cups. Depending on their Curie temperature, the samples were measured in different batches starting from 50 °C, 100 °C or 200 °C up to 610 °C or until they were demagnetized. After each heating step the (remaining) magnetization was measured on a 2G cryogenic magnetometer in a magnetically shielded room.

For the in-field steps a DC field of 50 μT was applied during heating and cooling. The NRM remaining was plotted against the pTRM gained in an Arai plot for each sample (Nagata et al., 1963). In the Thellier-Thellier method it is assumed there is a linear relationship between the NRM of a sample remaining after heating and the imparted TRM under a laboratory field. Many samples, however, exhibit non-ideal behaviour during thermal paleointensity experiments (Coe, 1967). Typical reasons for failure of paleointensity experiments are the presence of multi- or pseudo-single domain grains, resulting in a 'sagged' or downward curved Arai plot (Dunlop &

Table 3.1: Sampling sites and rock magnetic characteristics. Given are the sites, their assigned unit, in which the numbers represent the flow units defined by Bohrson et al. (1996), latitude and longitude, elevation (Elv), flow unit according to Bohrson et al. (1996), dominant Curie Temperatures (T_c) and alteration temperature determined from the magnetization vs temperature diagrams (T_{alt}). Observed domain state are single vortex state (A), uniaxial non-interacting single domain (B) and multidomain behaviour (C). *R10 is on the border of the two units, the radiocarbon age could be 4690±270 BP to 5040±460 BP.

Site	Unit	Lat (N)	Long (W)	Elv (m)	T_c (°C)	T_{alt} (°C)	Domain
SB1	1952-flow	19.3059	110.7967	5	150/580	375	A
SB2	1952-flow	19.3053	110.7967	5	180/580	375	A
SB3	1952-flow	19.3037	110.7967	5	200/570	375	AC
R1	15	18.7336	110.9433	80	200/550		A
R2	7	18.7335	110.9401	56	220	225	AD
R3	7	18.7327	110.9388	55	570	300	AB
R4	7	18.7325	110.9386	51	340/530	225	A
R5	17	18.7621	110.9684	383	580	525	AB
R6	17	18.7612	110.9688	380	140/560	375	A
R7	17	18.7598	110.9684	360	570		AC
R9	15	18.7462	110.9331	240	180/540	300	A
R10	7 and 8*	18.7322	110.9372	46	300/560	225	AB

Özdemir, 2001; Tauxe et al., 2021), or thermal alteration, resulting in failed pTRM checks. To check for non-ideal behaviour the paleointensity results are interpreted in the online analysis platform paleointensity.org (Béguin et al., 2020). We used the automated interpretation function and six different sets of selection criteria to assess the quality of our results: TTA and TTB (Leonhardt et al., 2004), SELCRIT2 (Selkin & Tauxe, 2000), PICRIT03 (Kissel & Laj, 2004), CLASS-A (L. V. de Groot et al., 2014a), and CCRIT (Cromwell et al., 2015b). The first four included the modifications as proposed by Paterson et al. (2014). The Arai plot curvature criteria k'<0.35 was applied to all except CCRIT to detect MD behaviour. CCRIT is the strictest criterion and has a threshold of k'<0.164. The other selection criteria values can be found in Supp. Table 3.3. All interpretations that pass one or more selection criteria are considered when calculating site mean paleointensities. Therefore, interpretations that pass more sets of selection criteria are deemed more reliable and are given a greater weight in the resulting paleointensity.

3.4. Results

3.4.1. Rock Magnetic Characteristics

The magnetization-vs-temperature diagrams (Fig. 3.2A-C and Supp. Fig. 3.1) reveal that the samples yield a range of Curie temperatures (Table 3.1). Several samples carry two Curie temperatures, an indication of the presence of two populations of magnetic minerals. Among the latter are the samples from all three sites of San Benedicto (Fig. 3.2A) and R1, R4, R6, R9, and R10 from Socorro. Sites R3, R5, and R7 yield a single T_C close to 580 °C; the dominant magnetic carrier in these samples is therefore magnetite. Except for sites R1 and R7 (Fig. 3.2C), which show re-

versible behaviour, all samples exhibit some degree of alteration. The alteration of R5 is small and only at the higher temperature step 520°C; this is the only sample with a cooling curve slightly lower than the heating curve. In contrast, R2 (Fig. 3.2B), R4, and R10 have a low alteration temperature around 225 °C. Site R2 in particular shows a high degree of alteration with a cooling curve much higher than the heating curve. These heating-cooling curve differences can be an indication of oxyexsolution during cooling, where the initial titanomagnetite with a lower T_C exsolves into intergrowths of Ti-rich ilmenite and Ti-poor magnetite, thereby raising the Curie temperature (Dunlop & Özdemir, 1997). The sites that indicate a high degree of alteration are considered not ideal for paleointensity experiments (Coe, 1967; Tauxe, 2010). Nonetheless, as perhaps not all samples of a site experienced the same amount of alteration regardless of their rock magnetic characteristics, all sites were subjected to paleointensity experiments.

Hysteresis experiments indicated that the domain structure of all samples is within the PSD domain (Fig. 3.2F) of the Day plot and they fall along the theoretical mixing lines of Dunlop (2002). This is expected for these lava flows because most basaltic samples plot within this PSD area (e.g., Tauxe et al., 2002). Examples of hysteresis curves are in Fig. 3.2D,E and Supp. Fig. 3.2. Back field curves are in Supp. Fig. 3.3. An initial interpretation is that these lavas contain a mixture of SD to MD titanomagnetite grains (e.g., Dunlop, 2002). Representative FORC diagrams are shown in Fig. 3.2G-I. The FORC diagrams mostly agree with the PSD field: the FORCs show consistent single-vortex (SV) behaviour (Table 3.1, Fig. 3.2G-I), which is the leading physical explanation of PSD behaviour (e.g., Roberts et al., 2017). Thus, we conclude that stable remanence in these lavas is carried by a mixture of SD and stable vortex-sized grains, with some unstable remanence carried by an MD component. In the Day-plot, M_{rs} and B_{cr} are largest for site R2, suggesting the presence of smaller sized grains. The FORC diagram of R2 (Fig. 3.2G) shows a vertical spread at Bc 40-100mT with a long central ridge tail, perhaps due to a higher coercivity content (Supp. Fig. 3.3). For R6 (Fig. 3.2E) the B_{cr}/B_c ratio is especially high, suggesting a larger magnetic contribution from multi-domain grains. The FORC diagram of this site is slightly anomalous, it yields some SV state grains but there is influence of other states. For sites R3, R5, and R10, besides the single vortex state we observe a well-defined central ridge and negative FORC distribution along the Bu axis (Fig. 3.2H-I), which is characteristic of uniaxial non-interacting SD magnetite (Egli, 2013; Newell, 2005; Roberts et al., 2014). This suggests an ideal assemblage for recording the magnetization. The presence of multidomain magnetite besides the SV behaviour is seen in R7 and SB3 (Supp. Figure 3.4), which would make them less ideal for paleointensity experiments (Dunlop & Özdemir, 2001; Fabian, 2001; Paterson, 2011).

3.4.2. Paleodirections

The paleodirectional data obtained from San Benedicto and Isla Socorro generally show consistent demagnetization behaviour between samples from the same site (Fig. 3.3A,B and Supp. Fig. 3.5, 3.6) and no overprints for most sites as expected for recent lavas. There are some exceptions, with three samples of site SB1 and two samples from R2 from the AF demagnetization experiments did not trend to the

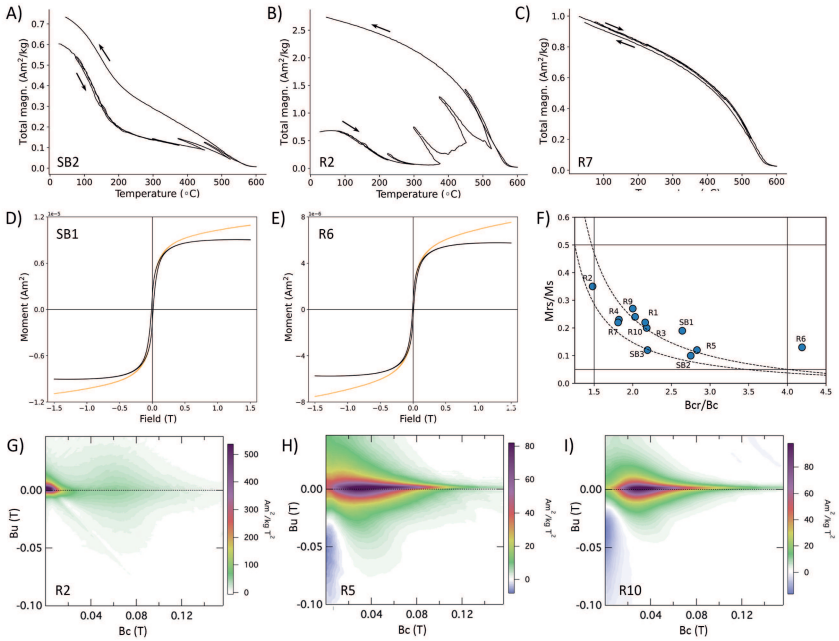


Figure 3.2: Magnetization as a function of temperature plot of A) SB2, B) R2 and C) R7. Arrow pointing down is the heating curve, arrow pointing up is the cooling curve. Examples of hysteresis curves are shown for D) SB1 and E) R6. The black loop is with a 70% correction for the paramagnetic contribution, in orange is the raw data. In (F) the results for M_{rs}/M_s and B_{cr}/B_c ratios of the samples are plotted in the Day-diagram. Vertical and horizontal lines indicate the boundaries for SD, PSD and MD domains. Dashed lines are the theoretical mixing curves of (Dunlop, 2002). FORC diagrams of R2, R5, and R10 are in G-I.

origin of the Zijderveld diagram (Supp. Fig. 3.5, SB1). Furthermore, the Zijderveld diagram of three samples from R6 are chaotic and the best fit shows a maximum angular deviation (MAD)>10°. These samples are therefore not used for further paleodirectional analyses. Samples from site R3 show univectorial demagnetization behaviour, and samples lost their magnetic signal around 550 °C or AF steps 60-150 mT with typical MAD values <3° (Supp. Fig. 3.5). The resulting directions, however, are scattered: when all samples are accepted the k-value is just 1.2 – an almost random distribution. We therefore excluded this site from further interpretation. The obtained mean paleomagnetic ChRM directions for all other sites are in Table 3.2 and Fig. 3.3C, rejected samples not described above did not pass the 45° VGP cut-off.

We could not use the solar compass due to overcast weather at sites SB1, SB2, SB3, and R1. The results from the sampling locations on Socorro for which we have both sun and magnetic compass readings show that the differences between these two orientations are generally small, on average just 1.2° (Table 3.2 and Supp. Table 3.1). The declination of R5 changes most, with a correction of 3.6°. Interestingly, the resulting k-values and α_{95} values show considerable differences between the sun and magnetic compass readings. Site R5 shows the largest variations. Compared to the magnetic readings, the solar compass results for site R5 show a decrease in α_{95} by 1° and an increase in the k-value by 82. Except for site R4, the k-value increases and the α_{95} value decreases for all paleomagnetic directions. The use of a magnetic compass therefore appears to introduce an additional noise or bias in the data compared to sun compass readings.

According to the IGRF, the expected paleomagnetic direction for the SB-sites is a declination of 10.5° and an inclination of 43.7° in December 1952. The site means of SB1, SB2, and SB3 deviate from these reference values by different amounts (Table 3.2), although these deviations are within the α_{95} range. The angular difference between the measured vector and the IGRF is smallest for SB2 at 4.7°, and largest for SB1 at 7°. The largest variation from the expected value in the mean declination is 6.1° for SB2. SB1 shows the largest inclination variation, at 6.1° lower than expected (Table 3.2). Surprisingly, the directions of SB1 and SB2 differ considerably from the direction of SB3: the declination of SB1 and SB2 are close together, whereas the declination of SB3 deviates approximately 12° from SB1 and SB2. The maximum difference in inclination is 10.3° between SB1 and SB3. Therefore, only SB1 and SB2 share a CTMD, whereas SB3 fails a CTMB test with both SB1 and SB2. When combining the specimens of the three sites, however, the mean direction is is only 1.3° off from the IGRF reference value.

The directions from sites R2 and R4 have the lowest precision parameter k and largest confidence limit α_{95}. A low k-value does not necessarily mean an unreliable result. This is, for example, reflected in the grouped SB1+2+3 sites, which yield more accurate results compared to a single SB-site, despite having a lower k-value of 63.3. However, the k-values of R2 and R4 are even lower. Site R2 has a k-value of 27 and an α_{95} of 10.1°. R4 has a k-value of 13.2 and an α_{95} of 13.1°, and therefore these two sites are unreliable. The paleomagnetic directions of all other R-sites have

Table 3.2: Directional results. The measured directions per site are given by the parameters: number of samples accepted/number of samples measured (n/N), the declination from magnetic or solar compass readings (Dec), inclination (Inc), 95 percent confidence interval (α_{95}), precision parameter (k) and the separate errors for declination (ΔD_x) and inclination (ΔI_x). ΔDec and ΔInc are the differences from the IGRF-values and ΔAngle is the angular difference between the two vectors.Results in italic are unreliable. For sites from similar units, the grouped directions are also given.

Site	n/N	Dec (°)	Inc (°)	α_{95}(°)	k	ΔD_x	ΔI_x	ΔDec	ΔInc	ΔAngle
SB1	5/8	15.1	37.6	7.9	93.9	9.9	13.2	4.6	-6.1	7.0
SB2	8/8	16.5	42.0	7.3	58.6	8.3	10.0	6.0	-1.7	4.7
SB3	8/8	5.2	47.9	5.0	123.0	7.1	7.3	-5.3	4.2	5.6
SB1+2+3	21/24	12.2	43.3	4.0	63.3	4.8	5.7	1.7	-0.4	1.3
R1	11/12	2.9	33.3	3.1	220.8	2.6	3.8			
R2	9/12	*-8.6*	*15.8*	*10.1*	*27.0*	*9.1*	*17.1*			
R3	0/12									
R4	12/12	*7.1*	*17.9*	*12.7*	*13.9*	*11.9*	*21.9*			
R5	12/12	4.0	29.9	3.2	190.8	2.8	4.4			
R6	7/12	29.1	28.9	4.7	165.6	6.0	6.9			
R7	12/12	0.8	28.9	6.0	53.4	6.0	9.4			
R9	10/12	-0.5	36.9	4.9	97.1	4.5	6.2			
R10	9/12	-7.4	4.2	4.0	163.7	3.8	7.5			
R1+R9	21/24	2.3	35.0	2.8	126.7	2.6	3.6			
R5+R7	24/24	3.6	29.5	3.8	63.0	3.9	6.1			
R5+R6+R7	31/36	9.7	29.8	4.5	34.8	4.9	7.6			

lower uncertainties and have an α_{95} value <7° and k>50. The inclination for all but one of these sites ranges from 28.9° to 36.9°, which is expected for this latitude based on the GAD hypothesis. Site R10 yields an interesting shallow inclination of 4.2° in combination with an easterly declination.

3.4.3. Paleointensities

Ninety samples were subjected to the IZZI-Thellier paleointensity technique: 64 of them passed one or more sets of selection criteria. However, some of the segments interpreted by paleointensity.org were unreliable because the samples gained almost no pTRM compared to the NRM lost during demagnetization; this produced extremely high paleointensity results between 100-700 μT (Supp. Fig. 3.5, R3). Some samples from sites R4 and R6, as well as all samples belonging to R3, were therefore removed from further analysis. Considering the scattered paleodirections and extreme paleointensity values, site R3 was most likely struck by lightning. Discarding site R3 results in 55 samples passing at least one of the sets of selection criteria, a success rate of 61%. One sample from SB1, one sample from R4, and two samples from R5 passed the strictest selection criteria CCRIT. The resulting paleointensities are in Table 3.3 and examples of Arai diagrams are shown in Fig. 3.3D-F.

Most samples from the SB-sites passed at least one set of selection criteria. Because the intensity in 1952 CE on San Benedicto is known, and was approximately 42.8 μT, we compare our results with this reference value. Of the three SB-sites, only SB1 is close to this value with a paleointensity of 41.9 μT. SB2 and SB3 produced lower paleointensities than expected: 27.4 μT and 38.5 μT, respectively (Supp. Fig. 3.5). The paleointensity of all interpretations from the three sites combined is therefore also

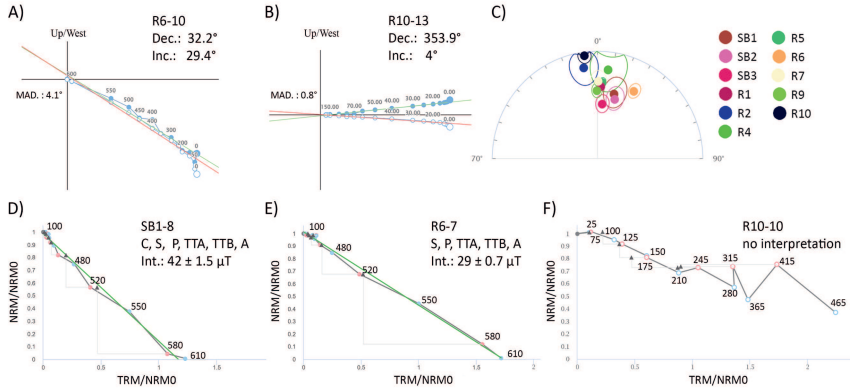


Figure 3.3: Zijderveld diagrams of thermal demagnetization experiments (A) and alternating field demagnetization experiments (B) of samples from sites R6 and R10. Closed circles are declination; open circles are inclination. Straight lines through the measurement steps indicate the ChRM direction. (C) The stereographic projection of the site mean directions and their confidence ellipses. (D-F) Arai plots of the IZZI-Thellier experiments from sites SB1, R6, and R10. Blue circles are the ZI-steps, red circles the IZ-steps, and triangles indicate pTRM-checks. Temperature steps are given, for readability only the first and last segments of SB1-8 and R6-7 are shown. The complete series of temperature steps can be found in Supp. Fig. 3.5, 3.6. Selection criteria are CCRIT (C), SELCRIT (S), PICRIT (P), TTA, TTB, and CLASSA (A). The green line is the largest segment that passed a selection criterium; intensity shown is the average result of all selection criteria.

8.3 μT lower than expected. Some of the SB-samples display non-ideal behaviour in the Arai diagrams. Two samples of SB1 and three samples of SB3 exhibit a curved Arai plot, indicative of multi-domain behaviour (Dunlop & Özdemir, 2001; Fabian, 2001). A small 'zigzag' pattern between temperature steps 350-480 °C is observed for one sample of SB1 and SB3 and in three samples of SB2.

The sites sampled on Socorro were less successful in the IZZI-Thellier measurements. R2 and R3 yielded no interpretable results. Only three samples from R4 could be interpreted and the resulting paleointensity is 7.3 μT. Even though one of the samples passed the strictest selection criteria (CCRIT), there are several reasons to question this anomalously low paleointensity. First, the paleodirection of R4 has a large α_{95} value; for some samples this is because of a small overprint which suggests there may be an issue with how the magnetization is recorded in the samples. Additionally, two paleointensity samples from R4 could not be interpreted because of the steep NRM/TRM slope; another sample exhibited sagging behaviour most often attributed to multi-domain behaviour. In combination with the low alteration temperature determined from the thermomagnetic curves, we therefore consider results from this site unreliable. From sites R7, R9, and R10, as many as six samples passed the selection criteria but all have a large scatter in the paleointensities from different samples (i.e., a large σ/PI ratio). Samples from site R7 especially show sagging behaviour in the Arai diagrams, and the first temperature steps pass some selection criteria and provide a paleointensity of 60-70 μT but the higher temperature steps yield paleointensities of 10-20 μT. The most reliable paleointensities are

Table 3.3: Paleointensity results. The obtained paleointensities per site are given by the parameters: number of samples that pass a set of selection criteria/number of samples measured (n/N), number of interpretations (n_int), resulting paleointensity (PI), standard deviation (σ), standard deviation divided by the paleointensity in percent (σ/PI) and the difference with the IGRF-value (ΔInt). Unreliable results are in italic.

Site	n/N	n_int	PI (μT)	σ	σ/PI	ΔInt
SB1	5/6	173	41.9	5.0	12.0	-0.9
SB2	6/6	212	27.4	4.1	14.9	-15.4
SB3	6/6	56	38.3	5.9	15.4	-4.5
SB1+2+3	17/18	439	34.5	5.8	12.2	-8.3
R1	7/8	86	47.3	5.8	12.2	
R2						
R3						
R4	3/8	*131*	*7.3*	*0.8*	*11.5*	
R5	8/8	378	29.8	5.4	18.0	
R6	6/8	338	34.7	7.3	21.0	
R7	5/8	*40*	*57.1*	*24.2*	*42.4*	
R9	7/8	*161*	*41.9*	*12.7*	*30.3*	
R10	2/8	*20*	*41.9*	*18.2*	*43.5*	
R1+R9	14/16	247	43.8	11.1	25.3	
R5+R6	14/16	716	32.1	6.8	21.1	
R5+R6+R7	19/24	*756*	*33.5*	*10.3*	*30.8*	

measured from sites R1, R5, and R6. These yield paleointensities of 29.8 μT, 34.7 μT, and 47.3 μT, respectively, which correspond to VADMs of 67.8, 79.1, and 106.2 ZAm^2.

3.5. Discussion

We obtained paleodirectional and paleointensity data from the islands of San Benedicto and Socorro. The dataset is discussed below according to the relative age of the sampled units, starting with the youngest flow from the 1952 CE eruption on San Benedicto and concluding with unit 15 of the Lomas Coloradas Formation on Socorro.

3.5.1. The 1952 San Benedicto flow

The three sampling sites on San Benedicto were from the 1952 CE lava flow. The expected IGRF field values are a declination of 10.5°, an inclination of 43.7°, and an intensity of 42.8 μT. The site level ChRM directions and intensity results deviate from these IGRF-values by different amounts (Table 3.2, 3.3). There are several possible explanations for these deviations. The declination variation could be due to the use of a magnetic compass to orient the samples: the magnetization of nearby rocks can influence the ambient magnetic field, offsetting the magnetic compass readings at these sampling locations. However, even though the declination deviation is limited to 6°, they are still too large to be explained by the magnetic compass alone - certainly because the difference between the sun and magnetic compasses yielded a deviation of only 1.2° on average for the Socorro sites. Therefore, we do

not conclude that the use of a magnetic compass is the sole explanation for the declination deviations, especially because the inclination also deviates from the expected value. The sites may have experienced post-cooling movement. Because samples were collected from a larger area and from different blocks, any individual block rotations should be detectable, whereas a uniform rotation of the entire site would affect all directions equally. In addition, the intensity values also show a deviation from the expected value, up to 15.4 μT lower for SB2. Lower-than-expected paleointensities are often reported for historical lavas (e.g., Biggin et al., 2007; L. V. de Groot et al., 2013; Meyer & de Groot, 2024; Smirnov et al., 2017; Tanaka et al., 2012). Frequently, such lower-than-expected values are attributed to rock magnetic characteristics such as multi-domain effects or alteration. This might also be the case for the SB-samples, because a few display minor amounts of zig-zagging or sagging in the Arai diagrams (Supp. Fig. 3.5), which are characteristic of these effects. However, multi-domain magnetite is only observed in the FORC diagram of SB3. Furthermore, the intensity of SB1 was consistent whereas it has the same rock magnetic characteristics as SB2, a similar alteration temperature around 375 °C and the Arai plots of SB2 do not clearly show more non-ideal behaviour than SB1 or SB3. We therefore evaluate other options for the large deviation of SB2. Possibly, the rocks could be affected by magnetic anomalies arising from the underlying flow. Magnetic anomalies create a local disturbance in the magnetic field, and thus influence the remanence stored in a new flow during cooling. This 'magnetic terrain effect' cannot be corrected by using a solar compass, and it also affects the inclination. Similar deviations from the actual geomagnetic field caused by magnetic anomalies were reported for Hawaii (Baag et al., 1995), La Palma, Tenerife (Valet & Soler, 1999), and Mt. Etna (Meyer & de Groot, 2024; Tanguy & Le Goff, 2004). Such local anomalies would be larger in areas with large topographic differences, which was the case for the 1952 CE flow on San Benedicto. The lava flow had a very irregular topography, with gullies up to 3m deep, there were large blocks, and sampling was performed in topographic lows within the lava.

Previous studies on the magnetic terrain effect found a correlation between lower inclinations and lower intensities (B. M. de Groot & de Groot, 2019; Meyer & de Groot, 2024). We do not see this for our SB-sites: the declination and inclination of all three SB-sites deviates from the IGRF-value in some amount but there appears to be no correlation with intensity deviation. Previous analyses also predict that magnetic anomalies are averaged when sampling is performed over sufficiently large distances (e.g., Meyer & de Groot, 2024; Tanguy & Le Goff, 2004; Villasante-Marcos & Pavón-Carrasco, 2014). This is the case for the average direction for sites SB1+2+3, which is statistically indistinguishable from the expected direction; we, however, do not see this reflected in the average intensity of the three SB sites. Magnetic anomalies may therefore explain a part of the disagreement between the paleodirections and the expected values, but the reason for the significantly higher intensity deviation of up to 15 μT remains unclear. In summary, we infer that the difference between the directions and intensities of the SB-sites and the reference value can be explained by a combination of the use of a magnetic compass and the magnetic terrain effect.

3.5.2. Lomas Coloradas Formation unit 7 and 8

Bohrson et al. (1996) did not distinguish between the ages of the Lomas Coloradas Formation unit 7 and 8, which are two scoria cones in the south of Socorro island. We sampled sites R2, R3, and R4, south of the northern cone (Fig. 3.1E). In both directional and paleointensity experiments the three sites show erratic paleomagnetic behaviour,and were deemed unreliable. The paleodirectional results from R2 and R4 have large error ranges, with an α_{95} larger than 10° and k-values as low as 27 and 13.2. During the IZZI-Thellier experiments most samples from R2 and R4 were affected by thermal alteration in the higher temperature steps, which was also observed in the magnetization-vs-temperature diagrams (Supp. Fig. 3.1). The largest heating-cooling curve differences and lowest alteration temperature was found for R2 (Fig. 3.2B); this sample also has a high coercive component revealed by the FORC measurements: this hampered interpreting the paleointensity in these samples.

Site R10 is in the saddle area between the two cones (Fig. 3.1E), on the border of unit 7 and 8. Although the other sampling sites from unit 7 yielded scattered results, site R10 successfully produced paleodirections and yielded an interesting inclination of only 4°. The geomagnetic implications of this result for the region are discussed below. Only two paleointensity samples passed a set of selection criteria, as most other samples suffered from thermal alteration during the higher temperature steps (Fig. 3.3F). One specimen passed three selection criteria but suffered from sagging. Therefore, only the lower temperature steps were interpreted and result in a paleointensity of 50.8±4.3 μT. The other sample only passed PICRIT, with a paleointensity of 6.3 μT. Two samples that are so far apart are not sufficient for a reliable paleointensity determination for this cooling unit.

The three sites within unit 7 failed to produce a reliable paleodirection and intensity, whereas site R10, located at the boundary between the two scoria cones, did yield a reliable paleodirection. It appears that the flow of R10 produced reliable directional data, whereas the volcanics from the northern scoria cone did not. Therefore, we advise future paleomagnetic studies to not sample unit 7.

3.5.3. Lomas Coloradas Formation unit 17

Sampling sites R5, R6, and R7 were obtained from flow unit 17. Their inclinations agree within 1°, but the declination of site R6 deviates 27° from the declinations of R5 and R7. Therefore, only R5 and R7 share a CTMD. In the field, this unit appeared to be a single massive flow, and at each site the samples were taken distributed over the flow. The difference in declination between site R6 and the other two sites is too large to be explained by the magnetic terrain effect. This result could imply that the area of site R6 was rotated by 27°, which seems untenable from field observations. Another explanation is that site R6 belongs to a currently unidentified underlying cooling unit with a different age. Without further age constraints, we cannot discriminate between these scenarios.

The magnetization-vs-temperature diagram of site R7 showed completely reversible behaviour (Fig. 3.2C) which would point to being an ideal recorder. However, the

FORC measurements indicate the presence of MD-grains which most likely hampered the paleointensity experiments as most Arai diagrams from samples from R7 show sagging behaviour. Moreover, the paleointensity interpretations of site R7 that do pass a set of selection criteria show an unacceptably low internal consistency: it has a σ/PI value of 42.4%. Of sites R5 and R6, based on the rock magnetic properties R5 (Table 3.1) is expected to yield the most reliable paleointensity results. From site R5 all samples are accepted, and the internal consistency of both site R5 and R6 is much better than that of R7, although still low with σ/PI values of 18% and 21%, respectively (Table 3.3). In some studies, a paleointensity result is deemed unreliable when the σ/PI exceeds 20% (Béguin et al., 2021), while in others this is set at 25% (Kissel & Laj, 2004; Paterson et al., 2010; Selkin & Tauxe, 2000). Given the large difference in the paleomagnetic direction between R5 and R6 and that they may not be from the same cooling unit, it is notable that their paleointensities do agree within error. This might point toward a post-remanence-acquisition block rotation – even though we are convinced that we would have noticed this in the field.

To summarize, we calculated the combined direction of sites R5 and R7 to have a declination of 3.6° and an inclination of 29.5°. The grouped direction of all three sites of unit 17 is also given (Table 3.2), which has a similar inclination but due to the declination of R6 results in an overall declination of 9.7°; this value should be treated with caution. Because in the field sampling sites R5 and R6 appeared to belong to the same lava flow unit, we calculated the average intensity from both sites, which is 32.1±6.8 μT and corresponds to a VADM of 72.1 ZAm^2. With R7 included, these values are similar, but with a larger uncertainty range of 33.5±10.3 μT or 75.7 ZAm^2 (Table 3.3).

3.5.4. Lomas Coloradas Formation unit 15

Site R1 and R9 were obtained 1.6 km apart but were located within the same cooling unit as mapped by Bohrson et al. (1996). The directional data of both sites have an α_{95} <5° and k values of 220.8 and 97.1 and are therefore deemed reliable. Furthermore, they share a CTMD, resulting in a direction with a declination of 2.3° and an inclination of 35° (Table 3.2). Site R1 yielded the most successful IZZI-Thellier results. For site R9, most samples pass at least one set of selection criteria, but the σ/PI value exceeds 30%. This is mainly due to sagging in the Arai diagram. When the paleointensity results from these two sites are combined, we obtain an intensity of 43.8±11.1 μT with an internal consistency σ/PI of 25%. This intensity corresponds to a VADM of 98.9 ZAm^2. Given that the two sites have the same rock magnetic characteristics, that they share a CTMD and their paleointensities overlap, we conclude that they are most likely from the same unit. Unit 15 covers a large area in the south; therefore one large eruption must have occurred or the eruption rate was high.

3.5.5. Geomagnetic implications

From the five cooling units we studied, two have associated radiometric ages: the 1952-flow (all SB-sites) and unit 7-8 (R10). From site R10 we obtained an unexpectedly low inclination of 4.2°. The expected average inclination for the Revillagigedo

Archipelago according to the GAD hypothesis is 35.0°. This implies that around or after the calibrated ages associated with site R10, 4052-2846 BCE and 4950-2846 BCE, the inclination at Revillagigedo was shallow. An inclination as low as 4.2° is not predicted in any of the recent geomagnetic models for this age (Constable et al., 2016; Nilsson et al., 2022; Schanner et al., 2022), although the reliability of these models is limited due to the lack of paleomagnetic data coverage in this region. It is possible, however, that the sampled volcanic deposit is not the basaltic flow Farmer et al. (1993) refers to as unit 7-8. Although we are convinced the sampling location is correct, the lack of GPS coordinates in Farmer et al. (1993)'s work introduces uncertainty. In the scenario in which we did not sample unit 7-8, but an older, underlying unit, it might be linked to older events such as negative inclinations identified at 26,000 BCE in the regional paleosecular variation (PSV) curve of Mexico (Mahgoub et al., 2019). In this PSV curve, the declination is also negative around 26,000 BCE, which would match with the negative declination of R10. However, due to the location in between the two scoria cones and the presence of lacustrine sandstones, we are convinced that the shallow inclination of site R10 does correspond to the 4052-2846 BCE to 4950-2846 BCE period. This suggests that around this period there was an unknown shallow inclination anomaly in the region.

Currently, the magnetic field at Revillagigedo also deviates from the expected GAD direction. In 2024 the declination was 7.5° and the inclination 44.6°, which is higher than the expected 35°. One possible explanation for the higher inclination in this region could be an influence related to behaviour similar to that of the present-day South Atlantic Anomaly (SAA). The SAA is usually characterized as a region of anomalously low intensity. The current minimum field strength at the Earth's surface is 22.5 μT and located in Paraguay (Pavón-Carrasco & De Santis, 2016), whereas based on the current dipole a strength of approximately 33 μT is expected at this latitude. In addition to the very low intensity, the magnetic equator is currently located further south in the Middle and South-American region (Abdu et al., 2005; Trivedi et al., 2005). While the magnetic equator is more northerly located in the African region and inclinations there are currently shallower than expected from a GAD field. The occurrence of the SAA has led to rapid directional variations in combination with low intensity values, for example in southern Africa (Hare et al., 2018) and Brazil (Trindade et al., 2018). If the rapid directional variations go beyond the area of the intensity anomaly, then an inclination anomaly in the north may be associated with an intensity anomaly in the south. A recurrence of the SAA has been hypothesized before (Engbers et al., 2022; Shah et al., 2016; Tarduno et al., 2015; Trindade et al., 2018). Therefore, we hypothesise that the shallow 4.2° inclination and negative declination of R10 is a local distortion in an episode in which the Earth's magnetic field was relatively non-dipolar. Such non-dipolar behaviour could be related to a recurrence of an SAA-like anomaly, somewhere else in the Southern Hemisphere than its current location in South America. Future studies on the Revillagigedo Islands could focus on obtaining more results and radiocarbon ages for this age to determine whether our observations arise from an as yet undocumented spurious occurrence of non-dipolar behaviour in this region, or whether the anomalous behaviour could be linked to recurrent behaviour of the SAA.

Three of our five sampled cooling units have only relative age constraints and can be compared broadly to the results of Sbarbori et al. (2009). They obtained an average paleointensity of 30±7.1 μT from older Pleistocene lavas from Socorro. Their results correspond to an average virtual axial dipole moment (VADM) of 67.6±16 ZAm^2, which is slightly lower than the current field strength at Socorro of 87 ZAm^2. Our three independent successful paleointensity sites on Socorro yield values in the range of 30-47 μT, corresponding to a VADM range of 67.8 - 106.2 ZAm^2 with an average of 84 ZAm^2 Our field strength calculations are thus slightly higher than the one documented by Sbarbori et al. (2009), although they all are within a plausible range of variations in field strength for the Pleistocene. In summary, the sampled Pleistocene lavas of Socorro do not record a markedly anomalous paleomagnetic field intensity.

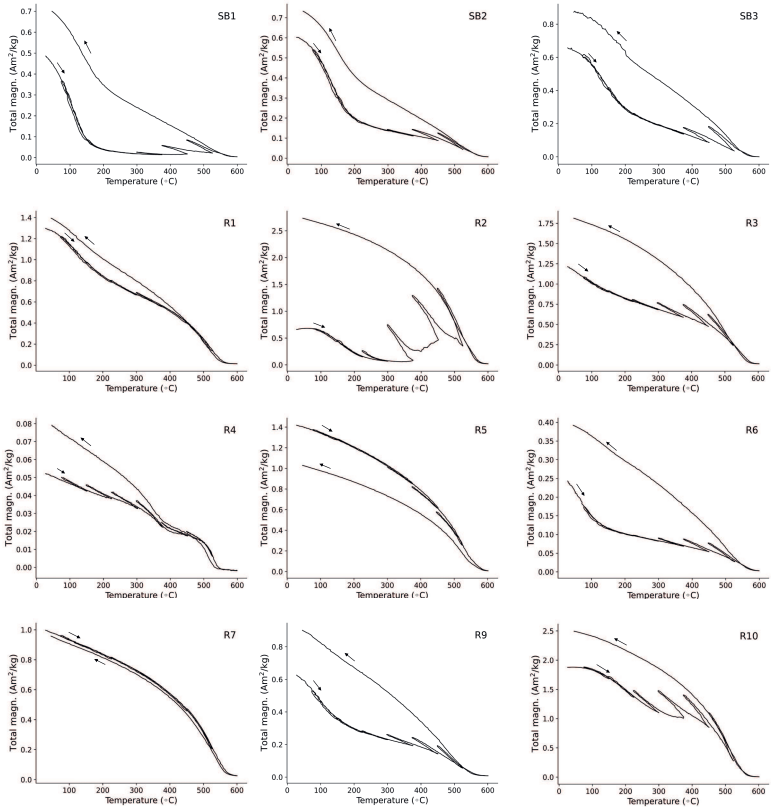
3.6. Conclusion

This reconnaissance study presents paleomagnetic data from three sampling sites on Isla San Benedicto and nine sampling sites on Isla Socorro, both uninhabited volcanic islands of the Revillagigedo Archipelago in the eastern Pacific Ocean. The sites on San Benedicto are from a 1952 CE lava delta, and site level directions varied from the expected IGRF-value. However, combining the three sites yielded a result consistent with the IGRF value emphasizing the need to obtain samples spread out and study several sites within a single lava flow. For paleointensity, almost all samples from San Benedicto Island passed at least one set of selection criteria, but only one site came close to the expected field value. The other two sites yielded lower than expected intensities. A combined mean intensity yields a value 8.3 μT lower than the IGRF-value. For the Socorro sampling sites, only one location has an age constraint of 4690±270 BP and 5040±460 BP determined by radiocarbon dating. This site yields an interestingly low inclination of 4.2°, more than 30° lower than expected for this latitude. We suggest that such a deviation is related to non-dipolar features of the Earth's magnetic field, such as a recurring anomaly in the South Atlantic. Future paleomagnetic results from dated volcanic deposits on the Revillagigedo Islands within this time period will provide insights into the variability of the Earth's magnetic field and occurrence of perhaps previously unknown geomagnetic anomalies. Other successfully obtained paleodirections and intensities from Socorro for the Pleistocene are consistent with expected values at this latitude and show that these Pleistocene lavas did not record strongly anomalous fields.

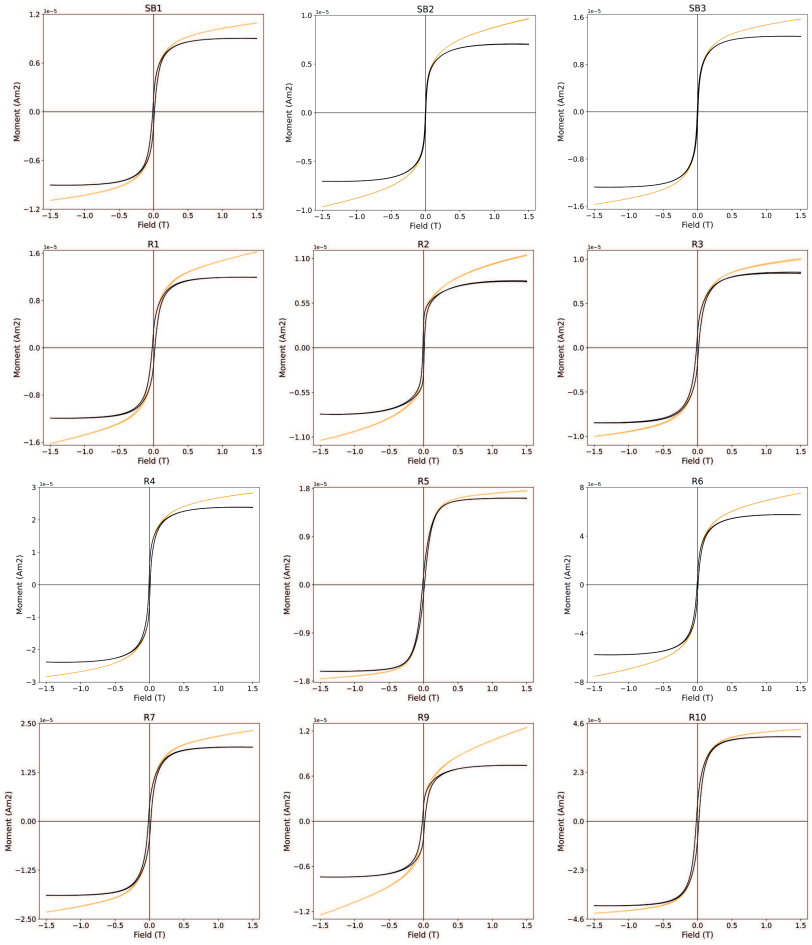
3.7. Acknowledgments

We thank Janne Koorneef, Yamirka Rojas-Agramonte, Christian Winter, Roberto Hassán Téllez Vizcaíno, Laurens Tromp, and the staff from the Quino el Guardian for their support on the boat. The Mexican Navy on Isla Socorro is thanked for their hospitality and help in transporting us on the island. We kindly acknowledge Erendida Frias and personnel from the CONANP Revillagigedo Park office, for granting the access to the protected area for research purposes. LVdG acknowledges funding from the Dutch Science Foundation (NWO): VIDI grant VI.Vidi.192.047. DJJvH acknowledges NWO XS grant OCENW.XS21.2.011 that funded the Revillagigedo expedition.

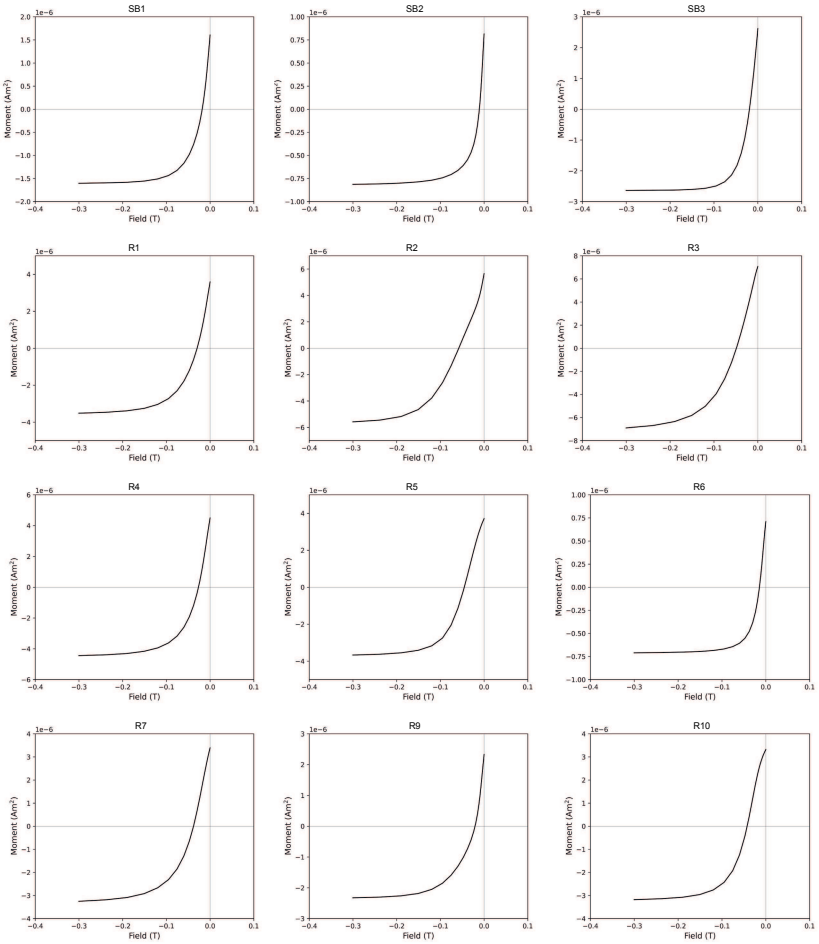
3.8. Supplementary Information



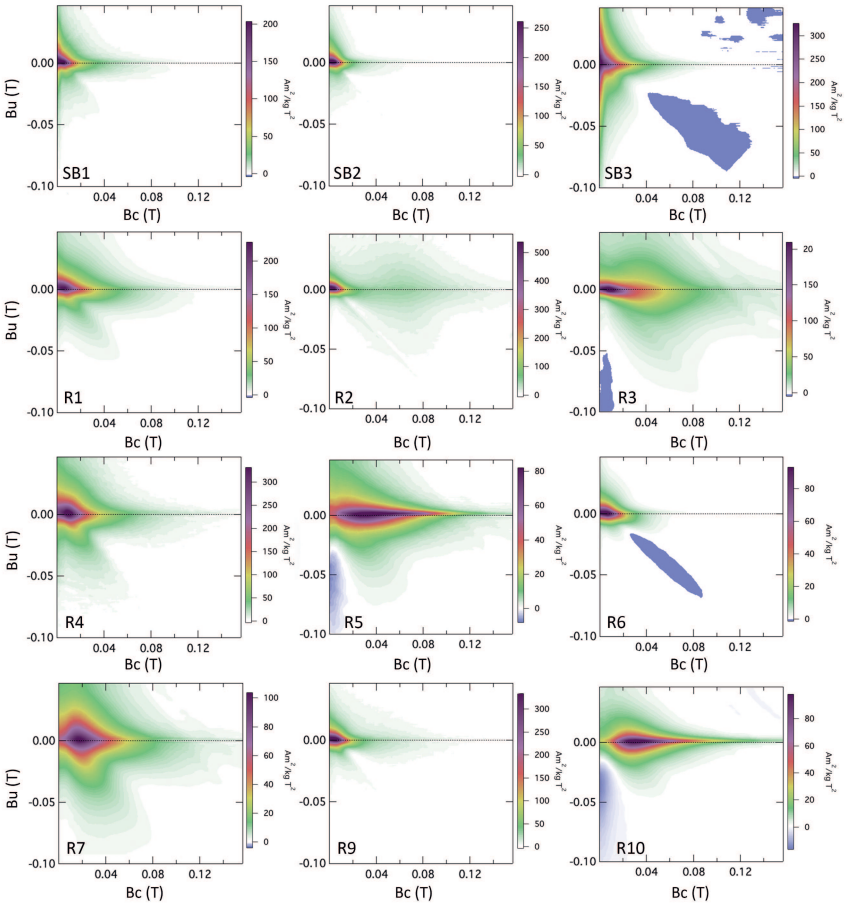
Supplementary Figure 3.1: Magnetization versus temperature plots for all sampling sites on the Revillagigedo Archipelago. The heating curve is the downward pointed arrow, the cooling curve is the upward pointed arrow.



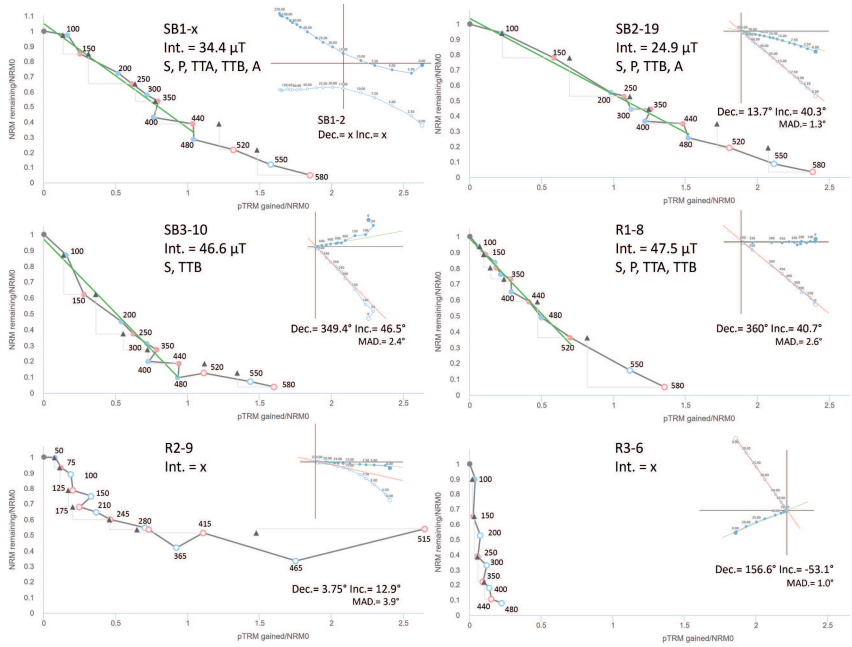
Supplementary Figure 3.2: Hysteresis loops for all sampling sites on the Revillagigedo Archipelago.



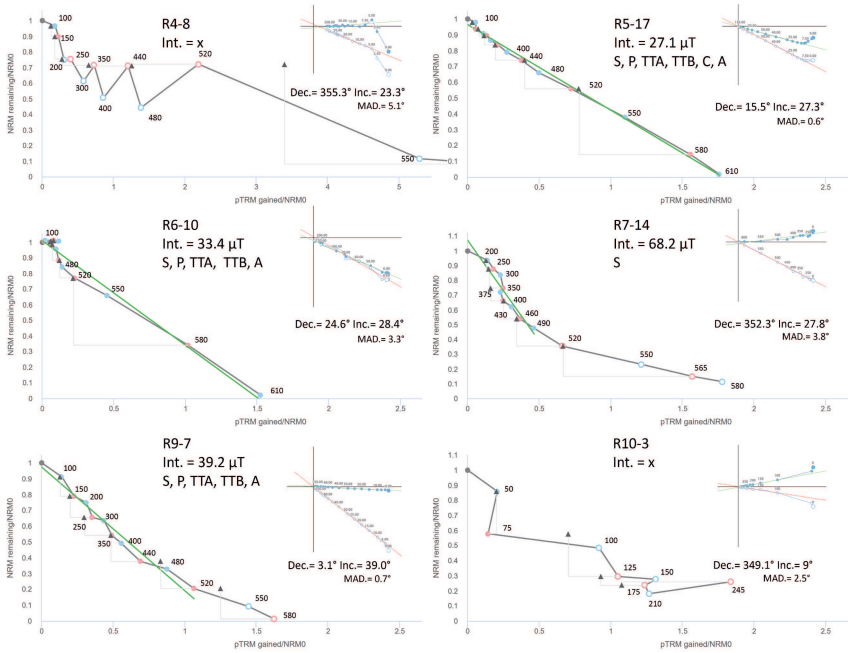
Supplementary Figure 3.3: DCD backfield curves for all sampling sites on the Revillagigedo Archipelago.



Supplementary Figure 3.4: First Order Reversal curves for all sampling sites on the Revillagigedo Archipelago. Smoothing parameters used are specified in Supp. Table 3.2.



Supplementary Figure 3.5: Examples of Zijderveld and Arai diagrams from specimens of sampling sites SB1-R3. In the Zijderveld diagram the top is up/west. Selection criteria used for interpreting the Arai plots are in Supp. Table 3.3. Blue circles are the ZI-steps, red circles the IZ-steps, and triangles indicate pTRM-checks. Selection criteria are CCRIT (C), SELCRIT (S), PICRIT (P), TTA, TTB, and CLASSA (A). The paleointensity given is according to the green line, which is the largest interpretable segment.



Supplementary Figure 3.6: Examples of Zijderveld and Arai diagrams from specimens of sampling sites R4-R10.

Supplementary Table 3.1: Paleomagnetic directions from magnetic compass readings.The obtained directions per site are given by the parameters: number of samples accepted/number of samples measured (n/N), the declination from magnetic compass readings corrected for the current declination of the field (Dec), inclination (Inc), 95 percent confidence interval α_{95}, precision parameter (k) and the separate errors for declination (ΔD_x) and inclination (ΔI_x). ΔDec and ΔInc are the difference with the IGRF values. Of SB1+2+3 the grouped directions are also given.

Site	n/N	Dec (°)	Inc (°)	α_{95}(°)	k	ΔD_x	ΔI_x	ΔDec	ΔInc
SB1	5/8	15.1	37.6	7.9	93.9	9.9	13.2	4.6	-6.1
SB2	8/8	16.5	42.0	7.3	58.6	8.3	10.0	6.0	-1.7
SB3	8/8	5.2	47.9	5.0	123.0	7.1	7.3	-5.3	4.2
SB1+2+3	21/24	12.2	43.3	4.0	63.3	4.8	5.7	1.7	-0.4
R1	11/12	2.9	33.3	3.1	220.8	2.6	3.8		
R2	9/12	-9.6	15.8	10.5	24.82	9.25	17.4		
R3	0/12								
R4	12/12	5.0	17.1	11.3	17.3	10.0	18.5		
R5	12/12	7.6	29.9	4.2	109.2	4.2	6.6		
R6	7/12	30.5	28.9	5.6	118.8	5.4	8.6		
R7	12/12	-0.3	28.9	6.2	49.7	6.2	9.9		
R9	10/12	1.5	36.9	5.1	89.4	4.8	6.6		
R10	9/12	-7.4	4.2	4.2	148.8	4.0	7.9		

Supplementary Table 3.2: Smoothing parameters used for processing FORC data in FORCinel 3.08.

Sample	Mass(g)	Sc0	Sc1	Sb0	Sb1	λ	Output
SB1-11	0.0168	6	6	4	5	0.1	1
SB2-6	0.0130	8	8	5	6	0	1
SB3-8	0.0123	6	6	5	5	0.15	1
R1-14	0.0148	10	10	4	8	0.1	1
R2-15	0.0115	10	10	6	8	0	1
R3-10	0.014	10	10	5	7	0.1	1
R4-1	0.0103	12	12	7	9	0	1
R5-3	0.0154	9	9	4	6	0.1	1
R6-24	0.0172	10	10	5	8	0.1	1
R7-14	0.0119	12	12	5	9	0.1	1
R9-2	0.0139	10	10	5	7	0.1	1
R10-13	0.0162	9	9	5	7	0.1	1

Supplementary Table 3.3: The six paleointensity selection criteria applied to assess the quality of the results. SELCRIT2 (Selkin and Tauxe, 2000), TTA and TTB (Leonhardt et al., 2004), PICRIT03 (Kissel and Laj, 2004), CCRIT (Cromwell et al., 2015b) and CLASS-A (L. V. de Groot et al., 2014a). The first four have the modifications as proposed by Paterson et al. (2014) and all have at least the curvature criterion k' set at ≤ 0.35. All definitions of the criteria can be found in the Standard Paleointensity Definitions v1.1 (Paterson et al., 2014).

Criterion		SELCRIT2	PICRIT03	TTA	TTB	CCRIT	CLASSA
n	≥	4	4	5	5		7
f	≥	0.35	0.35	0.35	0.35	0.7	
β	≤	0.1	0.1	0.1	0.15	0.1	
q	≥	1	2	5	0		
FRAC	≥				0.78		
Gap Max	≤				0.6		
SCAT	≤				TRUE		
DANG	≤				10		
k'	≤	0.35	0.35	0.35	0.35	0.164	0.35
MAD_{anc}	≤	15	7	6	15		7
MAD_{free}	≤					5	
α	≤		15	15	15		10
n_{pTRM}	≥		3				
DRAT	≤	10	10				12.5
CDRAT	≤		11				
δCk	≤			7	9		
δpal	≤			10	18		
$DRAT_{tail}$	≤	10					
δTR	≤			10	20		
δt	≤			9	99		

Supplementary Table 3.4: Specimens that passed at least one of the selection criteria as defined above

Specimen	SELCRIT2	PICRIT03	TTA	TTB	CLASSA	CCRIT
SB1-3	41.1	41.1			40.9	
SB1-8	41.8	41.8	41.5	41.2	42.2	42.1
SB1-12	51.8	52.7	47.7	50.2		
SB1-x1	44.6	46.7		58.8	46.5	
SB1-x2	33.1	33.8	34.6	34.5	30.2	
SB2-2	39.6	39.9			39.9	
SB2-6	27.6	27.9	28.1	27.6	27.9	
SB2-8	17.3	19.2		18.9		
SB2-17	33.4	33.1	33.3	33.4		
SB2-19	25.0	25.3		25.6	23.4	
SB2-20	24.1	23.6	23.8	24.7	22.0	
SB3-3	42.2	41.8	47.3	41.4		
SB3-4	43.6	43.6	43.6	42.0	44.2	
SB3-6	34.6			31.8	25.9	
SB3-8	34.6	34.6		35.8		
SB3-10	46.9			44.0		
SB3-11	32.7	32.7			33.9	
R1-1	50.8	50.8	47.7	50.2	47.9	
R1-2				43.6		
R1-8	46.0	39.9	42.8	42.8		
R1-10	50.8			50.8		
R1-13	48.6			48.6		
R1-14	48.5	44.3		47.1	49.1	
R1-16	41.0		41.0	41.0		
R4-4	6.4	6.4		6.4	6.4	6.4
R4-5	8.0	8.0	8.0	8.0	8.0	
R5-1	27.1	27.1	26.8	27.4	27.2	
R5-3	27.1	27.1	26.0	27.6	27.0	
R5-5	36.1	36.1	36.1	37.9	39.7	
R5-6	69.9	69.9			74.6	
R5-13		30.4				
R5-14	48.6					
R5-16	33.5	33.5	33.5	33.5	34.4	35.0
R5-17	26.2	26.6	26.3	26.3	26.2	26.1
R6-4	45.3	45.3	45.6	45.6	44.5	
R6-5	40.8	60.2	41.6	41.6	43.3	
R6-7	28.7	28.7	28.9	28.9	29.0	
R6-10	31.2	31.2	31.9	31.7	32.6	
R6-11	29.5	29.6	27.4	29.2	30.7	
R7-1	49.8	49.8	51.3	59.1		
R7-3	65.1	65.1	68.7	64.0	63.6	
R7-13	87.3					
R7-14	10.9					
R7-20			13.4	13.2		
R9-5	42.6		41.6	41.6		
R9-7	46.7	44.5	46.4	46.7	40.7	
R9-15	43.6		42.9	30.7		
R9-16	30.7	30.9	30.6	30.7	31.0	

Continued on next page

Table 3.4 (continued)

Specimen	SELCRIT2	PICRIT03	TTA	TTB	CLASSA	CCRIT
R9-18	57.0	56.5	57.0	57.0		
R9-22	57.6	55.2	56.1	58.7	55.9	
R10-9	51.7	51.7		49.9		
R10-13		6.3				



4

Paleomagnetic data from recent volcanics of Piton de La Fournaise, La Réunion: constraints on the evolution of the South Atlantic Anomaly

Romy Meyer, Liz van Grinsven, Lennart V. de Groot

Abstract *Competing hypotheses suggest that the South Atlantic Anomaly (SAA) either formed beneath the Indian Ocean and migrated westward, or originated below southern Africa. The origin and evolution of the SAA can only be unravelled by geomagnetic field models, but current versions are limited by a lack of paleomagnetic data from the Southern Hemisphere. Here, we present paleodirectional and paleointensity data obtained from recent volcanics of the Piton de La Fournaise on the island of La Réunion. La Réunion is located in the Indian Ocean and therefore ideal to study the formation of the SAA. Paleomagnetic data was obtained from 18 sampling sites of 15 different lava flows, deposited between approximately 583-2019 CE. From the successful sites of this study and two previous studies, a full-vector paleosecular variation (PSV) curve was generated, using both a simple prior and a global geomagnetic field model prior. The PSV curve of La Réunion reveals large paleodirectional changes between 1500-1750 CE, a high intensity (~45-53 μT) around 1400 CE, followed by a low intensity (~29-32 μT) around 1550 CE. These variations probably indicate the influence of the South Atlantic Anomaly at La Réunion at 1550 CE, and are therefore a valuable addition to be used in future geomagnetic field models.*

4.1. Introduction

The South Atlantic Anomaly (SAA), located under South America, is a remarkable feature of the Earth's magnetic field. In this region, the magnetic field intensity is significantly lower than expected from a geocentric axial dipole, and the Van Allen radiation belts are located at a lower altitude than usual (Domingos et al., 2017). This is problematic, as trapped charged particles in the belts may cause harm to spacecrafts crossing the area (Heirtzler et al., 2002). The present behaviour of the anomaly is analysed using satellite data, such as the Swarm mission from ESA (Friis-Christensen et al., 2006), and the anomaly is currently observed to be expanding and moving westwards. Depending on the definition of the centre location of the SAA, the average drift rates vary approximately between ~0.18 to ~0.3° per year (Fürst et al., 2009; Ye et al., 2017). Concurrent with the growing area of the SAA is the overall decrease of the Earth's dipole moment, which has been recorded since direct measurements of geomagnetic field strength started (Constable & Korte, 2006; Gubbins et al., 2006), showing a decrease of 9% between 1840 - 2015 CE (Olson & Amit, 2006). Whether a continuation of the decrease in the dipole moment will lead to a geomagnetic reversal is a topic of scientific debate (Pavón-Carrasco & De Santis, 2016), as does the question whether the South Atlantic Anomaly represents a precursor to such a reversal. Nonetheless, these recent changes in the behaviour of the geomagnetic field emphasise the importance of improving our understanding of the SAA's evolution.

The emergence of the anomaly is generally linked to the formation of reverse flux patches at the core-mantle boundary (CMB) (e.g. Amit et al., 2021; Campuzano et al., 2019; Hulot et al., 2002; Tarduno et al., 2015; Trindade et al., 2018, although modelling showed it might also be an interplay among multiple normal and reversed flux patches (Terra-Nova et al., 2017). Reverse flux patches represent areas where the polarity of the Earth's magnetic field at the CMB is opposite in direction compared to the surrounding magnetic field. The reason for the generation of re-

verse flux patches is a topic of debate. They may be due to protrusions at the CMB or thermal differences between the mantle and core, affecting outer core flow. This would suggest a top-down influence on the outer core (Beguin et al., 2023; Olson, 2016; Tarduno et al., 2015). In this scenario the formation of a reverse flux patch was connected to the large low shear velocity province (LLSVP) located underneath the African continent. The westward flow in the upper part of the outer core would be disturbed upon reaching the Eastern boundary of the LLSVP, therefore this region would be the preferential location for inducing geomagnetic anomalies (Constable et al., 2016). Instead of a top-down influence, a bottom-up control of the geodynamo was also suggested (Aubert et al., 2013; de Oliveira et al., 2024), in which the solid inner core influences flow in the outer core both through gravitational coupling between the inner core and mantle and through asymmetric inner core growth.

The location and timing of formation of these reverse flux patches, and therefore the formation of the SAA, are also under debate. A reverse flux patch may have emerged as early as 860 CE (Trindade et al., 2018), or as late as 1800 CE (Gubbins et al., 2006). For the location, some propose the SAA formed in the Indian Ocean region (Campuzano et al., 2019; Di Chiara & Pavón-Carrasco, 2022; Hellio & Gillet, 2018; Nilsson et al., 2022) and subsequently drifted westwards under the African continent since 1100 CE (Di Chiara & Pavón-Carrasco, 2022). Others propose the anomaly formed beneath Southern Africa (Tarduno et al., 2015; Terra-Nova et al., 2017). Further questions persist whether the anomaly is an abnormal expression of today's magnetic field (De Santis et al., 2013) and may indeed be a precursory event for a reversal, or whether it is a recurrent feature (Aubert, 2015; de Oliveira et al., 2024; Engbers et al., 2022; Tarduno et al., 2015; Trindade et al., 2018). Over the past 10 ky the geomagnetic field strength was found to be lower in the Southern Hemisphere than in the Northern Hemisphere, with larger values of paleosecular variation (Constable et al., 2016), which points to a recurrent low in the Southern Hemisphere.

Current global field models that track the onset and evolution of the anomaly are hampered by the scarcity of paleomagnetic data from the Southern Hemisphere, specifically around South-Africa. There is directional data available from archaeological sites in South-Africa, Botswana and Zimbabwe (Hare et al., 2018), sediment cores of Madagascar (Haberzettl et al., 2021), and some full vector paleomagnetic data obtained from archaeological sites in South-Africa (Neukirch et al., 2012; Tarduno et al., 2015) but for a global field model on the evolution of the SAA this is rather scarce. An additional location that might reveal the onset of the SAA is La Réunion, a volcanic island located in the Western Indian Ocean (21°S, 55°E) and therefore ideally suited to assess whether the SAA once moved from the Indian Ocean westwards, or whether it originated underneath the African continent. Two previous paleomagnetic studies on recent (<5ka) volcanic deposits were carried out on the island. Tanguy et al. (2011) reported directional data from 18 sites dated between 200 CE and 1976 CE. In addition to an inclination higher than expected from a geocentric axial dipole, they observed a steepening of the inclination between approximately 1500 CE and 1700 CE. Recently, this dataset was extended with paleodi-

rections from an additional 14 age units, and with the first recent paleointensities (Béguin, 2020). Béguin (2020) sampled 22 age units, and obtained paleointensities for 14 of them. They reported high paleointensities for La Réunion of 46.7-53.1 μT between 1410-1455 CE, after which the intensity drops to 29.2 μT at 1592 CE. For Southern Africa, Tarduno et al. (2015) found a decrease in field strength after 1250 CE and the lowest paleointensities at 1370 CE. If we are able to connect these two different datasets, this might reveal the onset of the South Atlantic Anomaly.

The reported high paleointensities on La Réunion are based on two data points, and only one low paleointensity was found. As these also suffer from large age uncertainties, improving the data coverage on La Réunion is important to study the emergence of the South Atlantic Anomaly. Here, we present full-vector paleomagnetic data obtained during a fieldwork in April 2022. We sampled an additional 18 sites from 15 different lava flows, 7 of them were deposited between 1450-1600 CE, which seems to be the crucial moment the magnetic field exhibits large changes in both direction and intensity. From the newly obtained data combined with the data of Tanguy et al. (2011) and Béguin (2020), a paleosecular variation (PSV) curve is created to visualise the short term behaviour of the Earth's magnetic field at La Réunion.

4.2. Geological setting and sampling

La Réunion is located in the Western Indian Ocean (21°S, 55°E) and consists of two volcanoes, the nowadays extinct Piton des Neiges (3071m) in the north and the frequently erupting basaltic shield volcano Piton de La Fournaise (2632m) in the south (Fig. 4.1). Piton de La Fournaise has been active from at least 360 ka ago (McDougall, 1971). Historical eruptions are known since the first humans settled on the island in 1638 CE, although during the first 70 years after settlement the eruptions at La Réunion were not reliably reported (Michon et al., 2013). There are six historical lava flows on the flanks of Piton de La Fournaise that erupted from fissures, with ages between 1708 CE to 1998 CE. However, most historical lava flows are concentrated within the U-shaped depression in the east, known as the Enclos Fouqué. The average eruption frequency is as much as one eruption per 9 months (Michon et al., 2013), an overview of the historical eruptions of Piton de La Fournaise is published in Tanguy et al. (2011) and Michon et al. (2013). To determine the ages of lava flows which were deposited prior to the historical lava flows we rely on radiometric dating techniques. For recent lava flows (<55,000 years) the radiocarbon dating technique on palaeosols or charcoal below volcanic deposits is used. Chevallier and Bachèlery (1981) and Morandi et al. (2016) reported various radiocarbon dates for lava flows in the area of Piton de La Fournaise, some of these lava flows were already sampled in Tanguy et al. (2011) and Béguin (2020).

Radiocarbon dating is a very useful technique but it has its limitations. First, carbon is not always present below a volcanic deposit and second, the radiocarbon dating method may give large age ranges. This is because the technique relies on changes in the atmospheric $^{14}C/^{12}C$ ratio, a given laboratory radiocarbon age must therefore be calibrated to obtain the absolute ages. There are several calibration curves

made using tree-rings (e.g. Hogg et al., 2020; Reimer et al., 2020 available. The ratio of $^{14}C/^{12}C$ is often not a linear relation but the calibration curves may contain plateaus or reversals, in these cases the calibrated age range becomes very wide (Guilderson et al., 2005; Taylor et al., 1996). Recently, Albert et al. (2020) created a statistical model that correlates the size of the pioneer tree Agarista Salicifolia to the age of the lava flows on La Réunion on which they grow. The Agarista tree is known to be among the first to grow on recently formed lava flows on La Reunion, and they do not regenerate once the flows are covered in vegetation (Albert et al., 2020). With this method 11 lava flows were dated on La Réunion, with average ages ranging from 1447 CE to 1823 CE. Because the Agarista model does not depend on calibrated ages, the uncertainty in age interval is Gaussian distributed and on La Réunion generally smaller than the uncertainty of the radiocarbon dated lava flows.

Five of our sampling sites were of lava flows which were dated with the pioneer-tree method, with ages between 1581-1753 CE. Besides the pioneer-tree sites we have 11 sites which were dated with the radiocarbon method (Morandi et al., 2016) and two historical flows (Fig. 4.1, Table 4.1. Of these sites we resampled a few flows which where previously sampled by Beguin et al. (2023) and Tanguy and Le Goff (2004). We resampled the Ravine d'Ango lava and the Piton Chisny flows (RE15, TGY-10 and RE16, TGY-16) because they gave interesting high paleointensity results. One location, Piton Taipoul, was resampled because it did not yield successful paleointensities in the previous study (RE33, and TGY-9). We also sampled the Mare Longue flow close to the GPS-coordinates in Albert et al. (2020), which Tanguy et al. (2011) sampled closer to the coast (TGY-14). Finally, we resampled the Petit Cratère cone (TGY-11). For calibration of the radiocarbon ages the calibration curve SHCal20 is used, this calibration curve is created specifically for the Southern Hemisphere (Hogg et al., 2020). Ages were converted using the age calibration program MatCal (Lougheed & Obrochta, 2016). SHCal20 is at time of publication the most recent calibration dataset, and is the update to the SHCal13 version, which was used in Béguin (2020), and SHCal04 which was used in Tanguy et al. (2011). Therefore, some of their calibrated ages shifted slightly in age compared to their previous interpretation. The probable age of RE16 shifted most, in Béguin (2020) the age was set at 1592 CE but the new age is 1499 CE. This is because of a reversal in the atmospheric $^{14}C/^{12}C$ ratio from 1550 CE to 1600 CE.

At each sampling site up to 20 standard paleomagnetic samples (up to 25mm in diameter and 10cm in length) were taken with a petrol-powered drill. Samples were taken as close as possible to the GPS coordinates given by previous studies but spread out over the outcrop. Samples were taken from as many different blocks as possible and mostly from the top of the lava flow. Except for site RN2, which was along a road, and RN14, where we obtained samples from the top and side of the flow. Unfortunately, because the East and Southern side of La Reunion are known for cloudy weather and because especially the sampling sites dated by the pioneer method were far into the rainforest, these conditions did not permit the use of a sun compass. Instead, samples were oriented with a magnetic compass. This is less preferable because of the possible influence of the magnetised rocks on the surrounding magnetic field and therefore the resulting declination may have a

small bias. The use of a magnetic compass does not influence the inclination or intensity of the samples.

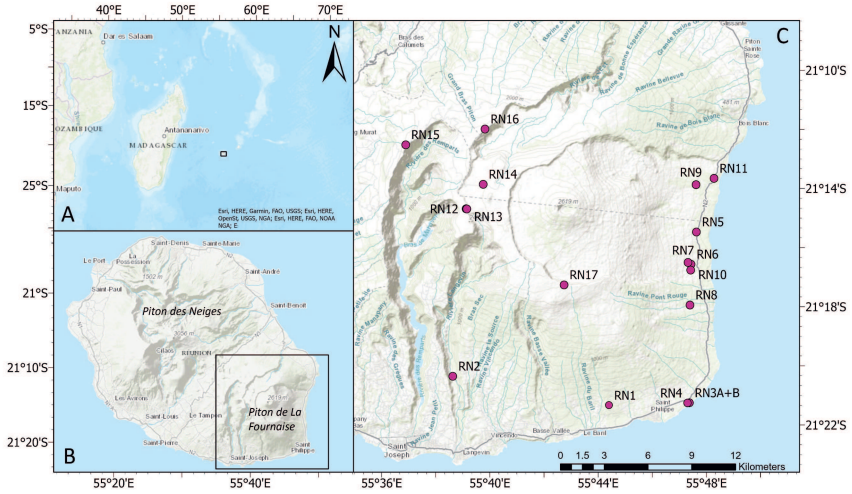


Figure 4.1: Map showing the location of La Réunion (A) and the sampling locations of this study around the Piton de La Fournaise in the southeast (B, C).

4.3. Rock magnetic characteristics

To define the magnetic carriers in the samples several magnetic properties were analysed. Curie temperatures were determined using a horizontal translation type Curie balance (Mullender et al., 1993). For each site one sample (20-45 mg) was heated from room temperature in several cycles up to 600°C, every other cycle the temperature was lowered by 75°C to check for reversibility of the signal to determine the alteration temperature. The alteration temperature was defined as the highest temperature to which the signal was still reversible. Curie temperatures are derived from the magnetization against temperature plots using the two-tangent method (Grommé et al., 1969) (Table 4.1, Figure 4.2A-C). Most samples show two Curie temperatures, the lower one in the range of 125-240°C indicative of titanomagnetite with a large Ti content. Higher Curie temperatures are around 500-555°C, closer to the characteristic temperature of magnetite. Most samples with a high Curie temperature loose their magnetization gradually. Except for RN2, RN14, RN15 and RN17 all thermomagnetic curves show irreversible behaviour during the heating-cooling cycles. The alteration temperature of RN1 and RN12 is low, around 300°C. Both sites have two Curie temperatures of which one is much higher than the alteration temperature, based on this these two sites are therefore not ideal for paleointensity experiments.

Hysteresis measurements were performed on an Alternating Gradient Magnetometer to assess the magnetic domain state of the samples (6-17 mg) (Figure 4.2D-E). The maximum field was set at 500 mT with an averaging time of 150 ms. From the

Table 4.1: Sampling sites. Given are the sites, year (BP and calibrated to CE), latitude and longitude, elevation (Elv) the method used to date the volcanics (which is radiocarbon (^{14}C), historical flows or the pioneer tree Agarista salicifolia), the age uncertainty (1-sigma interval for radiocarbon), and names of sampling sites possibly from the same flow of previous studies (TGY, Tanguy et al., 2011 and RE Beguin et al., 2023.

Site	Year (BP)	Year (CE)	Lat (N)	Long (E)	Elv (m)	Dating	Uncertainty	Prev. studies
RN1	364 ± 25	1523	-21.3554	55.7400	203	^{14}C	[1472-1519 (0.399), 1589-1620 (0.274)]	TGY-14
RN2	-	1598	-21.3392	55.6439	272	Pioneer	1540-1649	-
RN3A	455 ± 70	1459	-21.3541	55.7896	19	^{14}C	[1404-1503 (0.614), 1598-1616 (0.07)]	TGY-10, RE15
RN3B	455 ± 70	1459	-21.3541	55.7896	19	^{14}C	[1404-1503 (0.614), 1598-1616 (0.07)]	TGY-10, RE15
RN4	455 ± 70	1459	-21.3542	55.7884	30	^{14}C	[1404-1503 (0.614), 1598-1616 (0.07)]	TGY-10, RE15
RN5	-	1743	-21.2579	55.7939	147	Pioneer	1715-1769	-
RN6	-	1581	-21.2761	55.7906	216	Pioneer	1519-1635	-
RN7	-	1581	-21.2750	55.7887	256	Pioneer	1519-1635	-
RN8	385 ± 25	1492	-21.2991	55.7899	332	^{14}C	[1456-1501 (0.541), 1600-1615 (0.147)	-
RN9	-	1753	-21.2312	55.7936	202	Pioneer	1726-1777	-
RN10	-	2019	-21.2793	55.7903	208	Historic	-	-
RN11	-	2005	-21.2277	55.8047	86	Historic	-	-
RN12	868 ± 30	1188	-21.2450	55.6521	2365	^{14}C	[1165-1218 (0.686)]	-
RN13	620 ± 30	1349	-21.2449	55.6525	2358	^{14}C	[1302-1326 (0.295), 1348-1368 (0.233), 1380-1394 (0.171)]	-
RN14	381 ± 26	1499	-21.2310	55.6626	2287	^{14}C	[1457-1504 (0.508), 1597-1616 (0.180]	TGY-16, RE16
RN15	1495 ± 30	583	-21.2087	55.6148	2037	^{14}C	[555-603, (0.68)]	-
RN16	470 ± 75	1446	-21.2087	55.6637	2350	^{14}C	[1328-1337 (0.0296), 1396-1500 (0.608), 1601-1615 (0.046)]	TGY-11
RN17	355 ± 75	1552	-21.2877	55.7124	2102	^{14}C	[1460-1526 (0.314), 1554-1632 (0.370)]	TGY-9, RE33

hysteresis loops the saturation magnetization (M_s), remanent saturation magnetization (M_{rs}) and coercive force (B_c) are derived, after a slope correction for the paramagnetic contribution. The remanent coercive force (B_{cr}) is derived from the back-field (or DCD) curve. To determine the domain state of the samples, whether they are single domain (SD), pseudo-single domain (PSD), or multi domain (MD), the ratios of M_{rs}/M_s versus B_{cr}/B_c were plotted (Day et al., 1977) (Figure 4.2F). All sites fall within the pseudo-single domain range, and in between the theoretical SD-MD mixing curves (Dunlop, 2002). Some samples have a high coercivity and fall beneath the B_{cr}/B_c threshold of 1.5, reflecting a larger magnetic contribution from SD grains.

Classic hysteresis experiments suffer from the fact that it is a bulk magnetic measurement and therefore the measurement represents an average of the magnetic properties of all magnetic grains in a sample (Roberts et al., 2014). As a result practically all paleomagnetic samples are within the PSD range (Tauxe, 2010). In addition to the classic hysteresis measurements we measured First Order Reversal Curves (FORCs) (C. Pike & Fernandez, 1999). During a FORC experiment, a sample is brought to saturation in a strong positive applied field, after which the field is lowered to some reversal field, and brought to the saturation field again (Muxworthy & Roberts, 2007; Roberts et al., 2014). A FORC is the curve measured during this process, which is repeated many times to get a series of curves. FORCs give more information not only on the domain state of the sample but also about magnetostatic interactions between the particles within paleomagnetic samples. Samples with large amounts of magnetostatic interactions might hamper paleointensity experiments. On the same Alternating Gradient Magnetometer a suite of 200 FORCs were measured for each sample. The saturation field was 500 mT and the averaging time was set at 150 ms. To process the data FORCinel was used (Harrison & Feinberg, 2008). For the smoothing factor (SF) usually there is a balance between using the smallest SF while keeping the noise to an acceptable level (Roberts et al., 2000). We apply a variable smoothing of smoothing parameters Sc0=4, Sc1=7, Sb0=4, Sb1=7 and the horizontal lambda and vertical lambda are 0.1 (Egli, 2013). A lower branch of N=4 FORCs are subtracted to remove artefacts along the remanence diagonal. For RN6 and RN17 a drift correction was applied. Examples of representative FORC diagrams are in Fig. 4.2J-K. Some samples (e.g. RN14) indicate the presence of multi domain (MD) grains, with open contours and a vertical spread of FORC distribution along the Bu axis at low Bc values (Fig. 4.2K). In other cases we observe a single vortex state, with a 'boomerang shape' in the negative Bu region (RN9, RN16). Some sites (RN5, RN7) show besides a vortex state influence of uniaxial SD grains (Fig. 4.2J) with closed inner contours, a small spread along the Bu axis and a negative region along the Bu axis.

Finally, for each site one thin section of a sample was analysed under an optical microscope to observe the larger iron-oxide grains in the samples. The magnetite grains were imaged using reflected light. In sites RN2, RN4, RN13 and RN16 the iron-oxide grains are cubic in shape and around 10 μm in size (Figure 4.2G). In all other samples the titanomagnetite is smaller and dendritic shapes are observed. In RN3A, 3B and in some parts of RN8 and RN9, the titanomagnetite is sawtoothed or

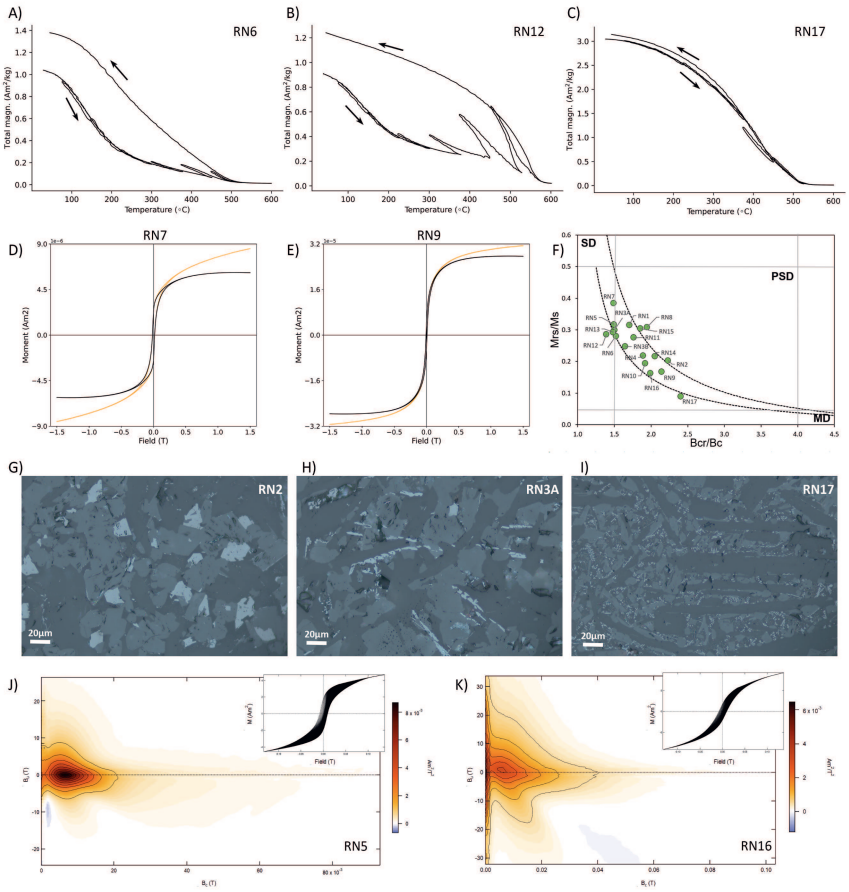


Figure 4.2: Rock magnetic results. In (A-C) are the magnetization as a function of temperature diagrams with the heating curve (arrow down) and cooling curves (arrow up). Examples of hysteresis curves are in (D-E). The black loop is with a 70% correction for the paramagnetic contribution, in orange is the raw data. In (F) the results for M_{rs}/M_s and B_{cr}/B_c ratios of the samples are plotted in the Day diagram. Dashed lines are the theoretical mixing curves for uniaxial shape anisotropy and negative cubic shape anisotropy from Dunlop (2002). (G-I) show the micrographs of RN2, RN3A and RN17, with the smallest dendrites observed for RN17. (J-K) FORC diagrams.

needle formed (Figure 4.2H). The smallest and largest amount of dendrites are seen in RN5, RN6, RN7 and RN17 (Figure 4.2I). Dendrites are assumed to form when the melt has cooled and crystallised rapidly. The size and morphology of dendrites affects the magnetic properties of the samples (Shaar & Feinberg, 2013). Thin and small dendrites are known to act as SD domain sized and are therefore ideal for paleointensity experiments Béguin, 2020. Table 4.1 indicates whether small or big dendrites are observed in samples. Although based on their rock magnetic characteristics some sites are more suitable for paleointensity experiments than others, all sites will still be subjected to all experiments.

4.4. Paleomagnetic directions

4.4.1. Methods

Paleomagnetic directions were obtained from both thermal and alternating field (AF) demagnetization experiments in a magnetically shielded room. For the thermal demagnetization experiments, all specimens were taken from different oriented samples. The natural remanent magnetization (NRM) of two to four specimens per site was thermally demagnetised in steps of 50°C up until 600°C. After each heating step the remaining magnetization was measured on a 2G-cryogenic magnetometer. Several specimens were magnetically so strong they exceeded the measurement range of the magnetometer, among them were all specimens from RN12, RN13 and RN15, two samples of RN16 and one sample of RN9 and RN17. These strong samples were measured on a spinner magnetometer instead. In addition to thermal demagnetization, between four to eight specimens were subjected to increasing alternating fields using a robotised 2G DC-SQUID cryogenic magnetometer (Mullender et al., 2016). Similar to thermal demagnetization, for most sites the specimens were taken from different samples, except for RN10 and RN11, of which two specimens were taken from one sample and were labelled A and B. These two specimens should have the same result. All specimens were demagnetised in AF steps of 0, 2.5, 5, 7.5, 10, 15, 20, 25, 30, 40, 50, 60, 70, 80, 100, 150, 200, 225, and 270 mT. The demagnetization results were analysed in paleomagnetism.org (Koymans et al., 2016, 2020) in which the demagnetization diagrams are plotted as Zijderveld diagrams (Zijderveld, 1967), The characteristic remanent magnetization (ChRM) is determined as the straightest line to the origin, with a maximum angular deviation (MAD) <10°. The site mean directions were calculated with Fisher statistics (Fisher, 1953). Of both RN5 and RN7 one sample was rejected because they were difficult to orient in the field, other outliers were identified in the Virtual Geomagnetic Pole (VGP) distribution using the 45°-cutoff.

4.4.2. Results

The Zijderveld diagrams indicate that the samples had no to small overprints, which were easily removed by not interpreting the first steps. Generally, the specimens decayed straight to the origin from step 50°C or 10 mT onwards and lost their magnetization gradually. The magnetic signal was almost always removed at their Curie temperature or ~150 mT, and the ChRM generally yielded MAD <5°. Three sites were more problematic: RN12, RN13 and RN15. The demagnetization steps did not decay straight to the origin and the specimens were often already deprived of

Table 4.2: Rock magnetic and directional results. Given are the dominant Curie Temperatures (T_c) and alteration temperature determined from the magnetization vs temperature diagrams (T_{alt}). Sites with dendrites (Den) are indicated as D_b (big dendrites) or D_s (small dendrites). The obtained directions per site are given by the parameters: (c/n/N) number of different cores / number of samples accepted / total amount of samples per site, the declination (Dec), inclination (Inc), precision parameter (k), 95 percent confidence interval α_{95} and the separate errors for declination (ΔD_x) and inclination (ΔI_x). Of RN3A+RN3B and RN6+RN7 the grouped results are also given.

Site	T_c (°C)	T_{alt} (°C)	Den	n/N	Dec (°)	Inc (°)	α95(°)	k	ΔD_x	ΔI_x
RN1	240/540	300	D_b	12/12	4.6	-43.0	3.6	148.7	4.6	5.4
RN2	125/510	-	-	12/12	-9.9	-31.1	2.6	279.1	2.4	3.7
RN3A	560	375	D_b	12/12	14.1	-38.6	3.6	148.6	3.6	4.8
RN3B	570	525	D_b	11/12	13.8	-38.6	3.7	154.4	4.2	5.5
RN4	545	525	-	12/12	-0.5	-38.9	3.7	137.3	3.8	5.0
RN5	125/510	450	D_s	10/12	-21.8	-57.0	3.7	172	5.8	4.3
RN6	210/500	375	D_s	12/12	-16.2	-31.5	4.1	115.2	3.5	5.3
RN7	155/535	375	D_s	11/12	-18.4	-32.2	5.6	66.8	5.6	8.5
RN8	120/550	375	D_b	12/12	-6.1	-26.3	2.2	407.9	1.8	2.9
RN9	235/520	525	-	12/12	-19.1	-58.3	3.7	135.5	6.1	4.3
RN10	185/515	525	D_b	10/10	-15	-52.4	7.1	46.8	8.2	7.3
RN11	165/505	450	D_s	12/12	-17.8	-51.9	3.4	160.7	5.2	4.7
RN12	215/560	300	D_b	0/12						
RN13	215/560	300	-	10/12	*5.2*	*-26.2*	*12.7*	*13.8*	*12.1*	*20.9*
RN14	540	-	D_s	7/10	-1.9	-35.0	11.3	29.5	13.1	18.6
RN14b	540	-	D_s	6/10	-7.6	-34.0	6.6	105.6	5.9	8.6
RN15	535	-	D_s	0/12						
RN16	205/550	375	-	8/12	-2.9	-33.2	9.6	34.2	9.4	13.8
RN17	515	-	D_s	10/11	-7.2	-44.0	4.1	138	5.5	6.3
RN3A+3B	-	-	-	23/24	13.9	-38.6	2.4	158.5	2.6	3.4
RN6+7	-	-	-	23/24	-17.3	-31.8	3.2	88.5	3.1	4.6

the magnetic signal around field step 25-40 mT. The specimens of RN12 measured thermally on the spinner yielded almost randomly distributed directions. Only four samples yielded interpretable results after AF demagnetization, but because they show large overprints in the initial field steps and their ChRM directions remain highly scattered in the VGP distribution, this site was discarded. Samples from site RN13 show broadly similar behaviour. Although the highest AF field steps of 6 specimens yield consistent directions (Fig. 4.3E) and the spinner samples are slightly less scattered, the mean direction reported for RN13 in Table 4.2 should be interpreted with caution. At site RN15, only one specimen (RN15-3) could be interpreted at the higher AF and thermal demagnetization steps. The remaining specimens retained a strong overprint up to 400 °C and were already demagnetized by 40 mT. As only a single sample yielded reliable results, this site was discarded from further interpretation. All other sites could be interpreted and their thermal and AF demagnetization results are grouped, as the two techniques yielded similar mean directions (Table 4.2). In general, the α_{95} values are below 5° and the k-values exceed 100, although RN10, RN14, and RN16 show somewhat lower k-values. For RN14, this is due to a single divergent specimen. Sample RN14-6 has a declination of 35°, whereas all other specimens from the site have declinations below 0°. Initially, there was no reason to question this measurement. However, when RN14-6 is excluded, the mean direction becomes similar to that of site RE16 from Beguin et al. (2023) (RE16: dec = 7.7°, inc = 33.9°), and these sites then share a CTMD. Therefore, RN14 without RN14-6 is reported as RN14b in Table 4.2, and this result is considered more reliable.

Sites located close to one another were tested for a Common True Mean Direction (CTMD) using the paleomagnetism.org implementation of the approach described by Tauxe, 2010. When this test is positive the sites represent the same spot reading of the paleofield and are most likely of similar age. RN3A and RN3B were sampled very close to one another and they share a CTMD. RN4 was sampled in close vicinity to RN3, however the declination is clearly different and there is no CTMD match. This site has to be of different age than RN3. The sites dated with the pioneer tree method were often hard to reach. In the field we were convinced that site RN6 was sampled on the 1817 CE dated flow. However, the site was sampled close to RN7 and rock magnetically the samples of the two sites behave very similarly. RN6 and RN7 also share a CTMD, therefore we assume we unintentionally sampled the same flow twice. Because of the appearance of the vegetation on satellite images, RN7 seems to be in the middle of a flow, whereas RN6 is on an edge towards similar looking vegetation. Therefore we assume RN6 to be the 1581 CE flow as well. The mean direction of the grouped sites RN3A+3B and RN6+RN7 are also given in Table 4.2, which results in a lower α95 than for the individual sites.

4.5. Paleointensity

In addition to the paleodirectional experiments, specimens from all 18 sites were subjected to paleointensity experiments. For each site, five to eight small specimens per site were glued with quartz wool and potassiumsilicate into glass cups. In total 139 specimens were subjected to the IZZI-Thellier paleointensity method

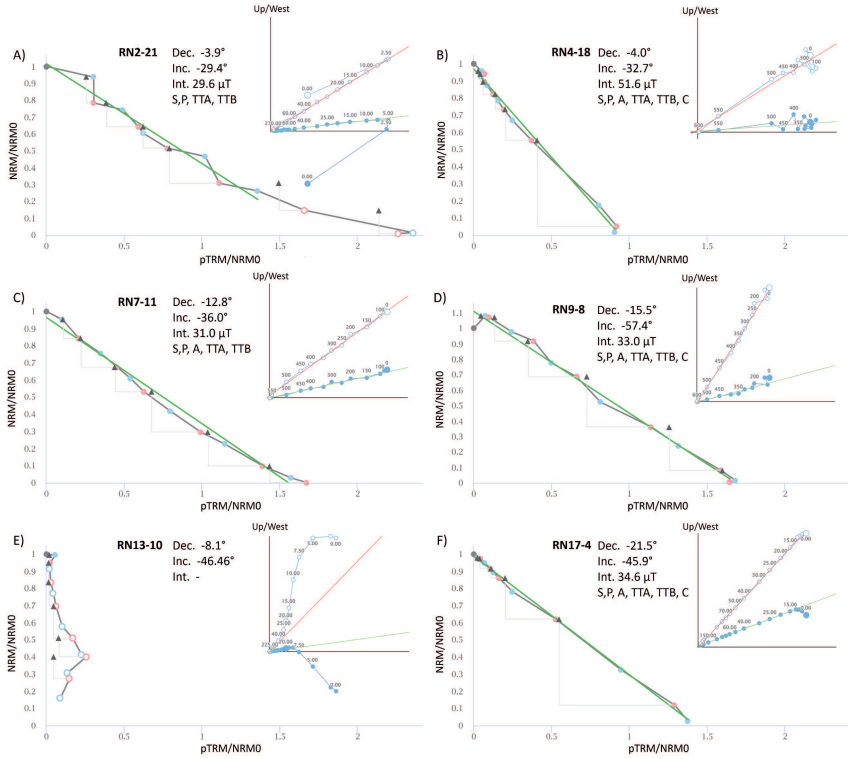


Figure 4.3: Representative directional and IZZI-Thellier results. Arai diagrams of several specimens are shown. The blue circles are the ZI-steps, red circles are the IZ-steps and the triangles indicate pTRM-checks. The green line is the largest temperature segment accepted by at least one of the selection criteria. Which selection criteria the specimens pass is given by SELCRIT (S), PICRIT (P), CLASSA (A), TTA, TTB and CCRIT (C). In the inset the Zijderveld diagram of thermal or alternating field demagnetization experiments is shown. Closed circles are declination, open circles are inclination. The straight lines through the measurement steps indicate the ChRM direction.

(Tauxe & Staudigel, 2004) whereby their NRM is progressively replaced by a partial thermal remanent magnetization (pTRM).

During the IZZI-Thellier experiment, or in our case the 'ZIIZP-Thellier' measurement scheme, samples are heated in several steps. First, samples are heated and cooled in a zero-field, after which the samples are heated again to the same temperature step but now while applying a laboratory bias field of 50 μT during the in-field steps. For the next temperature the order of the zero field and in-field measurements is switched. After each set of zero-field, in field (ZI) (Coe, 1967), and in-field, zero-field (IZ) (Aitken et al., 1988) measurements, a pTRM check is included to check for changes in the ability of the sample to carry a thermal remanence. The pTRM check is a repetition of a lower temperature step, and thus should be similar to the original partial thermal remanence gained at that temperature. Deviating pTRM-checks are an indication of alteration of the magnetic behaviour of the specimens during the experiment.

Depending on the thermal demagnetization behaviour of our samples, the specimens for the IZZI-Thellier method were divided in a low, medium, and high temperature batch. The low temperature batch had smaller step increments <350°C, the medium temperature batch was evenly divided in steps of 50°C and the high temperature batch had smaller temperature steps >350°C. The specimens were measured on a 2G cryogenic magnetometer and the experiment continued on each specimen until around 95% - 100% of the NRM was replaced. The samples were kept in a magnetically shielded environment throughout the experiment.

Because paleointensity experiments often suffer from a high failure rate due to non-ideal behaviour during the heating and cooling cycles, we applied two methods to assess the quality of the results. First, all specimens are interpreted in paleointensity.org (Béguin et al., 2020) where six different selection criteria are applied. These are TTA and TTB (Leonhardt et al., 2004), SELCRIT2 (Selkin & Tauxe, 2000), PICRIT03 (Kissel & Laj, 2004), CLASS-A (L. V. de Groot et al., 2014a) and CCRIT (Cromwell et al., 2015b). The first four have the modifications as proposed by Paterson et al. (2014). The curvature criteria k' is strictest for CCRIT, <0.164, all others have the curvature criteria set at k'<0.35. From the interpretations that passed a selection criterion the average paleointensity and standard deviation are calculated. This means that interpretations that passed more than one selection criteria are included multiple times in the data analyses, so these results that are deemed more reliable get more weight. The site average paleointensity is considered to be more reliable when the standard deviation divided by the mean (σ/PI) did not exceed 25% (Paterson et al., 2014) and when there are at least three specimens to interpret.

In addition to the previous interpretation method using selection criteria, the Bias Corrected Estimation of Paleointensity (BiCEP) method (Cych et al., 2021, 2023) is applied to our data. This paleointensity interpretation method uses a Markov Chain Monte Carlo (MCMC) method followed by a Bayesian approach to determine the paleointensities. This technique focuses on the curvature k' of the Arai plot to predict the bias for each specimen. The method attempts to correct this bias and

therefore all specimens that would otherwise have been excluded due to non-linear Arai plots are included as long as they do not show clearly visible alteration. The BiCEP method is most appropriate for sites that fail the traditional interpretation methods due to curvature or multi-domain behaviour and have at least five specimens. We applied it to all sites, and only excluded specimens with clear alteration. Below, we will first discuss the results from the selection criteria and then compare them with the outcome of the BiCEP method.

4.5.1. Interpretation using selection criteria

Of the 139 specimens subjected to the IZZI-Thellier method, 94 specimens passed at least one or more sets of selection criteria. This is a success rate of 68%, which is exceptionally high for paleointensity experiments. 19 specimens passed CCRIT, the strictest set of election criteria. Unfortunately, not all samples that passed a set of selection criteria also yielded meaningful paleointensity interpretations. Some specimens of sites RN12, RN13, RN15 and RN16 did pass certain sets of selection criteria, but the specimens gained almost no pTRM compared to the amount of NRM lost during demagnetization (Fig. 4.3E). This led to very high paleointensity site estimates: up to 600 μT. In combination with the failed paleodirection experiments, we expect this to be due to lightning to have occurred, and therefore they are rejected from further interpretations. In previous studies, paleointensity results were usually rejected when their σ/PI exceeded 20% (Béguin et al., 2021) or 25% (Paterson et al., 2010). Although the cut-off of this parameter is not theoretically defined sites with a percentage > 20% are generally considered less reliable. Of our sampling sites only RN1, RN2 and RN3A and 3B have a high σ/PI. Most samples from these sites show non-ideal behaviour in the Arai diagrams: they either suffer from sagging, kinked Arai-diagrams, or fail pTRM checks. For RN1 this was expected based on the thermomagnetic curve. The only sample (from RN3B) without sagging that passed all sets of selection criteria yielded a paleointensity of 44 μT. This suggests that the average paleointensity values of 75 μT and 58.6 μT from RN3A and RN3B (Table 4.3) are likely unreliable. Out of the 18 measured sites, 10 were accepted.

4.5.2. BiCEP

In contrast to the interpretation method based on sets of selection criteria, the BiCEP method includes specimens that show sagging in the Arai plots (Table 4.3). With BiCEP, only sites RN2, RN10 and RN17 have a few samples that are excluded because they exhibit a sudden loss of previously gained pTRM at one to two different temperature steps. All specimens from site RN5 can now be interpreted, but only the initial temperature steps (up to 150–210°C) are used for the paleointensity analysis, as most specimens already lost about 80% of their magnetization by 200°C and higher-temperature steps were affected by alteration (Fig. 4.4D). For sites RN3A and RN3B, only 16 specimens can be interpreted, as the sites separately gave too scattered results. The mean results of the successful sites are shown in Table 4.3 and all have a $\hat{R}$ of 1. $\hat{R}$ quantifies the convergence between chains in the method, and should be between 1.1 and 0.9. RN3A, RN3B, RN13, RN15 and RN16 failed BiCEP because the effective sample size n_eff, which represents the number of independent draws from the posterior that would provide the same estimation

		Selection criteria					BiCEP					
Site	Year (CE)	CCRIT/n/N	n_int	PI (μT)	σ	σ/PI	n/N	n_eff	Category	PI (μT)	σ	σ/PI
RN1	1559	0/7/8	285	57.3	12.5	21.7	8/8	22907	C	48.2	10.4	21.5
RN2	1598	0/3/8	19	*37.4*	*9.5*	*25.4*	5/8	18759	C	*26.3*	*9.2*	*34.9*
RN3A	1455	0/6/8	23	*75.0*	*57.0*	*76.0*						
RN3B	1455	1/7/8	229	*58.6*	*20.1*	*34.2*						
RN4	1455	4/8/8	792	45.4	8.0	17.6	8/8	31767	A	43.9	5.6	12.7
RN5	1743	0/3/8	102	37.4	3.0	8.1	8/8	35083	A	37.1	3.9	10.5
RN6	1581	1/5/8	623	33.3	3.3	9.9	8/8	20545	A	33.0	4.9	14.8
RN7	1581	3/8/8	954	32.7	4.8	14.5	8/8	23952	A	34.1	3.9	11.4
RN8	1556	1/8/8	405	38.0	3.7	9.7	8/8	18441	A	34.0	5.2	15.3
RN9	1753	2/8/8	412	40.3	7	17.4	8/8	25732	A	38.2	5.0	13.1
RN10	2019	1/3/6	176	31.9	3.8	11.8	4/6	9081	D	*31.1*	*12.6*	*40.5*
RN11	2005	1/5/6	513	34.9	2.9	8.3	6/6	12226	B	34.5	4.5	13.0
RN12	1177	0/2/8	4	*115.2*	*48.4*	*42.0*						
RN13	1349	0/3/8	8	*287.3*	*110.1*	*38.3*						
RN14	1499	3/8/8	532	30.1	2.0	6.7	8/8	9403	B	30.7	2.2	7.0
RN15	573	0/2/5	10	*678.2*	*37.2*	*5.5*						
RN16	1443	0/2/8	49	*275.4*	*141.9*	*51.5*						
RN17	1549	2/6/8	611	32.1	4.2	12.9	6/8	16459	B	35.6	6.6	18.5
RN3A+B	1455	1/15/16	271	*59.1*	*25.5*	*43.2*	16/16	15513	C	*49.8*	*15.5*	*31.1*
RN6+7	1581	4/12/16	1566	32.8	4.3	13.2	16/16	17980	A	33.3	2.7	8.0

Table 4.3: Paleointensity results. The obtained paleointensities per site are given for the selection criteria (left) and BiCEP-method (right). The parameters are: number of samples accepted by CCRIT, number of samples accepted by all selection criteria (n), total amount of samples measured (N), number of interpretations (n_int), resulting paleointensity (PI), standard deviation (σ) and standard deviation divided by the paleointensity (σ/PI). For BiCEP additionally the effective sample size (n_eff) and the category (A-D) are given. Of RN3A+B and RN6+7 the grouped results are also given. The results in italic are questionable due to the high σ/PI

accuracy as the correlated MCMC samples, was lower dan 1000. The low success rate of these sampling sites is most likely caused by the low alteration temperature (Table 4.1).

The mean intensities of the sites with a BiCEP category label A or B align closely with the outcome of the interpretation based on sets of selection criteria, confirming the reliability of these sites. For RN5, only three out of eight samples passed the selection criteria, but the average paleointensity of the selection criteria interpretation method and BiCEP is similar, further supporting the reliability of this site. The differences between selection criteria and BiCEP methods are largest for sites RN1, RN2 and RN3A+B. For all these sites the BiCEP category label is C, which indicates that more samples are required for a higher level of confidence. For RN1 and RN2 more samples could improve interpretation, but site RN3A and RN3B combined already have 16 samples. Therefore increasing the number of specimens is not necessarily better or feasible. The results from the historical flows RN10 and RN11 are categorised as D and B, respectively. Both sites have the lowest amount of samples, as RN10 only has 4 specimens that are interpretable. The results might improve with more samples, however, the large error does not seem to arise from sagging and it is unknown whether adding specimens will improve the BiCEP category label.

Previously, in some studies only samples that meet the CCRIT criteria were accepted and BiCEP was used as an alternative (Cych et al., 2021, 2023; Tauxe et al., 2022). Few of our samples pass the CCRIT selection criteria (Table 4.3). Applying only CCRIT would have resulted in no outcome for any of the La Réunion sampling sites. Instead, we accepted all interpretations that satisfied at least one of the six selection criteria. Therefore, interpretations that meet multiple selection criteria are weighted more and thus considered more reliable. The sites that work well with the BiCEP analysis align with the results from all selection criteria. This suggests that using all selection criteria together is a robust approach, and it seems it is not necessary to focus only on samples accepted by CCRIT. A combination of using multiple selection criteria and BiCEP will help finding the most reliable paleointensity results.

4.6. Discussion

In this study we obtained paleodirectional and paleointensity data from recent lava flows from the island of La Réunion. Below, we first discuss the paleomagnetic data obtained, compare it with results from previous studies, use our new data to produce a paleosecular variation curve for La Réunion, and discuss the impact our new data has on our understanding of the origin and behaviour of the SAA.

4.6.1. Paleomagnetic data

The paleomagnetic experiments were generally successfull, and produced new paleodirections for 14 of our 17 sites, and new paleointensities for 11 sites. Sites RN10 and RN11 are historical flows; their results can be compared with the International Geomagnetic Reference Field (IGRF, Alken et al., 2021) value. RN10 is the 2019 CE

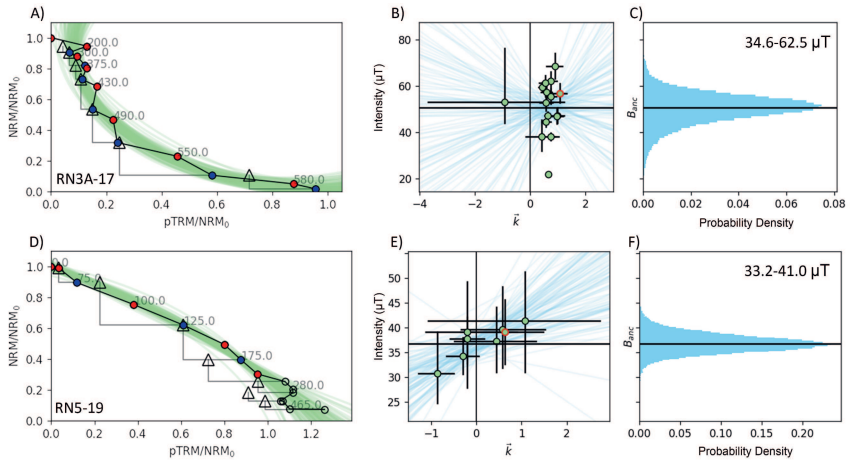


Figure 4.4: Example of BiCEP results. Arai plot of sample RN3A-17 (A) and RN5-19 (D). Symbols are similar to Fig. 4.3, open dots represent temperature steps that are not selected. The green lines are the fits from the BiCEP method. In (B) and (E) are the relationship between the intensity and the curvature criterion k. The red circle is the selected sample RN3A-17 or RN5-19, black lines around the sample are the uncertainties, black line on the intensity-axis is the mean intensity. In (C) and (F) are the corresponding site histogram of the mean intensities, and the lower and upper uncertainty interval.

lava flow, the expected declination of this flow is -19.6°, the expected inclination is -54.3° and the expected intensity is 38.5 μT. For RN11, a 2005 CE lava flow, the expected declination and inclination are -20° and -54.4°, and the intensity was 37.2 μT in 2005 CE. The directional results of both sites show small differences with the reference value. The measured declination of RN10 is -15°, and the inclination is -52.4°. The measured declination of RN11 is -17.8° and the inclination is -51.9°. Therefore, the declination of both sites is slightly higher and the inclination slightly lower than expected. In addition, the measured intensities of RN10 and RN11 are 6.8 μT and 2.5 μT lower than expected. RN10 did not pass BiCEP, therefore this paleointensity is not the most robust paleointensity in our dataset. However, lower than expected inclinations and intensities are a well known problem, and was also found for the historical flows on La Réunion by Béguin (2020). A bias towards lower values than predicted according to the IGRF was explained to arise from local magnetic anomalies from the underlying magnetised terrain (Baag et al., 1995; Meyer & de Groot, 2024; Tanguy & Le Goff, 2004; Valet & Soler, 1999). However, the modelling study of Baag et al. (1995) predicted the inclination anomaly to be reversed in the Southern Hemisphere, which is not observed here. As an alternative explanation, Chapter 2 of this thesis showed that a gradual decrease in intensity can occur after several years of sample storage. Future work should therefore examine whether this represents a systematic underestimation of the field strength and whether a corresponding correction is warranted.

Some of the sites from this study were sampled previously by Tanguy et al. (2011) and Beguin et al. (2023) (Table 4.1). Site RN1 was presumably obtained from the Mare Longue lava flow, we sampled around 60m from the GPS coordinates in Al-

bert et al. (2020). Tanguy et al. (2011) sampled this flow (TGY-14) further downslope. At the time of the study of Tanguy et al. (2011) the Mare Longue lava flow was not yet dated, and they concluded based on the obtained paleodirections of -6.1° in declination and -37.1° in inclination that the Mare Longue flow would be of an age between 1390-1500 CE. We obtained different results at our site RN1, as it gave a positive declination of 4.6° and an inclination of -43°. The paleodirection of site RN1 does not match with the results from any of the flows of similar age (e.g. RN6, RN7, RN8, RN17) and the intensity of around 50 μT and with a large σ/PI, is much higher. We therefore question whether RN1 corresponds to the Mare Longue flow. Moreover, the location of the radiocarbon dated Mare Longue flow was not the same in the figure of Albert et al. (2020) as it was according to their GPS coordinates: the figure shows a location 630m to the Northeast of our sampling location RN1. As the results from Tanguy et al. (2011) do fit the calibrated age of 1523 CE, we therefore assume their directions are from the Mare Longue flow.

Two other sites with positive declinations were sampling sites RN3A and RN3B. They were taken near site TGY-10 (Dec=-10.5°, Inc=-34.8°, Tanguy et al. (2011) and RE15 (Dec=-9.6°, Inc=-37.4°, Int=52.1 μT, Béguin (2020)), dated at 455±70 BP, and are presumed to be from the Ravine d'Ango lava. Although RN3A and RN3B yield high paleointensities in our study, with a large σ/PI, the declinations differ significantly from RE15 and TGY-10. Because these samples were taken farther from the GPS coordinates of the radiocarbon dated site, we trust the results of RE15 and TGY-10. Site RN4 was sampled nearby and shows a declination of -0.5°, still somewhat different from RE15 and TGY-10 but to a lesser extent. For this reason, we currently retain RN4 in our dataset.

Site RN14 was obtained from the Piton Chisny flow, at the exact same location as RE16 and from the same flow as TGY-16. As explained before, the directional results without the erroneous sample RN14-6 are comparable to the results from RE16 (Béguin, 2020) and TGY-16 (Tanguy et al., 2011). Additionally, the intensity of 30.1 μT is similar to the result of RE16. This confirms the low intensity around 1500 CE. The site with an age shortly prior to 1500 CE that was sampled previously is RN17, sampled at the same location as RE33 (dec=-3.3, inc=-43, Béguin (2020)) and TGY-9 (dec=-1.5, inc=-46.2, Tanguy et al. (2011). The declination again deviaties slightly, between 3.9° and 5.7°, and the inclination result of 44° is similar. Site RE33 did not give successful paleointensity results, whereas our site RN17 did. Although RN17 plots closest to the MD domain in the Day plot (Fig. 4.2F), its thermomagnetic curve was reversible (Fig. 4.2C) and the micrograph showed small dendrites (Fig. 4.2I). These rock-magnetic characteristics indicate RN17 was ideal for paleointensity experiments, and it yielded an intensity of 32.1 μT. This is consistent with the other relatively low intensities from this period.

4.6.2. Paleosecular variation curve

To understand changes in the Earth's magnetic field at La Réunion we construct a paleosecular variation curve of the last 2000 years. The paleomagnetic dataset of La Réunion contains a wide variety of types of dating. For many recent historical flows the age is absolutely known from historical sources. Others are dated based on ra-

diocarbon datings and may have a large and multimodal age uncertainty, or are dated with the pioneer tree method and therefore have a normally distributed age uncertainty. For this reason we use the Bayesian method of Schanner et al. (2026), which is built upon the method of Béguin et al. (2021), and can take all types of age datings into account. We created two full vector PSV curves at the location of Piton de la Fournaise on La Réunion. The first curve uses a simple prior: the current Geocentric Axial Dipole field, evaluated for La Réunion's location. With this prior all available data for La Réunion can be used: the paleomagnetic data from this study, Tanguy et al. (2011) and Béguin (2020). The second PSV curve is generated using a global geomagnetic field model as a prior. Here, only data that is not yet in the GEOMAGIA database (Brown et al., 2015) can be used to avoid circular reasoning, so only the data from this study and Béguin (2020) are included.

Some sites are excluded from the PSV curve as they were deemed unreliable. From this study, those are the sites in italic in Table 2 and Table 3, as well as sites RN1, RN3A and RN3B due to reasons described in section 6.1. Additional sites from Béguin (2020) and Tanguy et al. (2011) are excluded following the reasoning of Béguin (2020): site RE11 is not used for the construction of the PSV curve, as this site had an unusual declination and a very large age uncertainty. TGY-17 is also excluded because it did not match a flow of the same age (RE18) that was taken closer to the GPS coordinates of the radiocarbon dated deposit. Finally, Béguin (2020) observed that it is more likely that the direction of the 1800 CE flow of TGY-5 is actually the 1776 CE flow (TGY-6) and vice versa. Therefore the results of these two sampling sites are switched. The curves generated with a simple prior and geomagnetic field model prior are shown in Fig. 4.5 and discussed below.

Simple Prior

The first PSV curve is based on all paleomagnetic data known for La Réunion using a simple prior with a constant axial dipole strength that is equal to the current strength of the geocentric axial dipole evaluated for La Réunion (Fig. 4.5A-C). This PSV curve is compared to the model predictions from four geomagnetic field models: the gufm1 model (Jackson et al., 2000), CALS10k.2 (Korte et al., 2011), pfm9k.2 (Nilsson et al., 2022) and ArchKalmag14k (Schanner et al., 2022). Prior to 1000 CE we see that declination values are relatively steady over time, whereas there are some variations in inclination and intensity. The inclination increases until around 1000 CE, while the intensity may only have decreased a little during this period. There is a lack of data between 1000-1400 CE, so the PSV curve shows little variation. At 1400 CE there is a steeper inclination and a clearly stronger field of ~50 μT. After 1400 CE the PSV curve shows major changes in all three components: the declination decreases to $-18°$ in 1750 CE, the inclination increases to $-34°$ in 1550 CE and then drops to $-55°$ in 1850 CE; and the intensity drops to ~32 μT in 1550 CE.

Geomagnetic field models for La Réunion show a general agreement with the simple prior PSV curve of La Réunion, with some notable differences. For instance, the PSV curve indicates lower declination values between 200 to 1200 CE and higher intensities prior to 1500 CE. Also, the PSV curve clearly shows an intensity peak followed by a pronounced intensity low around 1500 CE, features that are absent from

geomagnetic models. The only period where the models and our PSV curve diverge strongly is between 1400 and 1600 CE, where especially the declination of our PSV curve is higher than that of the geomagnetic models. Here, the declination data points scatter and therefore the PSV curve follows the upper range of data points, but the models align more with the lower data points. It remains unclear whether the scatter in declination data indicates rapid variations during that time period or it is instead caused by the large age uncertainties.

Geomagnetic model prior

The second PSV curve is generated using the data of Béguin (2020) and this study, with a global model as a prior. Using a global model as a prior can be useful in regions with a low paleomagnetic data coverage. At La Réunion, this is for example the case around 500 CE and 1200 CE, where the PSV curve based on the simple prior can only connect the neighbouring data points. As a prior, the pfm9k.2 model was applied (Nilsson et al., 2022), Fig. 4.5D-F. The most obvious difference with the simple prior PSV curve is that the spread in the posterior ensemble members decreases, and therefore the uncertainty decreased. There are only minor differences between the declination and inclination curves of the simple and pfm9k prior–based models. For example, the geomagnetic model curve shows a shallower inclination around 800 CE, and a more pronounced steep inclination around 1250 CE. In the intensity curve, the model prior captures more variations and an intensity low around 750 CE, but it fails to reproduce the high intensities around 1450 CE and the low intensities around 1600 CE. This is likely because the new data points diverge too much from the pfm9k.2 model in this time interval.

In declination, both the simple and the geomagnetic field model prior indicate a positive peak around 1200-1300 CE. It is important to note that the paleomagnetic dataset for La Réunion for this interval only has a few data points, and all have large age uncertainties associated with their age. Site RN1, RN3A and RN3B have positive declinations, but were sampled too far from the GPS-location of the radiocarbon dated flow to be reliably attributed to their age. The Piton Indivis flow, sampling site TGY-18, resulted in a declination of 10.4°, however this flow was not yet dated at that time and only recently it received a dating of 420±80 BP. This dating results in a rather large age uncertainty, see Fig. 4.5A and B. A young lava flow sampled by Watkins (1973) close to the Piton Indivis location had a similar direction of 8.2° declination and -35.5° inclination. Lastly, the RE11 declination result of the Piton Moka from Béguin (2020) was 7.8°. All of these sites have inclinations ranging from 35-40°. Considering the positive declinations together with the inclinations, these sites align more closely with the 1200-1300 CE period. It should however be noted that data coverage in this time period is low, making the global model prior an interesting addition to the PSV curve.

When comparing the PSV curves generated with a simple prior and with a global field model prior, we consider the simple prior to be more appropriate for periods before 1750 CE. The global field model prior produces a curve that remains closer to the model which is inherently hampered from a lack of data in this region, which comes at the cost of smoothing out variability. For example, the sharp

changes around 1500 CE are largely suppressed, even though such rapid variations are strongly supported by the data. Since our primary interest is to capture the true variability recorded by the data, we therefore prefer the simple prior-based model. Nonetheless, it is useful to construct both curves to identify the most reliable result. For recent periods, i.e. after 1750 CE, the PSV curves generated with the global model prior are more accurate as they align with the gufm1 model.

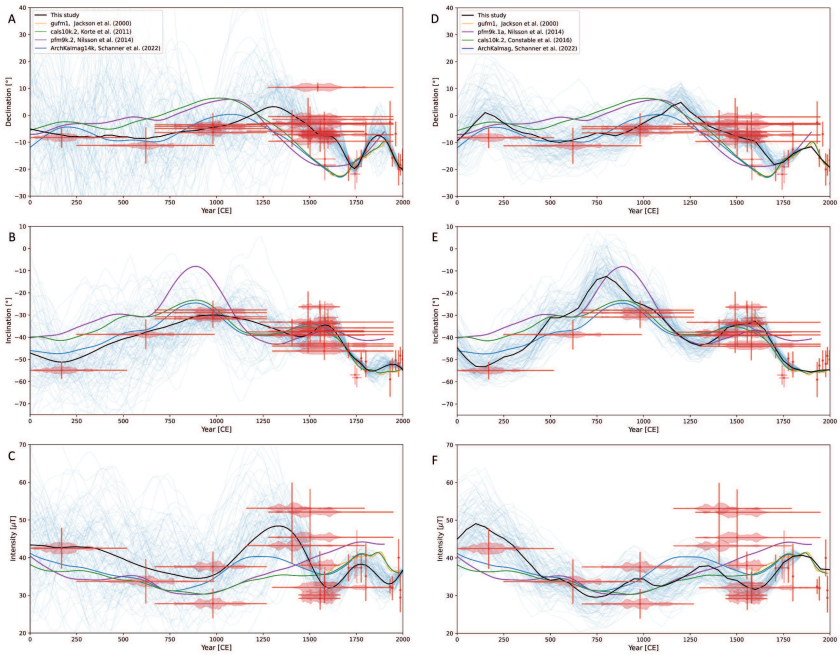


Figure 4.5: Paleosecular variation curves of La Réunion. In A-C are the declination, inclination and intensity curves made using a simple prior. In D-F are the PSV curves made using the pfm9k.2 model (Nilsson et al., 2022). In all plots, the black line is the PSV curve at the location of La Réunion. The light blue lines represent the posterior ensemble members. The coloured lines are the predictions from global magnetic field models. In red are the data results from this and previous studies. In D-F only the results of this study and Béguin (2020), in A-C also those of Tanguy et al. (2011) are included. The dots show the normally distributed errors in declination, inclination and intensity. Also the age uncertainties are shown, there is no error in age when the site was absolutely dated, the pioneer sites have a normal age distribution and the radiocarbon dated sites are shown as red violins with the middle point as the most probable age.

4.6.3. Implications geomagnetic field evolution La Réunion

The PSV curves generated in Fig. 4.5 give new insights on the behaviour of the Earth's magnetic field at the location of La Réunion. We will discuss some interesting observations regarding directional changes and intensity variations. In the intensity curve, the simple prior accurately catches the high intensities of the dataset of ~49 μT at 1300 CE (Fig. 4.5C), after which it drops to ~30-32 μT at 1550 CE. The estimated decrease in field strength would be ~0.068 μT per year. During this time there are also rapid directional changes, both the declination and inclination val-

ues decrease. The declination decreases from around 1625 CE to 1750 CE with 0.08° per year, while the inclination varies from 1600 CE to 1850 CE with around 0.092° per year. These directional variations in combination with the low intensity could be due to the presence of the South Atlantic Anomaly. Similar directional changes are found in Southern Africa (Tarduno et al., 2015) between 1225-1550 CE, with the lowest intensities at ca. 1370 CE. This dataset yielded directional changes of 0.11° to 0.12° per year and an intensity decrease of -0.054 ± 0.036 μT per year. The decline in field strength at La Réunion is therefore more pronounced than in South Africa. It is worth emphasizing that the intensity gradient at ca. 1370 CE is exceptionally steep. At that time, the low intensities in South Africa are contrasted with the high intensity at La Réunion, resulting in a difference of about 25 μT across a distance of roughly 2700 km. For comparison, a gradient of this magnitude in the present-day field would only occur over approximately twice that distance. Such a steep gradient highlights the complexity of the field behaviour around 1370 CE. To account for both the South African and La Réunion datasets, we propose two scenarios.

In the first scenario, the SAA migrated from the Indian Ocean underneath La Réunion to South Africa prior to 1300 CE, and grew or shifted slightly eastwards around 1550 CE. This could explain the slightly lower intensity at 750 CE in the simple prior PSV curve, but due to the scarcity of paleomagnetic data for these periods this low intensity is less certain than the one at 1550 CE. The second option is that the SAA formed under Southern Africa and influenced the field at La Réunion around 1550 CE, before moving westwards to its present-day location at South America. Currently, the SAA has a secondary minimum Southwest of Africa (Amit et al., 2021), a similar process may have occurred at La Réunion. In both scenarios, depending on whether La Réunion captured the Eastern edge of the SAA or the actual minimum was located underneath La Réunion, the drift rate of the SAA after 1550 CE would be around 0.19° to 0.23°, which fits with current estimated drift rates (Fürst et al., 2009; Ye et al., 2017). To distinguish between these scenarios, and assess whether the SAA is linked to a reverse flux patch beneath Southern Africa, more data from regions to the East of La Réunion are required, combined with a geomagnetic field modelling study based on the new data.

4.7. Conclusion

In this study we presented paleomagnetic data from recent volcanics (<2ka) from the island of La Réunion. Of our 18 sampling sites, 12 sites successfully yielded paleodirections and 10 sites gave reliable paleointensity results. We combined our data with paleomagnetic data from previous studies on La Réunion to generate a paleosecular variation curve spanning the last 2000 years. Using a new Bayesian method to reconstruct PSV curves while taking all uncertainties in dating properly into account we produced two PSV curves: the first using a simple prior for the Bayesian modelling, and the second with the pfm9k model as a global geomagnetic field model prior. The PSV curves indicate rapid directional variations around 1500-1750 CE, together with an intensity high ~1400 CE followed by an intensity low ~1550 CE. These findings support the presence of the South Atlantic Anomaly at La Réunion during this period and, when combined with paleomagnetic data

from Southern Africa, point to two possible scenarios for its origin. In the first, the anomaly migrated from the Indian Ocean prior to 1300 CE and moved slightly eastwards to La Réunion around 1550 CE before migrating Westwards again. Alternatively, in the second scenario the SAA formed under Southern Africa and grew, or shifted East, to influence the field at La Réunion around 1550 CE.

4.8. Supplementary Information

Supplementary Table 4.1: Results of Béguin, 2020. Given are the sites, lava flow age in years CE or BP, latitude and longitude. The obtained directions per site are given by the declination (Dec), inclination (Inc), 95 percent confidence interval α_{95} and the precision parameter (k). Also the intensity (PI) and intensity error (σ) are given.

Site	Age	Error	Lat (S)	Long (E)	Dec (°)	Inc (°)	α95(°)	k	PI (μT)	σ
RE18	1890BP	55	-21.2091	55.6432	-8.2	-54.9	111.6	3.9	42.5	5.4
RE19	1465BP	75	-21.2123	55.6818	-11.2	-38.7	78.4	6.7	33.7	5.9
RE26	1105BP	60	-21.3887	55.6459	-4.1	-30.8	106.2	5	37.6	4
RE29	1105BP	60	-21.3323	55.6423	-6.4	-27.7	175.7	4.2	27.8	3.9
RE30	1105BP	60	-21.3584	55.6466	-4.9	-28.9	345.1	3.3		
RE26,29,30	1105BP	60			-5.1	-29.2	184.7	2.3	37.1	4.5
RE4	575BP	75	-21.3546	55.7227	-3.2	-39.1	78.5	5.2	43.2	4.9
RE5	575BP	75	-21.3514	55.7067	-5.9	-37.6	79.9	5.8	53.1	6.8
RE4,5	575BP	75			-4.4	-38.5	80.7	3.6	46.7	7.4
RE15	455BP	70	-21.3533	55.7898	-9.6	-37.4	47.8	6.1	52.1	6.1
RE33	355BP	75	-21.2878	55.7124	-3.3	-43	90.5	4.6		
RE16	381BP	26	-21.2308	55.6622	-7.7	-33.9	325.2	3.1	29.2	3
RE10	1708CE		-21.1565	55.7619	-20.9	-45.9	170.1	3.5	37.3	3.6
RE14	1776CE		-21.3287	55.8067	-16.4	-52.2	274.4	2.8		
RE31	1776CE		-21.3288	55.8010	-15.5	-49.5	288.2	2.7	37.3	3.9
RE14,31	1776CE				-15.9	-50.8	187.9	1.9		
RE22	1801CE		-21.2981	55.7994	-12.6	-54.7	290.5	3.3	35.1	6.6
RE23	1801CE		-21.2817	55.7999	-6.9	-51	201.3	4.7	40.5	3.3
RE22,23	1801CE				-10	-53.2	156.4	2.8	39.8	4.2
RE20	1931CE		-21.2193	55.8051	-2.6	-59	59.1	7.9	32.4	2
RE24	1943CE		-21.2761	55.7918	-18.3	-54.3	160	4.4	29.6	4.4
RE25	1943CE		-21.2780	55.7916	-13.4	-51	115.9	5.2	32.3	2.8
RE24,25	1943CE				-15.8	-52.7	92.9	3.3	31.9	3.2
RE8	1961CE		-21.2312	55.8016	-6.9	-50.4	81	4.6		
RE9	1977CE		-21.1684	55.8018	-20	-51.9	85.2	6	40	4.9
RE2	1986CE		-21.3179	55.7949					29.4	3.9
RE3	1986CE		-21.3190	55.7955	-22.5	-47.6	36.5	9.3	31.1	3.1
RE32	1986CE		-21.3309	55.8068	-19.2	-49.5	136.2	4.8	27.1	3.6
RE3,32	1986CE				-18.4	-48.27	94.7	3.95	31.4	3.9
RE28	1998CE		-21.2230	55.8063	-16.6	-50	4.2	174.7	29.4	3.9
RE6	2002CE		-21.2522	55.7958	-29	-53.1	4.9	185.9		
RE21	2002CE		-21.2193	55.8050	-20.4	-56.9	5.8	176.3		
RE6+21	2002CE				-25.3	-54.9	3.7	107.7		
RE7	2004CE		-21.2413	55.7988	-14.2	-47.9	3.9	240.9		
RE1	2007CE		-21.2817	55.7956	-17.5	-50.3	35.4	10.3		



5

Recent geomagnetic field behaviour in Indonesia: paleodirections and paleointensities from the past 5,000 years from Bali

Romy Meyer, Aditya Pratama, Putu Billy Suryanata, Ahmad Fadillah, Wilfridus Ferdinando Supriyadi Banggur, Maria Karatzanou and Lennart V. de Groot

Abstract *Global geomagnetic field models critically depend on the availability and quality of paleomagnetic data. The paleomagnetic database, however, is highly biased towards the Northern Hemisphere, whereas the recent behaviour of the Earth's magnetic field in the Southern Hemisphere is characterised by intriguing anomalies. Here, we present paleodirectional and paleointensity results obtained from two volcanoes on the island of Bali, Indonesia. Global geomagnetic field models predict the emergence of the South Atlantic Anomaly (SAA) West of Bali, and the presence of the West Pacific Anomaly (WPA) North of Bali. Understanding the onset and evolution of these anomalies is hampered by extremely low data coverage in the region of the Indonesian archipelago, with only sedimentary records or much older paleomagnetic data available. On Bali, we sampled 8 recent lava flows on Gunung Batur that erupted between 1849-1974 CE. Those results can be compared to reference values from the International Geomagnetic Reference Field (IGRF). On Gunung Agung we sampled lava flows with approximate ages from 5960 ± 70 BP to the most recent flow from 1963 CE. Based on only the most reliable paleodirectional and intensity results we constructed two full-vector paleosecular variation (PSV) curves using a Bayesian approach. The first PSV curve was based on a simple dipole prior, the second on a global geomagnetic field model prior. The curves capture interesting variations in the period ~1000 CE until ~1300 CE, which is characterised by rapid directional variations combined with lower intensities. These new results fill a critical void in the global paleomagnetic database, and provide new constraints on regional field behaviour in Southeast Asia, with implications for understanding the emergence and evolution of the South Atlantic and West Pacific anomalies.*

5.1. Introduction

The behaviour of the Earth's geomagnetic field over the past millennia offers key insights into the dynamics of the geodynamo and long-term magnetic field variability. Short term variations over the last centuries are captured in global geomagnetic field models, while regional short term changes in the Earth's magnetic field are described by full-vector paleosecular variation (PSV) curves. The reliability of both global models and regional PSV curves critically depends on the amount of paleomagnetic data available, from either sediments, archaeological materials or volcanic rocks. Currently, the global paleomagnetic database is dominated by data from the Northern Hemisphere (Panovska et al., 2015). Paleomagnetic data from the Southern Hemisphere, equatorial regions and especially the West Pacific remain scarce. This is particularly unfortunate as these regions are currently, or have been recently, influenced by geomagnetic anomalies. One such anomaly is the South Atlantic Anomaly (SAA), a region of low field intensity currently centred over South America (Amit et al., 2021; Finlay et al., 2020) and of which the onset and evolution remain unclear. Additionally, there is evidence for a second historical low-intensity feature occurring in the West Pacific: the West Pacific Anomaly (WPA) (He et al., 2021; Yue et al., 2024). The WPA may have been present in the West Pacific from 1600 to 1820 CE (Yue et al., 2024). The evolution of both anomalies is mostly inferred from global field models, but regional paleomagnetic data coverage is extremely limited, hampering studies into the onset, origin and evolution of these geomagnetic anomalies.

Beyond their global relevance, high-quality PSV curves also serve as valuable tools for dating volcanic deposits (Béguin et al., 2021; Goguitchaichvili et al., 2019; Pavón-Carrasco et al., 2011). Radiocarbon dating remains the standard for recent volcanism, but suitable material is not always available below a lava flow and/or the calibrated ages may give large uncertainties. In these cases, PSV curves can offer an independent chronological framework to provide information on the eruption history of hazardous volcanoes.

Only a few paleomagnetic studies have been conducted so far in Indonesia. Available records include paleomagnetic data from lava flows and dykes of Brunhes and late Matuyama age from the islands Java and Bawean (Elmaleh et al., 2004); data from deep-sea sediment cores close to Indonesia and the Philippines (Lund et al., 2006); a paleosecular variation curve from stalagmites in East Java (Bijaksana et al., 2009); paleomagnetic secular variation data from Lake Kalimpaa on Sulawesi (Haberzettl et al., 2013); and relative paleointensity records for the last 60 kyr from Lake Towuti, Sulawesi (Kirana et al., 2018). To reconstruct the recent behaviour of the geomagnetic field over the last 5,000 years in detail, these studies are of limited use: either they cover periods too far in the past, or they provide sedimentary records that lack absolute paleointensity determinations.

To improve global geomagnetic field models and thereby our knowledge of the local geomagnetic field behaviour, we did paleomagnetic fieldwork on the island of Bali, Indonesia. Indonesia has many active Holocene volcanoes because of its location in the Pacific 'Ring of Fire'. Here, we present paleomagnetic data obtained from two volcanoes on the island of Bali. On the first volcano, Gunung Batur, we sampled eight sites from seven very recent lava flow units (between 1849-1974 CE) and one volcanic unit of disputed age. On Gunung Agung, we sampled twelve lava flow units with approximate ages according to the volcano's geological map (Nasution et al., 2004). In total we obtained samples from 25 sampling sites on Gunung Agung. Samples from all sites were subjected to both paleodirectional and paleointensity experiments to characterise the recent behaviour of the Earth's magnetic field in Indonesia. These directions and intensities are the first Holocene full-vector paleomagnetic data from the region between the Indian and Pacific Oceans, providing a valuable addition to close the gap in the global paleomagnetic record.

5.2. Geological setting and sampling

The island of Bali is part of the Sunda arc, which is generated by the subduction of the Indo-Australian plate beneath the Eurasian plate (Suryanata et al., 2024). Historically active volcanism on Bali occurs on the volcanoes Gunung Batur and Gunung Agung. Both are located in the Eastern part of the island (Fig. 5.1A). Gunung Batur is a 1717 m high stratovolcano, of which the centre lies within two caldera rims. The first caldera rim was formed around 29,300 BP, which created the Ubud Ignimbrite (Reubi & Nicholls, 2004; Sutawidjaja, 2009). The inner caldera rim was formed around 20,150 BP, during which the Gunungkawi ignimbrite deposit was formed. Since the 1800's, the volcano has erupted at least 22 times (Sutawidjaja,

2009). The locations of lava flows erupted between 1849 CE to 1974 CE are well documented (Sutawidjaja et al., 1992).

Gunung Agung, located east of the Batur Caldera, is the highest peak on Bali at 3031 m. There are four confirmed Holocene eruptive periods for Gunung Agung (GVP, Venzke, 2025). The largest of these occurred in 1963 CE (Self & King, 1996), when a disastrous volcanic eruption generated pyroclastic density currents and formed a lava flow on the north flank of the volcano (flow unit AL14, Fig. 5.1C). Besides this, there are multiple older lava flow deposits according to the geological map of Nasution et al. (2004), of which AL1 should be the oldest and AL14 corresponds to the youngest lava flow (1963 CE). Using radiocarbon dating, Fontijn et al. (2015) dated charcoal within pyroclastic density deposits and palaeosols between scoria fall deposits from Agung. Using geochemical and petrographical analysis Syafitri et al. (2021) made a correlated chronology by combining their own samples with Fontijn et al.'s samples and samples from Dempsey et al. (2013). They divided the lava flow units of Agung into four eruptive periods: pre-3200 ± 60 BP, 3200 ± 60 to 1870 ± 40 BP, 1870 ± 40 to 1040 ± 50 BP, and post-1040 ± 50 BP. The radiocarbon ages of Fontijn et al. (2015) were roughly correlated to the stratigraphy of the geological map by Syafitri et al. (2021), and the stratigraphic age correlations are shown in Fig. 5.2.

5.2.1. Sampling strategy

Fieldwork was done in February-March 2025 to collect paleomagnetic samples (25 mm in diameter and up to 10 cm in length) from Gunung Batur and Gunung Agung: sites from Gunung Agung are labelled as 'A' sites; sites from Gunung Batur as 'B'-sites. For each sampling site 10 to 25 samples were taken with a water-cooled petrol-powered drill. Samples were oriented with a magnetic compass, due to the rainy season it was often cloudy and at midday the sun was too high to use a sun compass for orientations. The lava flows on Gunung Batur were aa' like, with large boulders and an irregular topography. Samples were taken spread out over the outcrop from as many blocks as possible. Except for B7, all samples were obtained from historical flows for which the reference value according to the International Geomagnetic Reference Field (IGRF, Alken et al. (2021)) is known (Table 5.1). The IGRF describes the field values from 1900 CE until now; prior to that the expected values are according to the gufm1 model (Jackson et al., 2000) and might be less accurate. Site B7 was taken from the northern wall of the caldera: the Bunbulan lava flow. The moment of formation of the Bunbulan lava dome complex was bracketed in between the formation of the two caldera's at 29,300 BP - 20,150 BP by Reubi and Nicholls (2004). However, according to the geological map of Sutawidjaja et al. (1992) the Bunbulan lava formed around 5500 BP. Samples on Gunung Agung were obtained from outcrops along the road and often from riverbeds. The size of the outcrop in the river varied, from a massive lava flow to large boulders. Samples were always taken far apart from each other, and where possible from different boulders. Sampling sites on Agung are mostly located within the area of a lava flow unit according to Nasution et al. (2004) (Table 5.1), except for A4, A7 and A27. Site A4 is located slightly South of the AL5 unit; A7 is slightly north of the indicated location of the Pawon scoria cone but the outcrop corresponded to the geological

description (Fig. 5.2); and A27 was sampled in a riverbed a little bit north of unit AL4 (Fig. 5.2). Paleomagnetic samples were not obtained at AL11, where only soil was found, and AL17, where pyroclastics were sampled. In some cases the sampling location is also close to a sampling location of Syafitri et al. (2021) or Fontijn et al. (2015), including A1 (close to MTG-5A,B,C), A2 (near MTG-1B), A4 (at AG013), A6 (close to TAR-1,2); A8 (near GA-TU1) and A18 (close to GA-DA1).

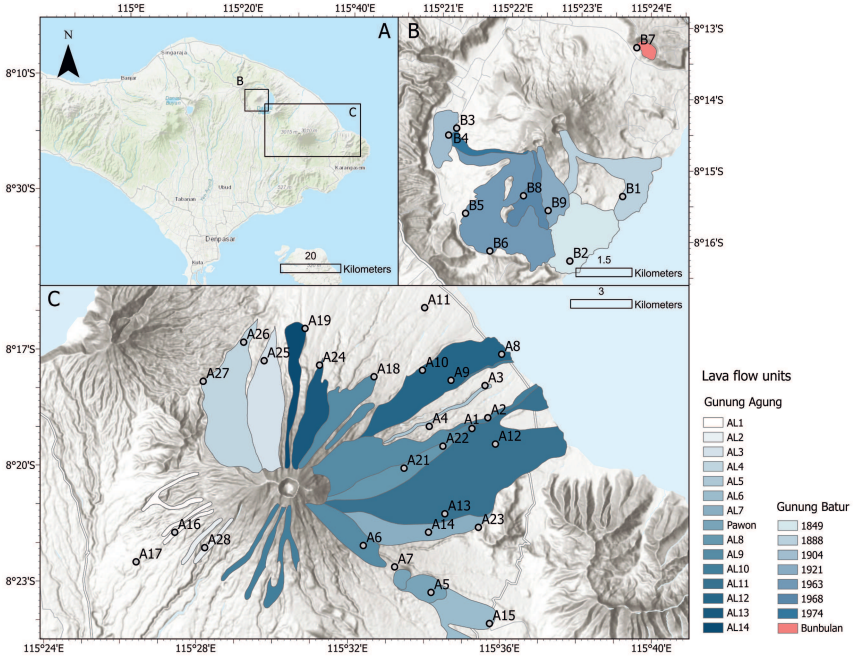


Figure 5.1: Sampling locations. Map showing the island of Bali (A) with the locations of Gunung Batur (B) and Gunung Agung (C). Sampling locations on both volcanoes are shown, lava flows in years CE on Batur are after the geological map of Sutawidjaja et al. (1992), locations of lava flow units on Agung are from Nasution et al. (2004).

5.3. Rock Magnetic Characteristics

To characterise the remanence-carrying minerals and to evaluate the suitability of the samples for paleointensity experiments, we performed rock magnetic analyses on representative specimens from all sites. The thermomagnetic behaviour of the samples was assessed using Curie balance experiments, and high-field hysteresis measurements were carried out to assess domain state properties. The thermomagnetic measurements were done on one sample per site (~15 mg) using a horizontal translation Curie balance (Mullender et al., 1993) to determine their Curie temperatures. Samples were heated sequentially from room temperature to 150°C, 225°C, 300°C, 375°C, 450°C, 525°C and 600°C, and then cooled down. After each step the temperature was lowered by 75°C to check for the reversibility of the signal. The alteration temperature was defined as the highest temperature step at which

Table 5.1: Sampling sites and rock magnetic characteristics for Gunung Batur and Gunung Agung. Given are the sites, lava flow in years CE or flow unit according to the geological maps (Nasution et al., 2004; Sutawidjaja et al., 1992), latitude and longitude, elevation (Elv), IGRF values for declination (D_{ref}), inclination (I_{ref}) and intensity (Int_{ref}), dominant Curie Temperatures (T_c) and alteration temperature determined from the magnetization vs temperature diagrams (T_{alt}).

Site	Unit	Lat (°S)	Long (°E)	Elv (m)	D_{ref} (°)	Inc_{ref} (°)	Int_{ref} (μT)	T_c (°C)	T_{alt} (°C)
B1	1888	-8.2559	115.3931	1103	1.8	-31.0	43.1	350/540	
B2	1849	-8.2710	115.3804	1109	0.4	-30.2	42.0	350/540	525
B3	1974	-8.2399	115.3532	1129	1.7	-34.8	44.8	310/540	525
B4	1904	-8.2416	115.3513	1120	1.6	-32.8	43.6	360/580	
B5	1963	-8.2598	115.3553	1143	2.2	-34.7	44.8	500/560	
B6	1963	-8.2686	115.3612	1129	2.2	-34.7	44.8	380/540	
B7	Bun.	-8.2212	115.3965	1184				600	
B8	1968	-8.2557	115.3693	1178	2.0	-34.8	44.8	310/540	525
B9	1921	-8.2592	115.3752	1156	1.5	-34.0	44.1	300/540	525
A1	AL9	-8.3176	115.588	236				550	
A2	AL10	-8.3129	115.5949	188				560	375
A3	AL5	-8.2991	115.5937	162				380/580	
A4	AL5	-8.3167	115.5693	461				580	
A5	PL	-8.3883	115.57	582				340/580	525
A6	AL9	-8.368	115.5403	1119				580	
A7	PS	-8.3773	115.5541	824				390/580	
A8	AL12	-8.2856	115.601	68				480/580	375
A9	AL12	-8.2968	115.5788	240				580	
A10	AL12	-8.2925	115.5663	339				580	
A12	AL11	-8.3243	115.5983	222				540	375
A13	AL11	-8.3544	115.5761	556				580	
A14	AL7	-8.3623	115.5689	662				380/580	450
A15	AL6	-8.4017	115.5957	383				410/580	
A16	AL1	-8.3623	115.4576	1166				560	
A18	AL9	-8.2953	115.545	566				480/580	375
A19	AL14	-8.2745	115.5148	502	2.2	-34.7	44.8	580	450
A21	AL8	-8.3347	115.5582	696				580	375
A22	AL8	-8.3252	115.5752	407				560	375
A23	AL7	-8.3602	115.5908	394				580	375
A24	AL13	-8.2903	115.5211	673	0.1	30.0	41.7	520	375
A25	AL3	-8.2884	115.4968	714				490/580	375
A26	AL4	-8.2804	115.4878	615				510/580	375
A27	AL4	-8.2973	115.4701	860				540	
A28	AL2	-8.369	115.4707	1139				580	

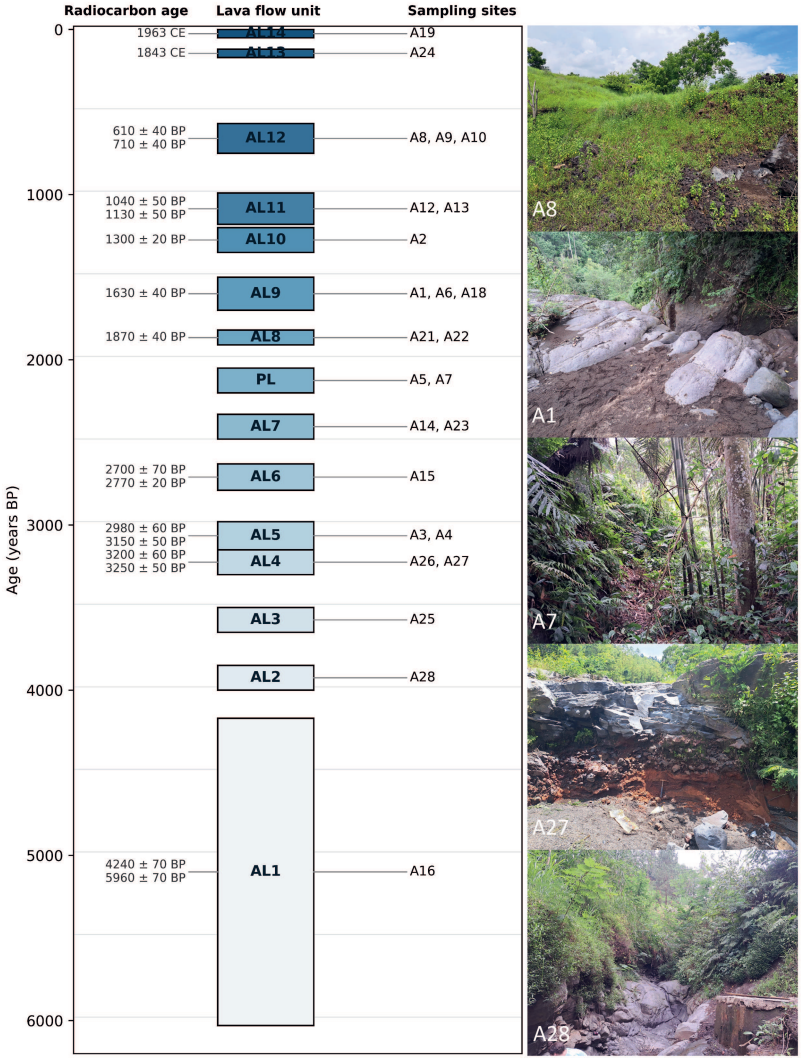


Figure 5.2: Stratigraphic correlation according to Syafitri et al. (2021) from the lava flow units of Gunung Agung.The radiocarbon ages on the left are the approximate top and bottom age assigned to the lava flow unit, note that these lava flow units were not directly dated with radiocarbon (Syafitri et al., 2021). In the middle are the sampling sites of this study, with some pictures of the sampling sites on the right. Ages of units AL1, AL2 and AL3 are estimated, for AL7 and PL (Pawon Lava) there are no assigned radiocarbon ages but the Pawon Lava and Pawon scoria cone erupted towards the end of the 3200 ± 60 to 1870 ± 40 BP period.

the heating and cooling curves were reversible.

Hysteresis measurements were obtained with a PMC 3900 Alternating Gradient Magnetometer. For one sample per site both a hysteresis loop and a back-field curve were measured to assess the magnetic domain state of the samples. The hysteresis loops were measured with a maximum field of 500 mT and an averaging time of 150 ms. The contribution of paramagnetic minerals to the signal was removed by a slope correction above 70% of the maximum field applied. The saturation magnetization (M_s), remanent saturation magnetization (M_{rs}) and coercive force (B_c) were derived from the hysteresis loop. The backfield demagnetization curve of 30 steps had a maximum field at 300 mT with an averaging time of 200 ms. The remanent coercive force (B_{cr}) was obtained from this DCD curve. The ratios of remanence (M_{rs}/M_s) and coercivity (B_{cr}/B_c) of the samples were plotted on a Day diagram (Day et al., 1977) (Fig. 5.3F). Depending on the ratio of M_{rs}/M_s and B_{cr}/B_c, the magnetic domain state of the samples is identified as single domain (SD), pseudo single-domain (PSD) or multi domain (MD). Although Day plots represent bulk magnetic measurements and thus provide only a first order estimate, they nonetheless give a useful impression of magnetic domain states.

5.3.1. Results Gunung Batur

The thermomagnetic measurements for the sites of Gunung Batur show broadly similar behaviour. All sites have a high Curie temperature (T_c) around 540-580°C and, except for site B7, a second lower Curie temperature between 300-500°C (Table 5.1, Fig. 5.3A). This indicates (titano-)magnetite as main magnetic carrier, with variable amounts of Ti-substitution. There is a minor amount of alteration present: sites B2, B3, B8 and B9 have a cooling curve slightly higher than the heating curve. These curves become reversible after the temperature step of 525°C, which is a very high alteration temperature. Site B7 shows a single high T_c of 580°C, indicating Ti-poor magnetite (Fig. 5.3B). Although this site shows a cooling curve below the heating curve, alteration again occurs above 525°C since all lower temperature steps are reversible.

On the Day plot (Fig. 5.3F), all Batur samples fall within the PSD range (Fig. 5.3F), which is expected for these extrusive basaltic rocks. Most samples plot slightly above the negative crystalline shape anisotropy mixing curve from Dunlop (2002), B3 plots furthest away and is the only outlier. The site closest to the single-domain range is B2, while B7 has the lowest M_{rs}/M_s ratio. Sites B4, B5 and B6 behave very similarly, and plot in between B2 and B7. Because all samples show either no alteration or only at very high temperatures, and fall within the PSD range, they are expected to perform well during paleodirectional and paleointensity methods.

5.3.2. Results Gunung Agung

Like the Batur samples, the Gunung Agung sites all have at least one high Curie temperature with the magnetization gradually decreasing until around 540°C-580°C (Table 5.1, Fig. 5.3C-E). Some sites, such as A3 or A15, also yield a second lower Curie temperature around 340°C-510°C. Most curves are largely reversible (Fig. 5.3E), while others point to an onset of alteration at 375°C, with cooling curves both lower

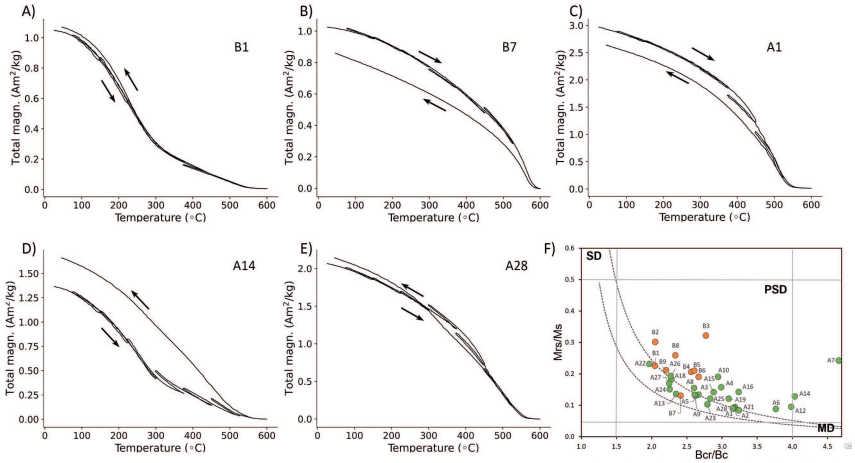


Figure 5.3: Representative rock magnetic results of Gunung Batur and Gunung Agung. Thermomagnetic measurement results are in A-E, arrows pointing down indicate the heating curve, pointing up is the cooling curve. In F) is the Day plot shown, horizontal and vertical lines are the boundaries of the single-domain, pseudo-single-domain or multi-domain range. Orange dots are Batur samples, green dots are Agung samples. Dashed lines are the theoretical mixing curves for uniaxial shape anisotropy and negative cubic shape anisotropy from Dunlop (2002).

and higher than the heating curves (Fig. 5.3C,D). In most cases the differences between the heating and cooling curves are modest (Fig. 5.3C). The largest differences, and thus most pronounced alteration, are seen in sites A14, A22 and A23. These sites are expected to behave less favourable during paleomagnetic measurements, compared to the other sites with high Curie temperatures.

Nearly all Agung samples fall in PSD range of the Day plot, except site A7 which shows a high B_{cr}. The results cluster in the lower half of the PSD range, and near the lower end of the theoretical SD-MD mixing curves (Dunlop, 2002). Hence the sampling sites from Gunung Agung exhibit magnetic properties that tend to be closer to MD than SD behaviour, which might not be ideal during paleointensity experiments as MD grain sizes tend to produce non-linear Arai plots. Sites A6, A7, A12 and A14 show the strongest influence from MD grains; while site A22 plots closest to the SD range. The samples from Gunung Agung appear to behave slightly less ideal than those from Batur. Nonetheless, because most curves indicate only minor alteration and all samples fall within the PSD domain, all sites were included in all paleodirection and paleointensity experiments.

5.4. Paleomagnetic directions

To obtain paleomagnetic directions specimens from both volcanoes were subjected to thermal and alternating field demagnetization experiments. At least 12 specimens per site were measured, except for site B7, A7 and A8 where sampling was difficult and the amount of material was limited. One (only for site B7) to four specimens per site were thermally demagnetised, in steps of 50°C up to 600°C. After

each step the remaining magnetization in the specimen was measured on a 2G-cryogenic magnetometer. Due to an instrument alignment issue, measurements below 150°C were oriented incorrectly (Fig. 5.4C). However, because most specimens lost only very little magnetization at these low temperatures this had almost negligible influence on the results. Very strongly magnetised samples were measured on a JR6 spinner magnetometer. Additionally, 7 to 12 specimens per site were subjected to alternating fields demagnetization experiments using a robotised 2G DC-SQUID magnetometer (Mullender et al., 2016), with steps of 0, 2.5, 5, 7.5, 10, 15, 20, 25, 30, 40, 50, 60, 70, 80, 100, 150, 200, 225, and 270 mT. Throughout all measurements the samples were kept in a magnetically shielded room to avoid bias due to viscous magnetizations. Paleodirections were interpreted using the online portal paleomagnetism.org (Koymans et al., 2016, 2020), where the demagnetization diagrams were plotted as Zijderveld diagrams (Zijderveld, 1967) from which the characteristic remanent magnetization (ChRM) direction was determined as the most stable linear component towards the origin. Site mean directions were calculated using Fisher statistics (Fisher, 1953); outliers were identified using a 45° cut-off. Paleodirectional results are given in Table 5.2, and results from historical sampling sites are compared to their corresponding IGRF value.

5.4.1. Results Gunung Batur

Most of the Batur samples demagnetise in a straight line to the origin of the Zijderveld diagram. Only site B7 and some specimens from B6 have a small overprint, which is easily removed by an alternating field step of 15 mT. The resulting paleomagnetic directions from the recent lava flows on Gunung Batur yield directions with declination ranging between -5.7° and 5.8°; and their inclinations vary from -23.7° to -45.3°. Except for site B2 and B4, all sites yield precision parameters (k) above 50. The oldest deposit, site B7, has the highest k-value, and site B2 shows the largest scatter, with a k-value of 21.7 and an α95 of 10° (Fig. 5.4A). There is no general consensus on the minimal k-value for a reliable paleodirection interpretation, and a lower k-value does not necessarily mean less accurate results (Meyer & de Groot, 2024). This is reflected in the result of B8: the k-value is in the lower range but its difference from the reference value is only 1.3° in declination and 2.3° in inclination (Table 5.1). On the other hand, site B4 has a low k-value of 35.6 and does have a 12.5° lower inclination than expected. Site B2 also has a lower inclination than predicted, all other sites show inclinations that are steeper than the IGRF value.

5.4.2. Results Gunung Agung

Specimens from most Agung sites demagnetise straight to the origin of the Zijderveld diagram, or have only a small overprint that is removed by applying a 5 mT alternating field (Fig. 5.4D). Sites A15, A21, A22 and A23 show slightly more pronounced overprints, until 15 - 30 mT; all paleodirections, however, are well interpretable by disregarding the first steps. From the 25 sampling sites on Gunung Agung, 15 sites yield high k-values between 51 and 565.7. The very high k-values around 500 are all from massive lava flows located in riverbeds (A1, Fig. 5.2). The lower k-value of 51 from sampling site A7, and 66.9 from site A5, were to be expected: site A7 was sampled on the northern part of the Pawon Scoria cone and sampling was challenging

due to many loose fragments in the scoria (Fig. 5.2, Fig. 5.4D). Site A5 was also from this unit, but from a blocky lava outcrop further East.

Not all sampling sites yielded interpretable results. Eight sites show a wide scatter in their VGP distribution, and could not be reliably interpreted. Among them are sites A9, A12, A21, A22 and A25, where the ChRM directions of individual specimens are a straight line to the origin, suggesting that the scatter is due to post-solidification movement of larger blocks. Specimens from A15 and A23 exhibit an overprint in the low alternating field (0-20 mT) and temperature steps (20-250°C), but their scattered directions are most likely also due to post-solidification movement. The last site with scattered directions is A18, whose specimens were so strongly magnetised that AF demagnetization was problematic. In an attempt to better constrain the paleodirection from sites A14 and A24 extra samples were measured, but despite this the k-values of the sites are still very low with 9.5 and 11.9, respectively. Site A14 was sampled on the side of a small road and some blocks might have been rotated during road construction. Sampling further inland was unfortunately not permitted. Site A24 was sampled on the edge of the very blocky aa' flow unit AL13 which might explain post-solidification movement of some blocks. Because the VGP distribution does show some clustering of directions, the results of A14 and A24 are given in italic in Table 5.2.

Two flow units on Gunung Agung are associated with absolute, historical, datings: flow unit AL13 from site A24 most likely has an age of 1843 CE, and the 1963 CE lava flow was sampled at site A19. The results of these two sites can therefore be compared to the International Geomagnetic Reference Field (IGRF, Alken et al. (2021)), although prior to 1900 CE the predicted directions might be less accurate. For 1843 CE the expected declination and inclination are 0.1° and -30.0°, respectively. The resulting declination at A24 was -3.1° and inclination -29.0°. Surprisingly, the average direction of A24 is actually very accurate, despite the unfavourable paleomagnetic statistics. The paleomagnetic direction of A19 could be interpreted from only 6 specimens out of 12. The 1963 CE lava flow front was very overgrown, it was therefore difficult to identify reliable blocks and samples were obtained from as many boulders as possible. Only the most reliable samples were interpreted. The expected direction in 1963 CE is 2.2° for declination and -34.7° in inclination. Site A19 yielded directions of -2.3° in declination and -26.2° for inclination, with an $\alpha 95$ of 5.7°. Thus especially the inclination is higher than expected.

For the successful sites, the declinations range from -9.8° to 6.3°, and the inclinations are between -26.2° and 1.7°. The mean inclination of all sites is -17.8°, which is in agreement with the -16.2° that is expected from a geocentric axial dipole (GAD) at this location. Especially site A13 and A26 diverge from this value, with very shallow inclinations of +1.7° and -4.5°, respectively (Fig. 5.4E,F).

5.5. Paleointensities

To obtain information about the past field strength in Indonesia, samples from each sampling site were subjected to paleointensity experiments. Only site A18 was not

subjected to the experiment, as it behaved very poorly in the paleodirectional experiments. Initially, for each site four specimens were subjected to the IZZI-Thellier paleointensity method (Tauxe & Staudigel, 2004), in two batches. Depending on the success rate of these first specimens and the quality of their Arai plots, an additional two to four specimens were measured in a third batch to improve the statistical accuracy of the average paleointensity at site level. The IZZI protocol alternates sets of zero-field, in field (ZI) steps (Coe, 1967), and in-field, zero-field (IZ) steps (Aitken et al., 1988). After each 'ZIIZ' set, a pTRM check was included to check for thermal alteration (Coe et al., 1978), resulting in a 'ZIIZP'-protocol. A laboratory field of 50 μT was applied during the in-field steps. The temperature increments were chosen based on the thermomagnetic measurements. The first group of samples were divided into two batches. The first batch was subjected to 40°C increments between 100 and 300°C, and then 50°C-steps to 500°C. The second batch used 50°C increments up to 400°C, before going in steps of 40°C. The third batch with the additional set samples was measured from 200°C in steps of 50°C to 400°C, followed by steps of 440, 480, 520, 540 and 580°C. All batches ended with steps of 540°C, 580°C and sometimes 600°C. To ease the handling of the specimens, all specimens were glued into small glass vials with quartz wool and potassium-silicate. They were heated in an ASC TD48-SC furnace and measured on a 2G cryogenic magnetometer, both housed in the same magnetically shielded room to avoid bias from viscous magnetizations.

The quality of the paleointensity results was assessed using paleointensity.org (Béguin et al., 2020). The results were analysed using six different sets of selection criteria: SELCRIT2 (Selkin & Tauxe, 2000), TTA and TTB (Leonhardt et al., 2004), PICRIT03 (Kissel & Laj, 2004), CLASS-A (L. V. de Groot et al., 2014a) and CCRIT (Cromwell et al., 2015b). The first four included the modifications as proposed by Paterson et al. (2014). The curvature criteria k' is strictest for CCRIT, k'≤0.164, all others have the curvature criteria set at k'≤0.35. All other selection criteria values are in Supp. Table 5.1. The auto interpreter function of paleointensity.org was used to avoid subjective interpretation bias. From the interpretations that passed a set of selection criteria, the average paleointensity and standard deviation was calculated at site level. This means that interpretations that passed more than one selection criteria were included as many times as they passed a set of selection criteria, and therefore received more weight in the site level average paleointensity. The site average paleointensity was considered to be more reliable when the standard deviation divided by the mean (σ/PI) did not exceed 25% (Paterson et al., 2014) and there were at least three specimens to interpret. All results are given in Table 5.2, with representative Arai diagrams in Fig. 5.4.

5.5.1. Results Gunung Batur

Rock magnetically, most samples from Gunung Batur indicated favourable behaviour for paleointensity experiments, which is reflected in relatively high success rates in these experiments. Out of 51 specimens measured, 47 passed at least one of the selection criteria, resulting in a success rate of 92%. All Batur sites had at least three specimens to interpret. Although site B6 and B7 have a σ/PI below 25%, most of their specimens suffered from 'sagging' in their Arai plot, most likely caused by

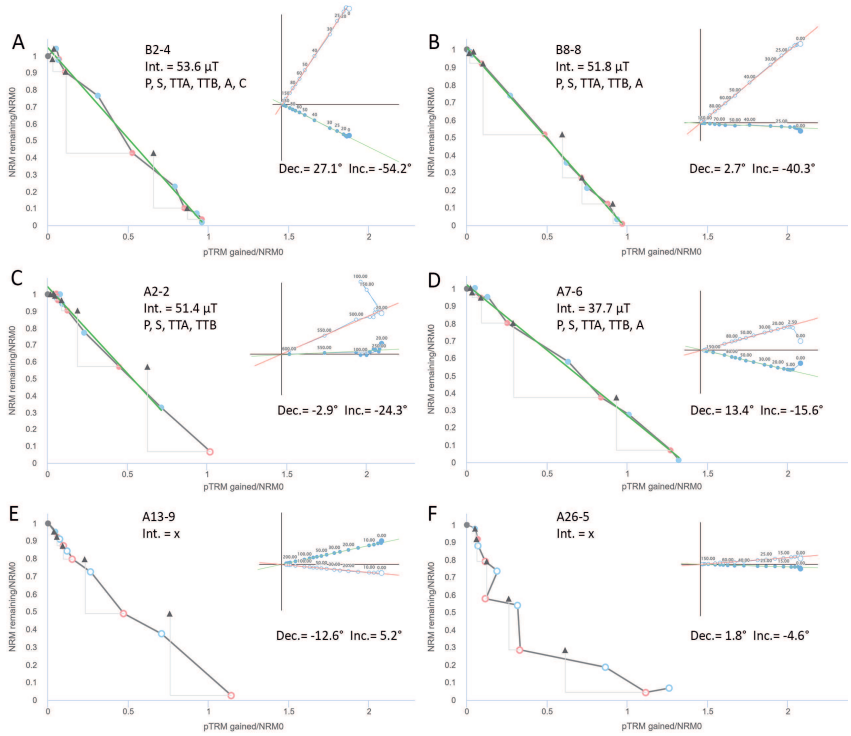


Figure 5.4: Representative paleodirectional and paleointensity results from six sampling sites of Gunung Agung and Gunung Batur. Of each site an Arai diagram is shown, where the blue circles represent the ZI-steps and the red circles the IZ-steps. Black triangles are the pTRM checks, the green line is the largest segment accepted by at least one of the selection criteria. The paleointensity result for each sample is given, as well as which selection criteria the specimen passes: PICRIT03 (P), SELCRIT2 (S), CLASSA (A), TTA, TTB and CCRIT (C). On the top right is the Zijderveld diagram. Closed circles are declination steps, open circles are inclination steps. The straight line through the measurement steps represent the ChRM direction for declination (green) and inclination (red).

MD behaviour; or failing pTRM checks after 400°C, an expression of high temperature alteration. Therefore, only limited numbers of either low or high temperature steps passed sets of selection criteria, resulting in a bimodal set of paleointensities. These two sites are therefore less reliable and we did not measure extra specimens. Specimens from the other sites yielded high quality results with intensities between 41.0 and 55.3 μT, and σ ranging from 3.7 to 7.5 μT. Compared to the expected IGRF value, only site B5 has an intensity that is lower than expected, by 3.8 μT. All other sites produced intensities that are higher than expected, between 1.8 μT higher for the 1888 CE flow at B1, to 10.5 μT for the 1974 CE flow at site B3.

5.5.2. Results Gunung Agung

Out of the 138 specimens measured for the sampling sites from Gunung Agung, 93 passed at least one of the selection criteria, a success rate of 67.4%. However, not all sites also yielded meaningful results. For each of the sites A21, A23, A25, A26 and A28 only one specimen was accepted, which is not enough for a reliable interpretation. Most of the specimens fail the selection criteria due to various ways of non-ideal behaviour. Almost all experience sagging and have a k'>0.35, so there seems to be a larger contribution from MD grains in these samples then expected based on the rock-magnetic analyses pointing to the PSD range (Fig. 5.3F). Additionally, some have failing pTRM checks at temperatures higher than 400°C, which is consistent with their alteration temperature at 375°C (Table 5.1). Specimens from A21 and A26 also display zigzagging behaviour (Fig. 5.4F) and some specimens of site A28 gain almost no TRM compared to the NRM lost. Other sites that we deem less reliable are those with a σ/PI larger than 25%, which are sites A10, A16, A22 and A24. Moreover, sites A10 and A16 each yielded only 2 successful specimens and therefore fail our reliability criteria for a site mean paleointensity. Specimens from A24 experience sagging and produced paleointensity values ranging from 15 to 70 μT, and therefore unreliable. Site A22 performed slightly better, but with a σ/PI of 26.9%, its result should be treated with caution.

Ultimately, paleointensities could be determined successfully from 73 samples from 14 sites; and ranged from 36.2 μT for sampling site A8, to 51.3 μT for sampling site A6. Some sites that yielded unsuccessful paleodirections due to post-solidification block rotations, such as A12 and A15, did give reliable paleointensity values. The mean paleointensity of all sites is 43.6 μT, which is in line with the average paleointensity at Bali island of 44.2 μT since 1850 CE (IGRF, Alken et al. (2021)), but much higher than the intensity of ~31 μT according to the Geocentric Axial Dipole (GAD) estimate based on the present day field. The historical flow at A19 yielded a paleointensity of 46.4 μT, which is only 1.6 μT higher than the expected intensity in 1963 CE.

Site	n/N	Dec (°)	Inc (°)	α95(°)	k	n/N	n_int	PI (μT)	σ	σ/PI	ΔDec	ΔInc	ΔInt
B1	11/12	2.8	-23.4	5.5	70.8	6/6	396	44.9	4.7	10.5	-0.9	7.6	1.8
B2	11/12	2.5	-37.9	10	21.7	6/6	664	50.3	7.0	13.9	2.1	-7.7	8.3
B3	11/12	0.7	-32	3.6	161.2	6/6	489	55.3	3.8	6.8	-1.0	2.9	10.5
B4	12/12	5.8	-45.3	7.4	35.6	6/6	380	52.4	7.5	14.3	4.2	-12.5	8.8
B5	12/12	-5.7	-25.9	3.7	139.3	5/6	188	41.0	3.7	9.0	-7.8	8.8	-3.8
B6	12/12	3.4	-30.3	3.1	203.3	*4/4*	*51*	*33.3*	*4.6*	*13.7*	1.3	4.3	*-11.5*
B7	8/9	-5.3	-23.4	3.7	225.4	*3/4*	*28*	*76.9*	*9.1*	*11.8*			
B8	10/12	3.2	-32.5	5.5	79	5/7	420	53.0	4.0	7.5	1.3	2.3	8.2
B9	12/12	-3.3	-24.7	4.5	92.8	6/6	298	51.7	3.4	6.5	-4.8	9.2	7.7
A1	12/12	-3.8	-23.7	1.8	565.7	6/7	203	43.1	6.9	16.0			
A2	11/12	-2.5	-24.7	2.1	493.9	5/6	143	48.1	9.3	19.3			
A3	11/12	6.3	-23.1	3.5	168.4	6/7	283	40.0	4.5	11.3			
A4	12/12	-9.8	-17.8	4.2	110.2	5/7	20	41.0	7.0	17.1			
A5	12/12	-8.9	-14	5.4	66.9	5/8	112	38.5	6.4	16.6			
A6	11/12	-5.8	-23.4	4.5	106.4	4/7	155	51.3	5.7	11.0			
A7	8/10	-0.6	-11.1	7.8	51.2	7/7	513	45.2	5.9	13.0			
A8	8/11	-0.6	-22.7	5.2	114.8	5/8	167	36.2	5.1	14.1			
A9	0/12					4/4	171	46.8	5.8	12.3			
A10	11/12	1.2	-18	3.6	159.9	*2/4*	*68*	*37.9*	*11.2*	*29.6*			
A12	0/12					6/6	216	41.8	5.3	12.7			
A13	11/12	-8.3	1.7	4.7	97.5	5/6	231	43.9	6.9	15.7			
A14	*16/16*	*-18.6*	*-9.6*	*12.6*	*9.5*	4/4	62	46.1	9.3	20.2			
A15	0/12					5/7	128	41.9	4.8	11.5			
A16	11/12	-0.3	-24.6	2.3	138.8	*2/4*	*8*	*49.4*	*26.0*	*52.6*			
A18	0/12												
A19	6/12	-2.3	-26.2	5.7	138.8	6/6	170	46.4	4.0	8.6	-4.5	8.6	1.6
A21	0/12					*1/4*	*16*	*35.5*	*0.7*	*2.0*			
A22	0/12					*4/4*	*111*	*57.7*	*15.5*	*26.9*			
A23	0/12					*1/4*	*1*	*52.1*					
A24	*13/16*	*-3.1*	*-29.0*	*12.5*	*11.9*	*4/8*	*10*	*36.5*	*15.3*	*41.8*			
A25	0/12					*1/4*	*29*	*41.8*	*2.6*	*6.2*			
A26	12/12	-2.7	-4.5	1.9	534.5	*1/4*	*34*	*54.0*	*8.0*	*14.9*			
A27	12/12	4.9	-16.1	4.5	93.3	*3/4*	*4*	*66.8*	*12.9*	*19.3*			
A28	9/12	0.9	-18.7	6.6	61	*1/4*	*22*	*25.6*	*1.1*	*4.2*			

Table 5.2: Paleodirectional and paleointensity results. The obtained directions per site are given by the parameters: (n/N) number of samples accepted / total amount of samples per site, the declination (Dec), inclination (Inc), 95 percent confidence interval α_{95} and the precision parameter (k). The obtained paleointensities per site are given by: number of samples accepted / total amount of samples per site (n/N), number of interpretations (n_int), resulting paleointensity (PI), standard deviation (σ) and the standard deviation divided by the paleointensity (σ/PI). The difference with the IGRF value given in Table 5.1 is declination (ΔDec) and inclination (ΔInc) and intensity (ΔInt). Paleodirections or paleointensities with a low reliability are in italic.

5.6. Discussion

Below, we will first discuss the paleomagnetic results from the historical lava flows on Gunung Batur and Gunung Agung. Then the age uncertainties in the dataset of Gunung Agung are addressed. Based on the data from only the reliable sites, we produce a paleosecular variation curve from 3000 BCE until 2000 CE for the island of Bali. Finally, we will discuss the implications of this curve for the behaviour of Earth's magnetic field.

5.6.1. Paleomagnetic results after 1800 CE

To assess the reliability of our paleomagnetic data, we compare the historical sites in our data-set with the expected paleomagnetic directions and paleointensities from the IGRF (Alken et al., 2021). Two sampling sites from Gunung Agung (A19 and A24) and all but one sites from Gunung Batur were from historical lava flows. Their results are plotted against the associated expected IGRF values in Fig. 5.5D-F. The declination results are scattered around the expected value, and except for B5 and B9, agree within error. The inclinations obtained are, except for site B2 and B4, steeper (higher) than expected. In the Northern Hemisphere, lava flows frequently yield inclinations that are more shallow (lower) than expected (Pavón-Carrasco et al., 2014; Tanguy, 1990; Urrutia-Fucugauchi et al., 2004). This bias may be explained by local magnetic anomalies, imposed by the strongly magnetised underlying rocks in a topographic rough volcanic terrain (Baag et al., 1995; Meyer & de Groot, 2024). A modelling study of inclinations in gullies (Baag et al., 1995) predicted a bias to more negative inclinations in topographic lows in the Northern Hemisphere and a bias towards positive inclinations in the Southern Hemisphere; which agrees with what we see in the results from the recent lava flows on Bali. Besides more negative inclinations, previous studies have also reported lower than expected intensities. Here, we observe the opposite, as we obtained higher than expected intensities. Higher than expected intensities were suggested by Yamamoto et al. (2003) to be caused by the acquisition of thermochemical remanent magnetization (TCRM) during initial lava flow formation. However, most Batur samples show ideal rock magnetic behaviour and linear slopes in the Arai diagrams, and do not show any signs of TCRMs.

A potential cause of the higher than expected intensities may also be the occurrence of local magnetic anomalies resulting from the magnetic terrain effect. If so, the intensity bias, like the inclination bias, would be reversed in the Southern Hemisphere compared to the Northern Hemisphere. If local magnetic anomalies are responsible for the bias in inclinations and intensities observed on Bali, we

could not minimise the effects by sampling across a large area on the lava flows, wherever possible. Future research should therefore examine whether this bias towards higher inclinations and intensities is systematic and whether it requires corrections.

5.6.2. Uncertainties

In Fig. 5.5A-C, the declination, inclination and intensity results from the Gunung Agung sampling sites are plotted against the variations of the field predicted by several geomagnetic field models. All ages are after those given in Fig. 5.2. The radiocarbon ages are converted to calendar ages using the age calibration program MatCal (Lougheed & Obrochta, 2016) with the SHCal20 calibration curve (Hogg et al., 2020). These radiocarbon ages are correlated approximately to the stratigraphy of the geological map. Therefore there is always some uncertainty about the age of the sampled flow as not a directly radiocarbon dated unit was sampled. Additionally, some units have two assigned radiocarbon dates which are usually very close, in Fig. 5.5A-C we use the average of these two ages with the largest age uncertainty. For sampling sites from lava flow units that are only bracketed between older and younger flows (AL2, AL3, AL7 and PL) a dashed age error bar is given. Sites with uncertain declination, inclination, or intensity results (for reasons described below) are shown in grey with dashed error bars and are not included in the PSV curves.

The sampling sites on Gunung Batur generally have well constrained ages, except for site B7 from the Bunbulan lava flow unit. This unit might have erupted between 29,300 - 20,150 BP (Reubi & Nicholls, 2004), or ~5500 BP (Sutawidjaja et al., 1992). It is difficult to resolve this with the paleomagnetic results obtained from B7, since the reliability of geomagnetic field models at <5500 BP remains uncertain. However, B7 does share a Common True Mean Direction (CTMD) with A16, which was sampled from AL1, the oldest lava flow known on Gunung Agung. Therefore, it is possible the Bunbulan unit and AL1 erupted at the same time, although lava flow unit AL1 has a very large age uncertainty. The result of A16 is shown in Fig. 5.5A,B but is not included while generating a PSV curve due to its large age uncertainty.

Lava flow units on Gunung Agung were often sampled at multiple locations, but not all results are similar across the units. For example, the directions of A1 and A6 agree and they share a CTMD, but their intensity results differ. Given that even the results from Gunung Batur, obtained from flows of similar age, show variability, we did not discard results based on these differences. Sites A4 and A27 are considered less certain, as they were sampled slightly outside of the lava flow unit area and may therefore be less reliable than the other site from the same unit. Nonetheless, they will be used to generate a PSV curve. The intensity result from A9 is most likely unreliable. A9 yielded no directional result due to block rotation after cooling, and the paleointensity values from similar aged sites A8 and A10, albeit a large σ/PI, are much lower than that of A9. Therefore, this site is excluded from the PSV curve construction.

Finally, the unsuccessful results from A14, A22 and A24 are plotted in grey for comparison. Site A22 yielded no successful directions while the paleointensity result

has a σ/PI only slightly higher than 25%. Therefore the result is shown in Fig. 5.5 but not used in the PSV curve. Despite the age uncertainties, the dataset presented here provides the most reliable basis currently available to generate a local PSV curve for Bali.

5.6.3. Regional PSV behaviour before 1800 CE

To construct a local PSV curve for Bali we apply the Bayesian method of Schanner et al. (2026), which builds upon the method of Béguin et al. (2021). This method begins with a prior distribution, which can be defined either as a simple constant prior or as an informative prior based on a global geomagnetic field model. Moreover, the Bayesian framework of this method allows for the consistent incorporation of the different types of age information used in this study, whether they are non-Gaussian distributions from calibrated radiocarbon dates, absolute ages, or stratigraphic units constrained only by bracketing layers. As described above, some units were associated with multiple radiocarbon ages. For PSV construction, we approximated these by using the mean of the reported ages together with the largest associated uncertainty, or a slightly higher uncertainty. This simplification may reduce the accuracy of the age constraints, but it provides the most consistent treatment possible with the data currently available. For lava flow units only bracketed between older and younger flows we used a Gaussian uncertainty of 100 to 300 years. All ages and uncertainties are shown in Supp. Table 5.2. We generated two PSV curves: the first uses a simple GAD prior, and the second uses a global geomagnetic field model as prior. A global geomagnetic field model may be useful in regions with low paleomagnetic data coverage as it does not rely solely on connecting the available data points where there are major gaps in the record. As a prior, we chose the pfm9k.2 model(Nilsson et al., 2022). Both PSV curves are shown in Fig. 5.6. Because unit AL1 (A16) is excluded, the PSV curves are generated from 3000 BCE until 2000 CE.

As expected, the PSV curve generated with a simple, GAD prior (Fig. 5.6A-C) gives a reconstruction that is closer to the data and exhibits a smoother trend. In contrast, the pfm9k.2 model prior (Fig. 5.6D-F) yields a PSV curve that in some intervals tracks the geomagnetic field model more closely and, as a result, shows larger variability. For the declination, the geomagnetic field models mostly follow the results we obtained and remain between -5 and +5°. The pfm9k.2 prior-based PSV curve has more variability but, on average, follows both the data and the prior model well. The spread in the posterior ensembles, and thus the uncertainty, of the PSV curve based on the pfm9k.2 model prior is very small for time periods after 0 CE. For the inclination, the differences between the PSV curves based on the simple and pfm9k.2 priors are more pronounced. The pfmk9k.2 prior shows an unexplained low inclination at 200 BCE, a time period for which no data are available, making this feature highly uncertain. After this interval the pfm9k.2 prior-based PSV curve aligns more closely with the site data. Notably, there is an interesting sweep in the pfm9k.2 prior-based PSV curve from almost positive inclinations, measured at site A13, at 1000 CE to steep values of -40° at 1500 CE. The global geomagnetic field models also predict inclination fluctuations during this period, from -15° in 1000 CE to -35° around 1500 CE. However, the result from A13 suggests that the incli-

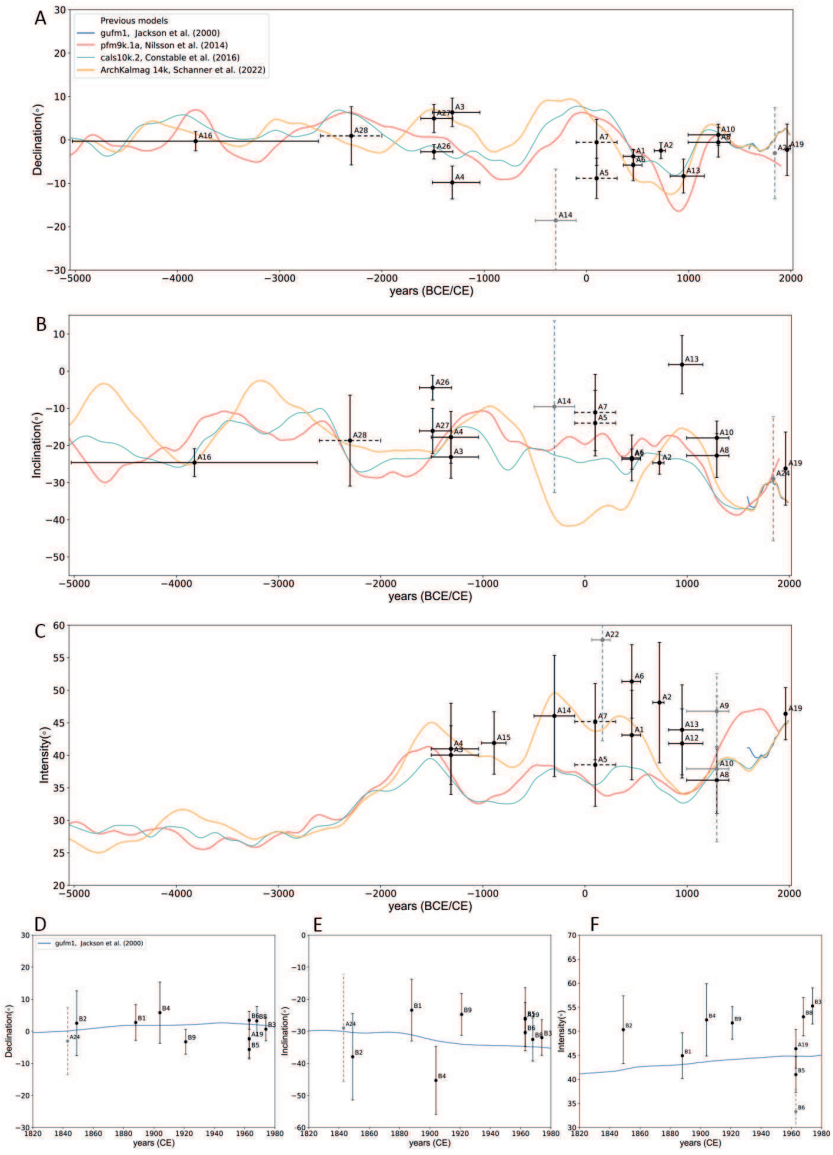


Figure 5.5: Paleomagnetic results from Bali, Indonesia, since 5000 BCE. Declination (A), inclination (B) and intensity (C) results are given for sampling sites from Gunung Agung. All ages are approximate after Fig. 5.2. Striped age errors are given for lava flow units without radiocarbon ages. In grey are the less reliable results. Coloured lines are geomagnetic field models (Constable et al., 2016; Jackson et al., 2000; Nilsson et al., 2014; Schanner et al., 2022). D-F shows the results for the historical lava flows.

nation change may have even been larger. The simple prior-based PSV curve also exhibits an inclination drop, but it is much less pronounced than the pfm9k.2 prior-based PSV curve.

Looking at the intensity results around 1000 CE, sampling sites A12 and A13 yielded intensities around 42 μT, whereas the global geomagnetic field models predict lower values, around 35 μT (Fig. 5.5C). In our PSV curve based on the simple prior the data are more closely followed, with intensities remaining around 40 μT until they reach a peak at 47 μT around 500 CE, followed by a decline of ~10 μT, reaching ~37 μT by 1500 CE. In contrast, the PSV curve using the pfm9k.2 model as prior shows a lower minimum, ~32 μT, which is reached earlier, at 1000 CE, before the field recovers to the current field strength. Although the PSV curves based on both the simple and pfm9k.2 priors generally follow the paleomagnetic data obtained in this study, the limited number of sites combined with the age uncertainties means that the PSV curve based on the simple prior has very large uncertainties and is not the preferred. In contrast, the pfm9k.2 based PSV curve not only reproduces the site data within their error ranges but also incorporates information from the global field behaviour, making it a more reliable representation of the local field behaviour in Bali. Future PSV curve reconstructions will become increasingly robust with additional data.

5.6.4. Implications for the South Atlantic and West Pacific Anomalies

Given the age uncertainties in the Bali dataset, we consider the local PSV curve constructed with a global geomagnetic field model prior to be the more reliable of the two. This curve indicates paleointensities of approximately 32 μT at ca. 1000 CE, followed by an increase in declination of ~0.033° per year and a rapid steepening of the inclination of ~0.092° per year until 1500 CE. Low intensities combined with rapid directional variations as observed in Bali, were also reported at La Réunion (Béguin (2020), Chapter 4). At La Réunion, the lowest paleointensity values occur around 1550 CE and are most likely related to the presence of the South Atlantic Anomaly (SAA). In Southern Africa, however, reduced intensities are documented as early as 1370 CE (Tarduno et al., 2015), whereas at that time La Réunion still recorded high intensities.

The SAA is often defined as the region where the surface magnetic intensity falls below 32 μT (Pavón-Carrasco & De Santis, 2016). The lower intensities of roughly 32 μT observed at Bali therefore do not place it within the centre of the anomaly, but rather along its northern margin, given that Bali lies approximately 14° more North of both South Africa and La Réunion. The South African site showing low intensities is located about 85° West in longitude relative to Bali, implying a westward drift rate of approximately 0.22° per year, which is consistent with estimates for the present-day drift rate of the SAA's centre (Fürst et al., 2009; Ye et al., 2017). Taken together, these results suggest that the anomaly may have originated near Indonesia, drifted westward underneath La Réunion toward Southern Africa, and subsequently shifted Eastward again to influence La Réunion.

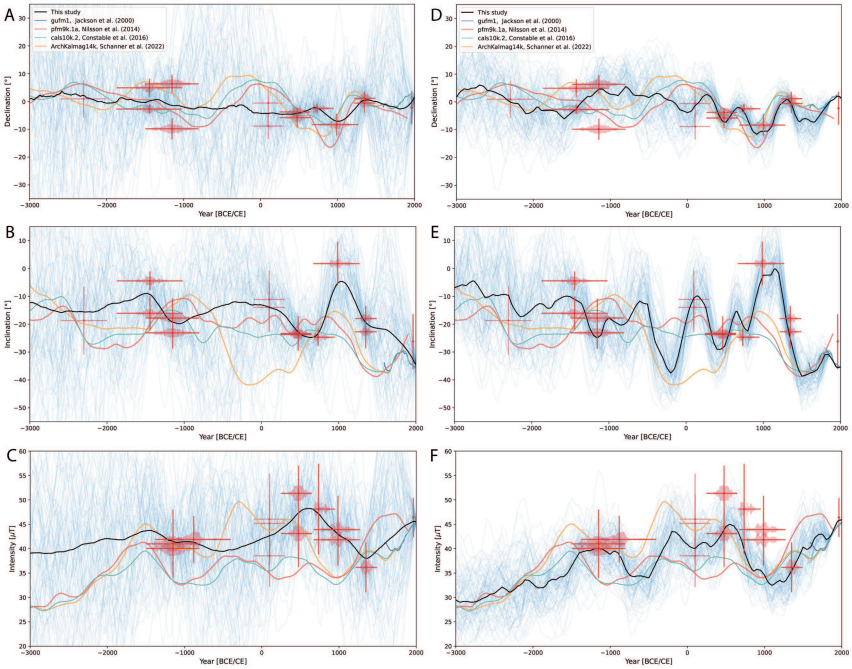


Figure 5.6: Paleosecular variation curve of Bali, Indonesia, from 3000 BCE until 2000 CE. In A-C is the PSV curve generated with a simple prior, in D-F using the pfmk.2 model as a prior. The black line is the PSV curve mean, the light blue lines show samples from the posterior ensemble. In red are the paleomagnetic data points, with error bars for ages and declination, inclination and intensity. Violins are radiocarbon age uncertainties.

If, instead of the pfm9k.2 prior-based PSV curve, the simple prior-based PSV curve best describes the geomagnetic field behaviour, the low intensity at Bali is not observed until 1290 CE. In this alternative scenario, the low intensities reported at Bali cannot be attributed to the SAA and are more likely related to the West Pacific Anomaly (WPA). The WPA is defined as the region where the surface field intensity falls below 35 μT (Yue et al., 2024), with its minimum at 1650 CE located in the ocean between the Philippines and Vietnam. The low intensities in Bali would imply that the WPA was already present before 1600 CE, and stretched farther South than previously recognized.

To determine whether the low intensities observed in the PSV curves from Bali represent the initial phase of the South Atlantic Anomaly, or the West Pacific Anomaly, improved age constraints from the Gunung Agung volcanics, as well as a more comprehensive global field model, are required. Nonetheless, the successful paleodirectional and paleointensity results obtained from these volcanoes indicate that this region is highly suitable for future paleomagnetic studies and it is ideally located to discriminate between these two scenarios.

5.7. Conclusion

We presented the first paleodirectional and paleointensity data for the last 5,000 years obtained from volcanic rocks from Bali, Indonesia. Results from recent lava flows (>1849 CE) from Gunung Batur show inclinations and intensities that are higher than the expected field values, in contrast to many previous studies in other regions that reported lower than expected inclinations and intensities for volcanic samples relative to the corresponding IGRF values. Lavas from Gunung Agung, dated between approximately 5960 ± 70 BP and 1963 CE, yielded 15 reliable directions and 13 paleointensity determinations. From the reliable data, we constructed local PSV curves using both a simple prior and a global geomagnetic field model prior. The latter approach is particularly valuable in regions with sparse paleomagnetic data coverage, such as Indonesia. The PSV curve based on a global geomagnetic field model as a prior records a decrease in paleointensity together with declination changing from negative to positive values around 1000 CE. This is followed by an inclination steepening of ~0.092° per year. Very similar field behaviour is observed a few centuries later in the dataset of La Réunion and Southern Africa. These directional and intensity variations recorded in the lavas of Gunung Agung may reflect the beginning of the South Atlantic Anomaly, or rather an earlier development of the lesser-known West Pacific Anomaly.

5.8. Supplementary Information

Supplementary Table 5.1: Selection criteria. The six paleointensity selection criteria applied to assess the quality of the results. SELCRIT2 (Selkin & Tauxe, 2000), TTA and TTB (Leonhardt et al., 2004), PICRIT03 (Kissel & Laj, 2004), CCRIT (Cromwell et al., 2015b) and CLASS-A (L. V. de Groot et al., 2014a). The first four have the modifications as proposed by Paterson et al. (2014) and all have at least the curvature criterion k' set at ≤ 0.35. All definitions of the criteria can be found in the Standard Paleointensity Definitions v1.1 (Paterson et al., 2014).

Criterion		SELCRIT2	PICRIT03	TTA	TTB	CCRIT	CLASSA
n	≥	4	4	5	5		7
f	≥	0.35	0.35	0.35	0.35	0.7	
β	≤	0.1	0.1	0.1	0.15	0.1	
q	≥	1	2	5	0		
FRAC	≥				0.78		
Gap Max	≤				0.6		
SCAT	≤				TRUE		
DANG	≤				10		
k'	≤	0.35	0.35	0.35	0.35	0.164	0.35
MAD_{anc}	≤	15	7	6	15		7
MAD_{free}	≤					5	
α	≤		15	15	15		10
n_{pTRM}	≥		3				
DRAT	≤	10	10				12.5
CDRAT	≤		11				
δCk	≤			7	9		
δpal	≤			10	18		
$DRAT_{tail}$	≤	10					
δTR	≤			10	20		
δt	≤			9	99		

Supplementary Table 5.2: Age uncertainties for the PSV curve. Successful sampling sites from Gunung Agung with their assigned ages and uncertainties. In case of two radiocarbon ages in Fig. 5.2, the average is used together with the highest or even slightly higher uncertainty. Ages and their uncertainties are given in BP or CE, as a Southern Hemisphere radiocarbon age (14C SH), Gaussian uncertainty or absolute age.

Site	Age	BP or CE	Age Type
A1	1630 ± 40	BP	14C SH
A2	1300 ± 20	BP	14C SH
A3	3225 ± 60	BP	14C SH
A4	3225 ± 60	BP	14C SH
A5	100 ± 100	CE	Gaussian
A6	1630 ± 40	BP	14C SH
A7	100 ± 100	CE	Gaussian
A8	660 ± 50	BP	14C SH
A10	660 ± 50	BP	14C SH
A12	1085 ± 60	BP	14C SH
A13	1085 ± 60	BP	14C SH
A14	100 ± 100	CE	Gaussian
A15	2735 ± 70	BP	14C SH
A19	1963 ± 0	CE	absolute
A26	3225 ± 60	BP	14C SH
A27	3225 ± 60	BP	14C SH
A28	-2300 ± 300	CE	Gaussian



6

Epilogue

This thesis explored the behaviour of the geomagnetic field during the Holocene at five different locations on Earth. Each chapter contributed their own piece to the puzzle of the field's complex variability. **Chapters 1 and 2**, with volcanic rocks from Mt. Etna and La Palma, provided insights into potential sources of bias in paleomagnetic data. **Chapters 3, 4 and 5**, based on field campaigns to the Revillagigedo archipelago, La Réunion and Bali, contributed new knowledge on geomagnetic variability in the Southern Hemisphere and equatorial regions, in particular regarding the South Atlantic Anomaly and the West Pacific Anomaly.

Sampling and Storage Recommendations

For paleomagnetic sampling aimed at constructing local PSV curves or improving global geomagnetic field models, I recommend taking samples distributed over a larger area across the lava flow. As demonstrated in **Chapter 1**, topographically rough and strongly magnetised volcanic terrains may generate local magnetic anomalies. Such local anomalies distort the ambient geomagnetic field and thereby influence the magnetisation a hypothetical new overlying lava flow records. These anomalies appear to be one possible explanation for the frequently observed lower than expected inclinations and intensities in paleomagnetic datasets. This mechanism may explain why recent lavas in this study from the Northern Hemisphere, at Mt. Etna, La Palma, and Revillagigedo, as well as at La Réunion, consistently yield lower than expected field values. In contrast, the recent lavas from Bali (**Chapter 5**), located in the Southern Hemisphere, record higher than expected inclinations and intensities. This raises the question of whether the observed bias is reversed in the Southern Hemisphere, although the data from La Réunion suggest the situation is more complex. Whether a general correction for such bias is possible and required therefore remains uncertain. In **Chapters 2 and 3**, we sampled a single lava flow not only across the flow at one site but also at three different locations. The site-mean directional result was very close to the reference value known from the IGRF. This not only supports the approach of spatially distributed sampling, but also shows the value of sampling the same flow at multiple locations whenever possible. Finally, it is essential to report whether sample orientation was performed using a

magnetic or a sun compass, with the sun compass being the preferred method.

In **Chapter 2**, we obtained samples from a very young lava flow of only up to 3.5 weeks old. Specimens were obtained from the interior and exterior of the flow. Five batches of intensity specimens were prepared: the first was measured immediately upon return to the laboratory in 2021, while four others were stored either randomly oriented in the Earth's magnetic field or in a zero-field environment and were measured in 2024 and 2025. The paleointensity result was on average very accurate, and the success rate of the differently stored batches seemed to be slightly affected by whether samples were stored in-field or in zero-field conditions. Additionally, samples taken from the outside of the lava flow generally yielded higher success rates than those from the interior. Therefore, I recommend that paleomagnetic studies, if possible: 1) store samples in a field free environment immediately after sampling to minimise the process of viscous remanent magnetisation and 2) for paleointensity experiments, use both samples taken from the surface of the flow and from its interior.

Constructing Paleosecular Variation Curves

In the second part of this thesis, we focused on obtaining paleodirectional and paleointensity data from previously underrepresented regions on Earth. We applied the IZZI-Thellier method and used six sets of selection criteria, with an auto-interpreter function to avoid bias, to assess the results. In this way, interpretations that pass more than one set of selection criteria are included as many times as they pass a set of selection criteria and therefore receive more weight. In **Chapter 4**, we also applied the BiCEP method to interpret the IZZI-Thellier data. Paleointensity results are approximately similar for both, confirming the reliability of using these six sets of selection criteria together and averaging the result.

In **Chapters 4 and 5**, we constructed a paleosecular variation (PSV) curve based on carefully selected and reliable paleomagnetic data. For PSV curve construction, we applied a new Bayesian method that allows the use of a prior, developed together with dr. Schanner from GFZ Potsdam and presented in Schanner et al. (2026). The prior can either be a simple constant value that represents a Geocentric Axial Dipole moment, or derived from a global geomagnetic field model. Additionally, with this method, declination, inclination and intensity errors are taken into account while dating uncertainties are explicitly addressed through four age types: absolute/historical ages, uniformly distributed intervals, calibrated radiocarbon ages, and normally distributed estimates. Applying a global field model prior is particularly useful in regions with sparse paleomagnetic data coverage, as it provides additional constraints and prevents the curve from merely connecting the often limited available data points. This code is openly available as the package *pypsv* on GitHub (https://github.com/arthus701/pypsv). For regions with little paleomagnetic data coverage or large age uncertainties, I recommend constructing a PSV curve using both a simple prior and a global geomagnetic field prior. The use of both priors allows comparison between a simple data driven curve and one constrained by global field behaviour, improving the reliability of the final reconstruction.

Tracing the South Atlantic Anomaly through time and space
The paleomagnetic data presented in this thesis helped to close the gap in global data coverage, and the new PSV curve construction method provides additional constraints on the emergence and evolution of the SAA. In **Chapter 4**, the PSV curve from La Réunion suggests that the SAA influenced this region around 1550 CE. Low paleointensities attributed to the SAA are seen in South Africa at 1390 CE (Tarduno et al., 2015). The Bali PSV curves indicate low intensities either around 1300 CE (simple prior) or around 1000 CE (global field prior). Both Bali and La Réunion records show paleointensity lows together with fast directional changes. To connect these datasets, we propose two scenarios. In the first, the SAA influenced the field in Indonesia around 1000 CE and subsequently drifted westwards to Southern Africa. After influencing Southern Africa the anomaly must have expanded or shifted slightly eastwards again to affect La Réunion. In the second scenario, Bali did not experience low field intensities until around 1300 CE. In this case the low intensity does not align with data from Southern Africa and La Réunion, and the SAA must have formed further west. The lower intensities and rapid directional changes at Bali may instead reflect the West Pacific Anomaly, which would mean this anomaly was then already present before 1600 CE, earlier than its currently accepted time of formation. In both scenarios, the La Réunion and Bali paleomagnetic datasets capture an interesting initial phase of either the SAA or WPA.

Outlook
Overall, this thesis provides new paleomagnetic data to improve global data coverage and offers new insights into the onset and development of the South Atlantic Anomaly. To distinguish between the two scenarios above it is important to incorporate all our new data into a new global geomagnetic field model and assess the behaviour of the Earth's magnetic field on the Southern Hemisphere over the past 2000 years. This effort is currently underway, and this new global geomagnetic field model will provide crucial insights into the origin, onset, and evolution of both the SAA and the WPA. Therefore, this future model will also help distinguish between the two scenarios outlined above and in **Chapters 4 and 5**. Ideally, it should also incorporate different types of age determinations and account for measurement uncertainties. Such a future model could also test the hypothesis that observed low intensities are linked to reverse flux patches forming at the margins of the large low shear velocity provinces (LLSVPs).

This thesis provided the first paleomagnetic data for the Holocene from this region and showed most volcanics are highly suitable for paleomagnetic studies, although age constraints are associated with rather large uncertainties. Future paleomagnetic work on recent volcanic products in Indonesia should therefore be done in close collaboration with volcanologists, to prioritise direct dating of the volcanic deposits with radiocarbon dating techniques. Reducing age uncertainties will yield a more robust local PSV curve, which can in turn assist with dating other deposits which in turn may be used to understand the eruption history of hazardous volcanoes and provide stronger constraints for global models. Together, these steps will help to resolve the complex variability of Earth's magnetic field.

Bibliography

Abdu, M., Batista, I., Carrasco, A., & Brum, C. (2005). South atlantic magnetic anomaly ionization: A review and a new focus on electrodynamic effects in the equatorial ionosphere. *Journal of Atmospheric and Solar-Terrestrial Physics*, *67*(17-18), 1643–1657.

Aitken, M., Allsop, A., Bussell, G., & Winter, M. (1988). Determination of the intensity of the earth's magnetic field during archaeological times: Reliability of the thellier technique. *Reviews of Geophysics*, *26*(1), 3–12.

Albert, S., Flores, O., Michon, L., & Strasberg, D. (2020). Dating young (< 1000 yr) lava flow eruptions of piton de la fournaise volcano from size distribution of long-lived pioneer trees. *Journal of Volcanology and Geothermal Research*, *401*, 106974.

Alken, P., Thébault, E., Beggan, C. D., Amit, H., Aubert, J., Baerenzung, J., Bondar, T. N., Brown, W. J., Califf, S., Chambodut, A., Chulliat, A., Cox, G. A., Finlay, C. C., Fournier, A., Gillet, N., Grayver, A., Hammer, M. D., Holschneider, M., Huder, L., … Zhou, B. (2021). International geomagnetic reference field: The thirteenth generation. *Earth, Planets and Space*, *73*(1), 49. https://doi.org/10.1186/s40623-020-01288-x

Amit, H., Terra-Nova, F., Lézin, M., & Trindade, R. I. (2021). Non-monotonic growth and motion of the south atlantic anomaly. *Earth, Planets and Space*, *73*(1), 38.

Aubert, J. (2015). Geomagnetic forecasts driven by thermal wind dynamics in the earth's core. *Geophysical Supplements to the Monthly Notices of the Royal Astronomical Society*, *203*(3), 1738–1751.

Aubert, J., Finlay, C. C., & Fournier, A. (2013). Bottom-up control of geomagnetic secular variation by the earth's inner core. *Nature*, *502*(7470), 219–223.

Baag, C., Helsley, C., Xu, S.-z., & Lienert, B. (1995). Deflection of paleomagnetic directions due to magnetization of the underlying terrain. *Journal of Geophysical Research: Solid Earth*, *100*(B6), 10013–10027.

Beguin, A., Panovska, S., & de Groot, L. (2023). Persistent anomalies in the geomagnetic field arise from top-down control on the geodynamo.

Béguin, A. (2020). Highs, lows, and puzzling intensity variations of the earth's magnetic field. *PhD Thesis, Utrecht University*.

Béguin, A., Paterson, G. A., Biggin, A. J., & de Groot, L. V. (2020). Paleointensity. org: An online, open source, application for the interpretation of paleointensity data. *Geochemistry, Geophysics, Geosystems*, *21*(5), e2019GC008791.

Béguin, A., Pimentel, A., & de Groot, L. V. (2021). Full-vector paleosecular variation curve for the azores: Enabling reliable paleomagnetic dating for the past 2 kyr. *Journal of Geophysical Research: Solid Earth*, *126*(2), e2020JB019745.

Biggin, A. J., Perrin, M., & Dekkers, M. J. (2007). A reliable absolute palaeointensity determination obtained from a non-ideal recorder. *Earth and Planetary Science Letters*, *257*(3-4), 545–563.

Bijaksana, S., Zulaikah, S., & Hodych, J. P. (2009). Magnetic anisotropy and the paleosecular variation record in stalagmites from njirak cave, east java: The effect of detrital magnetite emplaced in small cavities by flooding events. *Indonesian Journal of Physics*, *20*(3), 61–69.

Bohrson, W. A., Reid, M. R., Grunder, A. L., Heizler, M. T., Harrison, T. M., & Lee, J. (1996). Prolonged history of silicic peralkaline volcanism in the eastern pacific ocean. *Journal of Geophysical Research: Solid Earth*, *101*(B5), 11457–11474.

Boteler, D., Pirjola, R., & Nevanlinna, H. (1998). The effects of geomagnetic disturbances on electrical systems at the earth's surface. *Advances in Space Research*, *22*(1), 17–27.

Branca, S., Coltelli, M., Groppelli, G., & Lentini, F. (2011). Geological map of etna volcano, 1: 50,000 scale. *Italian Journal of Geosciences*, *130*(3), 265–291.

Brown, M. C., Donadini, F., Korte, M., Nilsson, A., Korhonen, K., Lodge, A., Lengyel, S. N., & Constable, C. G. (2015). Geomagia50. v3: 1. general structure and modifications to the archeological and volcanic database. *Earth, Planets and Space*, *67*, 1–31.

Bryan, W. B. (1959). *High-silica alkaline lavas of clarion and socorro islands, mexico - their genesis and regional significance*. The University of Wisconsin-Madison.

Bryan, W. B. (1966). History and mechanism of eruption of soda-rhyolite and alkali basalt, socorro island, mexico. *Bulletin Volcanologique*, *29*, 453–479.

Calvari, S., & Pinkerton, H. (1998). Formation of lava tubes and extensive flow field during the 1991–1993 eruption of mount etna. *Journal of Geophysical Research: Solid Earth*, *103*(B11), 27291–27301.

Calvo, M., Prévot, M., Perrin, M., & Riisager, J. (2002). Investigating the reasons for the failure of palaeointensity experiments: A study on historical lava flows from mt. etna (italy). *Geophysical journal international*, *149*(1), 44–63.

Calvo-Rathert, M., Vernet, E., Parés, J. M., Soler, V., Sánchez-Moreno, E.-M., Bógalo, M.-F., Carrancho, Á., Yamamoto, Y., & Rodríguez-Méndez, L. (2024). Reliability of the palaeomagnetic signal recorded in a lava flow erupted on 4 december 2021 in la palma (canary islands, spain). *Geophysical Journal International*, *239*(2), 841–861.

Campuzano, S. A., Gómez-Paccard, M., Pavón-Carrasco, F. J., & Osete, M. L. (2019). Emergence and evolution of the south atlantic anomaly revealed by the new paleomagnetic reconstruction shawq2k. *Earth and Planetary Science Letters*, *512*, 17–26.

Carracedo, J. C., Day, S. J., Guillou, H., & Gravestock, P. (1999). Later stages of volcanic evolution of la palma, canary islands: Rift evolution, giant landslides, and the genesis of the caldera de taburiente. *Geological Society of America Bulletin*, *111*(5), 755–768.

Chevallier, L., & Bachèlery, P. (1981). Evolution structurale du volcan actif du piton de la fournaise, ile de la réunion—océan indien occidental. *Bulletin volcanologique*, *44*, 723–741.

Coe, R. S. (1967). The determination of paleo-intensities of the earth's magnetic field with emphasis on mechanisms which could cause non-ideal behav-

ior in thellier's method. *Journal of geomagnetism and geoelectricity*, *19*(3), 157–179.

Coe, R. S., Grommé, S., & Mankinen, E. A. (1978). Geomagnetic paleointensities from radiocarbon-dated lava flows on hawaii and the question of the pacific nondipole low. *Journal of Geophysical Research: Solid Earth*, *83*(B4), 1740–1756.

Constable, C., & Korte, M. (2006). Is earth's magnetic field reversing? *Earth and Planetary Science Letters*, *246*(1-2), 1–16.

Constable, C., Korte, M., & Panovska, S. (2016). Persistent high paleosecular variation activity in southern hemisphere for at least 10 000 years. *Earth and Planetary Science Letters*, *453*, 78–86.

Courtillot, V., Gallet, Y., Le Mouël, J.-L., Fluteau, F., & Genevey, A. (2007). Are there connections between the earth's magnetic field and climate? *Earth and Planetary Science Letters*, *253*(3-4), 328–339.

Cromwell, G., Johnson, C., Tauxe, L., Constable, C., & Jarboe, N. (2018). Psv10: A global data set for 0–10 ma time-averaged field and paleosecular variation studies. *Geochemistry, Geophysics, Geosystems*, *19*(5), 1533–1558.

Cromwell, G., Tauxe, L., Staudigel, H., & Ron, H. (2015a). Paleointensity estimates from historic and modern hawaiian lava flows using glassy basalt as a primary source material. *Physics of the Earth and Planetary Interiors*, *241*, 44–56. https://doi.org/https://doi.org/10.1016/j.pepi.2014.12.007

Cromwell, G., Tauxe, L., Staudigel, H., & Ron, H. (2015b). Paleointensity estimates from historic and modern hawaiian lava flows using glassy basalt as a primary source material. *Physics of the Earth and Planetary Interiors*, *241*, 44–56.

Cromwell, G., Trusdell, F., Tauxe, L., Staudigel, H., & Ron, H. (2018). Holocene paleointensity of the island of hawaii from glassy volcanics. *Geochemistry, Geophysics, Geosystems*, *19*(9), 3224–3245.

Cych, B., Morzfeld, M., & Tauxe, L. (2021). Bias corrected estimation of paleointensity (bicep): An improved methodology for obtaining paleointensity estimates. *Geochemistry, Geophysics, Geosystems*, *22*(8), e2021GC009755.

Cych, B., Tauxe, L., Cromwell, G., Sinton, J., & Koppers, A. A. (2023). Changes in non-dipolar field structure over the plio-pleistocene: New paleointensity results from hawai'i compared to global data sets. *Journal of Geophysical Research: Solid Earth*, *128*(6), e2023JB026492.

Day, R., Fuller, M., & Schmidt, V. (1977). Hysteresis properties of titanomagnetites: Grain-size and compositional dependence. *Physics of the Earth and planetary interiors*, *13*(4), 260–267.

Dayton, K., Gazel, E., Wieser, P., Troll, V. R., Carracedo, J. C., La Madrid, H., Roman, D. C., Ward, J., Aulinas, M., Geiger, H., et al. (2023). Deep magma storage during the 2021 la palma eruption. *Science advances*, *9*(6), eade7641.

de Groot, B. M., & de Groot, L. V. (2019). A low-cost device for measuring local magnetic anomalies in volcanic terrain. *Geoscientific Instrumentation, Methods and Data Systems*, *8*(2), 217–225.

de Groot, L. V., Dekkers, M. J., & Mullender, T. A. (2012). Exploring the potential of acquisition curves of the anhysteretic remanent magnetization as a tool to

detect subtle magnetic alteration induced by heating. *Physics of the Earth and Planetary Interiors*, *194*, 71–84.

de Groot, L. V., Dekkers, M. J., Visscher, M., & ter Maat, G. W. (2014a). Magnetic properties and paleointensities as function of depth in a hawaiian lava flow. *Geochemistry, Geophysics, Geosystems*, *15*(4), 1096–1112.

de Groot, L. V., Dekkers, M. J., Visscher, M., & ter Maat, G. W. (2014b). Magnetic properties and paleointensities as function of depth in a hawaiian lava flow. *Geochemistry, Geophysics, Geosystems*, *15*(4), 1096–1112.

de Groot, L. V., Mullender, T. A., & Dekkers, M. J. (2013). An evaluation of the influence of the experimental cooling rate along with other thermomagnetic effects to explain anomalously low palaeointensities obtained for historic lavas of mt etna (italy). *Geophysical Journal International*, *193*(3), 1198–1215.

De Groot, L., Biggin, A., Dekkers, M., Langereis, C., & Herrero-Bervera, E. (2013). Rapid regional perturbations to the recent global geomagnetic decay revealed by a new hawaiian record. *Nature communications*, *4*(1), 2727.

de Oliveira, W. P., Hartmann, G. A., Terra-Nova, F., Pasqualon, N. G., Savian, J. F., Lima, E. F., da Luz, F. R., & Trindade, R. I. (2024). Long-term persistency of a strong non-dipole field in the south atlantic. *Nature Communications*, *15*(1), 9447.

De Santis, A., Qamili, E., & Wu, L. (2013). Toward a possible next geomagnetic transition? *Natural Hazards and Earth System Sciences*, *13*(12), 3395–3403.

Dekkers, M. J., & Böhnel, H. N. (2006). Reliable absolute palaeointensities independent of magnetic domain state. *Earth and Planetary Science Letters*, *248*(1-2), 508–517.

Dempsey, S., et al. (2013). *Geochemistry of volcanic rocks from the sunda arc* [Doctoral dissertation, Durham University].

Di Chiara, A., & Pavón-Carrasco, F. J. (2022). A first regional model of the past earth's magnetic field from africa for the last 4000 years. *Physics of the Earth and Planetary Interiors*, *325*, 106855.

Di Mauro, D., Regi, M., Lepidi, S., Del Corpo, A., Dominici, G., Bagiacchi, P., Benedetti, G., & Cafarella, L. (2021). Geomagnetic activity at lampedusa island: Characterization and comparison with the other italian observatories, also in response to space weather events. *Remote Sensing*, *13*(16), 3111.

Domingos, J., Jault, D., Pais, M. A., & Mandea, M. (2017). The south atlantic anomaly throughout the solar cycle. *Earth and Planetary Science Letters*, *473*, 154–163.

Dunlop, D. J. (2002). Theory and application of the day plot (mrs/ms versus hcr/hc) 1. theoretical curves and tests using titanomagnetite data. *Journal of Geophysical Research: Solid Earth*, *107*(B3), EPM–4.

Dunlop, D. J., & Özdemir, Ö. (1997). *Rock magnetism: Fundamentals and frontiers*. Cambridge university press.

Dunlop, D. J., & Özdemir, Ö. (2001). Beyond néel's theories: Thermal demagnetization of narrow-band partial thermoremanent magnetizations. *Physics of the Earth and Planetary Interiors*, *126*(1-2), 43–57.

Dunlop, D. J., Zhang, B., & Özdemir, Ö. (2005). Linear and nonlinear thellier paleointensity behavior of natural minerals. *Journal of Geophysical Research: Solid Earth*, *110*(B1).

Egli, R. (2013). Variforc: An optimized protocol for calculating non-regular first-order reversal curve (forc) diagrams. *Global and Planetary Change*, *110*, 302–320.

Elmaleh, A., Valet, J.-P., Quidelleur, X., Solihin, A., Bouquerel, H., Tesson, T., Mulyadi, E., Khokhlov, A., & Wirakusumah, A. (2004). Palaeosecular variation in java and bawean islands (indonesia) during the brunhes chron. *Geophysical Journal International*, *157*(1), 441–454.

Engbers, Y. A., Grappone, J. M., Mark, D. F., & Biggin, A. J. (2022). Low paleointensities and ar/ar ages from saint helena provide evidence for recurring magnetic field weaknesses in the south atlantic. *Journal of Geophysical Research: Solid Earth*, *127*(3), e2021JB023358.

Fabian, K. (2001). A theoretical treatment of paleointensity determination experiments on rocks containing pseudo-single or multi domain magnetic particles. *Earth and Planetary Science Letters*, *188*(1-2), 45–58.

Fabian, K. (2024). Trapdoor viscous remanent magnetization. *Geophysical Research Letters*, *51*(17), e2023GL107105.

Farmer, J. D., Farmer, M. C., & Berger, R. (1993). Radiocarbon ages of lacustrine deposits in volcanic sequences of the lomas coloradas area, socorro island, mexico. *Radiocarbon*, *35*(2), 253–262.

Finlay, C. C., Aubert, J., & Gillet, N. (2016). Gyre-driven decay of the earth's magnetic dipole. *Nature communications*, *7*(1), 10422.

Finlay, C. C., Kloss, C., Olsen, N., Hammer, M. D., Tøffner-Clausen, L., Grayver, A., & Kuvshinov, A. (2020). The chaos-7 geomagnetic field model and observed changes in the south atlantic anomaly. *Earth, Planets and Space*, *72*(1), 156.

Fisher, R. A. (1953). Dispersion on a sphere. *Proceedings of the Royal Society of London. Series A. Mathematical and Physical Sciences*, *217*(1130), 295–305.

Fleitout, L., & Moriceau, C. (1992). Short-wavelength geoid, bathymetry and the convective pattern beneath the pacific ocean. *Geophysical Journal International*, *110*(1), 6–28.

Fontijn, K., Costa, F., Sutawidjaja, I., Newhall, C. G., & Herrin, J. S. (2015). A 5000-year record of multiple highly explosive mafic eruptions from gunung agung (bali, indonesia): Implications for eruption frequency and volcanic hazards. *Bulletin of Volcanology*, *77*, 1–15.

Friis-Christensen, E., Lühr, H., & Hulot, G. (2006). Swarm: A constellation to study the earth's magnetic field. *Earth, planets and space*, *58*, 351–358.

Fürst, F., Wilms, J., Rothschild, R. E., Pottschmidt, K., Smith, D. M., & Lingenfelter, R. (2009). Temporal variations of strength and location of the south atlantic anomaly as measured by rxte. *Earth and Planetary Science Letters*, *281*(3-4), 125–133.

Goguitchaichvili, A., Greco, C., Ruiz, R. G., Domingorena, L. P., Cejudo, R., Morales, J., Gogorza, C., Scattolin, C., & Tarragó, M. (2019). First archaeointensity reference paleosecular variation curve for south america and its implica-

tions for geomagnetism and archaeology. *Quaternary Research*, *92*(1), 81–97.

Grommé, C., Wright, T., & Peck, D. (1969). Magnetic properties and oxidation of iron-titanium oxide minerals in alae and makaopuhi lava lakes, hawaii. *Journal of Geophysical Research*, *74*(22), 5277–5293.

Gubbins, D., Jones, A. L., & Finlay, C. C. (2006). Fall in earth's magnetic field is erratic. *Science*, *312*(5775), 900–902.

Guilderson, T. P., Reimer, P. J., & Brown, T. A. (2005). The boon and bane of radiocarbon dating. *Science*, *307*(5708), 362–364.

Guillou, H., Singer, B. S., Laj, C., Kissel, C., Scaillet, S., & Jicha, B. R. (2004). On the age of the laschamp geomagnetic excursion. *Earth and Planetary Science Letters*, *227*(3-4), 331–343.

Haberzettl, T., Kasper, T., Stoner, J. S., Rahobisoa, J. J., & Daut, G. (2021). Extending and refining the paleomagnetic secular variation database for southeastern africa (madagascar) to 2500 cal bp. *Earth and Planetary Science Letters*, *565*, 116931.

Haberzettl, T., St-Onge, G., Behling, H., & Kirleis, W. (2013). Evaluating late holocene radiocarbon-based chronologies by matching palaeomagnetic secular variations to geomagnetic field models: An example from lake kalimpaa (sulawesi, indonesia).

Hare, V. J., Tarduno, J. A., Huffman, T., Watkeys, M., Thebe, P. C., Manyanga, M., Bono, R. K., & Cottrell, R. D. (2018). New archeomagnetic directional records from iron age southern africa (ca. 425–1550 ce) and implications for the south atlantic anomaly. *Geophysical Research Letters*, *45*(3), 1361–1369.

Harrison, R. J., & Feinberg, J. M. (2008). Forcinel: An improved algorithm for calculating first-order reversal curve distributions using locally weighted regression smoothing. *Geochemistry, Geophysics, Geosystems*, *9*(5).

He, F., Wei, Y., Maffei, S., Livermore, P. W., Davies, C. J., Mound, J., Xu, K., Cai, S., & Zhu, R. (2021). Equatorial auroral records reveal dynamics of the paleowest pacific geomagnetic anomaly. *Proceedings of the National Academy of Sciences*, *118*(20), e2026080118.

Heirtzler, J. R., Allen, J. H., & Wilkinson, D. C. (2002). Ever-present south atlantic anomaly damages spacecraft. *EOS, Transactions American Geophysical Union*, *83*(15), 165–169.

Hellio, G., & Gillet, N. (2018). Time-correlation-based regression of the geomagnetic field from archeological and sediment records. *Geophysical Journal International*, *214*(3), 1585–1607.

Hill, M. J., & Shaw, J. (1999). Palaeointensity results for historic lavas from mt. etna using microwave demagnetization/remagnetization in a modified thellier-type experiment. *Geophysical Journal International*, *139*(2), 583–590.

Hill, M. J., & Shaw, J. (2000). Magnetic field intensity study of the 1960 kilauea lava flow, hawaii, using the microwave palaeointensity technique. *Geophysical Journal International*, *142*(2), 487–504.

Hogg, A. G., Heaton, T. J., Hua, Q., Palmer, J. G., Turney, C. S., Southon, J., Bayliss, A., Blackwell, P. G., Boswijk, G., Ramsey, C. B., et al. (2020). Shcal20 southern hemisphere calibration, 0–55,000 years cal bp. *Radiocarbon*, *62*(4), 759–778.

Hulme, G. (1974). The interpretation of lava flow morphology. *Geophysical Journal International*, *39*(2), 361–383.

Hulot, G., Eymin, C., Langlais, B., Mandea, M., & Olsen, N. (2002). Small-scale structure of the geodynamo inferred from oersted and magsat satellite data. *Nature*, *416*(6881), 620–623.

Incoronato, A., Angelino, A., Romano, R., Romano, A., Sauna, R., Vanacore, G., & Vecchione, C. (2002). Retrieving geomagnetic secular variations from lava flows: Evidence from mounts arso, etna and vesuvius (southern italy). *Geophysical Journal International*, *149*(3), 724–730.

Jackson, A., Jonkers, A. R., & Walker, M. R. (2000). Four centuries of geomagnetic secular variation from historical records. *Philosophical Transactions of the Royal Society of London. Series A: Mathematical, Physical and Engineering Sciences*, *358*(1768), 957–990.

Kilburn, C. R., & Lopes, R. M. (1988). The growth of aa lava flow fields on mount etna, sicily. *Journal of Geophysical Research: Solid Earth*, *93*(B12), 14759–14772.

Kirana, K. H., Bijaksana, S., King, J., Tamuntuan, G. H., Russell, J., Ngkoimani, L. O., Dahrin, D., & Fajar, S. J. (2018). A high-resolution, 60 kyr record of the relative geomagnetic field intensity from lake towuti, indonesia. *Physics of the Earth and Planetary Interiors*, *275*, 9–18.

Kissel, C., & Laj, C. (2004). Improvements in procedure and paleointensity selection criteria (picrit-03) for thellier and thellier determinations: Application to hawaiian basaltic long cores. *Physics of the Earth and Planetary Interiors*, *147*(2-3), 155–169.

Koenigsberger, J. G. (1938). Natural residual magnetism of eruptive rocks. *Terrestrial magnetism and atmospheric electricity*, *43*(3), 299–320.

Korte, M., Constable, C., Donadini, F., & Holme, R. (2011). Reconstructing the holocene geomagnetic field. *Earth and Planetary Science Letters*, *312*(3-4), 497–505.

Kosterov, A. A., & Prévot, M. (1998). Possible mechanisms causing failure of thellier palaeointensity experiments in some basalts. *Geophysical Journal International*, *134*(2), 554–572.

Koymans, M. R., Langereis, C. G., Pastor-Galán, D., & van Hinsbergen, D. J. (2016). Paleomagnetism. org: An online multi-platform open source environment for paleomagnetic data analysis.

Koymans, M. R., Van Hinsbergen, D., Pastor-Galán, D., Vaes, B., & Langereis, C. (2020). Towards fair paleomagnetic data management through paleomagnetism. org 2.0. *Geochemistry, Geophysics, Geosystems*, *21*(2), e2019GC008838.

Lanza, R., Meloni, A., & Tema, E. (2005). Historical measurements of the earth's magnetic field compared with remanence directions from lava flows in italy over the last four centuries. *Physics of the Earth and Planetary Interiors*, *148*(1), 97–107.

Lawrence, K., Tauxe, L., Staudigel, H., Constable, C., Koppers, A., McIntosh, W., & Johnson, C. (2009). Paleomagnetic field properties at high southern latitude. *Geochemistry, Geophysics, Geosystems*, *10*(1).

Leonhardt, R., Heunemann, C., & Krasa, D. (2004). Analyzing absolute paleointensity determinations: Acceptance criteria and the software thelliertool4. 0. *Geochemistry, Geophysics, Geosystems*, *5*(12).

Lougheed, B. C., & Obrochta, S. P. (2016). Matcal: Open source bayesian 14 c age calibration in matlab. *Journal of Open Research Software*, *4*(1), e42–e42.

Lund, S. P., Stott, L., Schwartz, M., Thunell, R., & Chen, A. (2006). Holocene paleomagnetic secular variation records from the western equatorial pacific ocean. *Earth and Planetary Science Letters*, *246*(3-4), 381–392.

Mahgoub, A. N., Juárez-Arriaga, E., Böhnel, H., Siebe, C., & Pavón-Carrasco, F. J. (2019). Late-quaternary secular variation data from mexican volcanoes. *Earth and Planetary Science Letters*, *519*, 28–39.

Mahgoub, A. N., Korte, M., & Panovska, S. (2023). Global geomagnetic field evolution from 900 to 700 ka including the matuyama-brunhes reversal. *Journal of Geophysical Research: Solid Earth*, *128*(6), e2023JB026593.

Mammerickx, J., Naar, D., & Tyce, R. (1988). The mathematician paleoplate. *Journal of Geophysical Research: Solid Earth*, *93*(B4), 3025–3040.

McDougall, I. (1971). The geochronology and evolution of the young volcanic island of réunion, indian ocean. *Geochimica et Cosmochimica Acta*, *35*(3), 261–288.

Meyer, R., & de Groot, L. V. (2024). Local magnetic anomalies explain bias in paleomagnetic data: Consequences for sampling. *Geochemistry, Geophysics, Geosystems*, *25*(5), e2023GC011319.

Michon, L., Di Muro, A., Villeneuve, N., Saint-Marc, C., Fadda, P., & Manta, F. (2013). Explosive activity of the summit cone of piton de la fournaise volcano (la réunion island): A historical and geological review. *Journal of volcanology and geothermal research*, *264*, 117–133.

Morandi, A., Di Muro, A., Principe, C., Michon, L., Leroi, G., Norelli, F., & Bachèlery, P. (2016). Pre-historic (< 5 kiloyear) explosive activity at piton de la fournaise volcano. *Active Volcanoes of the Southwest Indian Ocean: Piton de la Fournaise and Karthala*, 107–138.

Mullender, T. A., Frederichs, T., Hilgenfeldt, C., de Groot, L. V., Fabian, K., & Dekkers, M. J. (2016). Automated paleomagnetic and rock magnetic data acquisition with an in-line horizontal "2 g" system. *Geochemistry, Geophysics, Geosystems*, *17*(9), 3546–3559.

Mullender, T. A., Van Velzen, A., & Dekkers, M. (1993). Continuous drift correction and separate identification of ferrimagnetic and paramagnetic contributions in thermomagnetic runs. *Geophysical Journal International*, *114*(3), 663–672.

Muxworthy, A. R., & Roberts, A. P. (2007). First-order reversal curve (forc) diagrams.

Nagata, T., Arai, Y., & Momose, K.-i. (1963). Secular variation of the geomagnetic total force during the last 5000 years. *Journal of Geophysical Research*, *68*(18), 5277–5281.

Nasution, A., Haerani, N., Mulyadi, D., & Hendrasto, M. (2004). Peta geologi gunungapi agung. *Bali, Skala*, *1*(50.000).

Néel, L. (1949). Théorie du traınage magnétique des ferromagnétiques en grains fins avec application aux terres cuites. *Annales de géophysique*, *5*, 99–136.

Negredo, A. M., van Hunen, J., Rodríguez-González, J., & Fullea, J. (2022). On the origin of the canary islands: Insights from mantle convection modelling. *Earth and Planetary Science Letters*, *584*, 117506.

Neukirch, L. P., Tarduno, J. A., Huffman, T. N., Watkeys, M. K., Scribner, C. A., & Cottrell, R. D. (2012). An archeomagnetic analysis of burnt grain bin floors from ca. 1200 to 1250 ad iron-age south africa. *Physics of the Earth and Planetary Interiors*, *190*, 71–79.

Newell, A. J. (2005). A high-precision model of first-order reversal curve (forc) functions for single-domain ferromagnets with uniaxial anisotropy. *Geochemistry, Geophysics, Geosystems*, *6*(5).

Nilsson, A., Holme, R., Korte, M., Suttie, N., & Hill, M. (2014). Reconstructing holocene geomagnetic field variation: New methods, models and implications. *Geophysical Journal International*, *198*(1), 229–248.

Nilsson, A., Suttie, N., Stoner, J. S., & Muscheler, R. (2022). Recurrent ancient geomagnetic field anomalies shed light on future evolution of the south atlantic anomaly. *Proceedings of the National Academy of Sciences*, *119*(24), e2200749119.

Ogg, J. (2020). Geomagnetic polarity time scale. In *Geologic time scale 2020* (pp. 159–192). Elsevier.

Olson, P. (2016). Mantle control of the geodynamo: Consequences of top-down regulation. *Geochemistry, Geophysics, Geosystems*, *17*(5), 1935–1956.

Olson, P., & Amit, H. (2006). Changes in earth's dipole. *Naturwissenschaften*, *93*(11), 519–542.

Panovska, S., Korte, M., Finlay, C., & Constable, C. (2015). Limitations in paleomagnetic data and modelling techniques and their impact on holocene geomagnetic field models. *Geophysical Journal International*, *202*(1), 402–418.

Paterson, G. A. (2011). A simple test for the presence of multidomain behavior during paleointensity experiments. *Journal of Geophysical Research: Solid Earth*, *116*(B10).

Paterson, G. A., Heslop, D., & Muxworthy, A. R. (2010). Deriving confidence in paleointensity estimates. *Geochemistry, Geophysics, Geosystems*, *11*(7).

Paterson, G. A., Tauxe, L., Biggin, A. J., Shaar, R., & Jonestrask, L. C. (2014). On improving the selection of thellier-type paleointensity data. *Geochemistry, Geophysics, Geosystems*, *15*(4), 1180–1192.

Pavón-Carrasco, F. J., & De Santis, A. (2016). The south atlantic anomaly: The key for a possible geomagnetic reversal. *Frontiers in Earth Science*, *4*, 188187.

Pavón-Carrasco, F. J., Rodríguez-González, J., Osete, M. L., & Torta, J. M. (2011). A matlab tool for archaeomagnetic dating. *Journal of Archaeological Science*, *38*(2), 408–419. https://doi.org/https://doi.org/10.1016/j.jas.2010.09.021

Pavón-Carrasco, F. J., Tema, E., Osete, M. L., & Lanza, R. (2014). Statistical analysis of palaeomagnetic data from the last four centuries: Evidence of systematic inclination shallowing in lava flow records. *Pure and Applied Geophysics*, *173*(3), 839–848.

Pike, C., & Fernandez, A. (1999). An investigation of magnetic reversal in submicron-scale co dots using first order reversal curve diagrams. *Journal of applied physics*, *85*(9), 6668–6676.

Pike, C. R., Roberts, A. P., & Verosub, K. L. (1999). Characterizing interactions in fine magnetic particle systems using first order reversal curves. *Journal of Applied Physics*, *85*(9), 6660–6667.

Reimer, P. J., Austin, W. E., Bard, E., Bayliss, A., Blackwell, P. G., Ramsey, C. B., Butzin, M., Cheng, H., Edwards, R. L., Friedrich, M., et al. (2020). The intcal20 northern hemisphere radiocarbon age calibration curve (0–55 cal kbp). *Radiocarbon*, *62*(4), 725–757.

Reubi, O., & Nicholls, I. A. (2004). Variability in eruptive dynamics associated with caldera collapse: An example from two successive eruptions at batur volcanic field, bali, indonesia. *Bulletin of volcanology*, *66*, 134–148.

Richards, A. F. (1959). Geology of the islas revillagigedo, mexico: 1. birth and development of volcán bárcena, isla san benedicto (1). *Bulletin Volcanologique*, *22*, 73–123.

Richards, A. F. (1965). Geology of the islas revillagigedo, 3. effects of erosion on isla san benedicto 1952–61 following the birth of volcán bárcena. *Bulletin Volcanologique*, *28*, 381–403.

Richards, A. F. (1966). *Geology of the islas revillagigedo, méxico: 2. geology and petrography of isla san benedicto*.

Roberts, A. P., Almeida, T. P., Church, N. S., Harrison, R. J., Heslop, D., Li, Y., Li, J., Muxworthy, A. R., Williams, W., & Zhao, X. (2017). Resolving the origin of pseudo-single domain magnetic behavior. *Journal of Geophysical Research: Solid Earth*, *122*(12), 9534–9558.

Roberts, A. P., Heslop, D., Zhao, X., & Pike, C. R. (2014). Understanding fine magnetic particle systems through use of first-order reversal curve diagrams. *Reviews of Geophysics*, *52*(4), 557–602.

Roberts, A. P., Pike, C. R., & Verosub, K. L. (2000). First-order reversal curve diagrams: A new tool for characterizing the magnetic properties of natural samples. *Journal of Geophysical Research: Solid Earth*, *105*(B12), 28461–28475.

Roberts, A. P., Tauxe, L., Heslop, D., Zhao, X., & Jiang, Z. (2018). A critical appraisal of the “day” diagram. *Journal of Geophysical Research: Solid Earth*, *123*(4), 2618–2644.

Rolph, T. (1997). An investigation of the magnetic variation within two recent lava flows. *Geophysical Journal International*, *130*(1), 125–136.

Rolph, T., & Shaw, J. (1986). Variations of the geomagnetic field in sicily. *Journal of geomagnetism and geoelectricity*, *38*(12), 1269–1277.

Rolph, T., Shaw, J., & Guest, J. (1987). Geomagnetic field variations as a dating tool: Application to sicilian lavas. *Journal of archaeological science*, *14*(2), 215–225.

Sagnotti, L., Giaccio, B., Liddicoat, J. C., Nomade, S., Renne, P. R., Scardia, G., & Sprain, C. J. (2016). How fast was the matuyama–brunhes geomagnetic reversal? a new subcentennial record from the sulmona basin, central italy. *Geophysical Journal International*, *204*(2), 798–812.

Sagnotti, L., Scardia, G., Giaccio, B., Liddicoat, J. C., Nomade, S., Renne, P. R., & Sprain, C. J. (2014). Extremely rapid directional change during matuyama-brunhes geomagnetic polarity reversal. *Geophysical Journal International*, *199*(2), 1110–1124.

Santos, C. N., & Tauxe, L. (2019). Investigating the accuracy, precision, and cooling rate dependence of laboratory-acquired thermal remanences during pale-

ointensity experiments. *Geochemistry, Geophysics, Geosystems*, *20*(1), 383–397.

Sbarbori, E., Tauxe, L., Goguitchaichvili, A., Urrutia-Fucugauchi, J., & Bohrson, W. A. (2009). Paleomagnetic behavior of volcanic rocks from isla socorro, mexico. *Earth, planets and space*, *61*, 191–204.

Schanner, M., Korte, M., & Holschneider, M. (2022). Archkalmag14k: A kalman-filter based global geomagnetic model for the holocene. *Journal of Geophysical Research: Solid Earth*, *127*(2), e2021JB023166.

Schanner, M., Meyer, R., & de Groot, L. (2026). Bayesian inference of local paleosecular variation from sparse paleomagnetic data. *Journal of Geophysical Research: Solid Earth*, *131*(2), e2025JB032670.

Schurr, K., Soffel, H., Becker, H., et al. (1985). Archaeomagnetic study of medieval fireplaces at mannheim-wallstadt and ovens from herrenchiemsee (southern germany) and the problem of magnetic refraction. *Journal of Geophysics*, *56*(1), 1–8.

Self, S., & King, A. J. (1996). Petrology and sulfur and chlorine emissions of the 1963 eruption of gunung agung, bali, indonesia. *Bulletin of Volcanology*, *58*, 263–285.

Selkin, P. A., Gee, J. S., & Tauxe, L. (2007). Nonlinear thermoremanence acquisition and implications for paleointensity data. *Earth and Planetary Science Letters*, *256*(1-2), 81–89.

Selkin, P. A., & Tauxe, L. (2000). Long-term variations in palaeointensity. *Philosophical Transactions of the Royal Society of London. Series A: Mathematical, Physical and Engineering Sciences*, *358*(1768), 1065–1088.

Shaar, R., & Feinberg, J. M. (2013). Rock magnetic properties of dendrites: Insights from mfm imaging and implications for paleomagnetic studies. *Geochemistry, Geophysics, Geosystems*, *14*(2), 407–421.

Shaar, R., & Tauxe, L. (2015). Instability of thermoremanence and the problem of estimating the ancient geomagnetic field strength from non-single-domain recorders. *Proceedings of the National Academy of Sciences*, *112*(36), 11187–11192.

Shah, J., Koppers, A. A., Leitner, M., Leonhardt, R., Muxworthy, A. R., Heunemann, C., Bachtadse, V., Ashley, J. A., & Matzka, J. (2016). Palaeomagnetic evidence for the persistence or recurrence of geomagnetic main field anomalies in the south atlantic. *Earth and Planetary Science Letters*, *441*, 113–124.

Sherwood, G. J. (1991). Evaluation of a multi-specimen approach to palaeointensity determination. *Journal of geomagnetism and geoelectricity*, *43*(5), 341–349.

Siebe, C., Komorowski, J.-C., Navarro, C., McHone, J., Delgado, H., & Cortés, A. (1995). Submarine eruption near socorro island, mexico: Geochemistry and scanning electron microscopy studies of floating scoria and reticulite. *Journal of Volcanology and Geothermal Research*, *68*(4), 239–271.

Smirnov, A. V., Kulakov, E. V., Foucher, M. S., & Bristol, K. E. (2017). Intrinsic paleointensity bias and the long-term history of the geodynamo. *Science Advances*, *3*(2), e1602306.

Speranza, F., Branca, S., Coltelli, M., D'Ajello Caracciolo, F., & Vigliotti, L. (2006). How accurate is "paleomagnetic dating"? new evidence from historical lavas from mount etna. *Journal of Geophysical Research: Solid Earth*, *111*(B12).

Suryanata, P. B., Bijaksana, S., Dahrin, D., Nugraha, A. D., Harlianti, U., Putra, P. R. A., Fajar, S. J., Suandayani, N. K. T., Pratama, A., Gumilang, M. F., et al. (2024). Subsurface structure of bali island inferred from magnetic and gravity modeling: New insights into volcanic activity and migration of volcanic centers. *International Journal of Earth Sciences*, *113*(3), 523–538.

Sutawidjaja, I. S. (2009). Ignimbrite analyses of batur caldera, bali, based on 14c dating. *Indonesian Journal on Geoscience*, *4*(3), 189–202.

Sutawidjaja, I. S., Chaniago, R., Kamal, S., & Modjo, W. (1992). Geological map of batur caldera, bali, indonesia. *Volcanological Survey of Indonesia, Bandung*.

Syafitri, A., Sucipta, I. G. B. E., Arifa, A. N., Saepuloh, A., & Widiyantoro, S. (2021). Pre-1963 mount agung eruption history and magma evolution based on petrological, mineralogical, and geochemical analysis. *Indonesian Association of Geologists Journal (IAGI Journal)*, *1*(3), 121–136.

Tanaka, H., Hashimoto, Y., & Morita, N. (2012). Palaeointensity determinations from historical and holocene basalt lavas in iceland. *Geophysical Journal International*, *189*(2), 833–845.

Tanguy, J. (1990). Abnormal shallow palaeomagnetic inclinations from the 1950 and 1972 lava flows, hawaii. *Geophysical Journal International*, *103*(1), 281–283.

Tanguy, J., Bachèlery, P., & LeGoff, M. (2011). Archeomagnetism of piton de la fournaise: Bearing on volcanic activity at la réunion island and geomagnetic secular variation in southern indian ocean. *Earth and Planetary Science Letters*, *303*(3-4), 361–368.

Tanguy, J., Bucur, I., & Thompson, J. (1985). Geomagnetic secular variation in sicily and revised ages of historic lavas from mount etna. *Nature*, *318*(6045), 453–455.

Tanguy, J., Le Goff, M., Chillemi, V., Paiotti, A., Principe, C., La Delfa, S., & Patane, G. (1999). Secular variation of the geomagnetic field direction recorded in lavas from etna and vesuvius during the last two millennia. *COMPTES RENDUS DE L ACADEMIE DES SCIENCES SERIE II FASCICULE A-SCIENCES DE LA TERRE ET DES PLANETES*, *329*(8), 557–564.

Tanguy, J., & Le Goff, M. (2004). Distortion of the geomagnetic field in volcanic terrains: An experimental study of the mount etna stratovolcano. *Physics of the Earth and Planetary Interiors*, *141*(1), 59–70.

Tanguy, J., Le Goff, M., Principe, C., Arrighi, S., Chillemi, V., Paiotti, A., La Delfa, S., & Patanè, G. (2003). Archeomagnetic dating of mediterranean volcanics of the last 2100 years: Validity and limits. *Earth and Planetary Science Letters*, *211*(1-2), 111–124.

Tarduno, J. A., Watkeys, M. K., Huffman, T. N., Cottrell, R. D., Blackman, E. G., Wendt, A., Scribner, C. A., & Wagner, C. L. (2015). Antiquity of the south atlantic anomaly and evidence for top-down control on the geodynamo. *Nature Communications*, *6*(1), 7865.

Tarling, D., Hammo, N., & Downey, W. (1986). The scatter of magnetic directions in archaeomagnetic studies. *Geophysics*, *51*(3), 634–639.

Tarquini, S., Favalli, M., Mazzarini, F., Isola, I., & Fornaciai, A. (2012). Morphometric analysis of lava flow units: Case study over lidar-derived topography

at mount etna, italy. *Journal of volcanology and geothermal research*, *235*, 11–22.

Tauxe, L. (2010). *Essentials of paleomagnetism*. Univ of California Press.

Tauxe, L., Asefaw, H., Behar, N., Koppers, A. A., & Shaar, R. (2022). Paleointensity estimates from the pleistocene of northern israel: Implications for hemispheric asymmetry in the time-averaged field. *Geochemistry, Geophysics, Geosystems*, *23*(9), e2022GC010473.

Tauxe, L., Bertram, H. N., & Seberino, C. (2002). Physical interpretation of hysteresis loops: Micromagnetic modeling of fine particle magnetite. *Geochemistry, Geophysics, Geosystems*, *3*(10), 1–22.

Tauxe, L., & Kent, D. V. (2004). A simplified statistical model for the geomagnetic field and the detection of shallow bias in paleomagnetic inclinations: Was the ancient magnetic field dipolar? *Timescales of the paleomagnetic field*, *145*, 101–115.

Tauxe, L., Pick, T., & Kok, Y. (1995). Relative paleointensity in sediments: A pseudothellier approach. *Geophysical Research Letters*, *22*(21), 2885–2888.

Tauxe, L., Santos, C., Cych, B., Zhao, X., Roberts, A. P., Nagy, L., & Williams, W. (2021). Understanding nonideal paleointensity recording in igneous rocks: Insights from aging experiments on lava samples and the causes and consequences of "fragile" curvature in arai plots. *Geochemistry, Geophysics, Geosystems*, *22*(1), e2020GC009423.

Tauxe, L., & Staudigel, H. (2004). Strength of the geomagnetic field in the cretaceous normal superchron: New data from submarine basaltic glass of the troodos ophiolite. *Geochemistry, Geophysics, Geosystems*, *5*(2).

Taylor, R. E., Stuiver, M., & Reimer, P. J. (1996). Development and extension of the calibration of the radiocarbon time scale: Archaeological applications. *Quaternary Science Reviews*, *15*(7), 655–668.

Terra-Nova, F., Amit, H., Hartmann, G. A., Trindade, R. I., & Pinheiro, K. J. (2017). Relating the south atlantic anomaly and geomagnetic flux patches. *Physics of the Earth and Planetary Interiors*, *266*, 39–53.

Thellier, E. (1977). Early research on the intensity of the ancient geomagnetic field. *Physics of the Earth and Planetary Interiors*, *13*(4), 241–244.

Thellier, E. (1938). Sur l'aimantation des terres cuites et ses applications géophysiques. *Ann. Inst. Physique du Globe, Univ. Paris*, *16*, 157–302.

Thellier, E. (1959). Sur l'intensite du shamp magnetique terrestre dans le passe historique et geologique. *Ann. Geophys.*, *15*, 285–376.

Trindade, R. I., Jaqueto, P., Terra-Nova, F., Brandt, D., Hartmann, G. A., Feinberg, J. M., Strauss, B. E., Novello, V. F., Cruz, F. W., Karmann, I., et al. (2018). Speleothem record of geomagnetic south atlantic anomaly recurrence. *Proceedings of the National Academy of Sciences*, *115*(52), 13198–13203.

Trivedi, N., Pathan, B., Schuch, N. J., Barreto, M., & Dutra, L. (2005). Geomagnetic phenomena in the south atlantic anomaly region in brazil. *Advances in Space Research*, *36*(10), 2021–2024.

Troll, V. R., & Carracedo, J. C. (2016). *The geology of the canary islands*. Elsevier.

Urrutia-Fucugauchi, J., Alva-Valdivia, L., Goguitchaichvili, A., Rivas, M., & Morales, J. (2004). Palaeomagnetic, rock-magnetic and microscopy studies of historic lava flows from the paricutin volcano, mexico: Implications for the

deflection of palaeomagnetic directions. *Geophysical Journal International*, *156*(3), 431–442.

Valet, J.-P., & Soler, V. (1999). Magnetic anomalies of lava fields in the canary islands. possible consequences for paleomagnetic records. *Physics of the earth and planetary interiors*, *115*(2), 109–118.

van Grinsven, L., Béguin, A., Kuiper, K. F., & de Groot, L. V. (2025). The evolution of a mid-miocene geomagnetic reversal. *Earth and Planetary Science Letters*, *667*, 119464.

van Grinsven, L., van Leeuwen, T., & de Groot, L. V. (2023). An end-member modelling approach to pseudo-thellier palaeointensity data. *Geophysical Journal International*, *235*(3), 2707–2715.

Venzke. (2025). Volcanoes of the world (v. 5.3.1; 6 aug 2025) [Global Volcanism Program. Distributed by Smithsonian Institution, compiled by Venzke, E.]. https://doi.org/10.5479/si.GVP.VOTW5-2025.5.3

Villasante-Marcos, V., & Pavón-Carrasco, F. J. (2014). Palaeomagnetic constraints on the age of lomo negro volcanic eruption (el hierro, canary islands). *Geophysical Journal International*, *199*(3), 1497–1514.

Von Humboldt, A. (1811). *Political essay on the kingdom of new spain...* (Vol. 1). I. Riley.

Walton, D., Share, J., Rolph, T., & Shaw, J. (1993). Microwave magnetisation. *Geophysical research letters*, *20*(2), 109–111.

Watkins, N. (1973). Brunhes epoch geomagnetic secular variation on reunion island. *Journal of Geophysical Research*, *78*(32), 7763–7768.

Yamamoto, Y., Tsunakawa, H., & Shibuya, H. (2003). Palaeointensity study of the hawaiian 1960 lava: Implications for possible causes of erroneously high intensities. *Geophysical Journal International*, *153*(1), 263–276.

Ye, Y., Zou, H., Zong, Q., Chen, H., Wang, Y., Yu, X., & Shi, W. (2017). The secular variation of the center of geomagnetic south atlantic anomaly and its effect on the distribution of inner radiation belt particles. *Space Weather*, *15*(11), 1548–1558.

Yu, Y. (2011). Importance of cooling rate dependence of thermoremanence in paleointensity determination. *Journal of Geophysical Research: Solid Earth*, *116*(B9).

Yu, Y., Dunlop, D. J., & Özdemir, Ö. (2003). Are arm and trm analogs? thellier analysis of arm and pseudo-thellier analysis of trm. *Earth and Planetary Science Letters*, *205*(3-4), 325–336.

Yu, Y., & Tauxe, L. (2006). Acquisition of viscous remanent magnetization. *Physics of the Earth and Planetary interiors*, *159*(1-2), 32–42.

Yue, Y., Gao, J., He, F., Wei, Y., Cai, S., Wang, H., Wang, Y., Rong, Z., Yao, Z., Lin, W., et al. (2024). Evolution and disappearance of the paleo-west pacific anomaly: Implications to the future of south atlantic anomaly. *Physics of the Earth and Planetary Interiors*, *353*, 107214.

Zijderveld, J. (1967). A.c. demagnetization of rocks: Analysis of results. In *D.w. collinson, k.m. crees, s.k. runcorn (eds.), methods in paleomagnetism* (pp. 254–286). Elsevier, Amsterdam.

Curriculum Vitæ

Romy Meyer

18-03-1996	Born in Gouda, the Netherlands.

Working Experience

2021–2025	PhD Candidate Utrecht University, the Netherlands
2019–2020	Teaching Assistant Utrecht University, the Netherlands
2013–2019	Various service oriented roles Restaurant de Zakkendrager, Doen Uitzendbureau, Axioncontinu, Jaarbeurs Utrecht, MCD

Education

2019–2021	M.Sc. in Earth Structure and Dynamics Utrecht University, the Netherlands
2014–2017	B.Sc. in Earth Sciences Utrecht University, the Netherlands

Extracurricular activities

2021–2022	Board member of the bouldering association UBoulder
2020–2021	Volunteer at a homeless shelter in Utrecht
2018–2019	Secretary at the Utrechtse Aardwetenschappen Vereniging
2017–2018	Gap year with a trip through Australia, New-Zealand, South-East Asia, China and Tibet.
2015–2020	Committee member at the Utrechtse Aardwetenschappen Vereniging.

Supervision

2025	Guided Research Duco van der Woude *The effects of ageing on the success rate of paleointensity studies: A case study for La Palma, Canary Islands, Spain*
2025	Guided Research Maria Karatzanou *Obtaining paleomagnetic data from recent lava flows in Indonesia*

Publications

Meyer, R., & de Groot, L. V. (2024). Local magnetic anomalies explain bias in paleomagnetic data: Consequences for sampling. Geochemistry, Geophysics, Geosystems, 25(5).

Schanner, M. A., **Meyer, R.**, & de Groot, L. V. (2026). Bayesian Inference of local paleosecular variation from sparse paleomagnetic data. Journal of Geophysical Research: Solid Earth, 131(2).

Meyer, R., van Hinsbergen, D.J.J., Dávila-Harris, P., Lippert, P.C., Philippon, M. & de Groot, L.V. A reconnaissance of Quaternary paleomagnetic directions and paleointensities in the East Pacific Ocean (Isla Socorro and Isla San Benedicto, Revillagigedo Archipelago, Mexico). Submitted to Physics of the Earth and Planetary Interiors.

Outreach

2024	NPO Radio 1 interview about the South Atlantic Anomaly
2023	Article in the Dutch Physics journal about the Earth's magnetic field and the fieldwork on Fiji
2022	Summer School Science Communication
2021	NPO Radio 1 interview about the fieldwork on the active Cumbre Vieja volcano
2021	NOS Jeugdjournaal covered our research on La Palma
2021	The Volkskrant, extensively covered our fieldwork during the Cumbre Vieja eruption on La Palma

List of pictures

vi Gunung Agung, Indonesia
10 Fort Hoofddijk in winter
20 Samples of site R1 on Socorro Island
68 Tajogaite volcanic eruption, La Palma
95 Sampling on Socorro Island, with Mélody Philippon
128 Sunset from Taveuni Island, Fiji
153 Sunrise on Gunung Agung, Indonesia
179 Cycling along the Carretera Austral, Chile
202 Ice skating with the parents, the Netherlands



Acknowledgements

Dit boekje is tot stand gekomen met de steun van een heleboel mensen, al vanaf de start van mijn studie Aardwetenschappen in 2014. Allereerst natuurlijk **Lennart**, bedankt voor alle begeleiding tijdens deze PhD. Zoals ik al vaker zeg: een baan zoals deze ga ik niet snel meer vinden. Dank voor al het vertrouwen in mijn veldwerkplan skills! Ik ben je ook dankbaar voor de vrijheid die je geeft, en voor je enthousiasme voor alles wat naast de wetenschap speelt, zoals de wetenschapscommunicatie. Ook veel dank aan mijn tweede promotor, **Wout**, voor de gezellige praatjes in het Fort en het doorlezen van de laatste versie van mijn scriptie. **Douwe**, bedankt voor de begeleiding van zowel mijn bachelorscriptie als mijn master guided research, voor het vertrouwen in mijn veldwerkenthousiasme en natuurlijk voor dat fantastische veldwerk naar de Revillagigedo eilanden.

Deze vier jaar zijn vooral ook zo leuk geworden door de fijnste mede PhD'ers in het Fort. Allereerst **Liz**, veldwerk partner in crime en mijn paranimf. Wat een team waren we. Je bent een heel fijn persoon om mee samen te werken en ook de lange reisdagen (Amsterdam-Fiji, of de 24-uurs boot vanaf Taveuni) werden een stuk leuker met jou. Wat een fantastische avonturen hebben we beleefd! Daarnaast mijn office-maatje **Rosa**, bedankt dat ik altijd bij je terecht kon om een beetje te klagen, koffie te halen, of met je kon lachen om rare e-mails. Dan natuurlijk **Martha** en **Frenk** in het andere kantoor, waar ik altijd even mocht aanschuiven voor een praatje, of om te puzzelen. **Bertwin** en **Maxim**, bedankt voor alle hulp bij alles met een stekker of met het voorbereiden van de veldwerkmaterialen, wat natuurlijk altijd op het laatste moment moest gebeuren. Ook dank aan alle andere collega's op het Fort die er over deze vier jaar heen geweest zijn, **Mark, Chiang, Ge, Dan, Sophie, Gijs, David, Yong Fa, Mike, Sergei en Federico**. Aan het team van het eerstejaarsveldwerk voor alle gezelligheid en leermomenten in Aliaga en Pompidou: **Lydian, Erik, Suzanna, Bram, Leo, Eldert, Kalijn, Emilia, Niklas, Andrea** en **Alejandra**. Dit veldwerk bracht me weer heel dicht bij de geologie. Daarnaast een bedankje aan alle andere mensen bij de UU, **Rûna, Hen, Agnes** en **Vincent**

All the fieldwork would not have happened without the help of many people. For Revillagigedo: **Pablo Davila-Harris , Peter C. Lippert, Mélody Philippon, Janne Koorneef, Yamirka Rojas-Agramonte, Christian Winter, Roberto Hassán Téllez Vizcaíno, Laurens Tromp** and the staff from the *Quino el Guardian*. For the fieldwork to Fiji, **Livai, Nilesh, Ili** and **Maureen**. The fieldwork to Bali would not have happened without **Annemarie, Maria, Aditya, Fadil, Billy** and **Willy**. I would also like to thank the local people at all locations for their hospitality and for making me feel welcome.

Natuurlijk was mijn studie en PhD tijd niet zo leuk geweest zonder een hele fijne vriendengroep. Dankjulliewel **Silke, David, Tycho, Rens, Ymke, Kari-Ann, Katinka,**

Ana, Tjeerd, Thomas, Bram en mijn paranimf **Job** voor alle gezelligheid op weekenden weg, (ski)vakanties, festivals en etentjes. Ook een dankjewel aan **Simone**, voor de fijne lunches op de Uithof en al die jaren vriendschap. Buiten de PhD heb ik ook veel gehad aan de mensen bij UBoulder, de wielrengroepjes, het U.A.V. bestuur, en mijn oude huisgenoten. In het bijzonder: **Kathy** voor alle gezelligheid bij een goed glas wijn, en degenen die me voor het eerst op een racefiets hebben gezet, dankjewel **Jannie** en **Daan**!

Als laatste een dankjewel aan mijn oma en alle andere familie, die me altijd zo enthousiast op Polarsteps volgen. Mijn leuke broer(tje) **Maarten**, bedankt voor alle Strava kudo's en wat vet dat jij nu ook zo'n mooie reis hebt gemaakt.

Heel veel dank gaat uit naar mijn lieve **papa** en **mama**. Jullie staan altijd achter me, halen en brengen me het liefst weg voor elk veldwerk, en hebben zeker mijn liefde en interesse voor de aarde aangewakkerd met die fossielen- en goudzoekacties op zomervakanties.

Lieve **Elise**, wat een fantastische avonturen hebben wij al beleefd. Dankjewel dat je me support met alles wat ik wil doen, met me op een fiets stapt in Zuid-Amerika, bordspelletjes leuk maakt en me aanspoort om voor dromen te gaan. Ik ben benieuwd naar onze toekomst samen!

Utrecht University
Faculty of Geosciences
Department of Earth Sciences



ISSN 2211-4335